IN-SITU ANALYSIS OF $La_{0.6}Sr_{0.4}Co_{0.2}Fe_{0.8}O_{3-\delta}$ SURFACES IN AMBIENT ATMOSPHERES



MATHEW A. R. NIANIA

2016

SUBMITTED IN PART FULFILMENT OF
THE REQUIREMENTS FOR THE
DEGREE OF DOCTOR OF
PHILOSOPHY AT IMPERIAL COLLEGE
LONDON DEPARTMENT OF
MATERIALS

DECLARATION

I hereby declare that this thesis and the work reported within is a product of my own original research. Information derived from sources beyond this work has been given dueful acknowledgment and been referenced appropriately.

The copyright of this thesis rests with the author and is made available under a Creative Commons Attribution Non-Commercial No Derivatives licence. Researchers are free to copy, distribute or transmit the thesis on the condition that they attribute it, that they do not use it for commercial purposes and that they do not alter, transform or build upon it. For any reuse or redistribution, researchers must make clear to others the licence terms of this work.

Mathew A. R. Niania, 2016



Ko te pae tawhiti, whaia kia tata
Ko te pae tata, whaia kia tina

Seek those distant horizons
Once achieved, hold them steadfastly with sincerity

— Maori proverb

Dedicated to the loving memory of Robert W. Jones
1929 – 2013

He tohu whakamaharatanga mo taku arohanui, ki taku tipuna whaea, a Ramari Niania
1936 – 2016

ABSTRACT

The $La_{0.6}Sr_{0.4}Co_{0.2}Fe_{0.8}O_{3-\delta}$ material system is a desirable material for a Solid Oxide Fuel Cell (SOFC) cathode due to its Mixed Ionic-Electronic Conducting (MIEC) properties. It has been utilised commercially for many years, however, the cell lifetime is inhibited by degradation processes passivating the surface of the electrode. A-site cation segregation is believed to be a primary degradation mechanism due to the formation of electronically insulating secondary phase particles reducing the active surface area that facilitates the oxygen reduction reaction. Numerous reports have studied the overall effect that degradation has on SOFC cell performance, however, it is still unclear the extent to which microstructural changes affect a material's oxygen exchange properties.

To date, many studies measuring the oxygen exchange rate utilised pure oxygen atmospheres in order to isolate the effect of oxygen. However, for cost and practicality reasons, the desired gas stream for SOFC is ambient air. Multiple oxygen-containing gaseous components and impurities (such as CO, CO_2, H_2O, SO_2 and NO_x) are contained within ambient air and have been shown to alter the oxygen exchange rate or enhance the degradation of MIEC materials. This work focuses upon characterising the effect ambient air has upon the surface microstructure and oxygen exchange rate of the $La_{0.6}Sr_{0.4}Co_{0.2}Fe_{0.8}O_{3-\delta}$ system.

In-situ High-Temperature Environmental Scanning Electron Microscopy (HT-ESEM) was used to analyse the growth rate and growth behaviour of strontium-based particles in pure O_2, pure H_2O, ambient air and vacuum environments. The HT-ESEM data was directly compared to Electron Backscattered Diffraction crystal orientation data in order to understand what effect the $La_{0.6}Sr_{0.4}Co_{0.2}Fe_{0.8}O_{3-\delta}$ domain structure had upon the segregation of strontium. It was observed that the surface microstructure has a strong influence on the growth behaviour and growth kinetics of the particles.

A common methodology for measuring oxygen self-diffusivity and surface exchange rates is Isotopic Exchange Depth Profiling (IEDP). This traditionally has used pure oxygen as the anneal environment to isolate the exchange properties of the O_2 species, however, in the presence of other oxygen containing species the exchange process will be more complicated. In order to analyse the surface

exchange rate in ambient air (or any other atmosphere containing a consistent oxygen partial pressure), the novel 'back-exchange' technique was developed. Initial development of the technique has demonstrated its validity and confirmed enhancement of the oxygen exchange rate in ambient air over pure oxygen.

Time-of-Flight (ToF) SIMS was used to measure isotopically exchanged diffusion profiles. For materials with a high oxygen self-diffusivity, such as $La_{0.6}Sr_{0.4}$-$Co_{0.2}Fe_{0.8}O_{3-\delta}$, the 'line-scan' method must be employed instead of a standard depth profile. The ToF-SIMS utilises a statistical method in order to correct for detector 'dead time', however, this method relies upon the total ion count to remaining constant across each pixel of the raster area. The line-scan method relies upon analysis of a surface perpendicular to the original exchange surface and as such will not have a constant ion count near the sample edge. Errors associated with the measured diffusion profile are discussed and an optimised sample preparation has been proposed.

"Beer solves everything"
— J. Kilner

ACKNOWLEDGMENTS

Firstly, I must thanks my supervisors Prof. John Kilner and Prof. Stephen Skinner. Through success and adversity their continued support and keen critical dexterity has lead me down a delightfully interesting and fulfilling path both in and outside the lab. It has been a pleasure and a privilege to have been presented with the opportunity to work and learn from them both.

To all of my colleagues in the Electroceramics group: I am indebted to you for ceaselessly providing a warm, supportive and, above all, highly academic environment. Members new and old, everyone's company has been a joy and I will remember all of the adventures we've had together. To those still around I'm sure there's plenty left to explore. To those who've flown the nest, Friday afternoon will never be the same again. I must extend a particular thanks to my collaborator and good friend Dr Sam Cooper; where, without his tireless enthusiasm, mathematical prowess and coding fascination I would probably not be here now to write this.

I would also like to thank Dr Sarah Fearn and Dr Richard Chater for their patience, support and guidance on all things SIMS; Dr Helena Tellez, Dr John Druce and Prof. Tatsumi Ishihara for indulging my experimental idea and bringing it from idea to reality (also for providing me with a truly wonderful Japanese experience!); Dr Ben Britton for going out of his way to help me with a large chunk of work despite (literally) being introduced to the work in passing; and Dr Renaud Podor for being possibly the most genuine and kind individual I have had the pleasure of meeting. At every point our collaboration has been enjoyable and I can only hope the future holds more work together.

For funding this PhD, sending me to numerous international conferences and funding international collaborations, thanks are of course due to the Engineering and Physical Sciences Research Council (EP/J003085/1).

To my fellow MEng reprobates. Without years of diligent distraction I would probably have gone mad. Cheers!

Finally, I would like to thank my family around the world for their ever present loving support. Much love; Arohanui. Mathew.

CONTENTS

I PROLOGUE 1

1 INTRODUCTION 2

1.1 Intermediate-Temperature Solid Oxide Fuel Cells (IT-SOFCs) . . . 2
1.1.1 Loss mechanisms . . . 5
1.1.2 Triple Phase Boundaries and Oxygen Reduction . . . 7
1.2 IT-SOFC Cathode Materials . . . 8
1.2.1 The Perovskite Structure . . . 9
1.2.2 Defect in Solids . . . 11
1.2.3 Point Defects . . . 12
1.2.4 Diffusion . . . 16
1.2.5 Ionic Conductivity . . . 18
1.2.6 Surface Exchange . . . 20
1.2.7 IT-SOFC Mixed Ionic-Electronic Conducting Materials . . . 20

2 LITERATURE REVIEW 27

2.1 The LSCF system . . . 27
2.1.1 Defect Chemistry of $La_{1-x}Sr_xCo_{1-y}Fe_yO_{3-\delta}$ . . . 27
2.1.2 Effect of A-site substitution of $La_{1-x}Sr_xCo_{0.2}Fe_{0.8}O_{3-\delta}$ . . . 30
2.1.3 Effect of B-site substitution of $La_{0.6}Sr_{0.4}Co_{1-y}Fe_yO_{3-\delta}$ . . . 32
2.1.4 Electronic Properties of $La_{0.6}Sr_{0.4}Co_{0.2}Fe_{0.8}O_{3-\delta}$ . . . 32
2.1.5 Oxygen Diffusion and Exchange in $La_{0.6}Sr_{0.4}Co_{0.2}Fe_{0.8}O_{3-\delta}$ 34
2.1.6 Ferroelastic Properties of LSCF . . . 36
2.2 SOFC Degradation . . . 39
2.2.1 SOFC Cathode Degradation . . . 41
2.2.1.1 Cation Segregation . . . 41
2.2.1.2 Cathode Poisoning . . . 45
2.2.1.3 Effect of Humidty . . . 46
2.3 Concluding Remarks . . . 49

II MATERIALS AND METHODS 61

3 SAMPLE PREPARATION 62

3.1 Powder Characterisation . . . 62
3.1.1 X-Ray Diffraction . . . 62
3.1.2 Inductively Coupled Plasma Atomic Emission Spectroscopy 65
3.2 Sample Fabrication . . . 65
3.2.1 Pressing and Sintering . . . 66
3.2.2 Density Measurements . . . 67
3.2.3 Polishing and Sectioning Regime . . . 68

4 INSTRUMENTATION AND EXPERIMENTAL TECHNIQUES 71
4.1 Electron Microscopy . . . 72
4.1.1 High Temperature Environmental Scanning Electron Microscopy . . . 74
4.1.2 Electron Backscattered Diffraction . . . 77
4.1.3 Auger Electron Spectroscopy . . . 80
4.2 Diffusion Measurements . . . 81
4.2.1 Isotopic Exchange . . . 81
4.2.2 Back Exchange . . . 87
4.3 Ion Beam Analysis . . . 89
4.3.1 Secondary Ion Mass Spectrometry (SIMS) . . . 90
4.3.1.1 Quadrupole SIMS . . . 91
4.3.1.2 Time-of-Flight SIMS (ToF-SIMS) . . . 92
4.3.2 Analysis of Diffusion Data . . . 94
4.3.2.1 Depth Profiles . . . 95
4.3.2.2 Line Scans . . . 97
4.3.3 Low Energy Ion Scatting (LEIS) . . . 99
4.4 Topography Measurments . . . 102
4.4.1 White Light Interferometry . . . 102
4.4.2 Atomic Force Microscopy . . . 105

III RESULTS AND DISCUSSION 110

5 POWDER AND SAMPLE CHARACTERISATION 111
5.1 Powder Characterisation . . . 111
5.1.1 X-Ray Diffraction . . . 111
5.1.1.1 High Temperature X-ray Diffraction . . . 112
5.1.1.2 Theoretical Density . . . 115
5.2 Inductively Coupled Plasma Atomic Emission Spectroscopy . . . 116
5.3 Initial Surface Characterisation . . . 117
5.4 Conclusion . . . 121

6 SURFACE EVOLUTION AND DEGRADATION IN HUMID ATMOSPHERES 123
6.1 High-Temperature Environmental SEM . . . 123
6.1.1 Pure O_2 . . . 124
6.1.2 Pure H_2O . . . 129
6.1.3 Ambient Air . . . 135
6.1.4 Vacuum . . . 137
6.1.5 Image Analysis Technique . . . 140
6.2 The surface and sub-surface . . . 141
6.2.1 Surface Chemistry . . . 142
6.2.1.1 Auger Electron Spectroscopy . . . 142
6.2.1.2 Low Energy Ion Scattering . . . 143
6.2.2 Surface Topography . . . 148
6.2.2.1 Atomic Force Microscopy . . . 148

6.3 Summary and Conclusions 154

7 CRYSTALLOGRAPHIC EFFECT UPON DEGRADATION 158
7.1 Pseudo-symmetry of LSCF 158
7.1.1 Definition of Pseudo-Symmetry 158
7.1.2 Pseudo-Symmetry Correction in LSCF 159
7.2 Twinning in LSCF 161
7.2.1 Twinning Habit Plane 163
7.3 Effect of Domains on Particle Growth 169
7.4 Summary and Conclusions 177

8 BACK EXCHANGE TECHNIQUE DEVELOPMENT 180
8.1 Back-Exchange Theory 180
8.2 Experimental Development 183
8.2.1 Experimental Validation 183
8.2.2 State of the Surface 186
8.2.2.1 Removing the Pre-Anneal step 187
8.2.2.2 Increasing Pre-Anneal time 191
8.3 Summary and Conclusions 193

9 TOF-SIMS ERROR ANALYSIS 196
9.1 Line-scan Surface Error 196
9.1.1 The Poisson Problem 196
9.1.2 Geometric Effects 198
9.1.3 Analysis Orientation 199
9.1.4 Effect on Isotope Ratio 200
9.2 Surface Error Quantification 201
9.3 Summary and Conclusions 208

10 CONCLUSIONS AND FUTURE WORK 211
10.1 Conclusions 211
10.2 Mechanistic Conclusions 213
10.3 Future Work 216

IV APPENDIX 219

A APPENDIX 220
A.1 Isotopic Exchange Methodology 220

LIST OF FIGURES

Figure 1 Schematic of an SOFC showing the basic components, chemical components and current flow. 3
Figure 2 Loss mechanisms and their effect upon cell voltage. 4
Figure 3 Detailing Tafel plots for slow and fast reactions. 6
Figure 4 Some mechanisms thought to govern oxygen reduction in SOFC cathodes. Phases α, β and γ refer to the electronic phase, gas phase, and ionic phase, respectively: (a) Incorporation of oxygen into the bulk of the electronic phase (if mixed conducting); (b) adsorption and/or partial reduction of oxygen on the surface of the electronic phase; (c) bulk or (d) surface transport of O^{2-} or O^{n-}, respectively, to the α/γ interface, (e) Electrochemical charge transfer of O^{2-} or (f) combinations of O^{n-} and e^{-}, respectively, across the α/γ interface, and (g) rates of one or more of these mechanisms wherein the electrolyte itself is active for generation and transport of electroactive oxygen species. Adapted from [7]. 8
Figure 5 The idealised perovskite structure showing the A and B cation sites and oxygen co-ordination. 9
Figure 6 Energetic changes during the formation of an intrinsic defect. 10
Figure 7 Intrinsic and extrinsic defect mechanisms. 12
Figure 8 Showing Schottky (left) and Frenkel (right) intrinsic defect processes. 14
Figure 9 Schematic of ion migration showing the energy cost at each position of the hopping process. 17
Figure 10 Brouwer diagram for the $La_{1-x}A_xBO_{3\pm\delta}$ system showing defect concentration as a function of partial pressure. Five distinct regions define the majority defect type over these ranges. Adapted from [11]. 30
Figure 11 Pseudo-cubic lattice parameter and orthorhombic-rhombohedral transition temperatures as a function of Sr content (mol) [14]. 31
Figure 12 Electronic conductivity with respect to temperature of $La_{1-x}Sr_x$-$Co_{0.2}Fe_{0.8}O_{3-\delta}$ for the range of $0 < x < 0.4$ [14] 33
Figure 13 Showing (a) The temperature dependence of oxygen content for $La_{1-x}Sr_xCo_{0.2}Fe_{0.8}O_{3-\delta}$, $0 < x < 0.4$, between 200°C and 1200° and (b) the oxygen non-stoichiometry of $La_{0.6}Sr_{0.4}$-$Co_{0.2}Fe_{0.8}O_{3-\delta}$ under increasingly reducing conditions between 650°C and 950°. Adapted from [14, 28], respectively. 35
Figure 14 Temperature dependence of oxygen tracer diffusivity (D^*) and surface exchange coefficient (k) of $La_{0.6}Sr_{0.4}Co_{0.2}Fe_{0.8}O_{3-\delta}$. Data adapted from [32]. 36

Figure 15 Deformation twinning caused by the spontaneous reorientation of a crystal system showing perpendicular twinning between the (001) and (010) pseudo-cubic planes. Adapted from [41]. 38
Figure 16 3D reconstructions of Atomic Force Microscope data showing the surface roughness effects of Sr segregation in $SrTiO_3$ [62] 42
Figure 17 Showing (a) the stacking of AO and BO_2 in a 2:4 perovskite [59] and (b) crystal charge as a function of plane number, illustrating the periodic charge across the atomic planes in the bulk and deviation from neutrality near the surface. Adapted from [66]. 43
Figure 18 (a) Oxygen surface exchange and diffusivity properties of YSZ at 600°C showing the increase in surface exchange rate in the presence of 20 mbar $p(H_2O)$, and (b) Coverage of chemisorbed water molecules ($\theta_c h$) with respect to temperature and oxygen exchange rate. Adapted from [90]. 47
Figure 19 Showing the temperature dependence of each gas mixture and the regions which certain exchange paths dominate in (a) LSM and (b) LSCF. Adapted from [96]. 48
Figure 20 Oxygen tracer diffusion and surface exchange for current and next generation SOFC cathode materials over a range of temperatures, such as Ruddlesden-Popper phase (LNO/LCO) and Double Perovskite (GBCO/PBCO) phase materials. Adapted from [97]. 49
Figure 21 Schematic showing two atomic planes with spacing d and an incident X-ray at angle θ diffracting under the Bragg condition. 63
Figure 22 Schematic diagram of (a) the stainless steel bar die and cartoon of a sealed and (b) evacuated sample prior to isostatic pressing 67
Figure 23 Schematic diagram showing (a) the polishing stub with the sample and silica slides prior to grinding and polishing, (b) the polishing plate and sample holder with direction of rotation, and (c) removal of the sample by re-heating the stub. 68
Figure 24 Summary of surface analysis techniques showing approximate depth resolution and detection range for each technique 72
Figure 25 Schematic of (a) the resulting phenomena generated during an electron-material interaction and (b) the enhancement of electron emission due to a change in incidence angle. 74
Figure 26 Schematic of (a) the differential pumping system of an ESEM, (b) the effect of scattering on the incident beam profile and (c) electron cascade amplification process. . . . 76

Figure 27 Schematic of (a) the formation of Kikuchi bands from electron diffraction and (b) the Gnomonic projection of an EBSD pattern onto the EBSD camera 78
Figure 28 Showing a schematic of the sample holder and equipment setup for colloidal silica polishing. 79
Figure 29 Showing a schematic of the isotopic exchange equipment. Inset: how the surface roughness of a sample affects the shape of the diffusion front. 82
Figure 30 Typical temperature/time profiles for a forward exchange using a 1000°C pre-anneal step, (b) a standard forward exchange and (c) back exchange experiment. 85
Figure 31 Schematic diagrams showing the tracer isotope profiles using (a) labelled impurity species, (b) the saturated exchange technique and (c) a typical 'Back Exchange' experiment. 87
Figure 32 Schematic of ion impact on a material showing collision paths and secondary particle emission. 89
Figure 33 Schematic of a quadrupole mass analyser showing (a) the stable and unstable ion trajectories and (b) a cross section of the rods with applied voltages. 91
Figure 34 (a) A schematic of the TOF-SIMS[5] equipment including both ion guns and 'electrostatic mirror' and (b) a schematic diagram illustrating the main beam modes. 93
Figure 35 Illustrative examples of a forward exchange profile and a back-exchange profile showing the 'effective' inverted diffusion profile during the back-exchange. 95
Figure 36 Schematic of a standard sputter crater and its relation to the diffusion profile showing analysis and sputter areas when depth profiling with ToF-SIMS. 96
Figure 37 A schematic diagram showing sample preparation for line-scan samples showing the resulting diffusion profile from a line-scan. 98
Figure 38 Schematic of the 'tulip' detector employed in the qtac[100] showing beam incident angle and ion detection. The inset shows a schematic of the scattering process and a typical peak shape. 99
Figure 39 Schematic diagram of the optics of a white light interferometer and an example interference pattern. 103
Figure 40 Showing the observed powder x-ray diffraction pattern for the as-received LSCF, the associated Le Bail fit and residual showing the difference between the two data sets. 113
Figure 41 Comparison of diffraction patterns for the as-received powder and after two years of storage. 113

Figure 42 Showing the diffraction pattern taken at room temperature before heat treatment, at 600°C, 1000°C and after cooling back to room temperature. The inset shows the lattice parameter change during heating. 114
Figure 43 Representation of a Trigonal, or rhombohedrally-centred hexagonal, unit cell. 115
Figure 44 ICP experimental standard results showing the linear relationship of photon intensity against concentration. . . . 117
Figure 45 Secondary electron SEM image of (a) polished LSCF surface annealed in 'stagnant air' at 900°C for 50 hours [5] and (b) the LSCF surface after an initial exchange experiment showing secondary phase particle growth and thermal etching of the surface. 118
Figure 46 Schematic temperature-time profiles representing Oh et al. [5] and initial exchange experiments carried out in this work. 119
Figure 47 FIB-SIMS elemental maps for (a) ^{16}O and (b) ^{18}O showing that strontium-based particles prevent the oxygen exchange reaction from occurring directly underneath them. It should be noted that the ^{16}O map was collected *after* the ^{18}O map. As this is a quadrupole system, the particles were likely removed during collection of the ^{18}O map and thus do not appear strongly on the ^{16}O image. 120
Figure 48 Showing an SEM micrograph of the LSCF after a 50 hour anneal in ambient air. 121
Figure 49 Showing (a) the surface prior to any noticeable surface modification and (b) the final image collected showing secondary phase precipitation after the anneal in pure oxygen. 125
Figure 50 Showing average particle area and percent coverage with respect to time and temperature for an initial sample annealed in pure oxygen. 126
Figure 51 Showing the initial growth in pure oxygen between 550-650°C. 126
Figure 52 Showing directional trends of particle growth along polishing induced mechanical damage. 128
Figure 53 Showing (a) the surface prior to any noticeable surface modification and (b) the final image collected showing secondary phase precipitation after the anneal in pure water. 130
Figure 54 Showing average particle area and percent coverage with respect to time and temperature for a sample annealed in pure water. 130
Figure 55 Comparing number of particles seen to grown in pure oxygen, pure water and ambient air as they were heated from RT-1000 °C.
Figure 56 Showing a micrograph of LSCF heating in pure water where multiple grains show different particle growth patterns. . 131

Figure 57 Growth rate of grains A & E and grain B - D respectively. 132
Figure 58 Showing the positioning scratch on the sample at (a) 250x magnification and (b) at 2500x magnification. The inset in (b) shows a backscattered electron image confirming that the phase covering the scratch differs to that of the bulk material. 133
Figure 59 Showing cracking due to the scratch and preferential agglomeration across these features 134
Figure 60 Showing (a) a micrograph of LSCF annealed in water where Sr-based particles are observed as well as an additional (black) phase in both SE and BSE (inset) mode, and (b) EDX image confirming the large white particles are strontium based. 135
Figure 61 Showing (a) the surface prior to any noticeable surface modification and (b) the final image collected showing secondary phase precipitation after the anneal in ambient air. 136
Figure 62 Showing average particle area and percent coverage with respect to time and temperature for a sample annealed in ambient air. 136
Figure 63 Showing (a) the surface prior to any noticeable surface modification and (b) the final image collected showing secondary phase precipitation after the anneal in a vacuum (10^{-6} mbar).
Figure 64 Showing average particle area and percent coverage with respect to time and temperature for a sample annealed in a vacuum (10^{-6} mbar). 139
Figure 65 Showing polishing induced mechanical damage without preferential particle growth in a reducing environment. . . 140
Figure 66 Showing (a) the original image, (b) the image after edge detection and (c) and conversion into a binary image. . . . 140
Figure 67 Showing AES spot analysis position at the (1) particle and (2) the grain surface for (a) pure oxygen, (b) pure water and (c) a vacuum. 142
Figure 68 Showing (a) spot analysis position in an 'unsegregated' grain surface and 'segregated' grain surface, (b) a crystallographic particle in the centre of the grain and (c) a crystallographic particle on a grain boundary. 143
Figure 69 LEIS 3keV Helium survey spectra for a LSCF samples annealed in pure oxygen and ambient air. 145
Figure 70 LEIS 5keV neon spectra for LSCF samples annealed at 650°C in 200 mbar pure oxygen and ambient air.
Figure 71 Showing an as polished LSCF surface spectra collected using a 5 keV neon primary ion beam with the peak fitting (dash-dot lines) superimposed onto the data. 146

Figure 72 LEIS depth profiles of a sample (a) annealed in pure oxygen and (b) in ambient air. 148
Figure 73 Showing an AFM topography map of an as polished LSCF sample taken with a 20x20 μm scan area using 512x512 px. 149
Figure 74 Showing edge 'smoothing' as a result of the AFM tip radius. 150
Figure 75 Showing an AFM topography map of a sample annealed in pure oxygen taken with a 10x10 μm scan area using 512x512 px with two grains exhibiting differing RMS roughness values.
Figure 76 Showing an AFM topography map of a sample annealed in pure oxygen taken with a 3x3 μm scan area using 512x512 px with two grains exhibiting differing RMS roughness values. 151
Figure 77 Showing an AFM topography map of a sample annealed in ambient air taken with a 10x10 μm scan area using 512x512 px.
Figure 78 Showing an AFM topography map of a sample annealed in ambient air taken with a 5x5 μm scan area using 512x512 px. 152
Figure 79 SEM micrograph of an LSCF sample annealed in ambient air at 800°C showing surface corrosion and particle growth. 153
Figure 80 Showing (a) the trigonal crystal structure of $La_{0.6}Sr_{0.4}Co_{0.2}Fe_{0.8}O_{3-\delta}$ (where $a = b, c$, $\alpha = \beta = 90°$ and $\gamma = 120°$) and (b) the corresponding EBSD grain orientation map (where z-axis is out of plane) of $La_{0.6}Sr_{0.4}Co_{0.2}Fe_{0.8}O_{3-\delta}$ with a pseudo-symmetry problem. 160
Figure 81 Showing experimentally collected EBSP of LSCF (trigonal phase). The green lines represent the expected position of the Kikuchi bands based on a BCC crystal structure and the white lines show missing high-order reflectors absent from the indexing. 161
Figure 82 Showing the similarities between the experimentally measured electron diffraction pattern, simulated diffraction pattern for a simple ferrite BCC crystal and LSCF trigonal crystal at the same crystal orientation. 162
Figure 83 Showing the effect of simplifying the indexing process from a trigonal phase to a BCC phase. 162
Figure 84 Showing (a) a forescattered electron image of $La_{0.6}Sr_{0.4}Co_{0.2}Fe_{0.8}O_{3-\delta}$ and (b) an image constructure from the EBSPs. The contrast in both images is representative of orientational differences and thus isoloated regions confirms domains and twinning. 164

Figure 85 Image generated from the EBSPs after conversion to Rodrigues-Frank space where the shift in RGB from white represents a rotation of the crystal. Each grain is treated separately, therefore the colour contrast is non-comparable across the image. 164
Figure 86 Showing the experimental EBSPs from two different domains within the same grain. The greyscale intensity was normalised then the pattern of domain 1 was subtracted from domain 2 to produce a difference image. 165
Figure 87 Schematic of (a) an isometric view of a grain containing twinning (from Figure 85) where the viewing plane is perpendicular to the surface of the material, (b) the rotational degree of freedom of the plane constructed by the trace, (c) the same plot with the perpendicular plane (yellow) defined by the trace, (d) the grain rotated around the trace direction and the corresponding plane orientation and equatorial interaction (note that this is perpendicular to the trace direction) and (e) the plane in its original orientation but with the viewing plane rotated. 166
Figure 88 Showing the twin structure and associated texture on pole figures of the {100}, {110} and {111} family of planes. The trace of the twin plane and bi-sector (dotted line) has been overlaid across the pole figures. The crosses on the pole figures represent the crystal orientation of a pixel within the selected grain. 167
Figure 89 Showing a sterographic projection of the EBSP and unit cell along the z-axis for both the BCC and trigonal crystal structure. Equivalent planes between the two structures gave been indicated. 168
Figure 90 Showing the twin structure and associated texture on pole figures of the {001}, {110} and $\{\bar{1}20\}$ family of planes for the grain outlined. The trace of the twin plane and bi-sector (dotted line) has been overlaid across the pole figures. The crosses on the pole figures represent the crystal orientation of a pixel within the selected grain. 169
Figure 91 Showing the twin structure and associated texture on pole figures of the {001}, {110} and $\{\bar{1}20\}$ family of planes for the grain outlined. The trace of the twin plane and bi-sector (dotted line) has been overlaid across the pole figures. The crosses on the pole figures represent the crystal orientation of a pixel within the selected grain. 169
Figure 92 Showing (a) a forscattered electron image of a polished sample prior to the thermal anneal in the HT-ESEM and (b) the EBSD orientation map indexed using a simple BCC unit cell. Both images show the area analysed during the pure water HT-ESEM analysis. 171

Figure 93 Showing a frame of the sample annealed in pure water (Video 3) prior to the particle agglomeration. The EBSD map shown in Figure 92(b) has been overlaid on top of the SE image. Discrepancies between the two images are to the low resolution of the EBSD orientation map in comparison to the SE image. 171
Figure 94 Showing the HT-ESEM/BCC EBSD map, forescattered electron image and trigonal EBSD map. The low resolution of the forescattered image prevents observation of twin orientations within some grains. 172
Figure 95 Showing the bi-sector analysis and trigonal crystal orientation for the different pixel colours found within grains 1 and 2. 173
Figure 96 Showing the bi-sector analysis and trigonal crystal orientation for the different pixel colours found within grains 3. As seen in the analysis of grains 1 & 2, grains 3 & 4 are equivalent but orientated slightly differently. 174
Figure 97 Showing a schematic of {001} type twinning where the twin habit plane is orthogonal to the surface or orientated at an angle θ. If the twin habit plane not orthogonal the effective 'width' of the twinning is reduced at the surface. 176
Figure 98 Showing the crystallographic orientation of the trigonal unit cell for the dominant pixel colour found in grains 5 and 6. 177
Figure 99 Plot containing normalised back-exchange profiles across the full range of possible exchange time ratios, where D is constant for both exchanges. A family of curves is shown at 7 values of the time ratio, θ. Each family is generated by varying the ratio of effective surface exchange coefficients, k_2/k_1. The maximum depth of the turning point is shown for each family, as well as the maximum surface concentration. To account for variation in k_1, all profiles have been normalised with respect to the surface concentration found in the $\theta = 0$ case. Recreated with permission from [1]. 181
Figure 100 Surface isotopic fraction against $h\sqrt{Dt}$ for a single value of D. 182
Figure 101 Showing schematic temperature-time profiles for the validation experiment where (a) is a standard forward exchange, (b) is the back-exchange using pure oxygen and (c) is the back-exchange using ambient air. 183
Figure 102 Showing (a) the forward exchange diffusion profile for the validation and (b) uncertainty contour map in D and k as a result of data noise. 185

Figure 103 Showing (a) the back-exchange diffusion profile for the validation and (b) uncertainty contour map in k_1 and k_2 as a result of data noise. 185
Figure 104 Showing (a) the back-exchange diffusion profile for the validation and (b) uncertainty contour map in k_1 and k_2 as a result of data noise. 185
Figure 105 Schematic of uncertainty 'bands' when fitting both forward and back-exchange diffusion profiles. 186
Figure 106 Showing the indent depth with respect to polishing time. The polishing rate was found to be 0.45 $\mu m\, min^{-1}$. 187
Figure 107 Showing an AFM topographic map of the sample surface immediately after a standard exchange at 650°C. 189
Figure 108 Showing an AFM topographic map of the sample surface after 1 minute of hand polishing using 1/4 micron diamond suspension. 189
Figure 109 Showing an AFM topographic map of the sample surface after 2 minutes of hand polishing using 1/4 micron diamond suspension. 190
Figure 110 Showing an AFM topographic map of the sample surface after 3 minutes of hand polishing using 1/4 micron diamond suspension. 190
Figure 111 Showing (a) the forward exchange diffusion profile for a sample that has not been exposed to a 'pre-anneal' step, and (b) uncertainty contour map in D and k as a result of data noise. 191
Figure 112 Showing (a) the back exchange diffusion profile after 3 minutes of polishing and (b) uncertainty contour map in k_1 and k_2 as a result of data noise. 191
Figure 113 Showing the surface of a polished LSCF sample annealed at 650°C for (a) 20 hours and (b) 40 hours. 192
Figure 114 Showing D, k_1 and k_2 values for back-exchange sample sets. 194
Figure 115 A plot of measured and corrected secondary ion yield per pulse against primary ion per pulse. Recreated from [1]. . 197
Figure 116 Showing a schematic of (a) the effect edge rounding has on the ion beam and (b) the effect of non-orthogonal surfaces and (c) the sputter rate of each component of $La_{0.6}Sr_{0.4}$-$Co_{0.2}Fe_{0.8}O_{3-\delta}$ with respect to incidence angle. 198
Figure 117 Showing (a) a schematic of an ion beam at an incident angle of 45° parallel to the sample edge and (b) a schematic of the ion beam at an incident angle of 45° perpendicular to the sample edge. 200

Figure 118 A comparison of the total ion line-scan profiles for the sample prepared using method (3) (detailed in Section 9.2). The profiles have been normalised and offset for comparison. A false change in non-linear ion count may be seen in the sample aligned perpendicular to the incident ion beam. 201
Figure 119 Showing (a) a false colour image of the ^{18}O signal and (b) the back-exchange curves for both the corrected and uncorrected data. Total ion counts (arbitrary units) are overlaid over both figures. 202
Figure 120 Showing (a) two samples adhered together using a liquid-based adhesive, (b) the sample after polishing away the excess adhesive from the surface and (c) further polishing to remove the edges of the sample. 202
Figure 121 Showing false colour images of $La_{0.6}Sr_{0.4}Co_{0.2}Fe_{0.8}O_{3-\delta}$ total ion images (ion counts per pixel). The samples were mounted with (a) no sample at the edge, (b) samples adhered together after the second polish step and (c) samples glued together before the second polishing step. A total ion 'linescan' is overlaid across the image. Ion counts (arbitrary units) have been normalised to the final data point of (a) to compare the relative 'depth' of the gap between samples. Ion images were rotated by 90° to aid in comparison with the total ion count. 204
Figure 122 Showing a false colour WLI image of the gap between samples prepared using method (2). The 'overhang' between samples may be seen from the linescan profiles (below). 205
Figure 123 Showing a false colour WLI image of the gap between samples prepared using method (3). As can be seen the gap is non-uniform and in some places the samples are directly in contact. Representative profiles have been taken from a region where the samples are touching, a large gap and a small gap. 205
Figure 124 A direct comparison between the total ion and topographic line-scan profiles showing the non-linear ion count region to be between approximately 4-5.5 μm. The profiles have been normalised to the final data point and aligned to the minima of each profile. 206
Figure 125 Showing the effect of extrapolating or ignoring the non-linear ion count region of the diffusion profile for (a) a forward exchange and (b) a back-exchange. The linear region indicated on the graphs only applies to the extrapolated curve. 207

Figure 126 Schematic of the proposed particle formation process. The numbers in the figure may be related to the corresponding process described in the text. 214

LIST OF TABLES

Table 1 Approximate values for the mean free path of a particle under different pressures [6] 75
Table 2 EBSD analysis settings used for both the HT-ESEM and twin analysis. 80
Table 3 Atomic mass and natural abundance for the three stable oxygen isotopes [22]. 83
Table 4 Summary of practical diffusion length limts for depth profile and linescan analysis modes (using a single region). . 86
Table 5 Associated properties of the 10x and 50x object lenses used in this work - data from the Zygo documentation [43]. . . 104
Table 6 Crystallographic data presented by Itoh and Nakayama [1] and experimentally calculated from the Le Bail refinement. 112
Table 7 A comparison between the theoretical and experimentally calculated cation stoichiometry. 117
Table 8 Temperature conversion table for HT-ESEM videos. Values in brackets represent the set temperature (seen on the HT-ESEM micrographs) when the actual temperature was 1000 °C. 124
Table 9 Table of values corresponding to the AES spot analysis seen in Figure 67. 143
Table 10 Table of values corresponding to the AES spot analysis seen in Figure 68. 144
Table 11 Cation ratio at the surface for LSCF samples annealed in pure oxygen and ambient air. 147
Table 12 Cation ratio at the surface for LSCF samples annealed in pure oxygen and ambient air. 186
Table 13 D, k_1 and k_2 values for back-exchange sample sets. 194
Table 14 Analysis and sputter beam settings used to analyse the samples prepared using methods (1)-(3). 203
Table 15 Cation ratio at the surface for LSCF samples annealed in pure oxygen and ambient air. Where Exc. = excluded data and Extp. = extrapolated data. 208

SUPPLEMENTARY MATERIALS

Video 6.1 LSCF annealed in pure O_2 from RT to 1000°C at a heating rate of 300°C/hr, magnification 5000x 124
Video 6.2 LSCF annealed in pure O_2 from RT to 1000°C at a heating rate of 300°C/hr, magnification 10000x 125
Video 6.3 LSCF annealed in pure H_2O from RT to 1000°C at a heating rate of 300°C/hr, magnification 5000x 129
Video 6.4 LSCF annealed in pure H_2O from RT to 1000°C at a heating rate of 300°C/hr, magnification 10000x 129
Video 6.5 LSCF annealed in ambient air from RT to 1000°C at a heating rate of 300°C/hr, magnification 5000x 135
Video 6.6 LSCF annealed in ambient air from RT to 1000°C at a heating rate of 300°C/hr, magnification 10000x 135
Video 6.7 LSCF annealed in ambient air from RT to 1000°C at a heating rate of 300°C/hr, magnification 5000x 137
Video 6.8 LSCF annealed in ambient air from RT to 1000°C at a heating rate of 300°C/hr, magnification 10000x 137
Video 8.9 LSCF annealed in pure O_2 at 600°C for 24 hours, magnification 5000x 192

ACRONYMS

AES Auger Electron Spectroscopy

AFM Atomic Force Microscopy

ASR Area Specific Resistance

BCC Body Centred Cubic

BSE Backscattered Electron

CCD Charge Coupled Device

EBSD Electron Backscattered Diffraction

EDX Energy-Dispersive X-ray Spectroscopy

FEG Field Emission Gun

FIB Focussed Ion Beam

HT-ESEM High-Temperature Environmental Scanning Electron Microscopy

HT-XRD High-Temperature X-ray Diffraction

ICP Inductive Coupled Plasma

IEDP Isotopic Exchange Depth Profile

IT-SOFC Intermediate-Temperature Solid Oxide Fuel Cell

LEIS Low Energy Ion Scattering

LMIG Liquid Metal Ion Gun

LSM $La_{1-x}Sr_xMnO_{3-\delta}$

LSC $La_{1-x}Sr_xCoO_{3-\delta}$

LSCF $La_{1-x}Sr_xCo_{1-y}Fe_yO_{3-\delta}$

MIEC Mixed Ionic-Electronic Conducting Materials

OCV Open Cell Voltage

ORR Oxygen Reduction Reaction

PLA Pressure Limiting Aperature

RMS Root Mean Square

SE Secondary Electron

SEM Scanning Electron Microscopy

SIMS Secondary Ion Mass Spectrometry

SOFC Solid Oxide Fuel Cell

TEC Thermal Expansion Co-Efficient

TEM Transmission Electron Microscopy

ToF Time-of-Flight

TPB Triple Phase Boundary

WLI White Light Interferometry

XRD X-ray Diffraction

YSZ Yttria-Stabilised Zirconia

Part I

PROLOGUE

$La_{0.6}Sr_{0.4}Co_{0.2}Fe_{0.8}O_{3-\delta}$ is the primary candidate for intermediate temperature solid oxide fuel cells. The bulk properties of this material are well understood, however, the literature surrounding the nature of the surface is less comprehensive, particularly in regard to degradation mechanisms and their effect on the catalytic properties of the material. Part I will introduce the fundamentals of solid oxide fuel cell operation and then review the current body of literature available for this material; providing context to the experiments carried out over the course of this work.

1

INTRODUCTION

The aim of this chapter is to introduce the relevant scientific principles behind solid oxide fuel cell (SOFC) operation. Although this work is principally a scientific endeavour focusing upon the properties of SOFC cathode materials, it is important to maintain a broader understanding in order to appreciate how the properties of a material may affect a complete device.

1.1 INTERMEDIATE-TEMPERATURE SOLID OXIDE FUEL CELLS (IT-SOFCS)

A fuel cell is a device designed to convert chemical energy to electrical energy. There are many variants of fuel cell which may be differentiated by their operational temperature. This work focusses upon the high temperature variety of fuel cell, in particular the Solid Oxide Fuel Cell (SOFC). SOFCs are currently a highly efficient form of fuel cell [1] and are based on the discovery of solid oxide electrolytes by Nernst and his colleagues [2]. They can be applied to both transport and stationary applications, however, currently, the primary interest for SOFCs is for localised small and medium scale stationary power generation [3]. SOFCs offer a number of advantages over other styles of fuel cell due to their very high operating temperatures (600-1000°C). This includes: not requiring expensive precious metal catalysts, the ability to reform heavy hydrocarbon fuels internally and utilisation of excess heat when concerned with localised domestic power generation [4]. Initially SOFCs operated at approximately 900-1000°C due to electrode material limitations, however, working at lower temperatures enables the use of cost-efficient metallic-based interconnect materials. Advancements in electrode and electrolyte materials has enabled SOFCs to be operated at temperature range of 600-800°C [4] and are therefore referred to as Intermediate-Temperature SOFCs (IT-SOFC).

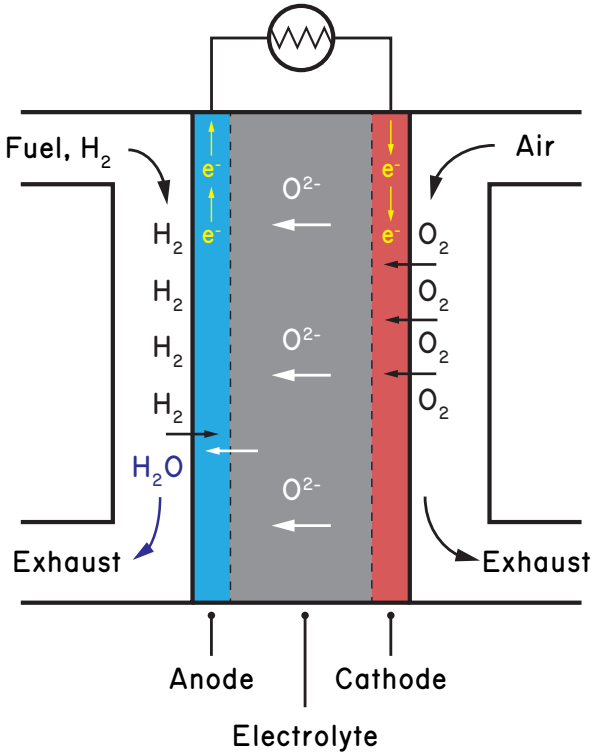


Figure 1: Schematic of an SOFC showing the basic components, chemical components and current flow.

Generally speaking, fuel cells operate through two different, 'half-cell', chemical reactions separated by a selective electrolyte material capable of transporting a relevant ionic species. The chemical reactions occur at the electrodes: the anode and the cathode. Figure 1 shows a basic schematic of an SOFC. Oxygen is reduced from the cathodic gas stream (commonly ambient air) to form oxygen ions (Equation 1.1). The oxygen ions are then incorporated into the cathode/electrolyte and before being transported across the electrolyte where they oxidise hydrogen fuel at the anode. The reaction using pure H_2 as a fuel can be seen in Equation 1.2 and therefore the overall reaction is that of Equation 1.3.

$$\text{Cathode}: \frac{1}{2}O_2 + 2e^- \rightarrow O^{2-} \tag{1.1}$$

$$\text{Anode}: H_2 + O^{2-} \rightarrow H_2O + 2e^- \tag{1.2}$$

$$\text{Overall Reaction}: H_2 + \frac{1}{2}O_2 \rightarrow H_2O \tag{1.3}$$

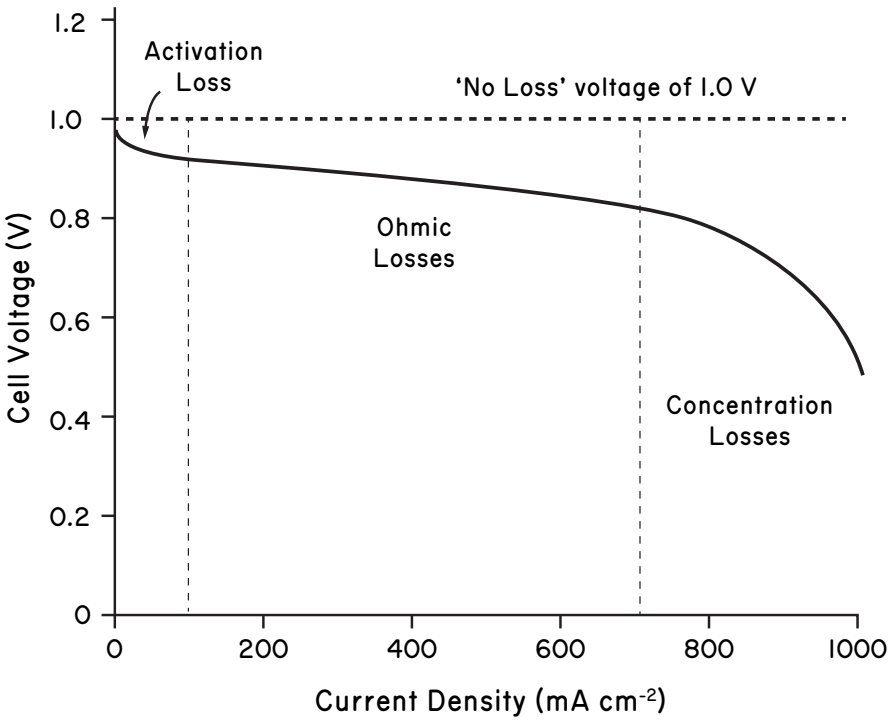


Figure 2: Loss mechanisms and their effect upon cell voltage.

However, as previously mentioned a major advantage of an SOFC is the ability to reform heavier hydrocarbons internally. Equation 1.4 and 1.5 show dry and steam reformation of methane (CH_4, or natural gas) to form the hydrogen fuel:

$$\mathrm{Dry\,reforming}: CH_4 + CO_2 \rightarrow 2H_2 + 2CO \tag{1.4}$$

$$\mathrm{Steam\,reforming}: CH_4 + H_2O \rightarrow 3H_2 + CO \tag{1.5}$$

The overall process is endothermic and thus requires external heat input to occur. Using the Nernst equation it is therefore possible to calculate the maximum reversible cell voltage for both hydrogen and methane; Equation 1.6 and Equation 1.7, respectively. Observing the Nernst equation it can be seen that temperature and gas composition will affect the voltage of a cell directly [5]. Higher temperatures will reduce the maximmum potential of a cell and as such is another reason to reduce SOFC operating temperatures. The *measured* maximum voltage (including losses) is reffered to as the Open Cell Voltage (OCV).

$$E_{Nernst} = E_0 - \frac{RT}{2F} \ln \left(\frac{p\,(H_2O)}{p\,(H_2)\,.p\,(O_2)^{\frac{1}{2}}} \right) \tag{1.6}$$

$$E_{Nernst} = E_0 - \frac{RT}{2F} \ln \left(\frac{p\,(CO_2)\,.p\,(H_2)^4}{p\,(CH_4)\,.p\,(H_2O)^2} \right) \tag{1.7}$$

Where E_0 is the idealised cell potential under standard conditions (1 mol/dm^3, 1 atm and 298 K) [6], R is the universal gas constant (J K^{-1} mol^{-1}), F is the Faraday constant (C mol^{-1}) and T is the temperature (K).

The OCV defines the total available energy of the system to perform electrical work. During operation the cell potential is limited by the first law of thermodynamics which determines that heat lost to the surroundings as well as inherent loss mechanisms will reduce the available energy. The difference between the OCV and operational potential is defined as an 'overpotential'. Loss mechanisms are connected to the working current density of a cell and can be described generally as: activation losses, ohmic losses and mass transport/concentration losses (Figure 2).

1.1.1 *Loss mechanisms*

Activation losses: At low current densities the efficiency of the electrode reactions is primarily limited by the rate of charge transfer and ion incorporation at the surface of the electrodes. This process is highly non-linear and is defined by the activation energies of the reactant species, electrode material and electrode morphology. In order to characterise the reversibility of an electrochemical process, the Tafel equation (1.8) can be used.

$$\Delta V = A \ln \left(\frac{j}{j_0} \right) \tag{1.8}$$

Where ΔV is the Overpotential (V), A is a constant defined by the linear fit, j is the current density (A/m^2) and j_0 is the exchange current density.

The equation defines overpotentials with respect to operational current densities. At zero operational current density, reactions are still occurring at the elec-

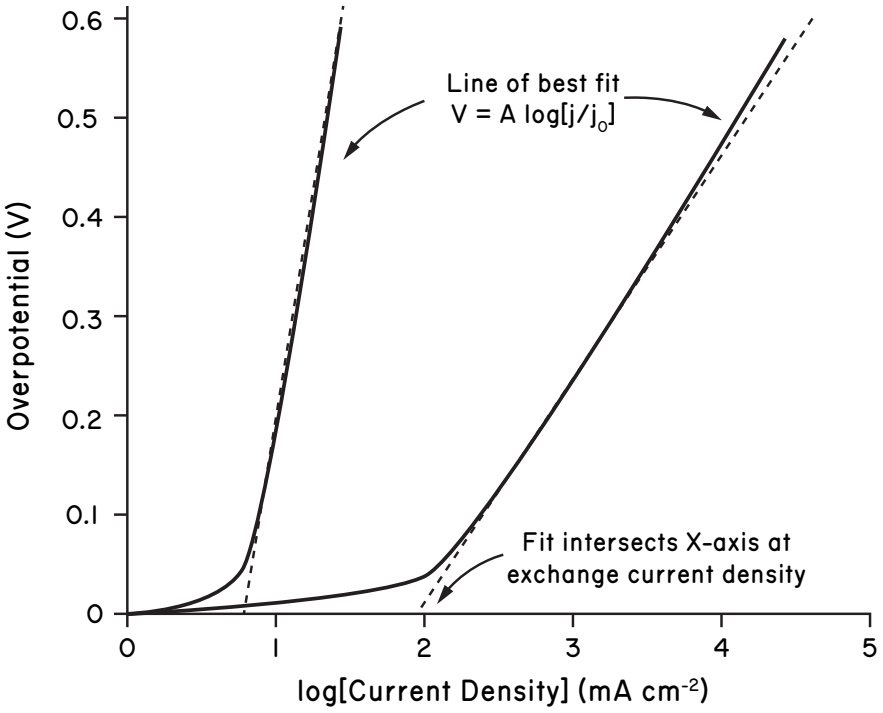


Figure 3: Detailing Tafel plots for slow and fast reactions.

trodes, however, the forward reaction rate is equal to the reverse of the reaction (at equilibrium); this is the exchange current density (i_0). When there is a net flux of a species (i.e. the forward reaction is greater than the reverse) an operational current density will be observed. As can be seen in Figure 3, reducing activation losses, the exchange current density must be increased. This can be achieved by using higher operational temperatures, highly catalytic materials and thin electrodes with large surface areas to increase catalyst site occupancy. One method of characterising a 'classical' electrode's[1] quality is to define the Triple Phase Boundary (TPB) length. TPBs are points where the electrode, electrolyte and gas phases all contact one another. They are the most direct route for oxygen to be reduced and incorporated in a SOFC cathode [7] . TPBs are discussed in more detail in 1.1.2.

Ohmic losses: Above the region where activation losses dominate the loss mechanisms are dominated by electrical resistances, simply defined by Ohms law. However, to be consistent with the other loss mechanisms the resistance of the cell is

1 That is, not an MIEC material.

represented as an Area Specific Resistance (ASR). Modifying Ohm's law to use current density the voltage drop is as follows:

$$\Delta V = jr \tag{1.9}$$

Where ΔV is the Overpotential (V), j is the current density and r is the area specific resistance (Ωm^2).

Mass Transport/Concentration Losses: At very high current densities the rate limiting step is often the ability to replenish gas at the electrode surface as it is consumed; often referred to as the fuel utilisation. At the anode this will refer to the oxidation of hydrogen and at the cathode the reduction and incorporation of oxygen. The extent to which concentration losses affect the overpotential depend heavily upon the ease with which the gases can circulate through a given electrode morphology, but also the nature of the gas mixture and gas pressure. Higher fuel concentrations increase the probability it will reach an active site on the electrode. For practical reasons ambient air is often used as the SOFC cathode gas stream despite being less efficient than pure O2. Concentration losses are minimised by using excess air [1] .

1.1.2 *Triple Phase Boundaries and Oxygen Reduction*

Equation 1.1 shows the Oxygen Reduction Reaction (ORR) for a SOFC cathode, however, it does not describe precisely where or by what mechanism it occurred. For traditional catalyst materials, such as platinum, it was generally accepted that triple phase boundaries were the primary location where oxygen is reduced and incorporated into the system. However, with the discovery of Mixed Ionic-Electronic Conducting (MIEC) materials the oxygen reduction mechanism is more complex. The Adler-Lane-Steele (ALS) model presented by Adler et al. [8, 7] is currently the accepted model for the reduction mechanisms of MIEC cathodes.

The ALS model describes the relationship between the adsorption rate of a gaseous adsorbate (at a uniform partial pressure) onto the surface of an MIEC and the diffusive (D) and surface exchange (k) properties of the MIEC. It shows

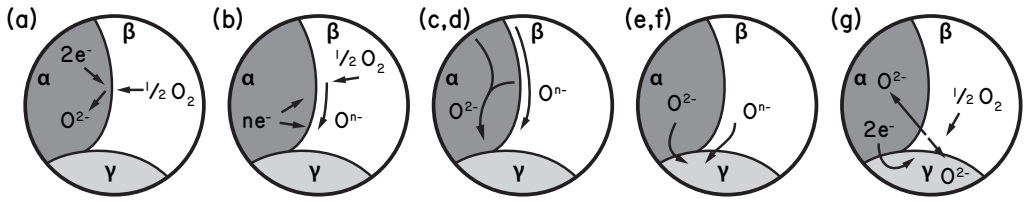


Figure 4: Some mechanisms thought to govern oxygen reduction in SOFC cathodes. Phases α, β and γ refer to the electronic phase, gas phase, and ionic phase, respectively: (a) Incorporation of oxygen into the bulk of the electronic phase (if mixed conducting); (b) adsorption and/or partial reduction of oxygen on the surface of the electronic phase; (c) bulk or (d) surface transport of O^{2-} or O^{n-}, respectively, to the α/γ interface, (e) Electrochemical charge transfer of O^{2-} or (f) combinations of O^{n-} and e^-, respectively, across the α/γ interface, and (g) rates of one or more of these mechanisms wherein the electrolyte itself is active for generation and transport of electroactive oxygen species. Adapted from [7].

that losses occuring at the electrode may be related to the "utilisation length" (l_δ) of the electrode. This metric defines the size of the active region within a porous electrode where it is possible for oxygen reduction and incorporation to occur. The utilisation length is proportional to $\sqrt{D/k}$ as it is defined by the reduction, adsorption *and* incorporation of oxygen ions. Figure 4 details the potential processes for oxygen reduction and incorportation in an MIEC. The co-dependance of the these processes means that MIEC electrodes are often defined as "co-limited" by the ratio between D and k. Due to the complexity of the system, debate is still ongoing regarding the rate-limiting step of the oxygen reduction reaction [9, 10] as most techniques used to measure these properties determine the *overall* reaction kinetics meaning that individual processes cannot easily be decoupled.

It is clear that catalytic properties at the surface of these materials is vital to the operation of an SOFC. This work focusses upon the IEDP-SIMS technique [11] (see Section 4.2.1) to calculate the self-diffusivity and surface exchange rate of the material.

1.2 IT-SOFC CATHODE MATERIALS

SOFC cathode materials have a number of specific materials requirements: (i) high electronic conductivity (over 100 S/cm in an oxidising environment [12]) to provide electrons for the ORR, (ii) stability under an oxidising environment during operation, (iii) chemical compatibility and matching thermal expansion coefficient with electrolyte and interconnect materials, (iv) controllable morphology

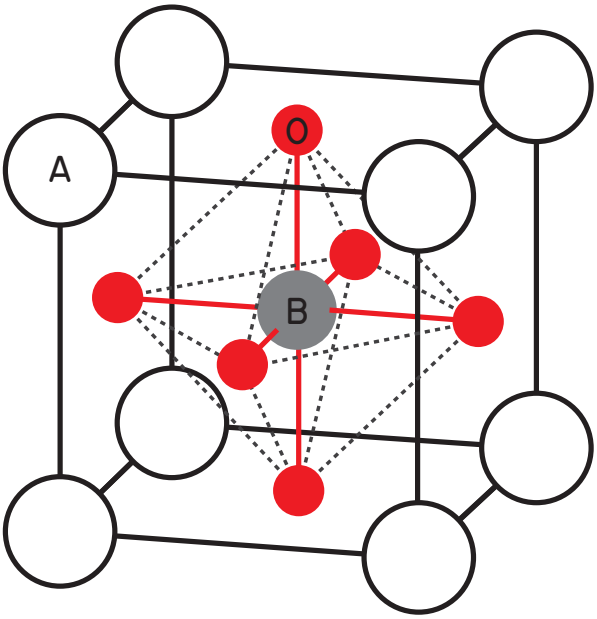


Figure 5: The idealised perovskite structure showing the A and B cation sites and oxygen co-ordination.

during fabrication (specifically porosity control) to allow and (v) low cost. Initial research on SOFC cathode materials was focussed upon moving away from expensive metal catalysts such a platinum. The primary candidates for practical alternatives have been perovskite-structured materials. Of primary concern today are MIEC perovskite structured materials. To understand how MIEC perovskite materials gain their properties defect chemistry must be introduced.

1.2.1 *The Perovskite Structure*

The idealised perovskite structure (so named due to its similarity to the Perovskite mineral $CaTiO_3$) has a general formula of ABO_3. Its overall structure is not close packed, however, as can be seen in Figure 5 the A site atoms arrange to form a simple cubic structure with twelve-fold co-ordination with the oxygen atoms. The B site atom occupies octahedral sites of this cubic structure and have six-fold co-ordination by oxygen atoms.

A unique property of the perovskite structure is its ability to accommodate many different combinations of cations on both the A and B site, allowing for different valences and atomic radii. The general formula can therefore be expressed as $A^{x+}B^{y+}O_3$ where $x + y$ must equal $+6$. This gives rise to three categories of

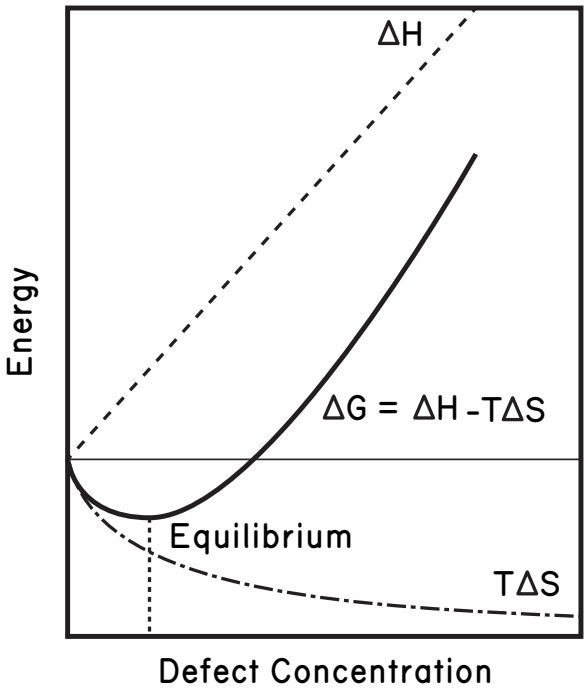


Figure 6: Energetic changes during the formation of an intrinsic defect.

perovskite structures: (i) [3:3] where $x + y = +3$, (ii) [2:4] where x = 2 and y = 4 and (iii) [1:5] where x = 1 and y = 5. Of more importance to the crystal structure however is the ionic radii of the A and B atoms. In general, the A site atom must be larger than the B site atom and approximately similar to the oxygen, however, the perovskite structure has the capability of accommodating significant lattice distortions. Equation 10 defines the Goldschmidt tolerance factor (t) [13] which characterises the change in lattice structure due to the A/B atomic radii ratio:

$$t = \frac{r_A + r_O}{\sqrt{2}\,(r_O + r_B)} \tag{1.10}$$

Where r_A is the ionic radii of the A atom, r_B is the ionic radii of the B atom and r_O is the ionic radii of oxygen.

For $t = 1$ the perovskite is cubic, $0.9 < t < 1.0$ the perovskite structure will exhibit a pseudo-cubic form, however, as $0.71 < t < 0.9$ the structure will deform to either an orthorhombic or rhombohedral structure as the A site atoms become too small to remain in contact with the oxygen atoms [14] .

Another characteristic of the perovskite structure is its ability to withstand deviation from stoichiometry on both the cation and anion sites. Of particular concern

for SOFC cathode materials is the non-stoichiometry of the oxygen ($ABO_{3\pm\delta}$); where positive values of δ refer to an oxygen excess and negative values oxygen deficiency. An oxygen deficient system is one where a proportion of the oxygen lattice sites are empty (referred to as vacancies - see Section 1.2.2). An oxygen excess system contains extra oxygen in non-lattice sites (commonly interstitial sites). In both cases the change of oxygen concentration remains in equilibrium with the metal cation concentration and charge neutrality laws. Therefore, defects within the system can alter both the crystal structure and the electronic properties of the material. Using the perovskite system it is therefore possible optimise the properties of a material by altering the chemistry of the system [15]. The most commonly used materials for SOFC cathodes have oxygen deficiencies [12] and therefore contain vacancies as the primary defect for the ionic transport of oxygen.

1.2.2 *Defect in Solids*

Defects within a material account for many of the properties of a material: including the electronic and ionic conductivity. To engineer a material to have MIEC properties the defect chemistry of a system must be understood. In nature, every material contains a degree of intrinsic defects (except, theoretically, at absolute zero). They arise through the minimisation of free energy (ΔG) of the system. In the case of a vacancy there is an energy cost (ΔH) associated with removing a lattice atom and breaking bonds, but there is also an increase in configurational entropy as there are increased available positions for the atoms. When there are very few vacancies in the system the entropic term in Equation 1.11 will be greater than the formation enthalpy and as such the free energy of the system is reduced when defects are formed. At high vacancy concentration there will be greater disorder in the crystal, and therefore the enthalpy of formation will be greater than the change in entropy of the system, preventing defect formation. The intrinsic defect concentration can be found where the derivative of free energy is zero, or the minima shown in Figure 6.

$$\Delta G = \Delta H - T\Delta S \tag{1.11}$$

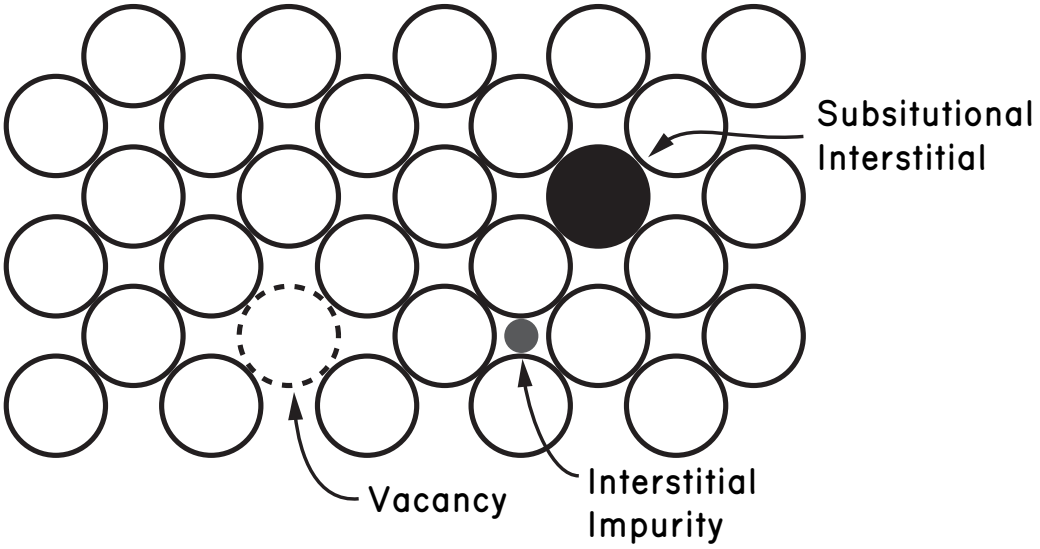


Figure 7: Intrinsic and extrinsic defect mechanisms.

Where ΔG is the free energy change, ΔH is the Enthalpy of defect formation, ΔS is the total change in entropy and T is the temperature (K).

1.2.3 *Point Defects*

Defects can be generally defined as either planar, line or point defects. Planar and line defects are large scale defect systems that arise due to misalignment and/or miss-orientation of the crystal lattice. They are primarily related to the mechanical properties of the material. Point defects, however, deal with single atomic sites and are vital in defining the electro-chemical properties of a system. Figure 7 shows with main types of point defect: vacancy, interstitial and impurity. Vacancies are defined by an atom that is missing from its lattice site; interstitials are defined by atoms occupying sites not defined by the crystal structure; impurities are defined by foreign atoms occupying either a lattice site (replacing the original atom) or in an interstitial site.

Defect equations are written in a similar manner to regular chemical equations, however, use the Kröger-Vink model and notation to describe disorder within a system [16]. The Kroger-Vink model makes the assumption that defects behave like an ideal solution where the enthalpy of mixing is zero. This leads to an uncertainty regarding the true chemical potential of each species, therefore, a 'virtual' chemical potential is ascribed for each species [17]. This form of notation takes

into account the site on which the species sits as well as the effective charge. In this notation the main symbol defines the species. Atoms are simply represented by their chemical symbol whereas vacancies are represented by a '*V*'. The atomic position of the species is shown by the sub-script. This is either an atomic site (therefore a chemical symbol) or an interstitial '*i*'. The effective charge of the species is defined by the super-script where a cross ($\times$) represents a neutral site, a dot ($\bullet$) represents a positive charge and a dash ($'$) represents a negative charge. The effective charge is defined as the net excess charge on the crystal caused by the introduction of a defect. If an atom sits on the correct site this will be neutrally charged, however, if the species differs the effective charge is the difference from its normal state. Examples can be seen in Equation 1.12-1.15 which show the Kroger-Vink notation for (i) a lanthanum (La^{3+}) atom on its normal atomic position, (ii) a strontium (Sr^{2+}) dopant atom replacing a lanthanum atom, (iii) a lanthanum vacancy and (iv) a Lanthanum interstitial.

$$La_{La}^{\times} \tag{1.12}$$

$$Sr_{La}^{'} \tag{1.13}$$

$$V_{La}^{'''} \tag{1.14}$$

$$La_{i}^{\bullet\bullet\bullet} \tag{1.15}$$

Electronic species are not bound to specific atomic sites and as such only require a charge definition: $e^{'}$ and $h^{\bullet}$ for electrons and holes, respectively.

In a perovskite system there are three primary intrinsic defect systems : Schottky, Frenkel and electronic disorder.

Schottky disorder defines a process where cation-anion pairs spontaneously generate vacancies at a surface (such as a grain boundary). These vacancies may then migrate through the bulk as can be seen in Figure 8. For a binary system such as a [3:3] ABO_3 perovskite this is defined by Equation 1.16:

$$A_{A}^{\times} + B_{B}^{\times} + 3O_{O}^{\times} \Leftrightarrow A_{A_s}^{\times} + B_{B_s}^{\times} + 3O_{O_s}^{\times} + V_{A}^{'''} + V_{B}^{'''} + 3V_{O}^{\bullet\bullet} \tag{1.16}$$

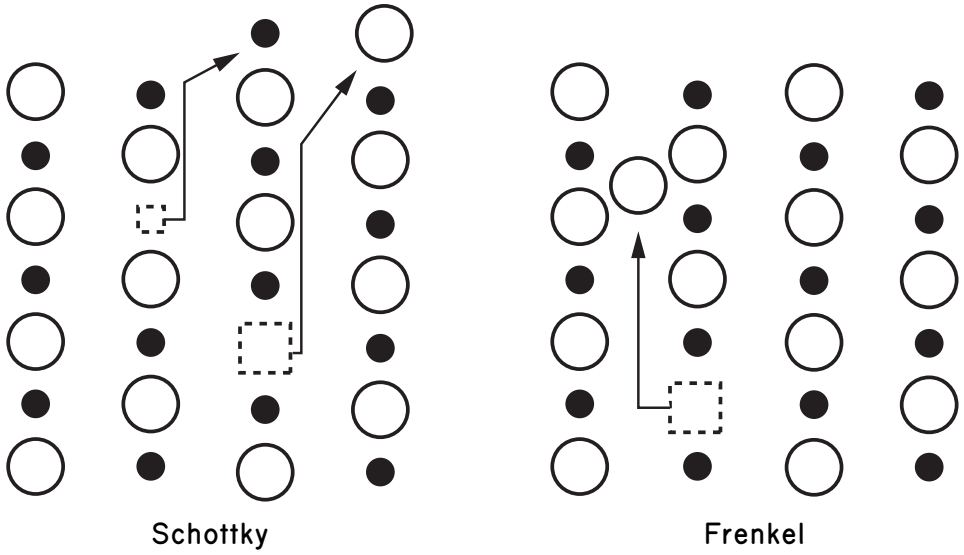


Figure 8: Showing Schottky (left) and Frenkel (right) intrinsic defect processes.

Where $A^{\times}_{A_s}$, $B^{\times}_{B_s}$ and $O^{\times}_{O_s}$ represent atoms at a surface position. Schottky disorder may be simplified into Equation 1.17 as the atoms have not left the system.

$$null \Leftrightarrow V'''_A + V'''_B + 3V^{\bullet\bullet}_O \tag{1.17}$$

Frenkel disorder defines a situation where an atom is displaced into an interstitial site, leaving behind a vacancy, as shown in Figure 8(b). The process is defined by Equation 1.18.

$$O^{\times}_O \Leftrightarrow V^{\bullet\bullet}_O + O''_i \tag{1.18}$$

Electronic disorder simply defines the generation of electronic species.

$$null \Leftrightarrow e' + h^{\bullet} \tag{1.19}$$

The overall concentration of each defect type is dependent upon the formation enthalpies of each defect, the temperature of a system and the partial pressure of oxygen in the gas. For the most commonly used SOFC cathode materials Schottky disorder is the dominant intrinsic disorder as oxygen interstitials (and thus anion Frenkel disorder) have very high formation energies due to geometric restrictions in the crystal lattice [18]. Intrinsic defect concentrations for most materials are

very low and as such must be enhanced to provide sufficient electronic and ionic conductivities for practical application.

Atomic substitution is the process of replacing atoms within the structure with a different atom. If the foreign atom has a different valence the doping is referred to as *aliovalent*. Due to charge neutrality law if you dope aliovalently the excess or deficit of charge must be compensated. Observing again a binary [3:3] perovskite system (ABO_3) we can see that doping the A site with a metal, M, with a valence of +2 can be charge compensated by either the formation of oxygen vacancies (Equation 1.20) or electronic defects by altering the valence of the B atom (Equation 1.21).

$$2MO \xrightarrow{ABO_3} 2M'_A + V^{\bullet\bullet}_O + 2O^{\times}_O \tag{1.20}$$

$$2MO + 2B^{\times}_B + \frac{1}{2}O_2 \xrightarrow{ABO_3} 2M'_A + 2B^{\bullet}_B + 3O^{\times}_O \tag{1.21}$$

As mentioned previously the preferential formation of defects depends on which is energetically favourable. When considering point defects as part of a system [19] they are commonly modelled as individual chemical species within a solid solution, each with a chemical potential. Therefore, the total free energy in a system can be defined by the summation of partial molar free energies as shown in Equation 1.22.

$$G = \mu_1 n_1 + \mu_2 n_2 ... \mu_i n_i \tag{1.22}$$

Where n_i is the number of moles for species i and μ_i us the chemical potential for species i.

For example, in a 4 component system (where components 'a' and 'b' refer to the reactants, and components 'c' and 'd' to the products), the change in free energy (ΔG) can be described by Equation 1.23.

$$\Delta G = c\mu_C + d\mu_D - (a\mu_A + b\mu_B) \tag{1.23}$$

The chemical potential can be related to an activity using Equation 1.24.

$$\mu_i = \mu_i^0 + RT\ln a_i \tag{1.24}$$

Combining Equation 1.23 with Equation 1.24 the change in free energy is therefore defined by:

$$\Delta G = \Delta G^0 + RT\ln\left(\frac{a_C^c a_D^d}{a_A^a a_B^b}\right) \tag{1.25}$$

In an ideal solution the formation of a defect does not influence the formation of the next defect and therefore the activity of a species is equal to the species concentration. However, in reality a solution can never be ideal and true chemical potentials cannot be measured experimentally [17]. It is therefore only valid to assume that systems behave ideally for very dilute solutions. At higher defect concentrations interactions will occur between defects and can form associated pairs of defects [20] which can have significant effects upon the MIEC material properties. Despite this, for practicality sake, equations used to define the defect system at equilibrium tend to make the assumption the system is an ideal solution.

1.2.4 *Diffusion*

Oxygen vacancies enable oxygen mobility within a solid oxide material and the chemical diffusion (D_C) of ions will move from regions of high concentration to low concentration. Mass-transport of a system is defined by Fick's first law of diffusion, which states that the flux of a species (J) at a given position (x) is proportional to the self-diffusivity (D) and a concentration gradient:

$$J = -D\frac{dC}{dx} \tag{1.26}$$

Where J is the diffusion flux (mol/m²s), D is self diffusivity (m²/s), C is the concentration per unit volume (mol/m³) and x is the position (m).

Fick's second law defines the change in concentration with respect to time:

$$\frac{dC}{dt} = D\frac{\delta^2 C}{\delta x^2} \tag{1.27}$$

Self-diffusivity is a material property and defines the random motion of ions within a material. Oxygen ions migrate through the material by 'hopping' into

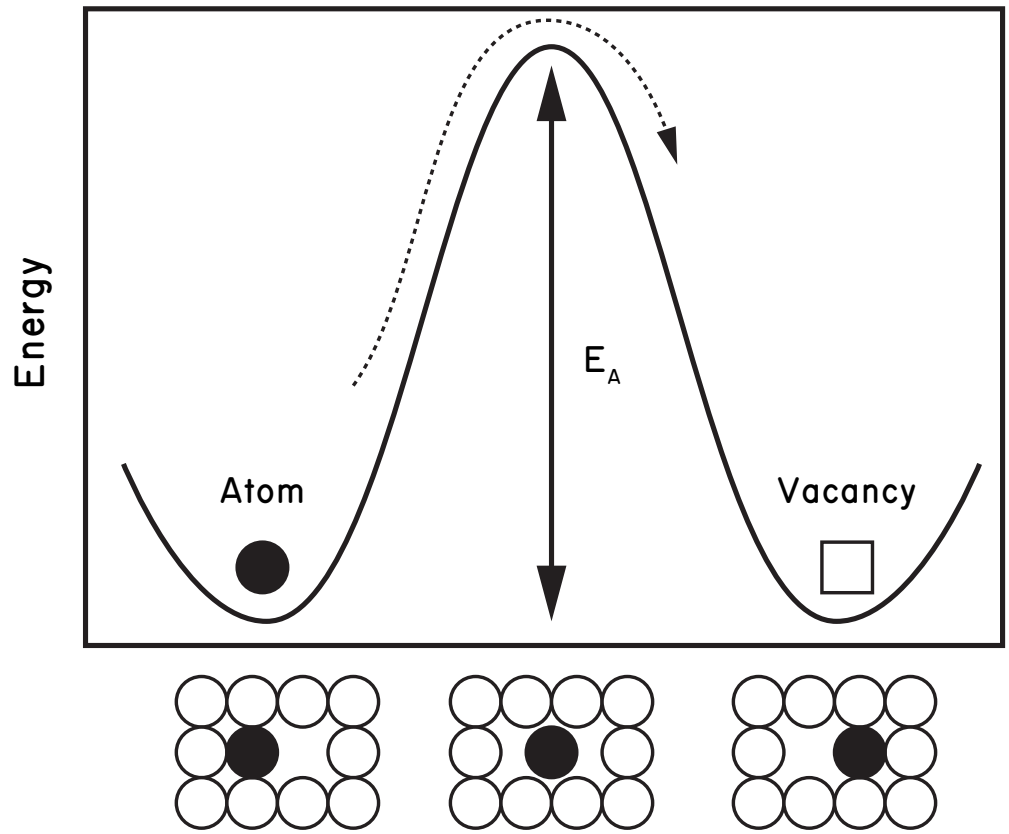


Figure 9: Schematic of ion migration showing the energy cost at each position of the hopping process.

vacant sites. The process requires a degree of structural distortion and as such there is an energy barrier (or activation energy, 'E_a') that must be overcome for diffusion to occur as shown in Figure 9. Empirically it is seen that diffusion is a thermally activated process and as such exhibits Arrhenius behaviour. Considering a single ion, the migration frequency (ν) can be defined by Equation 1.28.

$$\nu = \nu_0 exp\left(\frac{-\Delta G_m}{kT}\right) \tag{1.28}$$

Where ν is the migration frequency (jumps/s), ν_0 is the jump attempt frequency (jumps/s), ΔG_m is the free energy change for migration (J), k is Boltzmann's constant (J/K) and T is temperature (K).

For a simple cubic lattice each site is co-ordinated by 6 equivalent sites. Therefore, there is a $z/6$ probability that an ion will hop to a vacant site where 'z' is the number of relevant defect sites amongst the co-ordinated atoms. Each migra-

tion also has an associated length which is referred to as the diffusion length, 'L'. It is possible to relate the probability of a single hop to the whole system by considering the concentration of oxygen vacancies:

$$\begin{aligned} D &= \frac{z}{6}\left[V_O^{\bullet\bullet}\right] L^2 \nu \\ &= \frac{z}{6}\left[V_O^{\bullet\bullet}\right] L^2 \nu_0 exp\left(\frac{\Delta S_m}{kT}\right) exp\left(\frac{-\Delta H_m}{kT}\right) \end{aligned} \tag{1.29}$$

Therefore:

$$D = D_0 exp\left(\frac{-E_a}{RT}\right) \tag{1.30}$$

Where D_o refers to the maximum possible diffusivity of the system (if there were no activation energy barrier to diffusion):

$$D_0 = \frac{z}{6}\left[V_O^{\bullet\bullet}\right] L^2 \nu_0 exp\left(\frac{\Delta S_m}{kT}\right) \tag{1.31}$$

Self-diffusivity is a property of the material and independent of species concentration, however, as can be seen diffusivity is highly dependent upon temperature and crystal structure, therefore, defect type and concentration. Measuring self-diffusivity is possible using a number of experimental techniques including isotopic gas phase analysis [21], Isotopic Exchange Depth-Profiling (IEDP) [11] and Nuclear Reaction Analysis [22]. This thesis will primarily deal with the IEDP method (which is expanded upon in Section 4.2.1).

1.2.5 *Ionic Conductivity*

The mobility (μ) of a species defines rate of which a particle can move through a system under the influence of a driving force (such as a chemical potential or an electrical potential). Electronic mobility is therefore defined as the rate of flow of a charge carrier (electron and/or hole) per unit electric field. Electronic

conductivity (σ) is therefore the flux per unit electric field and is described by Equation 1.32.

$$\sigma_e = en_e\mu_e + hn_h\mu_h \tag{1.32}$$

Where σ_e is the total electronic conductivity (S/m), e/h is the charge of an electron and hole respectively (C), n_e/n_h is the number of charge carries and μ_e/μ_h is the mobility of the charge carries (m^2/Vs).

The driving force for the transport of ions can be both electronic and chemical. The Nernst-Einstein relationship (Equation 1.33) relates the diffusivity of a material to the ionic mobility of the species.

$$\mu_i = \frac{z_i eD}{kT} \tag{1.33}$$

Where D is self-diffusivity (m^2/s), μ_i is the mobility of species i (m^2/Vs), $z_i e$ is the charge of the ion, k is the Boltzmann's constant (J/K) and T is temperature (K).

Therefore, ionic conductivity is defined as:

$$\sigma_i = \frac{c_i z_i^2 e^2 D}{kT} \tag{1.34}$$

Where c_i is the concentration of anionic sites per unit volume. The total conductivity of a system is simply the summation of each mobile charged species. Therefore, ionic conductivity of a system can be directly compared to the electronic conductivity. The fraction of which the total conductivity is ionic (referred to as the transference number (t_i) [23, 24]) can be used to define relevant application for the material:

$$t_i = \frac{\sigma_i}{\sigma_{Total}} \tag{1.35}$$

For materials with negligible electronic conductivity (transference number $\approx$ 1) the material would be suitable as an *electrolyte* material, however, the primary focus of this thesis are MIEC materials with both ionic and electronic properties.

1.2.6 *Surface Exchange*

As detailed in Section 1.1.2 there are multiple possible paths an oxygen ion may take in order to be reduced and incorporated into the bulk of the material. The overall rate of exchange of oxygen from the gas phase to the atoms at the surface of the MIEC may be measured in terms of the surface exchange coefficient 'k' (cm/s). A simple expression for k has been derived by Kilner *et al.* [25]:

$$k = a_0 m^{-\frac{1}{3}} [V_O^{\bullet\bullet}]^{\frac{2}{3}} \upsilon_E exp\left(-\frac{\Delta S_E}{k}\right) exp\left(-\frac{\Delta H_E}{kT}\right) \tag{1.36}$$

Where a_0 is the lattice parameter of the cubic unit cell, m is the number of oxygen sites per unit cell and υ_E is the frequency of one atom being adsorbed, $\left[V_O^{\bullet\bullet}\right]$ is the bulk concentration of oxygen vacancies, ΔS_E and ΔH_E are the entropic and enthalpy quantities for the exchange process.

At risk of over-simplification surface exchange may be generalised into three stages: *Adsorption*, *Dissociation* and *Incorporation*. Once incorporated the oxygen ion migrates away from the surface regenerating the surface vacancy leaving it available for further reactions. At this point in time it is not known where the molecular oxygen is adsorbed, dissociated or incorporated, nor what is the rate limiting step. For years it has been assumed the B-site transition metals are the primary catalytic sites for the oxygen reduction reaction, however, it has been shown that the surface termination layer tends to be dominated by A-site atoms [26]. The current model for the ORR assumes that the surface is a direct termination of the bulk, however, (as will be discussed in detail in Section 2.2) this is very rarely the case. It is often true that the surface is a meta-stable system dependent upon temperature, $p(O_2)$ and gas stream impurities.

1.2.7 *IT-SOFC Mixed Ionic-Electronic Conducting Materials*

Generally speaking, the higher the ionic conductivity and electronic conductivity the better an MIEC material will perform as an SOFC cathode, however, as outlined at the beginning of Section 1.2 there are a number of properties a material must have in order to be considered. The story of the SOFC cathode can be very briefly summarised by the progression from expensive transition metals

(ie platinum) to high temperature MIEC materials; then intermediate temperature MIEC materials. Today, the most widely used material commercially are perovskite structured oxides [27]. As will be explained throughout Chapter 2 these are the materials that provides the most desirable balance of material properties. Many alternative MIEC structures are in development [28] but will not be discussed in detail in this thesis.

The first perovskite cathode material system to be utilised commercially was $La_{1-x}Sr_xMnO_{3\pm\delta}$ (LSM). With strontium substitution in the range of 10 - 20% LSM is predominantly electronic conductor and exhibits catalytic properties similar to that of platinum [29]. Sr^{2+} on the A site enhances the electronic conductivity by oxidising the manganese ion (Equation 1.37), reaching a maximum at approximately 55 mol% [30] . However, as the system tends to exhibit oxygen excess, there are no oxygen vacancies and hence a very low ionic conductivity. The material therefore behaves as a TPB and cathodic overpotentials become significant at temperatures below 700°C [31].

$$La_{La}^{\times} + Mn_{Mn}^{\times} + SrO \xleftrightarrow{LaMnO_3} Sr_{La}^{'} + Mn_{Mn}^{\bullet} + O_O^{\times} \tag{1.37}$$

Originally investigated for their magnetic properties, cobalt containing perovskites such as LaCoO3 were shown to exhibit high catalytic activity due to a high concentration of conduction electrons at the surface [32, 33]. Again, doping of Sr^{2+} on the A site enhances the properties of the material by forming both oxygen vacancies (Equation 1.38) and electronic species (Equation 1.39); providing suitable properties over IT-SOFC temperature ranges. The defect structure of $La_{1-x}Sr_xCoO_{3-\delta}$ (LSC) is complex and a full defect model will be discussed in Chapter 2. LSC has excellent catalytic properties and ionic conductivity, however, the large cobalt content significantly increases the Thermal Expansion Coefficient (TEC) of the perovskite due to a chemical expansion of the lattice in response to oxygen loss. When the expansion of the cathode and electrolyte are significantly different there will be a marked increase in mechanical stresses at the cathode-electrolyte interface; reducing mechanical stability at operating temperatures significantly. Cobaltite cathodes also react readily with common electrolyte

materials forming insulating compounds at the interface, reducing overall cell performance [34].

$$2SrO \xleftrightarrow{LaCoO_3} 2Sr'_{La} + V^{\bullet\bullet}_{O} + 2O^{\times}_{O} \tag{1.38}$$

$$2SrO + \frac{1}{2}O_2 + 2Co^{\times}_{Co} \xleftrightarrow{LaCoO_3} 2Sr'_{La} + 2Co^{\bullet}_{Co} + 3O^{\times}_{O} \tag{1.39}$$

Attempts to reduce the TEC of LSC without reducing the properties of the material have included replacing lanthanum on the A site (e.g. $Sm_{1-x}Sr_xCoO_{3-\delta}$ or $Pr_{1-x}Sr_xCoO_{3-\delta}$) and using dopants on the B site (e.g. $La_{1-x}Sr_xCo_{1-y}Cu_yO_{3-\delta}$) [35]. Many of these materials have shown promise but have not yet been optimised; either exhibiting poor electronic conductivity, ionic conductivity or chemical stability. The most successful material has been a variant of $La_{1-x}Sr_xCo_{1-y}Fe_yO_{3-\delta}$ (LSCF) where x = 0.4 and y = 0.8. The material exhibits ionic and electronic conductivities slightly lower than LSC at the same temperatures, however, increased mechanical and chemical stability across larger partial pressures of oxygen make LSCF a more desirable material practically. This thesis focusses upon the structural, chemical and kinetic changes of LSCF at operating temperatures and as material will be discussed in detail in the following chapter.

BIBLIOGRAPHY

[1] S C Singhal and K Kendall. *High Temperature Solid Oxide Fuel Cells: Fundamentals, Design, and Applications*. Electronics & Electrical. Elsevier, 2003. ISBN 9781856173872. URL https://books.google.com/books?id=LjSBsqGdxvsC.

[2] W. Nernst. On the electrolytic conduction of solid bodies at high temperatures. *Z.Elektrochem*, 6:41, 1899.

[3] C Pianese and M Sorrentino. Modelling Methodologies for Design and Control of Solid Oxide Fuel Cell APUs. In *Power Control and Optimisation*, volume 1159, pages 3–10, 2009. ISBN 978-0-7354-0696-4. doi: 10.1063/1.3223952.

[4] Daniel Marinha, Laurent Dessemond, and Elisabeth Djurado. Comprehensive Review of Current Developments in IT-SOFCs. *Current Inorganic Chemistry*, 3(1):2–22, 2013. ISSN 18779441. doi: 10.2174/1877944111303010003. URL http://www.eurekaselect.com/openurl/content.php?genre=article{&}issn=1877-9441{&}volume=3{&}issue=1{&}spage=2.

[5] G. Chiodelli and L. Malavasi. Electrochemical open circuit voltage (OCV) characterization of SOFC materials. *Ionics*, 19:1135–1144, 2013. ISSN 09477047. doi: 10.1007/s11581-013-0843-z.

[6] David R Lide and Henry V Kehiaian. CRC handbook of thermophysical and thermochemical data, 1994.

[7] Stuart B Adler. Factors governing oxygen reduction in solid oxide fuel cell cathodes. *Chemical reviews*, 104(10):4791–843, oct 2004. ISSN 0009-2665. URL http://www.ncbi.nlm.nih.gov/pubmed/15669169.

[8] S B Adler. Electrode Kinetics of Porous Mixed-Conducting Oxygen Electrodes. *Journal of The Electrochemical Society*, 143(11):3554, 1996. ISSN 00134651. doi: 10.1149/1.1837252. URL http://jes.ecsdl.org/cgi/doi/10.1149/1.1837252.

[9] S. Dou. Mechanism of Oxygen Permeation Through Lime-Stabilized Zirconia. *Journal of The Electrochemical Society*, 132(8):1843, 1985. ISSN 00134651. doi: 10.1149/1.2114228. URL http://jes.ecsdl.org/cgi/doi/10.1149/1.2114228.

[10] E. N. Armstrong, K. L. Duncan, D. J. Oh, J. F. Weaver, and E. D. Wachsman. Determination of Surface Exchange Coefficients of LSM, LSCF, YSZ, GDC Constituent Materials in Composite SOFC Cathodes. *Journal of The Electrochemical Society*, 158(5):B492, 2011. ISSN 00134651. doi: 10.1149/1.3555122.

[11] JA Kilner, BCH Steele, and L Ilkov. Oxygen self-diffusion studies using negative-ion secondary ion mass spectrometry (SIMS). *Solid State Ionics*, 12 (1984):89–97, 1984. URL http://www.sciencedirect.com/science/article/pii/0167273884901346.

[12] Chunwen Sun, Rob Hui, and Justin Roller. Cathode materials for solid oxide fuel cells: a review. *Journal of Solid State Electrochemistry*, 14(7):1125–1144, oct 2009. ISSN 1432-8488. doi: 10.1007/s10008-009-0932-0. URL http://link.springer.com/10.1007/s10008-009-0932-0.

[13] V M Goldschmidt. Die Gesetze der Krystallochemie. *Naturwissenschaften*, 14(21):477–485. ISSN 1432-1904. doi: 10.1007/BF01507527. URL http://dx.doi.org/10.1007/BF01507527.

[14] Robert Ian. Hines. *Atomistic simulation and ab initio studies of polar solids*. PhD thesis, University of Bristol, 1997.

[15] D M Smyth. The Defect Chemistry of Metal Oxides, 2000.

[16] F. a. Kröger and H. J. Vink. Relations between the Concentrations of Imperfections in Crystalline Solids. *Solid State Physics - Advances in Research and Applications*, 3(C):307–435, 1956. ISSN 00811947. doi: 10.1016/S0081-1947(08)60135-6.

[17] Truls Norby. Defect Equilibria, 2004. URL http://www.uio.no/studier/emner/matnat/kjemi/KJM4120/v04/undervisningsmateriale/.

[18] A. Reller. Chemical and physical implications of cationic and anionic modifications in perovskite related metal oxides. *Philosophical Magazine A*, 68 (4):641–652, 1993. ISSN 0141-8610. doi: 10.1080/01418619308213988. URL http://www.tandfonline.com/doi/abs/10.1080/01418619308213988.

[19] B.C.H. Steele. Oxygen ion conductors and their technological applications. *Materials Science and Engineering: B*, 13(2):79–87, mar 1992. ISSN 09215107. doi: 10.1016/0921-5107(92)90146-Z. URL http://linkinghub.elsevier.com/retrieve/pii/092151079290146Z.

[20] A. Petrov. Crystal structure, electrical and magnetic properties of La1-xSrxCoO3-y. *Solid State Ionics*, 80(3-4):189–199, sep 1995. ISSN 01672738. doi: 10.1016/0167-2738(95)00114-L. URL http://linkinghub.elsevier.com/retrieve/pii/016727389500114L.

[21] B.a. Boukamp, B.a. van Hassel, I.C. Vinke, K.J. De Vries, and a.J. Burggraaf. The oxygen transfer process on solid oxide/noble metal electrodes, studied with impedance spectroscopy, dc polarization and isotope exchange. *Electrochimica Acta*, 38(14):1817–1825, 1993. ISSN 00134686. doi: 10.1016/0013-4686(93)80303-H.

[22] R Robin, A R Cooper, and A H Heuer. Application of a nondestructive single-spectrum proton activation technique to study oxygen diffusion in zinc oxide. *J. Appl. Phys.*, 44(8):3770–3777, 1973. ISSN 00218979. doi: 10.1063/1.1662839.

[23] W. Hittorf. No Title. *Ann. Physik*, 106:543, 1859.

[24] C Tubandt and Sophie Eggert. Über Elektrizitätsleitung in festen kristallisierten Verbindungen. Erste Mitteilung: Nachweis der exakten

Gültigkeit des Faraday schen Gesetzes bei der Elektrolyse fester Schwermetallsalze. *Zeitschrift für anorganische und allgemeine Chemie*, 110(1):196–236, 1920. ISSN 1521-3749. doi: 10.1002/zaac.19201100114. URL http://dx.doi.org/10.1002/zaac.19201100114.

[25] JA Kilner, RA De Souza, and IC Fullarton. Surface exchange of oxygen in mixed conducting perovskite oxides. *Solid State Ionics*, 86-88:703, 1996. URL http://www.sciencedirect.com/science/article/pii/0167273896001531.

[26] John Druce, Tatsumi Ishihara, and John Kilner. Surface composition of perovskite type materials studied by Low Energy Ion Scattering (LEIS). *Solid State Ionics*, 262:893–896, 2014. ISSN 01672738. doi: 10.1016/j.ssi.2013.09.010. URL http://dx.doi.org/10.1016/j.ssi.2013.09.010.

[27] a. Esquirol, N. P. Brandon, J. a. Kilner, and M. Mogensen. Electrochemical Characterization of La[sub 0.6]Sr[sub 0.4]Co[sub 0.2]Fe[sub 0.8]O[sub 3] Cathodes for Intermediate-Temperature SOFCs. *Journal of The Electrochemical Society*, 151(11):A1847, 2004. ISSN 00134651. doi: 10.1149/1.1799391. URL http://jes.ecsdl.org/cgi/doi/10.1149/1.1799391.

[28] John a. Kilner and Mónica Burriel. Materials for Intermediate-Temperature Solid-Oxide Fuel Cells. *Annual Review of Materials Research*, 44(1):365–393, jul 2014. ISSN 1531-7331. doi: 10.1146/annurev-matsci-070813-113426. URL http://www.annualreviews.org/doi/abs/10.1146/annurev-matsci-070813-113426.

[29] J. Van Herle, A.J. J Mcevoy, and K.Ravindranathan Thampi. A study on the La1-xSrxMnO3 oxygen cathode. *Electrochimica Acta*, 41(9):1447–1454, 1996. ISSN 00134686. doi: 10.1016/0013-4686(95)00393-2. URL http://www.sciencedirect.com/science/article/pii/0013468695003932.

[30] Tatsumi Ishihara and Takanari Kudo. Doped Perovskite Oxide, PrMnO3, as a New Cathode for Solid Oxide Fuel Cells that Decreases the Operating Temperature. *Journal of the American ...*, (193928):1993–1995, 1994. URL http://onlinelibrary.wiley.com/doi/10.1111/j.1151-2916.1994.tb09779.x/abstract.

[31] R Bell. Influence of synthesis route on the catalytic properties of La1-xSrxMnO3. *Solid State Ionics*, 131(3-4):211–220, 2000. ISSN 01672738. doi: 10.1016/S0167-2738(00)00668-8. URL http://www.sciencedirect.com/science/article/pii/S0167273800006688.

[32] RJH Voorhoeve, DW Johnson, JP Remeika, and PK Gallagher. Perovskite Oxides : Materials Science in Catalaysts. *Science*, 195(4281):827–833, 1977.

[33] I Kojima, H Adachi, and I Yasumori. Electronic structures of the LaBO3 (B = Co, Fe, Al) perovskite oxides related to their catalysis. *Surface Science*, 130(1):50–62, jul 1983. ISSN 0039-6028. doi: http://dx.doi.org/10.1016/0039-6028(83)90259-5. URL http://www.sciencedirect.com/science/article/pii/0039602883902595.

[34] M Shiono, K Kobayashi, T Lannguyen, K Hosoda, T Kato, K Ota, and M Dokiya. Effect of CeO2 interlayer on ZrO2 electrolyte/La(Sr)CoO3 cathode for low-temperature SOFCs. *Solid State Ionics*, 170(1-2):1–7, may 2004. ISSN 01672738. doi: 10.1016/j.ssi.2004.02.018. URL http://linkinghub.elsevier.com/retrieve/pii/S0167273804001018.

[35] F Riza, Ch Ftikos, F Tietz, and W Fischer. Preparation and characterization of Lno.8Sro.2Feo.8Coo.2O3-x (Ln=La, Pr, Nd, Sm, Eu, Gd). *Journal of the European Ceramic Society*, 21(10-11):1769–1773, jan 2001. ISSN 09552219. doi: 10.1016/S0955-2219(01)00112-1. URL http://linkinghub.elsevier.com/retrieve/pii/S0955221901001121.

2

LITERATURE REVIEW

2.1 THE LSCF SYSTEM

Original interest in the Lanthanum Cobaltate system dates back to the 1950s where $LaCoO_3$ and $La_{1-x}Sr_xCoO_{3-\delta}$ were studied for their magnetic and electronic properties [1, 2, 3, 4]. The $La_{1-x}Sr_xFeO_{3-\delta}$ system was also subject to similar attention [5], however, it was not until 1969 that these materials were considered as fuel cell electrode materials [6] given their catalytic properties. Since then, a large amount of research has been conducted on these materials in an attempt to optimise their properties as an SOFC electrode material [7, 8, 9].

As mentioned in the previous chapter, LSC has a large thermal expansivity which tends to lead to poor mechanical stability. The first results of LSC co-doped with iron on the B-site, $La_{1-x}Sr_xCo_{1-y}Fe_yO_{3-\delta}$, exhibited slightly lower oxygen diffusivities [10], however, the material exhibited significantly greater mechanical and chemical stability. The $La_{1-x}Sr_xCo_{1-y}Fe_yO_{3-\delta}$ system has therefore been studied in great detail and to this day is still the most commonly used MIEC material for both academic and industrial applications. For this reason, it was chosen as the focus of this work and will discussed throughout the following sections.

2.1.1 *Defect Chemistry of $La_{1-x}Sr_xCo_{1-y}Fe_yO_{3-\delta}$*

The perovskite structure can be manipulated to exhibit a wide variety of properties and as such $La_{1-x}Sr_xCo_{1-y}Fe_yO_{3-\delta}$ is not a trivial system to define. The accepted model for $La_{1-x}A_xBO_{3\pm\delta}$ was proposed by Steele *et al.* [11], however, may only be used to *qualitively* define the $La_{1-x}Sr_xCo_{1-y}Fe_yO_{3-\delta}$ defect system. The model takes into account both intrinsic and extrinsic defects and defines the dominant type of disorder with respect to the oxygen partial pressure.

Due to the close-packed nature of the perovskite lattice it first assumed that the dominant intrinsic structural defects arise through Schottky disorder. Frenkel interstitial defects are neglected due to atomic size constraints. The Schottky reaction is therefore:

$$null = V_{La}^{'''} + V_{B}^{'''} + 3V_{O}^{\bullet\bullet} \tag{2.1}$$

Where the equilibrium constant K_s is given by:

$$K_s = \left[V_{La}^{'''}\right]\left[V_{B}^{'''}\right]\left[V_{O}^{\bullet\bullet}\right]^3 \tag{2.2}$$

The spontaneous generation of electronic defects may be defined by:

$$null = e^{'} + h^{\bullet} \tag{2.3}$$

The equilibrium constant for this reaction if therefore:

$$K_e = np \tag{2.4}$$

Assuming electronic defects are localised as valency defects, the formation reaction may be defined as:

$$2B_B^{\bullet} + O_O^{\times} = 2B_B^{\times} + V_O^{\bullet\bullet} + \frac{1}{2}O_2 \tag{2.5}$$

With a corresponding equilibrium constant:

$$K_{def} = \frac{\left[B_B^{\times}\right]^2\left[V_o^{\bullet\bullet}\right]p\,(O_2)^{\frac{1}{2}}}{\left[B_B^{\bullet}\right]^2\left[O_O^{\times}\right]} \tag{2.6}$$

Extrinsic defects by aliovalent substitution of the A site[1] must be compensated for to maintain charge neutrality. This may be achieved by the generation of oxygen vacancies or oxidation (formation of a hole) of the B site cation[2]. At low

1 Where the charge of A is 2+

2 As previously show in Equation 1.38 and Equation 1.39

temperatures and high oxygen partial pressures charge compensation is primarily electronic [12]:

$$2AO + \frac{1}{2}O_2 + 2B_B^{\times} \xleftrightarrow{LaBO_3} 2A_{La}^{'} + 2B_B^{\bullet} + 3O_O^{\times} \tag{2.7}$$

As the temperature is increased and/or the partial pressure of oxygen is reduced, the charge is compensated by the formation of oxygen vacancies:

$$2AO \xleftrightarrow{LaBO_3} 2A_{La}^{'} + V_O^{\bullet\bullet} + 2O_O^{\times} \tag{2.8}$$

For a material to be an MIEC both of these mechanisms must be in operation simultaneously. The overall electroneutrality condition for an MIEC is therefore defined as:

$$\left[A_{La}^{'}\right] + \left[B_B^{'}\right] + 3\left[V_{La}^{'''}\right] + 3\left[V_B^{'''}\right] = \left[B_B^{\bullet}\right] + 2\left[V_O^{\bullet\bullet}\right] \tag{2.9}$$

Figure 10 shows the defect model proposed by Anderson [13] and modified by Steele *et al.* which simplifies the electronic and defect behaviour into five distinct regimes, with each regime exhibiting a majority defect type. Experimental data suggests that LSCF (where A = Sr^{2+}) exists primarily within regime **II** where the primary defect system is under typical IT-SOFC operating conditions[3] [12]:

$$\left[Sr_{La}^{'}\right] = p + 2\left[V_O^{\bullet\bullet}\right] \tag{2.10}$$

Depending upon temperature, $p(O_2)$ and composition LSCF may also perform under regime **III**. This regime increases the material's electronic conductivity, however, this increase is linked to a reduction in oxygen vacancy concentration and thus ionic conductivity. Under typical IT-SOFC operating conditions the primary determinant of the crystal structure, electronic and ionic properties of LSCF is the material composition. Tai *et al.* [14, 15] have performed extensive studies on the crystallographic properties of the $La_{1-x}Sr_xCo_{1-y}Fe_yO_{3-\delta}$ system which will be discussed over the following sections.

3 Temperature range of 600-800°C and $p(O_2)$ of 200 mbar

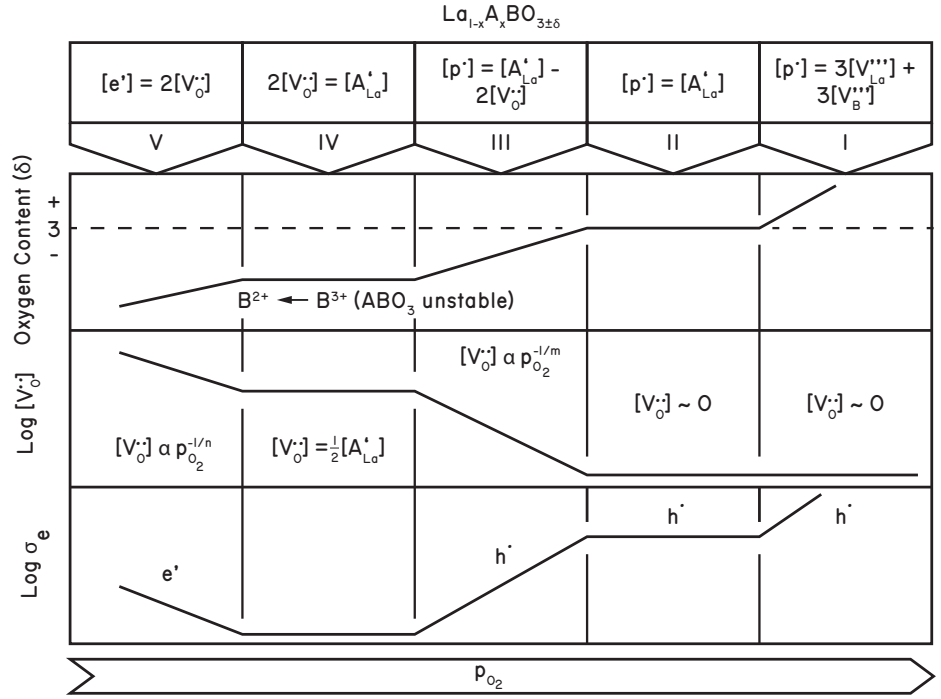


Figure 10: Brouwer diagram for the $La_{1-x}A_xBO_{3\pm\delta}$ system showing defect concentration as a function of partial pressure. Five distinct regions define the majority defect type over these ranges. Adapted from [11].

2.1.2 *Effect of A-site substitution of $La_{1-x}Sr_xCo_{0.2}Fe_{0.8}O_{3-\delta}$*

The aliovalent substitution of Sr^{2+} on the La^{3+} site has been shown to generate oxygen vacancies and hole generation in the B atoms. As shown in Figure 11 at room temperature low strontium substitution levels ($x < 0.2$) exhibit an orthorhombic crystal structure. From $0.2 < x < 0.8$ the structure is a rhombohedral structure and above $x = 0.8$ the structure becomes cubic, however, at this point it begins to lose structural stability. The pseudo-cubic[4] lattice parameter was found to decrease with increasing strontium content [14] despite the ionic radii of strontium (1.44 Å) being greater than that of lanthanum (1.36 Å)[16]. This cell volume decrease is associated with oxidation of B site atoms (Equation 2.7) that occur to maintain charge neutrality. According to Pauling's rules for bond strength [17] the oxised B^{IV}-O bond will be stronger and shorter than the B^{III}-O bond. As a result the BO_6 octahedral shrink in size in the presence of $B^{\bullet}_{B}$[5] and hence contribute significantly to the overall drop in cell volume.

4 The cubed root of the calculated cell volume rather than actual lattice parameter
5 Ionic radii of Fe^{III} = 0.65 Å, Fe^{IV} = 0.59 Å, Co^{III} = 0.65 Å and Co^{IV} = 0.55 Å

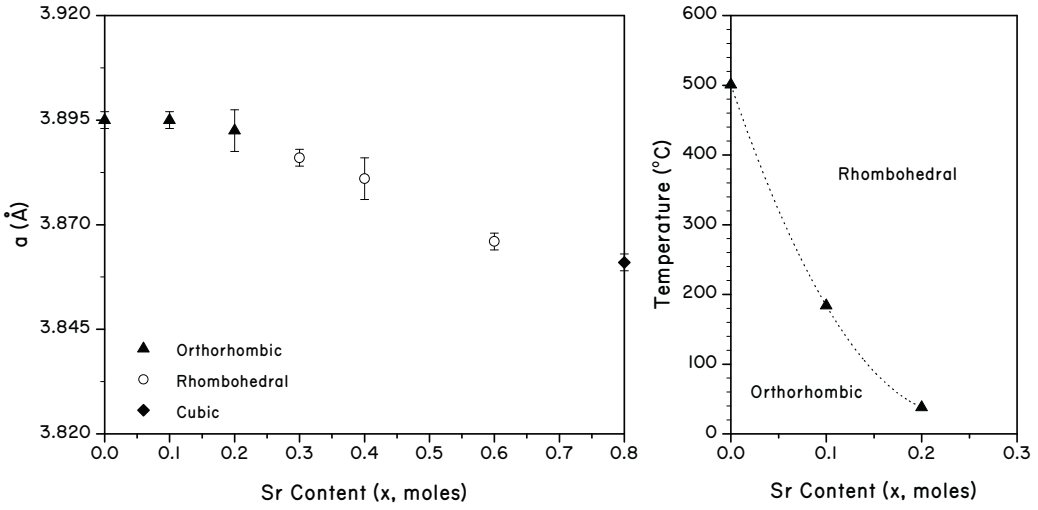


Figure 11: Pseudo-cubic lattice parameter and orthorhombic-rhombohedral transition temperatures as a function of Sr content (mol) [14].

At elevated temperatures the LSCF structure, if it is not already, tends to transform into the more stable rhombohedral phase [18]. At $x = 0.1$ the transition temperature is approximately 520-580°C whereas at $x = 0.2$ the transition temperature is reduced to approximately 170-250°C. When the rhombohedral phase is stable at room temperature Tai *et al.* demonstrated there was no further crystallographic transition up to 700°C. Wang *et al.* [19] also demonstrated no further transition up to 900°C and found similar lattice parameter values for $x = 0.4$.

Thermal expansion varies slightly ($15 \pm 2 \times 10^{-6}$/°C) with no apparent trend over $0 < x < 0.8$, however, there are additional lattice expansion effects associated with the loss of lattice oxygen at temperatures above 600°C. Lattice expansion is believed to be due to the repulsive forces between mutually exposed cations and the increase in ionic radii of the Fe and Co ions from higher to lower valences to preserve charge neutrality during the formation of oxygen vacancies. However, it has been shown that the radius of an oxygen vacancy is smaller than that of an oxygen atom [20]. The contribution from each effect is currently under investigation. Zhang *et al.* [21] noted that the majority of oxygen desorption at high temperatures occurs from the bulk of the material, therefore, the expansion due to oxygen desorption increases with Sr content as the intrinsic oxygen vacancy concentration is greater.

2.1.3 *Effect of B-site substitution of $La_{0.6}Sr_{0.4}Co_{1-y}Fe_yO_{3-\delta}$*

Substitution of the B site is generally considered to stabilise a particular crystal structure and alter the electronic properties of the material. In the case of $La_{0.6}Sr_{0.4}Co_{1-y}Fe_yO_{3-\delta}$ the introduction of iron offers the advantage of (i) stabilising the rhombohedral phase, (ii) lowering the TEC of the material to a value similar to common electrolyte materials and (iii) increasing electronic conductivity at high temperatures. The $La_{1-x}Sr_xCoO_{3-\delta}$ system has a high TEC value approximately two times larger than common electrolyte materials [22] and as such is not a suitable material despite its very high catalytic properties. It is believed that thermal effects, ionic radii and oxygen vacancy chemical expansivity all contribute to the TEC of a material. Currently there is debate [23, 24, 25] as to which has the greatest contribution, however, for the case of LSC it is believed that the TEC is strongly tied to the oxygen vacancy concentration [26]. The introduction of iron into LSC tends to suppress oxygen vacancy formation as the binding energy of the Fe-O bond is greater than that of Co-O and as such reduce the TEC of the material. This also has a pronounced effect upon the electronic properties of LSCF, however, this will be discussed in the following section.

The introduction of iron also causes the formation of ferroelastic domains within the microstructure [27]. The main effect of this is upon the mechanical properties of the material and will be discussed in more detail in Section 2.1.6.

2.1.4 *Electronic Properties of $La_{0.6}Sr_{0.4}Co_{0.2}Fe_{0.8}O_{3-\delta}$*

The electrical properties of LSCF can be described as both semiconductor-*like* and metallic-*like*. At low temperatures the material behaves like a semi-conductor as the oxygen *2p* - cobalt *3d* orbitals do not overlap and exhibit a band energy gap [28]. However, LSCF is metallic-*like* as electrical conductivity increases with temperature. However, LSCF deviates from typical metallic behaviour as carrier concentrations tend to account for changes in conductivity (rather than carrier mobility).

As is shown in Figure 12 the electrical conductivity of LSCF has been shown to rise linearly [14] until it reaches a maximum value (the temperature of the maxima is Sr concentration dependent), however, it then decreases as the temperature is increased further. The rise in electrical conductivity is thought to be generated

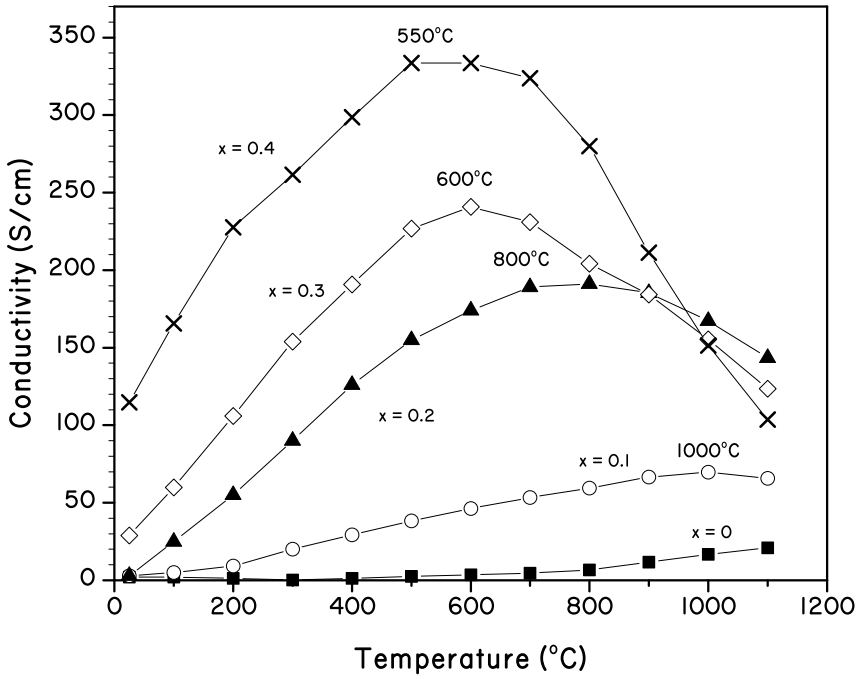


Figure 12: Electronic conductivity with respect to temperature of $La_{1-x}Sr_xCo_{0.2}Fe_{0.8}O_{3-\delta}$ for the range of $0 < x < 0.4$ [14]

by the disproportionation of the cobalt ions (Equation 2.11) [3]. This has the effect of introducing additional n and p-type charge carriers into the system, although the contribution from n-type carriers is low due to the high concentration of holes.

$$2Co^{3+} = Co^{2+} + Co^{4+} \tag{2.11}$$

The drop in conductivity at high temperatures is related to the oxygen vacancy concentration of the system due to oxygen desorption. Assuming that both methods of charge compensation are occurring the charge neutrality equation for LSCF may be written as:

$$\left[Sr'_{La}\right] = \left[B^{\bullet}_{B}\right] + 2\left[V^{\bullet\bullet}_{O}\right] \tag{2.12}$$

Therefore, an increase of oxygen vacancy concentration decreases the hole concentration by a factor of two in order to retain charge neutrality. In $La_{1-x}Sr_xFeO_{3-\delta}$

disproportionation of the Fe also introduces n and p-type charge carriers [29], however, in LSCF Lankhorst *et al.* [28] suggests that the energy to form the Fe^{2+} state is too high for charge disproportionation. Therefore this has the effect of stabilising the Fe^{4+} state (or $\left[Fe^{\bullet}_{Fe}\right]$), making metallic oxidation a more preferable charge compensation mechanism to oxygen vacancy formation.

2.1.5 *Oxygen Diffusion and Exchange in $La_{0.6}Sr_{0.4}Co_{0.2}Fe_{0.8}O_{3-\delta}$*

Oxygen diffusion may be measured using multiple techniques [30, 31], each obtaining different (yet related) parameters such as the chemical diffusion coefficient (D_C) and tracer diffusion coefficient (D^*). Chemical diffusion may be related to self-diffusivity using a thermodynamic enhancements factor (γ):

$$D^* = \gamma D_C \tag{2.13}$$

Where γ is defined by:

$$\gamma = -\frac{1}{2}\left(\frac{\delta \ln p(O_2)}{\delta \ln\left[V^{\bullet\bullet}_O\right]}\right) \tag{2.14}$$

There is not a preferred measurement technique throughout the literature and, for this reason, care should be taken when comparing D_C and D^* values.

Oxygen non-stoichiometry is a characteristic of many transition metal oxides. Generally, the phenomena arises from generation of oxygen vacancies by changing the oxidation state of the transition metal. As shown previously in this chapter, oxygen vacancy generation in LSCF is also a function of A-site aliovalent substitution and $p(O_2)$. Additionally, there is a strong temperature dependence for the oxygen content in $La_{0.6}Sr_{0.4}Co_{0.2}Fe_{0.8}O_{3-\delta}$. At room temperature $La_{0.6}Sr_{0.4}$-$Co_{0.2}Fe_{0.8}O_{3-\delta}$ was found to be slightly oxygen deficient by Tai *et al.* [14] ($\delta = 0.05$) and 'essentially' stoichiometric by Lankhorst *et al.* [28] ($\delta \approx 0.01 - 2$). Figure 13(a) shows that oxygen deficiency tends to increase with temperature as the thermal energy begins to break cation-oxygen bonds. The onset temperature decreases with increasing Sr content whereas the magnitude of oxygen loss is greater with

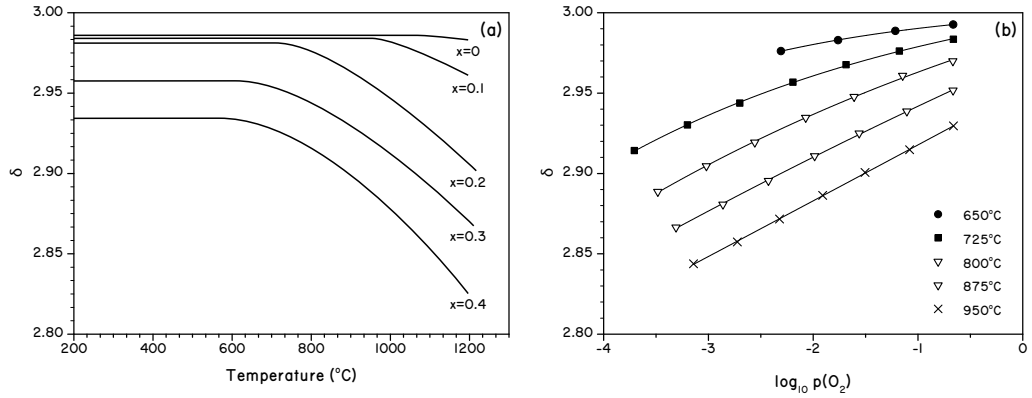


Figure 13: Showing (a) The temperature dependence of oxygen content for $La_{1-x}Sr_xCo_{0.2}Fe_{0.8}O_{3-\delta}$, $0 < x < 0.4$, between 200°C and 1200° and (b) the oxygen non-stoichiometry of $La_{0.6}Sr_{0.4}Co_{0.2}Fe_{0.8}O_{3-\delta}$ under increasingly reducing conditions between 650°C and 950°. Adapted from [14, 28], respectively.

increasing Sr content. For $La_{0.6}Sr_{0.4}Co_{0.2}Fe_{0.8}O_{3-\delta}$ it is apparent this mass loss occurs at $\approx$ 600°C.

Figure 13(b) shows reducing the oxygen partial pressures results in a reduction of total oxygen. By observing Equation 2.7 it can be seen that reducing the available gaseous oxygen that there will be a reduction in hole concentration and thus an increase in oxygen vacancy formation to retain charge neutrality. A similar temperature dependence is observed where the total oxygen loss is greater at higher temperatures.

Figure 14 shows an Arrhenius plot of tracer-diffusivity and surface exchange values measured by Benson [32] using the IEDP-SIMS technique (see Section 4.2.1) for information of the IEDP technique). It is clear that, despite the changes in oxygen stoichiometry over this temperature range, the diffusivity behaviour of $La_{0.6}Sr_{0.4}Co_{0.2}Fe_{0.8}O_{3-\delta}$ appears uncomplicated and retains a single activation energy at every temperature.

The surface exchange coefficient (also shown in Figure 14), however, exhibits two distinct activated temperature regions. Above 600°C the activation energy is 171 kJ/mol, whilst the activation is 61 kJ/mol below 600°C. This transition suggests a change in rate limiting step in the oxygen reduction and incorporation reaction. This behaviour has been reported before in $La_{0.6}Sr_{0.4}CoO_{3-\delta}$ [33] and flourite structured materials [34]. For LSCF, surface exchange above 600°C was found to have a relatively low $p(O_2)$ dependence. The activation energy of surface exchange was also found to be very similar to the value for diffusivity, suggesting

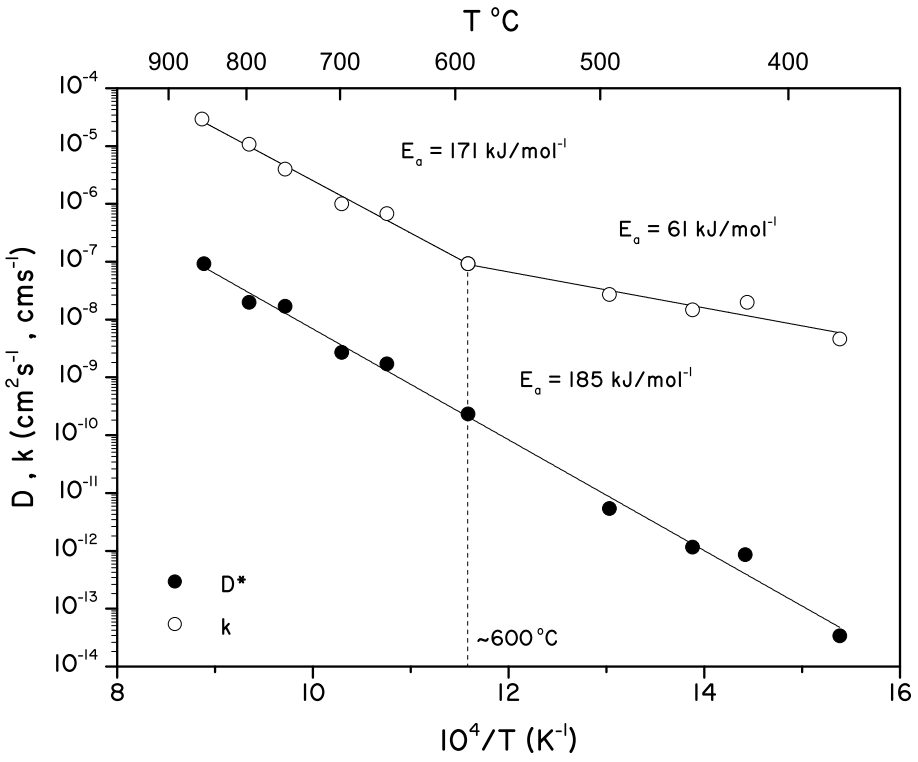


Figure 14: Temperature dependence of oxygen tracer diffusivity (D^*) and surface exchange coefficient (k) of $La_{0.6}Sr_{0.4}Co_{0.2}Fe_{0.8}O_{3-\delta}$. Data adapted from [32].

that the rate limiting step of the reaction is due to the incorporation of oxygen into the bulk [32, 35]. It should also be noted that the transition temperature is very close to the onset of thermally generated oxygen vacancies. Although increasing the vacancy concentration has the effect of reducing the number of holes, dissociation is still relatively facile at this temperature range.

The low temperature regime has a much greater $p(O_2)$ dependence and as such the reduction reaction is assumed to be limited by the adsorption and dissociation of the O_2 molecule. The lower activation energy is thought to be associated with the dissociation of molecular oxygen into two monoatomic surface species [32], however, the precise nature of the reduction mechanism is still not known.

2.1.6 *Ferroelastic Properties of LSCF*

For most perovskite based MIEC materials the electrical properties, oxygen non-stoichiometry and crystallographic properties are very well characterised. Dis-

cussion about the mechanical properties of these systems are less prominent [36] and rarely are they linked to the other properties of the system. However, it has been shown that the presence of long range defects such as dislocations and twin planes have a pronounced effects upon the oxygen vacancy concentration and mobility through a system [37, 38].

Most perovskites undergo a phase transition from a more symmetrical system at high temperature phase (i.e. cubic) to a lower symmetry system at lower temperatures (i.e. rhombohedral), in which some phases may exhibit ferroelastic properties. Ferroelastic properties are defined by a stress-strain hysteresis response to an external load. This commonly arises from a 'superstructure' present in the material. A superstructure is a crystallographic system with additional symmetry (observed using diffraction experiments), often caused by long range, periodic defect ordering within a system. Many common superstructures form 'domains' within the grains of the material which are separated by domain walls where the crystallographic relationship between domains tends to define the type of superstructure. The mechanical hysteresis response arises from domain wall mobility, enabling increased resistance to strain as they 'rotate'. The existence of a (ferroelastic) domain structure also gives rise to ferroelectric and ferromagnetic properties [39, 40], however, these will not be discussed here.

Currently there are few studies characterising superstructures in $La_{0.6}Sr_{0.4}Co_{0.2}Fe_{0.8}O_{3-\delta}$, however, the $La_{0.8}Ca_{0.2}CoO_{3-\delta}$ (LCC) and $La_{0.5}Sr_{0.5}Co_{0.5}Fe_{0.5}O_{3-\delta}$ systems have been extensively characterised by Vullum *et al.* [41]. In $La_{0.8}Ca_{0.2}CoO_{3-\delta}$ a phase change induced during cooling after sintering causes spontaneous reorientation of the structure, forming a ferroelastic phase. The ferroelastic phase tends to form 'domains' or 'twin systems' where domains are twinned along the {100} and {110} family of planes. The twin wall width ranges from 50-200 nm and interestingly the number of grains exhibiting this twin structure increased over time after the initial sintering; suggesting that the defect-rich structure has a higher stability at room temperature. $La_{0.5}Sr_{0.5}Co_{0.5}Fe_{0.5}O_{3-\delta}$ does not undergo a phase change (refer back to Figure 11) during cooling. Whilst no standard twinning, however, a doubling of the lattice parameter along the pseudo-cubic (see Figure 43) $\langle 100 \rangle$ directions was observed; suggesting that the presence of a 'twin-like' superstructure. It was found that this structure occurred across 90-100% of the material. The reason this structure is 'twin-like' is that the material does not exhibit discreet domain walls. As shown in Figure 15 the domain boundary is

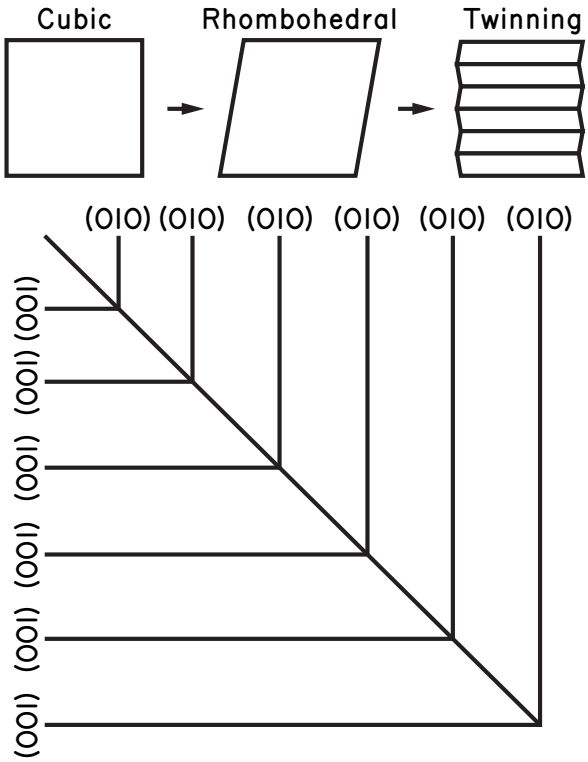


Figure 15: Deformation twinning caused by the spontaneous reorientation of a crystal system showing perpendicular twinning between the (001) and (010) pseudo-cubic planes. Adapted from [41].

shared between domains and the only difference is a rotation in the xy plane (that is related to the crystallographic angle α). Small, periodic domains of 5-20 nm width are observed with atomic twinning along the (010) and (001) planes (Figure 15), however, it is unclear precisely why this structure is formed.

Known superstructures in perovskite materials exist due to oxygen vacancy, cation or charge ordering. For the general formula $A_xB_xO_{3x-1}$ periodic oxygen vacancy ordering can exist for specific values of x [42]. Van Doorn *et al.* [43] attributed a superstructure in $La_{0.3}Sr_{0.7}CoO_{3-\delta}$ to oxygen vacancy ordering, however, this required oxygen non-stoichiometry values between $ABO_{2.5}$ and $ABO_{2.67}$ which is far below values for $La_{0.6}Sr_{0.4}Co_{0.2}Fe_{0.8}O_{3-\delta}$ across the entire temperature and $p(O_2)$ range reported in the literature. Cation ordering may be possible in LSCF due to the two different B atoms, however, the size difference of Fe and Co in sixfold coordination is too small for ordering to be likely [16]. Charge ordering is a temperature dependent reversible process which usually occurs far below room temperature. Although there have been no studies related to these

properties on LSCF, it is unlikely to exhibit charge ordering. Therefore, the periodic domain structure is currently the best model available to describe the LSCF superstructure although there is still a long way to go to understand its true nature.

Although a domain structure has a pronounced effect upon the mechanical properties it has also been shown that the superstructure is related to the ionic properties of a material. Calleja *et al.* [37] showed that oxygen vacancies in $CaTiO_3$ tend to affect the mobility of domain walls by effectively 'pinning' the structure. Harrison *et al.* [44] also showed that oxygen vacancies preferentially reside within the domain walls of $Ca_{1-x}Sr_xTiO_3$. It is therefore possible that domain walls contain an elevated number of oxygen vacancies, potentially increasing ionic conductivity through these regions. However, there is no direct evidence of this as of yet.

2.2 SOFC DEGRADATION

One of the largest problems facing SOFCs is material degradation over time reducing cell performance. Degradation may occur due to several factors but may be summarised as:

1. Chemical instability of the electrode, electrolyte and interconnect materials causing secondary phase formation at the electrode surface and electrode-electrolyte interface.

2. Mechanical instability causing electrode-electrolyte or electrode-interconnect causing delamination.

As with any system where charge is flowing, good contact between components is vital to reduce ohmic resistances. To prevent delamination of components at operating temperature it is necessary to match TEC between the electrode and electrolyte. Cell geometry will also influence the overall mechanical stability of a cell. In general, SOFCs are designed to be planar or tubular and may be anode or interconnect supported [45]. Tubular fuel cells tend to exhibit higher tolerance to thermal expansion, whereas current collection in planar cells tends to be more effective [46]. More recently miniaturisation of cells has offered increased volumetric power density and resistance to thermal cycling [47], however, present

additional difficulties in cell fabrication. Mechanical stability of a cell is of great importance, but is not the focus of this work and as such will not be discussed.

Chemical instability can have a significant impact upon the performance of a cell due to the formation of electronically and/or ionically insulating secondary phases. If these form at the electrode surface the active area available will be reduced and as such increase activation losses. Similarly, formation at the electrode-electrolyte interface will increase the ohmic losses of a cell. This review will focus upon degradation at the cathode surface, however, will briefly cover the cathode-electrolyte interface as material selection and cell design is strongly influenced by reactions at this interface.

Cathode-electrolyte degrdation: The first SOFC systems utilised the $La_{1-x}Sr_xMnO_{3\pm\delta}$ material system ($0.1 < x < 0.3$) as a cathode and Yttria-stabilised Zirconia (YSZ) as an electrolyte. At operating temperature (~1000°C) $LaMnO_3$ reacts with YSZ to form $La_2Zr_2O_7$ at the electrode-cathode interface [48]. The introduction of Sr descreases the reactivity of LSM with YSZ, however, forms $SrZrO_3$ for Sr values above 30 mol % [49]. It has been shown that degradation caused by LSM-YSZ secondary phase formation is reversible by switching between fuel cell and electrolysis mode [50], however, direct observation of the reversible reaction has not yet been achieved. As previously mentioned the LSM system is unsuitable for operation in an IT-SOFC, thus the move to MIEC materials such as LSCF. Due to the high Sr content in $La_{0.6}Sr_{0.4}Co_{0.2}Fe_{0.8}O_{3-\delta}$, YSZ is unsuitable as an electrolyte due to the rapid formation of both $La_2Zr_2O_7$ and $SrZrO_3$ [51, 52]. Due to the low cost and availability of YSZ, attempts have been made to mitigate these reactions by introducing ionically conducting 'interlayers' between the LSCF and YSZ. Interlayers such as $Sm_{0.2}Ce_{0.8}O_{1.9}$ and $Ce_{0.8}$ $Gd_{0.2}O_{2-\delta}$ (CGO) have been shown to limit secondar phase formation significantly without detrimental effects to cell performance [52, 53]. The $Ce_{1-x}Gd_xO_{2-\frac{x}{2}}$ (CGO)[6] system has also showed promise as a replacement for YSZ due to its high ionic conductivity and similar TEC to LSCF. There are also no known chemical reactions between LSCF and CGO [54]. It has been shown that LSCF-CGO composite materials have enhanced surface exchange coefficients [55, 56] and as such CGO is becoming the preferred electrolyte material for use with LSCF.

6 Sometimes referred to as Gadolinia-doped Ceria (GDC)

2.2.1 *SOFC Cathode Degradation*

Degradation at the cathode arises from two main processes: (i) cation segregation effects causing migration of A-site cations towards the surface and (ii) reaction with impurity species in the cathode gas stream. Both have the effect of forming insulating secondary phases reducing the active areas for oxygen reduction and incorporation. The Adler-Lane-Steele model for porous MIEC electrodes [57] is the generally accepted model for the oxygen incorporation into the bulk of the system. In order for an oxygen ion to be incorporated into the system it must first be dissociated and adsorbed onto the surface of the MIEC or MIEC/-electrolyte. This involves the process of charge transfer and it has been widely assumed that the transition metals on the B-site are the primary providers of electrons to facilitate reduction. Clearly then, the state of the surface is of the utmost importance, however, highly sensitive techniques cannot be operated *in-situ* or *in-operando*. Therefore, much of the literature to this date has been limited to characterising post-mortem devices or samples. This has made it difficult to study the complicated mechanisms involved with the oxygen reduction reaction on MIEC materials and correlate them to kinetic properties such as the surface exchange coefficient. Degradation has been studied extensively over the years, however, the literature surround surface properties has only arisen very recently as a response to improved analysis equipment. As such, there are still large gaps in knowledge with regards to the true effect of degradation in these materials.

2.2.1.1 *Cation Segregation*

In binary transition metal alloys surface segregation is phenomena dependent upon the size and chemical nature of the atoms involved [58]. It was also noted that segregation is more common than not in these systems. Oxide materials tend to exhibit similar phenomena [59]. The creation of the surface breaks the symmetry of the crystal and as such causes changes in the electronic and geometric properties of the material. Bonds are broken to create the surface and as such there is a free energy associated to 'the surface'[7]. In a system with multiple atoms the surface free energy of each component will differ in relation to atomic radii (lattice strain). It therefore follows that the is a preferential surface state in most

7 Surface free energy is intrinsically higher such that spontaneous generation of a surface is less favourable

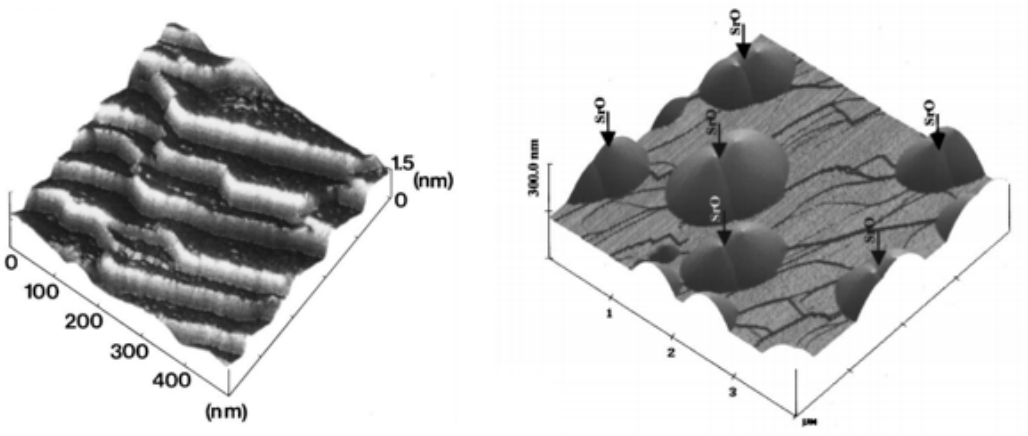


Figure 16: 3D reconstructions of Atomic Force Microscope data showing the surface roughness effects of Sr segregation in $SrTiO_3$ [62]

materials. For ionic crystals where Schottky disorder dominates a 'space charge' region will exist a finite distance from the surface depending upon the defect system [60]. A space charge region occurs when a specific defect (positive or negative) has a preferential surface formation energy. An excess of this defect will form at the surface, forcing the other defect type to form a depth below the surface. The charge distribution causes a dipole region (the space charge 'layer') and this typically provides a strong chemical potential that further drives segregation [61].

In a simple perovskite system (ABO_3) decomposition into the binary oxides (AO and BO_2)[8] may occur due to chemical gradients, externally applied fields or mechanical stress [63]. Szot *et al.* [62] observed that segregation in $SrTiO_3$ caused the surface to change from a simple perovskite into a Ruddlesden-Popper (RP) phase [64] [$SrO^*(SrTiO_3)_n$] ($n = 1$) when heated between 800-900°C. At the elevated temperature SrO layers are able to form and the crystal is able to restructure and form the RP phase. It should be noted that fast diffusion pathways are necessary for this reorganisation to occur. Kubicek *et al.* [65] have shown more recently that strontium diffusion along grain boundaries is faster than in the bulk, thus it is most probable that grain boundaries facilitating fast diffusion of the strontium. As shown in Figure 16(a) the observed crystal reorientation was associated with a crystallographic shear, causing a significant increase in surface roughness. SrO secondary phases were also observed to form at the surface as 'droplets' as seen in Figure 16(b). These experiments were performed at constant temperature

8 For a 2:4 perovskite

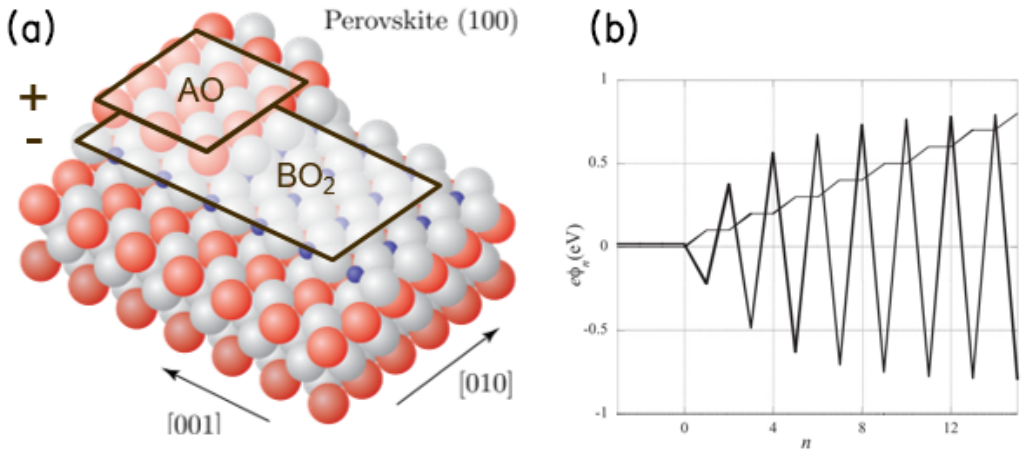


Figure 17: Showing (a) the stacking of AO and BO_2 in a 2:4 perovskite [59] and (b) crystal charge as a function of plane number, illustrating the periodic charge across the atomic planes in the bulk and deviation from neutrality near the surface. Adapted from [66].

and $p(O_2)$ and samples were not subjected to an external electrical field or mechanical stress. Therefore, the decomposition and segregation of the material was assumed to be driven by internal electric fields between the bulk and surface.

Strontium segregation has been observed on SOFC relevant perovskite materials for a number of years [67, 68, 61], however, Harrison [66] was the first to theoretically explain strontium segregation. In $La_{0.65}Sr_{0.35}MnO_3$ they noted that the surface charge layer existed due to a distribution of charged A and B atoms at the surface. In order to neutralise the surface it is possible to modify the valence of the Mn ions, however, forming an AO or BO_2 termination at the surface is an alternative method to achieve neutralisation. As shown in Figure 17(a) the stacking of a perovskite material is AO followed by BO_2. Within the bulk the charge of a 3:3 perovskite the charge of each AO and BO_2 plane is equal and opposite, thus retaining overall charge neutrality throughout the system [66]. However, towards the surface, the fraction of La^{3+} (and $\left[V_{La}'''\right]$), Sr^{2+} (and $\left[V_{Sr}''\right]$), Mn^{3+} and Mn^{4+} begins to change within the space charge layer. Figure 17(b) shows the resulting charge imbalance and thus potential difference between the surface and bulk. The electronic driving force causes charged La species to move *into* the bulk, however, the consequence is that strontium segregates to the surface. This analysis only takes into account the electronic properties of the system and as such neglects ionic radii and strain effects.

Multiple segregation studies have been performed on LSC/LSCF [69, 70, 71, 72] and all report increasing surface strontium concentration over time at elevated

temperatures. Oh *et al.* [73] first observed strontium/oxygen based secondary phase formation on the surface. Interestingly, they showed that the precipitates grow primarily in the centre of the grain, rather than on (potentially) low energy sites such as the grain boundaries. Transmission Electron Spectrocopy (TEM) data showed that the sub surface directly below a precipitate was strontium deficient, again suggesting that Sr diffusion through the bulk is slow. The following formation reactions were devised:

$$Sr'_{La} + \frac{1}{2}O_2\,(g) \rightarrow SrO\,(ppt) + V'''_{La} + 2h^{\bullet} \tag{2.15}$$

$$Sr'_{La} + \frac{1}{2}O_2\,(g) + O^{\times}_{O} \rightarrow SrO_2\,(ppt) + V'''_{La} + V^{\bullet\bullet}_{O} \tag{2.16}$$

Equation 2.15 will be less favourable as any Co/Fe^{4+} species generated due to increasing hole concentrations are less stable at high temperature [74]. Consistent with Harrison's observations in LSM the generation of charged, mobile lanthanum species appears causes strontium segregation in LSCF. It is also clear from Equation 2.16 that there will be a $p(O_2)$ dependence upon SrO formation. This is observed by Oh *et al.* as they annealed LSCF in atmospheres of pure N_2, N_2/0.1% O_2 and air (20% O_2). The quantity and size of precipitates was seen to increase with oxygen content in the gas stream.

Druce *et al.* [75] used Low Energy Ion Scattering (LEIS, see Section 4.3.3), a technique sensitive to the outermost atomic layer, to analyse samples after high temperature thermal anneals. It was shown that there was an increase of strontium concentration (and thus reduced lanthanum concentration) in samples annealed at temperatures as low as 400°C (where cation mobility is very low). The sample annealed at 800°C displayed near 100% strontium coverage at the surface. This suggests that strontium segregation is not thermodynamically limited (at least over IT-SOFC operating temperatures), rather, it will always occur but at different rates depending on operating conditions (kinetically limited). Harrison's model of strontium segregation neglects cation size, however, Lee *et al.* [76] showed that different cation sizes do not prevent A-site segregation, although it does alter the growth kinetics.

Many surface analysis techniques, such as LEIS, require a high vacuum and are typically performed at room temperature. Thus the surface state will be very different during the anneal and analysis. Assuming LSCF behaves in a similar

fashion to other, albeit un-doped, perovskites (such as $SrTiO_3$ [62]) there is a possibility that surface reconstruction is occurring at high-temperature, therefore the fraction of A and B atoms at the surface is not static. This would go some way to explaining why these material still exhibit catalytic properties at operating temperatures, despite overwhelming evidence that A-site cation segregation will always occur. Long term studies show reductions in cell performance, however, attention to surface properties post-mortem is often neglected [77, 78]. Surface stability studies and the effect this has on the exchange properties of LSCF has not yet been fully explored.

2.2.1.2 *Cathode Poisoning*

Ideally pure gas streams could be used to prevent unwanted chemical reactions from occuring (poisoning reactions), however, a gas purification system or the purchase of pure gases tends to be very expensive. Thus, ambient air is commonly used as the cathodic gas stream as it is an abundant and cost-effective resource. However, due to the catalytic nature of MIECs, molecular oxygen is not the only species that may react with the surface. Besides the main components (N_2, O_2), ambient air contains geographically and seasonally varying amounts of water vapour (~ 1-2 vol.%), carbon dioxide (0.03 vol.%) and trace quantities of CO, NO_X and SO_2 [79]. By volume percent the primary impurities are H_2O and CO_2, however, trace impurities such as SO_2 have been shown to cause degradation over long periods of time through the formation of $SrSO_4$ and $La_2O_2SO_4$ at the surface [80].

Another potential source of degradation is by the presence of volatile species at IT-SOFC operating temperatures (600-800°C). Of particular concern is the volatility of chromium species originating from the stainless steel interconnect material. Chromium poisoning has consistently been observed to degrade cathode materials containing lanthanum and strontium (forming an insulating $SrCrO_4$ and La_2CrO_3 phases) [81, 82]. Tucker *et al.* [83] investigated the reactions pathways of volatile chromium species and found that surface diffusion directly from the interconnect to the cathode contributed more to secondary phase formation than through the vapour phase. As such, there is a strong temperature dependence upon the formation of Cr based secondary phases and may potentially be able to be inhibited at temperatures below 700°C.

2.2.1.3 *Effect of Humidty*

The most prominent gas phase impurity is water. At high temperature, the presence of water has a pronounced effect upon the volatility of reactive species by facilitating the formation of hydroxide and oxy-hydroxide species [84]. For the case where volatile chromia species are present, in dry conditions $CrO_3(g)$ is the most abundant vapour species. However, in the presence of relatively low water vapour pressures (~1 mbar at 1000°C [84]), $CrO_2(OH)_2(g)$ becomes thermodynamically preferable species [85]. The saturation vapour pressure of water in air at room temperature (22°C) is on the order of 30 mbar [86]. Even in a relatively dry environment, for the case of chromium species, there is enough water present change the dominant vapour species. Zhao *et al.* [82] used electrical conductivity relaxation[9] to measure the chemical surface exchange coefficient (k_C) of LSCF in response to chromium poisoning. They observed significant faster decline in chemical surface exchange coefficient (k_C) in the presence of humidity as compared to dry conditions. The partial pressure of $CrO_2(OH)_2$ is approximately 100 times larger than the partial pressure of CrO_3 at 750°C [84, 87]. Therefore, it has been suggested that secondary phase formation is increased due to the greater quantity of chromium based reactants. Despite this, the thermodynamics for the formation of $CrO_2(OH)_2$ are not well characterised [85].

Humidity in the gas stream has also been shown to cause volatility in silicon from the quartz sealant material [88]. Silicon poisoning tends to form continuous, thin (20 nm) layer across the surface rather than individual precipitates which has a negative effect upon the surface exchange characteristics of LSC [80]. This phenomenon has not been widely studied, however, has also been implicated as a degradation mechanism in $La_{0.6}Sr_{0.4}Co_{0.2}Fe_{0.8}O_{3-\delta}$ [89].

It has also been suggested that the presence of humidity can increase the rate of cation segregation. Hjalmarsson *et al.* [91] observed a rapid decrease in cell performance (using an $La_{0.6}Sr_{0.4}CoO_{3-\delta}$ cathode) in a humidified atmosphere compared to dry oxygen. They speculated that absorbed water strongly associates

9 Relaxation experimentation measures a material's response to rapidly changing an experimental parameter before returning it back to normal. The response from the beginning to the end of the cycle is measured. In the case of conductivity relaxation on MIEC materials, the conductivity of a system is constantly measured when a sudden change in $p(O_2)$ is introduced. A transient conductivity response may be measured and correlated to the diffusivity and surface exchange properties of the material. As the technique does not retain a constant $p(O_2)$ there is a chemical potential action on the sample, thus the measured values are the *chemical* diffusivity (D_C) and surface exchange coefficient (k_C)

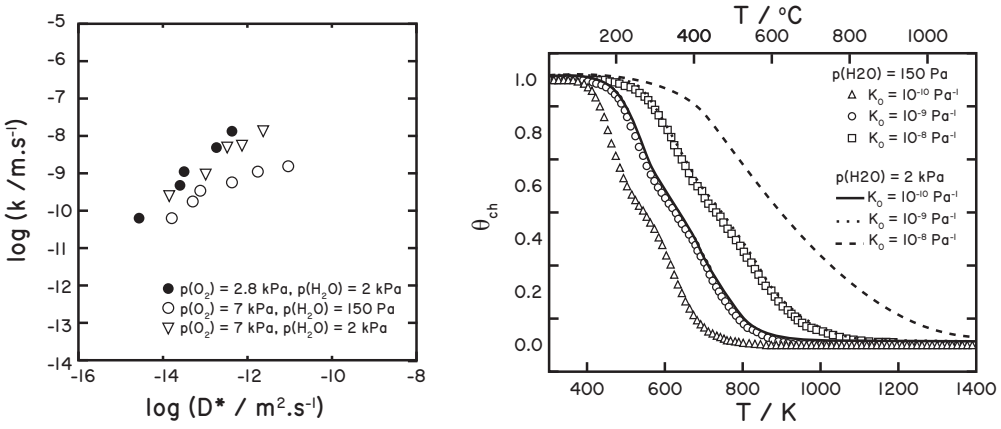


Figure 18: (a) Oxygen surface exchange and diffusivity properties of YSZ at 600°C showing the increase in surface exchange rate in the presence of 20 mbar $p(H_2O)$, and (b) Coverage of chemisorbed water molecules (θ_ch) with respect to temperature and oxygen exchange rate. Adapted from [90].

with strontium at the surface to form strontium hydroxide ($Sr(OH)_2$) species. This phase is not stable at high temperature and as such will evaporate or form SrO [92]. The effect of this is to either deplete the surface strontium concentration and create a larger chemical potential for the segregation of strontium, or form a passivating secondary phase.

Whilst secondary phase formation due to humidity has generally been observed to decrease cell performance [91, 93], it has been reported that the presence of water can *increase* the surface exchange rate of oxygen. Sakai *et al.* [90] first studied this phenomenon in YSZ, seeing a dramatic increase of 500-1000 times at 600°C (See Figure 18(a)). The diffusive properties appeared to be unaffected. It was found that a layer of chemisorbed water (as hydroxyl groups) molecules was present on the surface. The following reactions were proposed:

$$H_2O(g) \leftrightarrow H_2O_{ad} \tag{2.17}$$

$$\frac{1}{2}O_2(g) \leftrightarrow O_{ad} \tag{2.18}$$

$$H_2O_{ad} + O_{ad} + 2e' \leftrightarrow 2OH'_{ad} \tag{2.19}$$

$$2OH'_{ad} + V_O^{\cdot\cdot} \leftrightarrow O_O^{\times} + H_2O_{ad} \tag{2.20}$$

Enhancement was seen to increase with the partial pressure of water and therefore attributed to the total surface coverage of adsorbed species. Figure 18 shows surface coverage of water molecules as a function of temperature and oxygen

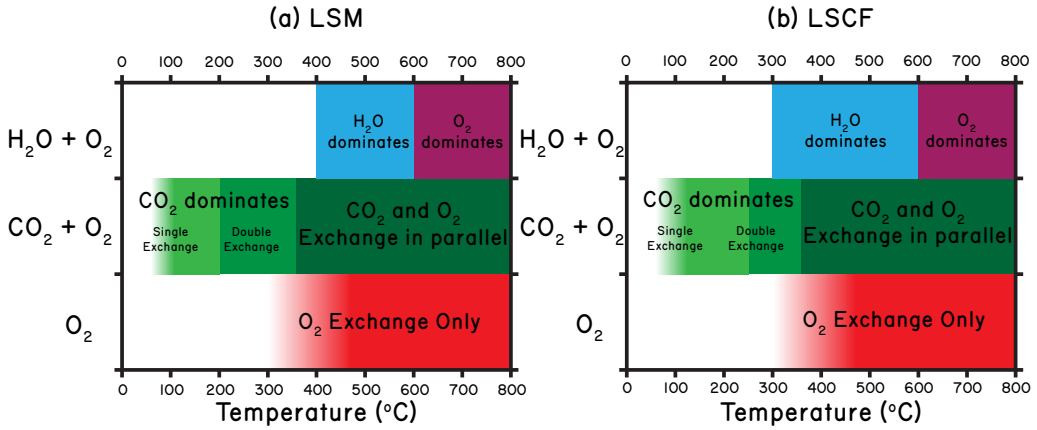


Figure 19: Showing the temperature dependence of each gas mixture and the regions which certain exchange paths dominate in (a) LSM and (b) LSCF. Adapted from [96].

exchange rate. At low temperature (400°C) the surface is 100% covered, however, there is a steady decrease of surface coverage as the temperature increases. A material with a greater oxygen exchange rate was seen to release and replenish the adsorbed species at a faster rate, therefore suggesting that the enhancement factor will change between materials. Isihara *et al.* [94] observed a 10 time oxygen exchange enhancement in $Ba_{0.6}La_{0.4}CoO_3$ (BLC), however, Benson *et al.* [95] saw only a small enhancement the surface exchange properties of LSCF in the presence of water and CO_2.

As can be seen from Equations 2.17 - 2.20 the presence of water adds an additional path for oxygen incorporation. It is generally accepted that the different adsorption/incorporation reactions are competing with one another, thus, using labelled molecules ($H_2{}^{16}O$, $H_2{}^{18}O$), attempts have been made to characterise the relative reaction rates. Ishihara *et al.* observed that the formation rate of $H_2{}^{18}O$ was significantly faster than $^{16}O^{18}O$ when both oxygen and water co-existed in the gas stream. Therefore, when co-existing, incorporation using surface hydroxyl species tends to be the dominant exchange mechanism. More recently Wachsman *et al.* [96] demonstrated the temperature dependence of these reactions on LSM and LSCF. Figure 19 demonstrates the dominant reactions for pure O_2, O_2+CO_2 and O_2+H_2O. As can be seen at low temperatures the adsorbed water dominates the reaction, whereas above 600 °C the reaction is primarily due to the oxygen. This agrees with the observations seen on YSZ where surface water concentration drops with temperature, however, characterisation in the same way has not yet been performed for LSM/LSCF. Also observed by Benson *et al.* [32, 95], CO_2 does

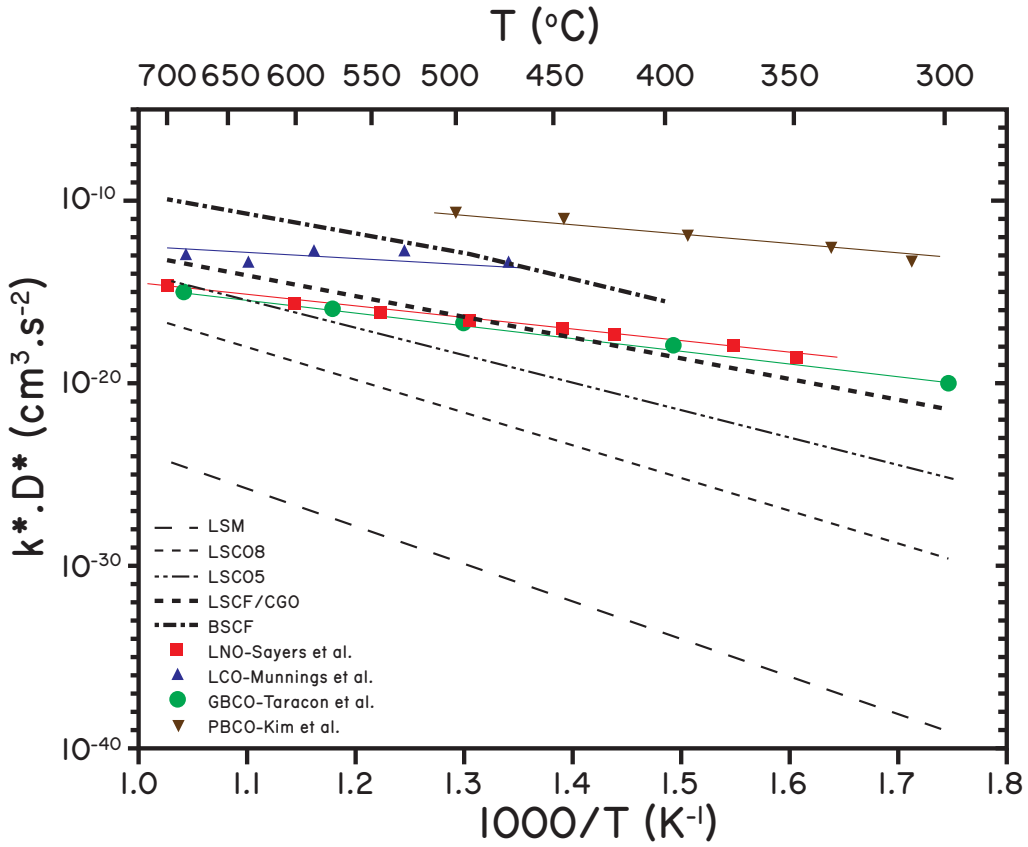


Figure 20: Oxygen tracer diffusion and surface exchange for current and next generation SOFC cathode materials over a range of temperatures, such as Ruddlesden-Popper phase (LNO/LCO) and Double Perovskite (GBCO/PBCO) phase materials. Adapted from [97].

not appear to significantly influence the oxygen exchange mechanism at IT-SOFC operating temperatures.

2.3 CONCLUDING REMARKS

$La_{0.6}Sr_{0.4}Co_{0.2}Fe_{0.8}O_{3-\delta}$ is a well characterised system from the crystal structure to performance in device level studies. Temperature and $p(O_2)$ dependence is well understood, and to a certain extent, so are the effect of gas stream impurities. From a materials properties perspective, however, there are gaps in the literature surrounding the processes of surface modification due to degradation. Surface analysis techniques often require highly sensitive equipment and as such compromise on 'realism' by studying materials under vacuum rather than *in-situ* or *in-operando*. Conversely, the most prevalent device level studies cannot observe

the surface of a material. Currently there is not a single method to achieve concurrent analysis. As shown in this review the surface of LSCF (and most other candidate cathode materials) is not the same at room temperature as at operating temperature, thus it is vital to study it in conditions as close to operating conditions as possible. More recently, researchers are attempting to study these materials in more representative environments to ensure that data from different types of study are comparable, however, it is not an easy task. This work is one such attempt, and in the proceeding chapters will describe the steps taken to ensure more realistic analysis of $La_{0.6}Sr_{0.4}Co_{0.2}Fe_{0.8}O_{3-\delta}$.

As is abundantly clear there are many issues surrounding the use of perovskite materials as SOFC cathodes. $La_{0.6}Sr_{0.4}Co_{0.2}Fe_{0.8}O_{3-\delta}$ was chosen for this work due to its prevalence in industry as well as academia, however, the next generation of materials are in development exhibiting increased diffusivity, oxygen exchange rates and chemical stability. Notable systems include 'Double Perovskite' (e.g. GBCO and PBCO) and 'Ruddlesden-Popper' (e.g. LNO and LCO) phase materials. These materials differ from traditional perovskite systems by exhibiting anisotropic properties. The advantage of this type of ordering translates to enhanced diffusive and exchange properties as can be seen in Figure 20. An additional benefit of these materials is that they often do not rely on A-site cation substitution to provide the desired materials properties, thus preventing many of the degradation mechanisms from occurring. At this point in time there are difficulties regarding efficient cell fabrication using these materials and as such have not yet been commercialised. For more information on these materials systems, please refer to [97].

BIBLIOGRAPHY

[1] Fred Askham, I. Fankuchen, and Roland Ward. The Preparation and Structure of Lanthanum Cobaltic Oxide. *Journal of the American Chemical Society*, 72(8):3799–3800, aug 1950. ISSN 0002-7863. doi: 10.1021/ja01164a505. URL http://pubs.acs.org/doi/abs/10.1021/ja01164a505.

[2] G.H. Jonker. Magnetic compounds with perovskite structure IV Conducting and non-conducting compounds. *Physica*, 22(6-12):707–722, 1956. ISSN 00318914. doi: 10.1016/S0031-8914(56)90023-4. URL http://www.sciencedirect.com/science/article/pii/S0031891456900234.

[3] R.R. Heikes, R.C. Miller, and R. Mazelsky. Magnetic and electrical anomalies in LaCoO3. *Physica*, 30(8):1600–1608, 1964. ISSN 00318914. doi: 10.1016/0031-8914(64)90182-X. URL http://www.sciencedirect.com/science/article/pii/003189146490182X.

[4] G. H. Jonker. Magnetic and semiconducting properties of perovskites containing manganese and cobalt. *Journal of Applied Physics*, 37(3):1424–1430, 1966. ISSN 00218979. doi: 10.1063/1.1708498.

[5] Aaron Wold and William Croft. Preparation and Properties of the Systems LanFe x Cr 1-x O 3 and LaFe x Co 1-x O 3. *The Journal of Physical Chemistry*, 63(3):447–448, mar 1959. ISSN 0022-3654. doi: 10.1021/j150573a030. URL http://pubs.acs.org/doi/abs/10.1021/j150573a030.

[6] C.S. Tedmon, H.S. Spacil, and S.P. Mitoff. Cathode Materials and Performance in High-Temperature Zirconia Electrolyte Fuel Cells. *Journal of The Electrochemical Society*, 116(9):1170–1175, 1969.

[7] E Bucher, W Jantscher, A Benisek, W Sitte, W Preis, I Rom, and F Hofer. Transport properties of Lao.4Sro.6CoO3-d. *Solid State Ionics*, 141-142:375–380, may 2001. ISSN 01672738. doi: 10.1016/S0167-2738(01)00809-8. URL http://linkinghub.elsevier.com/retrieve/pii/S0167273801008098.

[8] E Bucher and W Sitte. Defect chemical analysis of the electronic conductivity of strontium-substituted lanthanum ferrite. *Solid State Ionics*, 173(1-4):23–28, sep 2004. ISSN 01672738. doi: 10.1016/j.ssi.2004.07.047. URL http://linkinghub.elsevier.com/retrieve/pii/S0167273804005016.

[9] Ruhul Amin and Kunal Karan. Characterization of La[sub 0.5]Ba[sub 0.5]CoO[sub 3-δ] as a SOFC Cathode Material. *Journal of The Electrochemical Society*, 157(2):B285, 2010. ISSN 00134651. doi: 10.1149/1.3267879. URL http://jes.ecsdl.org/cgi/doi/10.1149/1.3267879.

[10] Y Teraoka, HM Zhang, and N Yamazoe. Oxygen-sorptive properties of defect perovskite-type La1-xSrxCo1-yFeyO3-δ. *Chemistry Letters*, (C):1367–1370, 1985. URL http://cat.inist.fr/?aModele=afficheN{&}cpsidt=8552806.

[11] B.C.H. Steele. Oxygen ion conductors and their technological applications. *Materials Science and Engineering: B*, 13(2):79–87, mar 1992. ISSN 09215107. doi: 10.1016/0921-5107(92)90146-Z. URL http://linkinghub.elsevier.com/retrieve/pii/092151079290146Z.

[12] J. W. Stevenson. Electrochemical Properties of Mixed Conducting Perovskites La[sub 1-x]M[sub x]Co[sub 1-y]Fe[sub y]O[sub 3-δ] (M = Sr, Ba, Ca). *Journal of The Electrochemical Society*, 143(9):2722, 1996. ISSN 00134651. doi: 10.1149/1.1837098. URL http://jes.ecsdl.org/cgi/doi/10.1149/1.1837098.

[13] HU Anderson. Review of p-type doped perovskite materials for SOFC and other applications. *Solid State Ionics*, 52:33–41, 1992. URL http://www.sciencedirect.com/science/article/pii/0167273892900898.

[14] L.-W. Tai, M M Nasrallah, H U Anderson, D M Sparlin, and S R Sehlin. Structure and electrical properties of La1-xSrxCo1-yFeyO3. Part 2. The system La1-xSrxCo0.2Fe0.8O3. *Solid State Ionics*, 76(3–4):273–283, mar 1995. ISSN 0167-2738. doi: http://dx.doi.org/10.1016/0167-2738(94)00245-N. URL http://www.sciencedirect.com/science/article/pii/016727389400245N.

[15] L.-W. Tai, M M Nasrallah, H U Anderson, D M Sparlin, and S R Sehlin. Structure and electrical properties of La1-xSrxCo1-yFeyO3. Part 1. The system La0.8Sr0.2Co1-yFeyO3. *Solid State Ionics*, 76(3–4):259–271, mar 1995. ISSN 0167-2738. doi: http://dx.doi.org/10.1016/0167-2738(94)00244-M. URL http://www.sciencedirect.com/science/article/pii/016727389400244M.

[16] R. D. Shannon. Revised effective ionic radii and systematic studies of interatomic distances in halides and chalcogenides. *Acta Crystallographica Section A*, 32(5):751–767, 1976. ISSN 16005724. doi: 10.1107/S0567739476001551.

[17] Linus Pauling. the Principles Determining the Structure of Complex Ionic Crystals. *Journal of the American Chemical Society*, 51(4):1010–1026, 1929. ISSN 0002-7863. doi: 10.1021/ja01379a006. URL http://pubs.acs.org/doi/abs/10.1021/ja01379a006.

[18] Robert S. Roth. Classification of Perovskite and Other ABO3-Type Compounds. *Journal of Research of the National Bureau of Standards*, 58(2):75–88, 1957. ISSN 0091-0635. doi: org/10.6028/jres.058.010.

[19] S Wang. High temperature properties of La0.6Sr0.4Co0.8Fe0.2O3-δ phase structure and electrical conductivity. *Solid State Ionics*, 159(1-2):71–78, mar 2003. ISSN 01672738. doi: 10.1016/S0167-2738(03)00027-4. URL http://linkinghub.elsevier.com/retrieve/pii/S0167273803000274.

[20] Dario Marrocchelli, Sean R. Bishop, Harry L. Tuller, and Bilge Yildiz. Understanding chemical expansion in non-stoichiometric oxides: Ceria and zirconia case studies. *Advanced Functional Materials*, 22(9):1958–1965, 2012. ISSN 1616301X. doi: 10.1002/adfm.201102648.

[21] H Zhang. Oxygen sorption and catalytic properties of La1$minus;xSrxCo1$minus;yFeyO3 Perovskite-type oxides. *Journal of Catalysis*, 121(2):432–440, feb 1990. ISSN 00219517. doi:

10.1016/0021-9517(90)90251-E. URL http://linkinghub.elsevier.com/retrieve/pii/002195179090251E.

[22] Chunwen Sun, Rob Hui, and Justin Roller. Cathode materials for solid oxide fuel cells: a review. *Journal of Solid State Electrochemistry*, 14(7):1125–1144, oct 2009. ISSN 1432-8488. doi: 10.1007/s10008-009-0932-0. URL http://link.springer.com/10.1007/s10008-009-0932-0.

[23] A. Zuev, L. Singheiser, and K. Hilpert. Defect structure and isothermal expansion of A-site and B-site substituted lanthanum chromites. *Solid State Ionics*, 147(1-2):1–11, 2002. ISSN 01672738. doi: 10.1016/S0167-2738(02)00010-3.

[24] a Fossdal, M Menon, I Waernhus, K Wiik, M a Einarsrud, and T Grande. Crystal structure and thermal expansion of La1-xSrxFeO3-delta. *Journal of the American Ceramic Society*, 87(10):1952–1958, 2004. ISSN 0002-7820. doi: 10.1134/S0036023613100148. URL isi:000225008200022.

[25] F. Boroomand, E. Wessel, H. Bausinger, and K. Hilpert. Correlation between defect chemistry and expansion during reduction of doped LaCrO3 interconnects for SOFCs. *Solid State Ionics*, 129(1):251–258, 2000. ISSN 01672738. doi: 10.1016/S0167-2738(99)00330-6.

[26] Xiyong Chen, Jinsong Yu, and Stuart B. Adler. Thermal and chemical expansion of Sr-doped lanthanum cobalt oxide (La 1-xSr xCoO 3-??). *Chemistry of Materials*, 17(17):4537–4546, 2005. ISSN 08974756. doi: 10.1021/cm050905h.

[27] B X Huang, R W Steinbrech, and J Malzbender. Direct observation of ferroelastic domain effects in LSCF perovskites. *Solid State Ionics*, 228:32–36, 2012. ISSN 0167-2738. doi: 10.1016/j.ssi.2012.08.025. URL http://dx.doi.org/10.1016/j.ssi.2012.08.025.

[28] M.H.R. Lankhorst and J.E. ten Elshof. Thermodynamic Quantities and Defect Structure of La0.6Sr0.4Co1-yFeyO3-δ(y=0-0.6) from High-Temperature Coulometric Titration Experiments. *Journal of Solid State Chemistry*, 130(2):302–310, 1997. ISSN 00224596. doi: 10.1006/jssc.1997.7378. URL http://linkinghub.elsevier.com/retrieve/pii/S0022459697973783.

[29] Junichiro Mizusaki, Tadashi Sasamoto, W. Roger Cannon, and H. Kent Bowen. Electronic Conductivity, Seebeck Coefficient, and Defect Structure of La1-xSrxFeO3 (x=0.1, 0.25). *Journal of the American Ceramic Society*, 66(4):247–252, 1983. ISSN 0002-7820. doi: 10.1111/j.1151-2916.1983.tb15707.x. URL http://onlinelibrary.wiley.com/doi/10.1111/j.1151-2916.1983.tb15707.x/abstract{%}5Cnhttp://doi.wiley.com/10.1111/j.1151-2916.1983.tb15707.x.

[30] JA Kilner, BCH Steele, and L Ilkov. Oxygen self-diffusion studies using negative-ion secondary ion mass spectrometry (SIMS). *Solid State Ionics*, 12 (1984):89–97, 1984. URL http://www.sciencedirect.com/science/article/pii/0167273884901346.

[31] J. E. ten Elshof. Oxygen Exchange and Diffusion Coefficients of Strontium-Doped Lanthanum Ferrites by Electrical Conductivity Relaxation. *Journal of*

The Electrochemical Society, 144(3):1060, 1997. ISSN 00134651. doi: 10.1149/1.1837531.

[32] Sarah Benson. *Oxygen Transport and Degradation Processes In Mixed Conducting Perovskites*. PhD thesis, Imperial College London, 1998.

[33] Bernard A. Boukamp, H.J.M. Bouwmeester, H. Verweij, and A.J. Burggraaf. Surface Oxygen Exchange Kinetics in Oxide-Ion Conducting Solids. *MRS Proceedings*, 293:361, jan 1992. ISSN 1946-4274. doi: 10.1557/PROC-293-361. URL http://journals.cambridge.org/abstract{_}S194642740046714X.

[34] P Manning. Oxygen self-diffusion and surface exchange studies of oxide electrolytes having the fluorite structure. *Solid State Ionics*, 93(1-2):125–132, 1996. ISSN 01672738. doi: 10.1016/S0167-2738(96)00514-0. URL http://linkinghub.elsevier.com/retrieve/pii/S0167273896005140.

[35] Stuart B Adler. Factors governing oxygen reduction in solid oxide fuel cell cathodes. *Chemical reviews*, 104(10):4791–843, oct 2004. ISSN 0009-2665. URL http://www.ncbi.nlm.nih.gov/pubmed/15669169.

[36] Wakako Araki and Jürgen Malzbender. Ferroelastic deformation of La0.58Sr0.4Co0.2Fe0.8O3-δ under uniaxial compressive loading. *Journal of the European Ceramic Society*, 33(4):805–812, 2013. ISSN 09552219. doi: 10.1016/j.jeurceramsoc.2012.10.035. URL http://linkinghub.elsevier.com/retrieve/pii/S0955221912006310.

[37] Mark Calleja, Martin T Dove, and E.K.H. Salje. Trapping of oxygen vacancies on twin walls of CaTiO 3 : a computer simulation study. *Journal of Physics: Condensed Matter*, 15(14):2301–2307, 2003. ISSN 0953-8984. doi: 10.1088/0953-8984/15/14/305. URL http://stacks.iop.org/0953-8984/15/i=14/a=305?key=crossref.8a93ef65921152f3e9fb5458a3fd218a.

[38] Y. Kimura, K. Yashiro, S.-i. Hashimoto, and T. Kawada. Ferroelastic Domain Reorientations and Its Influence on Mechanical Properties of La0.6Sr0.4Co0.2Fe0.8O3-d. *Journal of the Electrochemical Society*, 161(11):F3079–F3083, 2014. ISSN 0013-4651. doi: 10.1149/2.0131411jes. URL http://jes.ecsdl.org/cgi/doi/10.1149/2.0131411jes.

[39] A. Gupta, G. Q. Gong, Gang Xiao, P. R. Duncombe, P. Lecoeur, P. Trouilloud, Y. Y. Wang, V. P. Dravid, and J. Z. Sun. Grain-boundary effects on the magnetoresistance properties of perovskite manganite films. *Physical Review B*, 54(22):R15629–R15632, dec 1996. ISSN 0163-1829. doi: 10.1103/PhysRevB.54.R15629. URL http://link.aps.org/doi/10.1103/PhysRevB.54.R15629.

[40] F. Kubel and H. Schmid. Structure of a ferroelectric and ferroelastic monodomain crystal of the perovskite BiFeO3. *Acta Crystallographica Section B Structural Science*, 46(6):698–702, dec 1990. ISSN 01087681. doi: 10.1107/S0108768190006887. URL http://scripts.iucr.org/cgi-bin/paper?S0108768190006887.

[41] P E Vullum, H L Lein, M A Einarsrud, T Grande, and R Holmestad. TEM observations of rhombohedral and monoclinic domains in LaCoO3-based

ceramics. *Philosophical Magazine*, 88(8):1187–1208, 2008. ISSN 1478-6435. doi: 10.1080/14786430802082016.

[42] C N R Rao and J Gopalakrishnan. *New Directions in Solid State Chemistry*. Cambridge University Press, second edition, 1997. ISBN 9780511623141. URL http://dx.doi.org/10.1017/CBO9780511623141.

[43] R. H E Van Doorn and A. J. Burggraaf. Structural aspects of the ionic conductivity of La1-xSrxCoO3-δ. *Solid State Ionics*, 128(1-4):65–78, 2000. ISSN 01672738. doi: 10.1016/S0167-2738(99)00282-9.

[44] Richard J. Harrison, Simon A.T. Redfern, and John Street. The effect of transformation twins on the seismic-frequency mechanical properties of polycrystalline Ca 1-x Sr x TiO 3 perovskite. *American Mineralogist*, 88 (4):574–582, apr 2003. ISSN 0003-004X. doi: 10.2138/am-2003-0411. URL http://ammin.geoscienceworld.org/lookup/doi/10.2138/am-2003-0411.

[45] S C Singhal and K Kendall. *High Temperature Solid Oxide Fuel Cells: Fundamentals, Design, and Applications*. Electronics & Electrical. Elsevier, 2003. ISBN 9781856173872. URL https://books.google.com/books?id=LjSBsqGdxvsC.

[46] Seung Bok Lee, Tak Hyoung Lim, Rak Hyun Song, Dong Ryul Shin, and Sang Keun Dong. Development of a 700 W anode-supported micro-tubular SOFC stack for APU applications. *International Journal of Hydrogen Energy*, 33(9):2330–2336, 2008. ISSN 03603199. doi: 10.1016/j.ijhydene.2008.02.034.

[47] Kevin Kendall. Progress in microtubular solid oxide fuel cells. *International Journal of Applied Ceramic Technology*, 7(1):1–9, 2010. ISSN 1546542X. doi: 10.1111/j.1744-7402.2008.02350.x.

[48] W Wang and S Jiang. A mechanistic study on the activation process of (La, Sr)MnO3 electrodes of solid oxide fuel cells. *Solid State Ionics*, 177(15-16): 1361–1369, jun 2006. ISSN 01672738. doi: 10.1016/j.ssi.2006.05.022. URL http://linkinghub.elsevier.com/retrieve/pii/S0167273806003043.

[49] C. Clausen, C. Bagger, J. B. Bilde-S??rensen, and A. Horsewell. Microstructural and microchemical characterization of the interface between Lao.85Sro.15MnO3 and Y2O3-stabilized ZrO2. *Solid State Ionics*, 70-71(PART 1):59–64, may 1994. ISSN 01672738. doi: 10.1016/0167-2738(94)90287-9. URL http://linkinghub.elsevier.com/retrieve/pii/0167273894902879.

[50] C Graves, S D Ebbesen, S H Jensen, S B Simonsen, and M B Mogensen. Eliminating degradation in solid oxide electrochemical cells by reversible operation. *Nat Mater*, 14(2):239–244, 2015. ISSN 1476-1122. doi: 10.1038/nmat4165. URL http://www.ncbi.nlm.nih.gov/pubmed/25532070.

[51] Y. Huang, J. M. Vohs, and R. J. Gorte. An Examination of LSM-LSCo Mixtures for Use in SOFC Cathodes. *Journal of The Electrochemical Society*, 153(6): A951, 2006. ISSN 00134651. doi: 10.1149/1.2186183.

[52] L. Adijanto, R. K??ngas, F. Bidrawn, R. J. Gorte, and J. M. Vohs. Stability and performance of infiltrated Lao.8Sr 0.2CoxFe1-xO3 electrodes with and

without Smo.2Ceo.8O1.9 interlayers. *Journal of Power Sources*, 196(14):5797–5802, 2011. ISSN 03787753. doi: 10.1016/j.jpowsour.2011.03.022. URL http://dx.doi.org/10.1016/j.jpowsour.2011.03.022.

[53] Sun Jae Kim and Gyeong Man Choi. Stability of LSCF electrode with GDC interlayer in YSZ-based solid oxide electrolysis cell. *Solid State Ionics*, 262:303–306, 2014. ISSN 01672738. doi: 10.1016/j.ssi.2014.01.001. URL http://dx.doi.org/10.1016/j.ssi.2014.01.001.

[54] E. Perry Murray, M. J. Sever, and S. A. Barnett. Electrochemical performance of (La,Sr)(Co,Fe)O3-(Ce,Gd)O3 composite cathodes. *Solid State Ionics*, 148(1-2):27–34, 2002. ISSN 01672738. doi: 10.1016/S0167-2738(02)00102-9.

[55] V. Dusastre and J.a. Kilner. Optimisation of composite cathodes for intermediate temperature SOFC applications. *Solid State Ionics*, 126(1-2):163–174, nov 1999. ISSN 01672738. doi: 10.1016/S0167-2738(99)00108-3. URL http://linkinghub.elsevier.com/retrieve/pii/S0167273899001083.

[56] John Druce. Mixed Conducting CGO-LSCF Composites for Oxygen Separation in Oxyfuelled Carbon Capture and Storage Systems. *Department of Materials*, PhD(August):252, 2010.

[57] S B Adler. Electrode Kinetics of Porous Mixed-Conducting Oxygen Electrodes. *Journal of The Electrochemical Society*, 143(11):3554, 1996. ISSN 00134651. doi: 10.1149/1.1837252. URL http://jes.ecsdl.org/cgi/doi/10.1149/1.1837252.

[58] P. M. Ossi. Surface segregation in transition metal alloys: Experiments and theories. *Surface Science*, 201(3):127–133, 1988. ISSN 00396028. doi: 10.1016/0039-6028(88)90491-8.

[59] V Henrich and P Cox. The Surface Science of Metal Oxides. *Advanced Materials*, 7(1), jan 1995. ISSN 09359648. doi: 10.1002/adma.19950070122. URL http://doi.wiley.com/10.1002/adma.19950070122.

[60] K. L. Kliewer and J. S. Koehler. Space charge in ionic crystals. I. General approach with application to NaCl. *Physical Review*, 140(4A), 1965. ISSN 0031899X. doi: 10.1103/PhysRev.140.A1226.

[61] Hani Dulli, PA Dowben, SH Liou, and EW Plummer. Surface segregation and restructuring of colossal-magnetoresistant manganese perovskites La 0.65 Sr 0.35 MnO 3. *Physical Review B*, 62(22):629–632, 2000. URL http://journals.aps.org/prb/abstract/10.1103/PhysRevB.62.R14629.

[62] K Szot and W Speier. Surfaces of reduced and oxidized SrTiO3 from atomic force microscopy. *Physical Review B*, 60(8):5909, 1999. ISSN 0163-1829. doi: 10.1103/PhysRevB.60.5909.

[63] J Nowotny. *Volume 15. Transport in Non-Stoichiometric Compounds*. 1982. ISBN 9780444996794.

[64] S. N. Ruddlesden and P. Popper. New compounds of the K 2 NIF 4 type. *Acta Crystallographica*, 10(8):538–539, 1957. ISSN 0365-110X. doi: 10.

1107/S0365110X57001929. URL http://scripts.iucr.org/cgi-bin/paper?a02086.

[65] Markus Kubicek, Ghislain M Rupp, Stefanie Huber, Alexander Penn, Alexander K Opitz, Johannes Bernardi, Michael Stöger-Pollach, Herbert Hutter, and Jürgen Fleig. Cation diffusion in La(0.6)Sr(0.4)CoO(3-δ) below 800 °C and its relevance for Sr segregation. *Physical chemistry chemical physics : PCCP*, 16(6):2715–26, feb 2014. ISSN 1463-9084. doi: 10.1039/c3cp51906f. URL http://www.ncbi.nlm.nih.gov/pubmed/24390268.

[66] Walter a. Harrison. Origin of Sr segregation at La_{1-x}Sr_{x}MnO_{3} surfaces. *Physical Review B*, 83(15):155437, apr 2011. ISSN 1098-0121. doi: 10.1103/PhysRevB.83.155437. URL http://link.aps.org/doi/10.1103/PhysRevB.83.155437.

[67] H. D. Wiemhöfer and W. Göpel. Interface analysis for solid state electrochemical devices and chemical sensors. *Fresenius' Journal of Analytical Chemistry*, 341(1-2):106–111, 1991. ISSN 09370633. doi: 10.1007/BF00322118.

[68] I. C. Fullarton, J. P. Jacobs, H. E. van Benthem, J. A. Kilner, H. H. Brongersma, P. J. Scanlon, and B. C H Steele. Study of oxygen ion transport in acceptor doped samarium cobalt oxide. *Ionics*, 1(1):51–58, 1995. ISSN 09477047. doi: 10.1007/BF02426008.

[69] M. Finsterbusch, A. Lussier, J.a. Schaefer, and Y.U. Idzerda. Electrochemically driven cation segregation in the mixed conductor La0.6Sr0.4Co0.2Fe0.8O3-δ. *Solid State Ionics*, 212:77–80, mar 2012. ISSN 01672738. doi: 10.1016/j.ssi.2012.02.006. URL http://linkinghub.elsevier.com/retrieve/pii/S0167273812000744.

[70] Wakako Araki, Toru Yamaguchi, Yoshio Arai, and Jurgen. Malzbender. Strontium surface segregation in La0.58Sr0.4Co0.2Fe0.8O3 -δ annealed under compression. *Solid State Ionics*, 268(Part_A):1–6, 2014. ISSN 0167-2738. doi: 10.1016/j.ssi.2014.09.019. URL http://dx.doi.org/10.1016/j.ssi.2014.09.019.

[71] Yuki Orikasa, Ethan J Crumlin, Shinnosuke Sako, Koji Amezawa, Tomoya Uruga, Michael D Biegalski, Hans M Christen, Yoshiharu Uchimoto, and Yang Shao-Horn. Surface Strontium Segregation of Solid Oxide Fuel Cell Cathodes Proved by In Situ Depth-Resolved X-ray Absorption Spectroscopy. *ECS Electrochemistry Letters*, 3(4):F23–F26, 2014. ISSN 2162-8726. doi: 10.1149/2.006404eel. URL http://eel.ecsdl.org/content/3/4/F23.abstract.

[72] G M Rupp, A Limbeck, M Kubicek, A Penn, M Stoger-Pollach, G Friedbacher, and J Fleig. Correlating surface cation composition and thin film microstructure with the electrochemical performance of lanthanum strontium cobaltite (LSC) electrodes. *Journal of Materials Chemistry A*, 2(19):7099–7108, 2014. ISSN 2050-7488. doi: 10.1039/c3ta15327d.

[73] Dongjo Oh, Danijel Gostovic, and Eric D. Wachsman. Mechanism of La0.6Sr0.4Co0.2Fe0.8O3 cathode degradation. *Journal of Materials Research*, 27(15):1992–1999, jul 2012. ISSN 0884-2914. doi: 10.1557/jmr.2012.222. URL http://www.journals.cambridge.org/abstract{_}S0884291412002221.

[74] Tatsumi Ishihara. *Perovskite Oxide for Solid Oxide Fuel Cells*. 2009. ISBN 9780387777078.

[75] John Druce, Tatsumi Ishihara, and John Kilner. Surface composition of perovskite type materials studied by Low Energy Ion Scattering (LEIS). *Solid State Ionics*, 262:893–896, 2014. ISSN 01672738. doi: 10.1016/j.ssi.2013.09.010. URL http://dx.doi.org/10.1016/j.ssi.2013.09.010.

[76] Wonyoung Lee, Jeong Woo Han, Yan Chen, Zhuhua Cai, and Bilge Yildiz. Cation size mismatch and charge interactions drive dopant segregation at the surfaces of manganite perovskites. *Journal of the American Chemical Society*, 135(21):7909–25, may 2013. ISSN 1520-5126. doi: 10.1021/ja3125349. URL http://www.ncbi.nlm.nih.gov/pubmed/23642000.

[77] Edith Bucher and Werner Sitte. Long-term stability of the oxygen exchange properties of (La,Sr)1-z(Co,Fe)O3-δ in dry and wet atmospheres. *Solid State Ionics*, 192(1):480–482, jun 2011. ISSN 01672738. doi: 10.1016/j.ssi.2010.01.006. URL http://linkinghub.elsevier.com/retrieve/pii/S016727381000007X.

[78] J. Malzbender, P. Batfalsky, R. Va??en, V. Shemet, and F. Tietz. Component interactions after long-term operation of an SOFC stack with LSM cathode. *Journal of Power Sources*, 201:196–203, 2012. ISSN 03787753. doi: 10.1016/j.jpowsour.2011.10.117. URL http://dx.doi.org/10.1016/j.jpowsour.2011.10.117.

[79] William Haynes. *CRC Handbook of Chemistry and Physics*. 96 edition, 2015. ISBN 9781482260960.

[80] Edith Bucher, Christian Gspan, Ferdinand Hofer, and Werner Sitte. Sulphur poisoning of the SOFC cathode material Lao.6Sro.4CoO3-δ. *Solid State Ionics*, 238:15–23, may 2013. ISSN 01672738. doi: 10.1016/j.ssi.2013.03.007. URL http://linkinghub.elsevier.com/retrieve/pii/S0167273813001355.

[81] Na Ni and Stephen J Skinner. Transmission Electron Microscopy Study of Cr Poisoning of Lscf Cathodes. *Meeting Abstracts*, MA2015-03(1):79, 2015. URL http://ma.ecsdl.org/content/MA2015-03/1/79.abstract.

[82] L. Zhao, J. Zhang, T. Becker, and S. P. Jiang. Raman Spectroscopy Study of Chromium Deposition on Lao.6Sro.4Coo.2Feo.8O3-d Cathode of Solid Oxide Fuel Cells. *Journal of the Electrochemical Society*, 161(6):F687–F693, apr 2014. ISSN 0013-4651. doi: 10.1149/2.018406jes. URL http://jes.ecsdl.org/cgi/doi/10.1149/2.018406jes.

[83] Michael C. Tucker, Hideto Kurokawa, Craig P. Jacobson, Lutgard C. De Jonghe, and Steven J. Visco. A fundamental study of chromium deposition on solid oxide fuel cell cathode materials. *Journal of Power Sources*, 160(1):130–138, 2006. ISSN 03787753. doi: 10.1016/j.jpowsour.2006.02.017.

[84] K. Hilpert. Chromium Vapor Species over Solid Oxide Fuel Cell Interconnect Materials and Their Potential for Degradation Processes. *Journal of The Electrochemical Society*, 143(11):3642, 1996. ISSN 00134651. doi: 10.1149/1.1837264.

[85] M. Stanislowski, E. Wessel, K. Hilpert, T. Markus, and L. Singheiser. Chromium Vaporization from High-Temperature Alloys. *Journal of The Electrochemical Society*, 154(4):A295, 2007. ISSN 00134651. doi: 10.1149/1.2434690.

[86] Engineering Toolbox: Water Vapor and Saturation Pressure in Humid Air, 2016. URL http://www.engineeringtoolbox.com/water-vapor-saturation-pressure-air-d{_}689.html.

[87] Xinbing Chen, Yongda Zhen, Jian Li, and San Ping Jiang. Chromium deposition and poisoning in dry and humidified air at (Lao.8Sro.2)o.9MnO3+?? cathodes of solid oxide fuel cells. *International Journal of Hydrogen Energy*, 35(6):2477–2485, 2010. ISSN 03603199. doi: 10.1016/j.ijhydene.2009.12.185. URL http://dx.doi.org/10.1016/j.ijhydene.2009.12.185.

[88] Edith Bucher, Werner Sitte, Frederik Klauser, and Erminald Bertel. Impact of humid atmospheres on oxygen exchange properties, surface-near elemental composition, and surface morphology of Lao.6Sro.4CoO3-δ. *Solid State Ionics*, 208:43–51, feb 2012. ISSN 01672738. doi: 10.1016/j.ssi.2011.12.005. URL http://linkinghub.elsevier.com/retrieve/pii/S0167273811005972.

[89] Edith Bucher, Werner Sitte, Frederik Klauser, and Erminald Bertel. Oxygen exchange kinetics of Lao.58Sro.4Coo.2Feo.8O3 at 600°C in dry and humid atmospheres. *Solid State Ionics*, 191(1):61–67, jun 2011. ISSN 01672738. doi: 10.1016/j.ssi.2011.03.019. URL http://linkinghub.elsevier.com/retrieve/pii/S0167273811001755.

[90] Natsuko Sakai, Katsuhiko Yamaji, Teruhisa Horita, Yue Ping Xiong, Haruo Kishimoto, and Harumi Yokokawa. Effect of Water on Oxygen Transport Properties on Electrolyte Surface in SOFCs. *Journal of The Electrochemical Society*, 150(6):A689, 2003. ISSN 00134651. doi: 10.1149/1.1568938.

[91] Per Hjalmarsson, Martin S??gaard, and Mogens Mogensen. Electrochemical performance and degradation of (Lao.6Sro.4)o.99CoO3 - ?? as porous SOFC-cathode. *Solid State Ionics*, 179(27-32):1422–1426, 2008. ISSN 01672738. doi: 10.1016/j.ssi.2007.11.010.

[92] D. R. Glasson. Reactivity of lime and related oxides. Production of Strontium oxide. *Journal of Applied Chemistry*, 8(12):793–797, 1958. ISSN 00218871. doi: 10.1002/jctb.5010081204. URL http://doi.wiley.com/10.1002/jctb.5010081204.

[93] J. Nielsen, a. Hagen, and Y. L. Liu. Effect of cathode gas humidification on performance and durability of Solid Oxide Fuel Cells. *Solid State Ionics*, 181 (11-12):517–524, 2010. ISSN 01672738. doi: 10.1016/j.ssi.2010.02.018. URL http://dx.doi.org/10.1016/j.ssi.2010.02.018.

[94] Tatsumi Ishihara, Satoko Fukui, and Hiroshige Matsumoto. Effects of Water Coexisting on the Cathode Activity for the Solid Oxide Fuel Cells Using LaGaO 3 -Based Perovskite Oxide Electrolyte. *Journal of The Electrochemical Society*, 151:A2035–A2039, 2005. ISSN 00134651. doi: 10.1149/1.2032407.

[95] S. J. Benson. Degradation of La[sub 0.6]Sr[sub 0.4]Fe[sub 0.8]Co[sub 0.2]O[sub 3-δ] in Carbon Dioxide and Water Atmospheres. *Journal of The Electrochemical Society*, 146(4):1305, 1999. ISSN 00134651. doi: 10.1149/1.1391762. URL http://jes.ecsdl.org/cgi/doi/10.1149/1.1391762.

[96] Eric D Wachsman, Yi-lin Huang, Christopher Pellegrinelli, Joshua A Taillon, and Lourdes G Salamanca-Riba. Towards a Fundamental Understanding of the Cathode Degradation Mechanisms. *ECS Transactions*, 61(1):47–56, 2014. ISSN 19386737. doi: 10.1149/06101.0047ecst. URL http://ecst.ecsdl.org/content/61/1/47.abstract.

[97] Albert Tarancón, Monica Burriel, Jose Santiso, Stephen J Skinner, and John A Kilner. Advances in layered oxide cathodes for intermediate temperature solid oxide fuel cells. *Journal of Materials Chemistry*, 20(19):3799–3813, 2010. ISSN 0959-9428. doi: 10.1039/B922430K. URL http://dx.doi.org/10.1039/B922430K.

Part II

MATERIALS AND METHODS

Studying and understanding the surface properties of any material poses numerous challenges to any researcher. There is not one single technique that can provide a full description of a material as there are often compromises that must be made between lateral, depth and chemical sensitivity. Therefore, numerous techniques must be used. Observed consistently throughout this work is the importance of high quality sample preparation and full understanding of any experimental errors to ensure data is accurately comparable. This section details the theory and application of each analysis technique and the necessary sample preparation to achieve accurate results.

3

SAMPLE PREPARATION

3.1 POWDER CHARACTERISATION

$La_{0.6}Sr_{0.4}Co_{0.2}Fe_{0.8}O_{3-\delta}$ powder was obtained from the commercial suppler: Praxair™ Specialty Ceramics (Seattle, USA). The as-received sample was characterised for phase purity using X-Ray Diffraction (XRD), phase evolution from room temperature to 1000 °C using High Temperature XRD (HT-XRD) and correct stoichiometry using Inductive Coupled Plasma Atomic Emission Spectrometry (ICP-AES).

3.1.1 *X-Ray Diffraction*

When a wave meets an obstacle of comparable length scale it may interact to cause scattering of the wave. This phenomenon is referred to as 'diffraction'. X-Ray diffraction is a very common method for analysing the crystallographic properties of a material as the wavelength of an X-ray is similar to the atomic spacing of most crystal structures. Incident X-rays interact with the electron clouds within a target material and will interfere as they are scattered from subsequent crystallographic planes. The condition where the scattered X-rays constructively interfere is defined by Bragg's law (Equation 3.1, Figure 21) [1] where n is an integer, λ is the X-ray wavelength, d_{hkl} is the inter-plane spacing with respect to the hkl plane, and θ is the angle of incidence of the X-rays. Using equation 3.1 and collecting a diffraction pattern across multiple θ values it is possible to gain

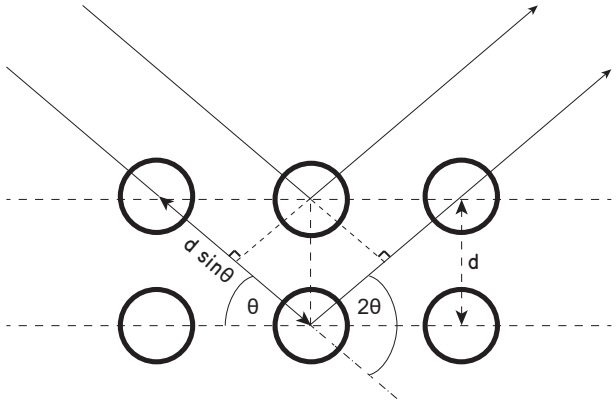


Figure 21: Schematic showing two atomic planes with spacing *d* and an incident X-ray at angle θ diffracting under the Bragg condition.

information on other properties of the crystal structure such as the space group and lattice parameters.

$$n\lambda = 2d_{hkl}\sin(\theta) \tag{3.1}$$

For a completely crystalline material and values of θ which satisfy Equation 3.1 will be explicitly defined. As such an ideal diffraction pattern will contain a series of sharp peaks at these values. In practice, however, instrumental effects and defects within samples will cause deviation from the ideal peak shape, typically in the form of peak broadening and asymmetry. These parameters are well understood and as such it is possible generate a theoretical diffraction pattern from a relevant structural model. Useful information may be obtained by refining the input parameters of the generated profile in order to minimise the difference between itself and experimental data. The most accurate and involved ab-initio method of structural refinement was developed by Hugo Rietveld [2]. "Rietveld refinement" allows complete characterisation of a material's crystal structure, however, once solved and the data is published it may be used as a starting point for future refinements and phase purity comparisons. A number of databases exist for this purpose but this work referred to the Inorganic Crystal Structure Database (ICSD) [3].

"Le Bail refinement" [4] differs from the Reitveld method by including a known space group and unit cell in its input parameters to generate the theoretical

diffraction pattern. This refinement method contains less structural information, but is suitable to refine accurate values of the lattice parameters: the primary aim of using XRD in this work. Combined with data from ICSD [5] Le Bail refinements were carried out using Bruker's Total Pattern Analysis Solution (TOPAS) [6].

Sample Preparation: The focus of XRD experiments performed in this work was to characterise the as-received LSCF powder. No additional processing of the powder was necessary for either standard XRD or high temperature XRD experiments.

Experimental Regime: In this work three pieces of instrumentation were used. For room temperature analyses a Panalytical X'Pert Pro MPD and Bruker D2 desktop instrument were used depending upon availability. Sample powder was required to be placed into the recess of a 'Silicon Zero Diffraction Plate'. This sample holder is fabricated from single crystal silicon where the surface has been cleaved along a high order plane such as the (511) plane [7]. This ensures no background component from the sample holder between 20 and 120°2θ using a copper x-ray source. Samples were analysed from 20-80° 2θ using a step size 0.02° 2θ.

High temperature XRD was performed using a Panalytical X'Pert diffractometer with a Bühler HDK 2.4 temperature stage. To prevent reaction with the holder at high temperature, this equipment employed the use of a thin platinum sheet rather than a silicon zero diffraction plate. The sample stage within this equipment was slightly convex, thus when the platinum holder was inserted it took on this curvature. To reduce systematic errors caused by sample height differences, a small analysis area was necessary using this technique. As such signal intensity tends to be lower using this technique. Samples were analysed from 20 -80°2θ using a step size 0.02°2θ at room temperature before heating, 600°C, 1000°C and room temperature after cooling.

3.1.2 *Inductively Coupled Plasma Atomic Emission Spectroscopy*

Inductively Couple Plasma Atomic Emission Spectroscopy (ICP-AES) is a technique use for determining chemical composition of material. With good experimental practice it is possible to achieve parts per billion (ppb) chemical sensitivity. The technique uses a plasma 'torch', which is a quartz tube with argon gas flowing through it. Surrounding the quartz tube is an induction coil. Upon application of a high power radio frequency (RF) the argon gas is ionised to form a plasma. Samples, dissolved in a relevant solvent, are injected into the plasma where the elements are ionised. During this process electrons are gained and lost frequently, thus emitting photons with characteristic wavelengths. The intensity of each wavelengths is collected to measure against standard solutions to calculate the concentration of each element in the solution.

Sample Preparation: Samples must be dissolved in a solvent in order to be injected into the argon plasma. In this work LSCF readily dissolves in nitric acid. The sensitivity of the technique is 1-20 ppm, therefore fairly dilute solutions are required. In this work 23.5 mg of sample was dissolved in 500ml of dilute nitric acid (50% nitric acid, 50% distilled water).

A total of 13 standard solutions were required to analyse LSCF. A dilute nitric acid solution was required to calibrate for the solvent and solutions of known concentration (5 ppm, 10 ppm and 20 ppm) were required for each element. ICP standard solutions were available for La, Co and Fe. These were mixed with dilute nitric acid to achieve the required metal concentrations. However, at the time of the experiment the ICP standard solution for Sr was unavailable. For this experiment appropriate weights of $SrCO_3$ were dissolved in dilute nitric acid to create the strontium standard solutions.

3.2 SAMPLE FABRICATION

Each of the experiments described in Part iii of this work required dense sintered LSCF samples. No further processing was required of the as-received powder to

consistently produce dense samples of 95 - 97%. The sample geometry required varied between each analysis technique and as such are detailed throughout Section 4, however, each sample was initially pressed, sintered, polished and sectioned identically. Any additional preparation is detailed in the relevant chapters.

3.2.1 *Pressing and Sintering*

Prior to sintering, a high quality green pellet must be produced. LSCF does not require additional binding agents and as such the powder was able to be pressed as received. In order to consistently produce samples, a two stage pressing regime was followed:

1. As received powder was a uniaxial pressed under a 2 tonne load within a stainless steel 'bar' die (Figure 22a) with dimensions of 3.5 x 25 mm. Due to the anisotropic dimensions of the die, sufficient powder was required in order to prevent the samples breaking during the subsequent pressing stage. 2 grams of powder was found to be sufficient.

2. After uniaxially pressing the powder, samples were isostatically pressed under 300 MPa of pressure. The isostatic press utilises the compression of a fluid to ensure isostatic conditions. In order to prevent contamination, samples were inserted into a flexible plastic container and sealed (Figure 22b). Prior to sealing, the container was evacuated using a scroll pump to ensure the container wrapped around the sample tightly. This step helps prevent fluid infiltration and deformation of the sample under pressure.

After pressing, samples were densified by sintering in ambient air. The pressed green samples were placed into alumina crucibles. To prevent possible reaction with the crucible a layer of as received LSCF powder lined the base of the crucible. Samples were sintered at 1250 °C for 8 hours using a 300 °C $hour^{-1}$ ramp rate. The cooling rate was nominally the same as the heating rate. Following this whole regime dense samples of approximately 3.5 x 3.5 x 25 mm dimensions could be reliably produced.

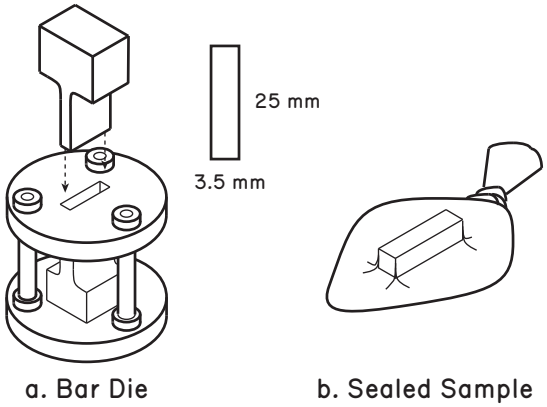


Figure 22: Schematic diagram of (a) the stainless steel bar die and cartoon of a sealed and (b) evacuated sample prior to isostatic pressing

3.2.2 *Density Measurements*

Samples produced for isotopic exchange measurements must not contain any open pores as they act as a short circuit for diffusion. It has been shown that if the density is greater than 95% of the theoretical density of the material then open porosity is eliminated [8]. To measure the density of a sintered sample the Archimedes method was used. This methodology involves measuring the weight of the sample in air and in a fluid (water in this case) using Equation 3.2 the experimental density can be calculated:

$$\rho_{exp} = \frac{M_{air} \cdot \rho_{fluid,t}}{M_{air} - M_{fluid}} \tag{3.2}$$

Where ρ_{exp} is the experimental density, M_{air} is the mass of the sample measured in air, M_{fluid} is the mass of the sample measured in the fluid and $\rho_{fluid,t}$ is the density of the fluid at a given temperature. This value can then be compared to the theoretical density of the material to provide the relative density of the sample. The theoretical density of a material can be calculated if the crystal structure and lattice parameters are known. It is described by the total mass of i species contained within the unit cell, divided by the unit cell's volume as shown in Equation 3.3:

$$\rho_t = \frac{\sum_i N_i \cdot A_i}{V_{cell} \cdot N_A} \tag{3.3}$$

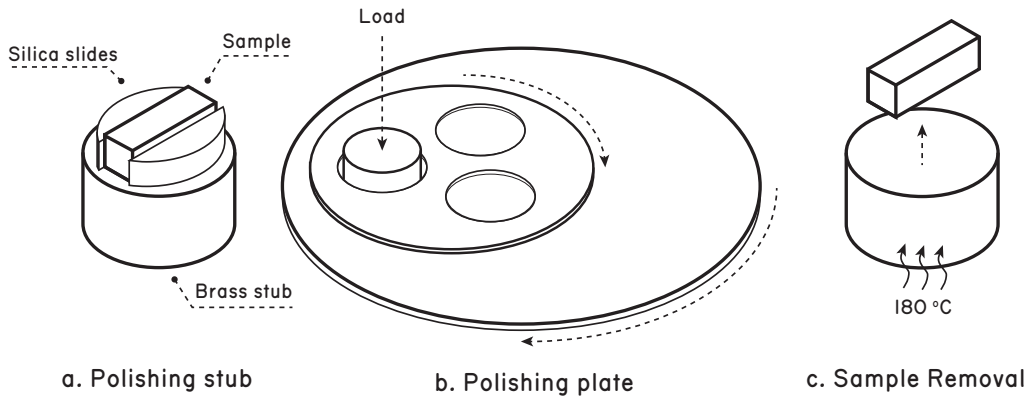


Figure 23: Schematic diagram showing (a) the polishing stub with the sample and silica slides prior to grinding and polishing, (b) the polishing plate and sample holder with direction of rotation, and (c) removal of the sample by re-heating the stub.

Where ρ_t is the theoretical density, N_i is the number of atoms per unit cell of species *i*, A_i is the atomic weight of species *i*, V_{cell} is the unit cell volume and N_A is Avogadro's number.

Other experiments presented in this work did not necessarily require a relative density greater than 95%, however, for consistency, the same sample preparation was used.

3.2.3 *Polishing and Sectioning Regime*

All of the experimental techniques presented in this work require 'mirror finish' polished samples. Primarily this was done to reveal the material's internal microstructure, but to also provide sufficiently flat surfaces to reduce experimental errors. The effect of surface roughness on each experiment is discussed throughout Part iii. However, the polishing regime remained constant between experiments and, unless otherwise stated, samples referred to as 'polished' will have been ground and polished using the following method:

1. Sintered samples were adhered to a cylindrical brass stub as can be seen in Figure 23a. This was achieved by heating the stub to approximately 180 °C on a hot plate and applying a resin onto the surface of the stub. Silica glass slides cut to an appropriate shape were adhered along each side of

the sample to prevent the sample from rocking during the polishing step[1]. Once positioned appropriately the sample was left to cool to room temperature[2] whilst applying a small amount of pressure orthogonal to the surface to ensure a strong bond (to prevent the sample or silica from coming off during the polishing step).

2. Once set the samples were ground subsequently at 200 RPM using P600 (~30 μm particle size), P800 (~22 μm) and P1200 (~15 μm) grade silicon carbide paper until the samples were flush with the silica glass.

3. Samples were then polished at 200 RPM subsequently using diamond suspensions of 9 μm, 3 μm, 1 μm and 1/4 μm particle size. Using a 'Struers RotoPol-15 Autopolisher' a constant 20N of force could be applied during the polish. Samples were also rotated in a special sample holder to reduce the effect of a preferential polishing (Figure 23b).

4. Once polished sufficiently, samples were removed from the stub by re-heating it on a hotplate at 180 °C (Figure 23c). To remove residue from the resin samples were cleaned subsequently in acetone, isopropanol and distilled water using an ultrasonicator.

SECTIONING SAMPLES: As previously mentioned the sample geometry for each experiment varied. To section an as-sintered pellet into the relevant dimensions a low speed diamond saw was used. Samples were adhered to a silica glass slide in a similar manner to the polishing stub, allowed to cool and then inserted into the saw. Appropriate sections were cut before removing the glass slide from the saw (still holding the samples) and re-applying heat to remove them. Samples were once again cleaned for residual resin using the same cleaning regime.

1 The total height of the stack should be lower than the sample. Each glass slide used in this work was 1 mm thick. Therefore, three pieces should be layered if the sample has a height of 3.5mm.
2 Quenching would deteriorate the consistency of the resin and reduce the strength of the bond.

BIBLIOGRAPHY

[1] W H Bragg and W L Bragg. The Reflection of X-rays by Crystals. *Proceedings of the Royal Society of London A: Mathematical, Physical and Engineering Sciences*, 88(605):428–438, jul 1913. URL http://rspa.royalsocietypublishing.org/content/88/605/428.abstract.

[2] H. M. Rietveld. A profile refinement method for nuclear and magnetic structures. *Journal of Applied Crystallography*, 2(2):65–71, 1969. ISSN 00218898. doi: 10.1107/S0021889869006558.

[3] Inorganic Crystal Structure Database. URL https://icsd.fiz-karlsruhe.de/search/index.xhtml.

[4] A. Le Bail, H. Duroy, and J. L. Fourquet. Ab-initio structure determination of LiSbWO6 by X-ray powder diffraction. *Materials Research Bulletin*, 23(3): 447–452, 1988. ISSN 00255408. doi: 10.1016/0025-5408(88)90019-0.

[5] Xinbing Chen and San Ping Jiang. Highly active and stable (La0.24Sr0.16Ba0.6)(Co0.5Fe0.44Nb0.06)O3-δ (LSBCFN) cathodes for solid oxide fuel cells prepared by a novel mixing synthesis method. *Journal of Materials Chemistry A*, 1(15):4871, 2013. ISSN 2050-7488. doi: 10.1039/c3ta10230k. URL http://dx.doi.org/10.1039/C3TA10230K{%}5Cnhttp://xlink.rsc.org/?DOI=c3ta10230k.

[6] A. Coelho. Topas Academic Version 4.1., 2007.

[7] Yang Chuan-zheng, H a O Jian-min, and P E I Guang-wen. Contributed Papers Brief Introduction of X-Ray Multiple Diffraction. *The Rigaku Journal*, 17(1):46–57, 2000.

[8] W. D. Kingery. Introduction to Ceramics, 1977. ISSN 00134651.

4

INSTRUMENTATION AND EXPERIMENTAL TECHNIQUES

As detailed in Part i there are numerous material properties that are required to produce a SOFC cathode material. Of particular concern throughout this work is how LSCF surface properties react to ambient atmospheres and what effect this has on the kinetic properties of the material. The first challenge comes when defining 'the surface'. The top atomic layer that is in immediate contact with another phase is logically the surface, however the properties of this layer will be strongly influenced by the atomic layers directly below. Therefore, a more reliable definition of the surface applies to approximately 2-10 atomic layers (~0.5-3 nm) [1]. There are numerous techniques that are capable of probing this depth, however, obtaining sufficient chemical sensitivity, depth resolution and lateral resolution from one analysis step is currently impossible. Therefore, multiple techniques must be used to accurately describe the surface properties of a material. A summary of common surface sensitive techniques is shown in Figure 24.

Ideally each technique should be able to be carried out *in-situ* and on the same analysis area to ensure complementary data is collected. However, most surface sensitive techniques require a high vacuum environment and using multiple techniques by definition requires samples to be transferred between each piece of equipment. In this work electron microscopy provided a flexible set of *in-situ* and *ex-situ* analysis regimes which, due to the technique's high lateral resolution, meant that subsequent analysis of the same region was easily attained. Due to restrictions of the ion beam analysis techniques employed, kinetic data (surface exchange and oxygen self-diffusivity) was only able to be collected *ex-situ*.

This chapter introduces the theory and practicalities of the techniques used in this work, any additional sample preparation and the experimental regime followed to collect data.

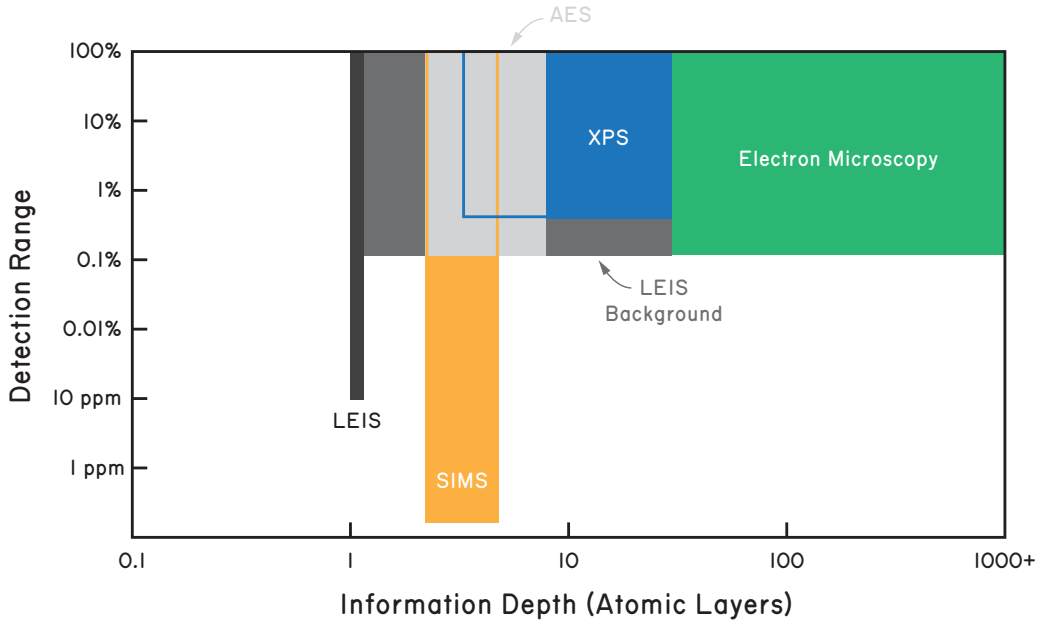


Figure 24: Summary of surface analysis techniques showing approximate depth resolution and detection range for each technique

4.1 ELECTRON MICROSCOPY

Electron microscopy is a form of microscopy that utilises a focussed beam of high energy electrons (1-30 keV) [2] as a source of illumination. Electrons exhibit properties of both a wave and a particle (referred to as wave-particle duality), and the associated wavelength of an electron is orders of magnitude shorter than a photon in the visible light spectrum. Thus, compared to an optical microscope, significantly smaller details of a sample may be resolved as described by the Rayleigh criterion [3].

When an electron interacts with a material there are numerous phenomena which may occur depending upon the beam energy and sample in question. A general summary of these phenomena can be seen in Figure 25a. The interaction volume is dependent upon the beam energy. A larger beam energy will increase the interaction volume, therefore reduce the surface sensitivity of the technique. A standard Scanning Electron Microscope (SEM) is designed to raster scan the electron beam in order to generate chemical and morphologic maps/images of a sample. Most SEM equipment utilises Secondary Electron (SE), Backscattered Electron (BSE) and characteristic X-Ray interactions to collect information from

the material.

Secondary electrons (<50 eV) are electrons emitted from the sample as a direct result of inelastic scattering interactions with the incident electron beam. The secondary electron escape depth is approximately 5-50 nm [4], and consequently, emission is greatly affected by the incident angle of the beam. As can be seen in Figure 25b if the incident angle of the electron beam is perpendicular to the sample then the interaction volume within the material is uniform. If the incident angle increases, the 'escape' distance decreases and there will be greater electron emission. Due to this effect, secondary electron images provide surface topography contrast and contain no chemical information.

Backscattered electrons (1-30 keV) are electrons elastically scattered by the electron clouds within the material. These electrons can be differentiated from secondary electrons as they will retain much of the kinetic energy during the scattering process. Atoms with greater a number of electrons (higher Z number) have a larger scattering cross section, therefore, have a greater probability of producing an elastic collision. Consequently, contrast within a backscattered image is proportional to the chemical composition or phase of the sample[1]. Topography (incident angle) will also affect BSE imaging, however, it is less pronounced than in secondary electron images due to the increased escape depth of backscattered electrons.

Energy-dispersive X-ray spectroscopy (EDX) utilises characteristic X-ray emission during electron-sample interaction. This phenomenon is observed when an incident electron beam promotes an electron within the material to a higher energy state, leaving behind an 'electron hole'. When an electron from a higher energy state (whether it is the originally excited electron or not) relaxes into this hole, the energy difference between the two states may be released in the form of an X-ray. The characteristic energy of this X-ray is directly related to the atomic structure of the material and as such elemental composition may be identified.

For standard SEM experiments samples must be stable in a vacuum (10^{-6} mbar) and must have sufficient electrical conductivity. If the material is insulating, elec-

1 The precise chemistry of the sample cannot be obtained using BSE. Prior understanding of the material can provide qualitative analysis of the phases present, however, further analysis is usually required to characterise the material's chemistry.

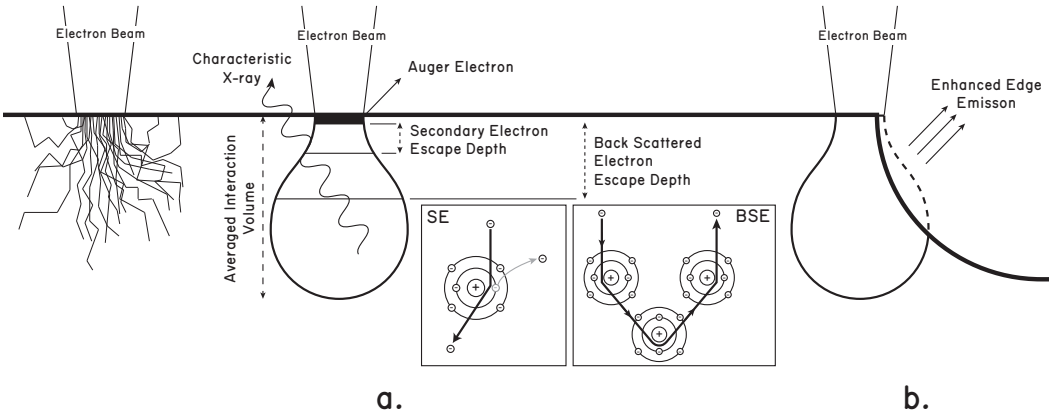


Figure 25: Schematic of (a) the resulting phenomena generated during an electron-material interaction and (b) the enhancement of electron emission due to a change in incidence angle.

trons that do not escape from the material will build up a negative charge layer at the surface of the material. This will deflect the incident beam and prevent further data from being collected. It is possible to coat a sample in a thin layer of a conducting material such as chromium or gold to negate this effect.

The equipment used for standard SEM in this work was a LEO Gemini 1525 FEGSEM. Samples were required to be placed on a stub in order to be inserted into the machine. Two options were available to adhere samples to the stub: double sided adhesive tape or silver paste dissolved in acetone. It was found that using silver paste to adhere the samples was preferable as it reduced sample drifting during analysis. Samples did not require any additional processing prior to SEM analysis as even the as sintered bar is within size restrictions of the equipment, LSCF is stable under a high vacuum and sufficiently conductive to avoid charging.

4.1.1 *High Temperature Environmental Scanning Electron Microscopy*

Standard SEM equipment described in the previous section requires the use of a high vacuum to prevent interference between the electron beam and the detectors. Environmental SEM (ESEM) equipment deviates from a standard SEM by utilising specialised electron detectors and a differential pumping process. Both of these steps enable the generation of a localised gaseous environment without

Table 1: Approximate values for the mean free path of a particle under different pressures [6]

Vacuum Range	**Pressure (mbar)**	**Mean Free Path**
Ambient	1013	68 nm
Low Vacuum	300 - 1	0.1 - 100 μm
Medium Vacuum	1 - 10^{-3}	0.1 - 100 mm
High Vacuum	10^{-3} - 10^{-7}	10 cm - 1 km

hindering concurrent SE and BSE analysis [5].

Gaseous Detection: As can be seen in Table 1 the mean free path of an electron in a high vacuum is sufficiently long such that it is unlikely to interact with another species either from source to sample or sample to detector. In a low vacuum this is no longer the case; there will be multiple interactions at both stages. It is therefore vital to control the pressure along the beam trajectory to prevent significant scattering of the beam. This is achieved by using a series of pressure limiting apertures (PLA) to create a differential pumping system (Figure 26a). Differential pumping allows the chamber pressure to remain relatively high (10's mbar) whilst limiting effects on the incident beam. Although scattering will still occur along the whole column the PLAs prevent most of these scattered electrons from ever reaching the sample. The primary region where scattering will affect the beam focus is between the final PLA and the sample, therefore the working distance is kept as short as possible.

The effect of scattering the beam can be seen in Figure 26b. In a standard SEM under a high vacuum the beam undergoes minimal scattering. As pressure increases there will be partial scattering of the beam until the pressure reaches the point where there is complete scattering of the beam. In the partial scattering regime, it can be seen that the beam predominantly retains a Gaussian shape except for a 'skirt' at the base of the profile. Scattering is a discrete process, not a continuous one. Each interaction an electron has with a particle has a probability of scattering. If it does not scatter it will continue along its original trajectory. Therefore, electrons can be separated as either scattered or un-scattered components (the distribution of which depends on the pressure of the system/number of collisions before hitting the sample). The scattered component forms the 'skirt'

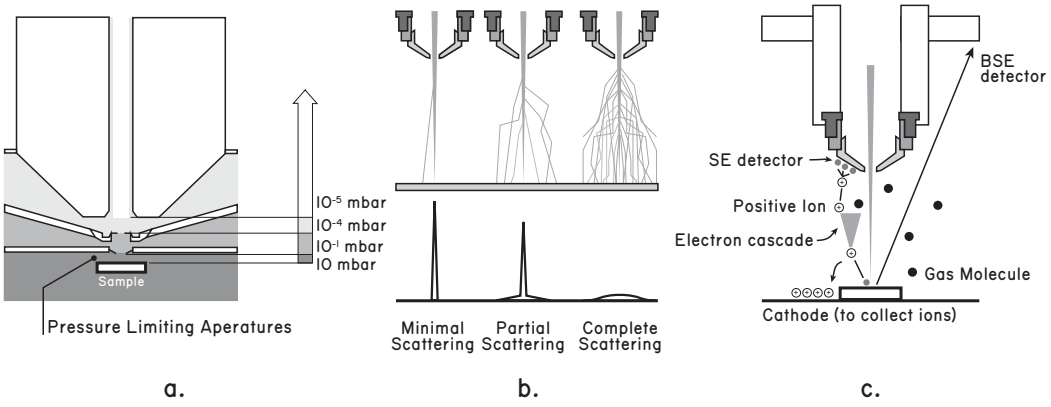


Figure 26: Schematic of (a) the differential pumping system of an ESEM, (b) the effect of scattering on the incident beam profile and (c) electron cascade amplification process.

of the profile and can simply be subtracted from the total count of un-scattered electrons. The width and intensity of the skirt will affect the resolution of the ESEM but is generally low enough that it only contributes to background noise [7].

Once a secondary or backscattered electron leaves the sample it is accelerated towards the relevant detector. During this stage the electrons have the chance of colliding with the gas, causing ionisation. The ionisation process generates more electrons and consequently starts a chain reaction which amplifies the electron signal. Commonly referred to as an 'electron cascade' this can be seen in Figure 26c.

When working with High-Temperature ESEM (HT-ESEM) there are additional considerations that must be considered, including accurate temperature measurement, compensation for thermally generated electrons and measurement of the local gas pressure. The following literature discusses in-depth the afore mentioned issues regarding HT-ESEM [8, 9, 10, 11, 12, 13, 14], however, the equipment used in this work was set-up appropriately by the technician in charge.

Sample preparation: The HT-ESEM heating stage used in this work had a limited analysis region and as such restricted sample size. Samples dimensions were required to be 1 x 1 x 1 mm. Prior to analysis in the HT-ESEM samples were prepared appropriately and analysed using EBSD (see Section 4.1.2 for full details).

Experimental Regime: The following work was carried out at the Institut de chimie séparative de marcoule [15] using a Quanta 200 ESEM FEG SEM under the kind supervision of Dr. Renaud Podor[2]. Sintered and polished samples were heated from room temperature to 1000 °C with a 300 °C/hour heating rate. Upon reaching 1000 °C samples were annealed isothermally for one hour. This heating regime was carried out under 4 different gaseous environments: 3 mbar Pure O_2, 3 mbar Pure H_2O, 3 mbar Ambient Air and a Vacuum of 10^{-6} mbar.

During the anneal process each sample was observed in SE mode to observe morphological changes at the surface. Images were taken approximately every 5 - 10 seconds to provide a timeline of images and allow particle growth rates to be calculated. Upon the end of the isothermal anneal the detection mode was switched from SE to BSE and phase maps were collected.

In order to collected EDX maps the chamber had to be cooled and vented in order to insert the appropriate detector. It should therefore be noted that EDX data collected from a sample using this equipment was at room temperature and samples will have been exposed to ambient air.

4.1.2 *Electron Backscattered Diffraction*

Electron Backscattered Diffraction (EBSD) is a technique that provides quantitative microstructural information about a material's crystallography; primarily grain size, grain orientation, texture and phase identity. The technique utilises scattered electrons diffracting under the Bragg condition (Equation 3.1 in Section 3.1.1) to form a electron backscattered pattern (EBSP). EBSPs are representative of crystallographic orientation and may be indexed if the crystal structure and experimental setup is well defined. Due to the use of electrons it is possible to obtain high lateral resolution crystallographic maps of a material.

Compared to standard SEM experiments, EBSD requires a unique experimental setup. Although EBSD utilises the same illumination source, the beam incidence angle must be set at a specific shallow angle (usually around 20°) and the electrons are detected in a different manner. The detector, or 'EBSD camera', is essentially a digital camera (charge-coupled device, CCD) behind a phosphor screen. The phosphor screen converts impinging electrons into light suitable for the CCD and builds the EBSP image.

2 http://www.icsm.fr/podor_fr.html

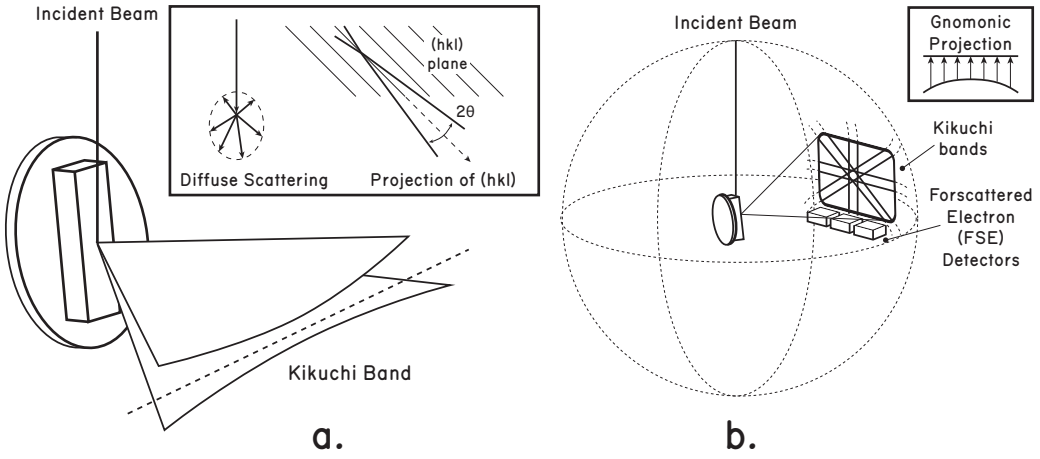


Figure 27: Schematic of (a) the formation of Kikuchi bands from electron diffraction and (b) the Gnomonic projection of an EBSD pattern onto the EBSD camera

An EBSP image is a collection of 'Kikuchi Bands' [16]. As can be seen in Figure 27a diffracted electrons may be scattered in many different directions leading to a diffuse scattering situation in three dimensions. However, electrons that have scattered under the Bragg condition have a characteristic Bragg angle. Therefore, there is preferential scattering at these angles and consequently will appear more intense or 'brighter' on the EBSP. Due to the diffuse nature of the electron scattering process this may occur in either direction from the crystal plane, as shown in Figure 27a. This process causes the formation of 'Kikuchi band'. The centre of the band is the direct projection of the diffracted plane (*hkl*) and as such may be indexed if the EBSP band edges are sufficiently defined. As electrons are diffracted in three dimensions the diffracted beam creates a spherical representation of the crystal structure, therefore the crystal orientation may also be calculated from the EBSP. Typical CCD detectors have flat detection surfaces and as such EBSPs are Gnomonic projections[3]. This is geometrically accounted for in most modern EBSD software.

Forescattered Electron Imaging: The equipment utilised for this work was a Zeiss Auriga FIB-SEM with a Bruker 'e$^-$Flash' EBSD detector [17]. This detector has an additional imaging mode that utilises 'forescattered electrons' (FSE) to provide qualitative orientation contrast (OC). As can be seen in Figure 27b there are three FSE detectors, corresponding to a red, green and blue (RGB) detection channel respectively, at the base of the phosphor screen. Electrons that are scattered for-

3 https://en.wikipedia.org/wiki/Gnomonic_projection

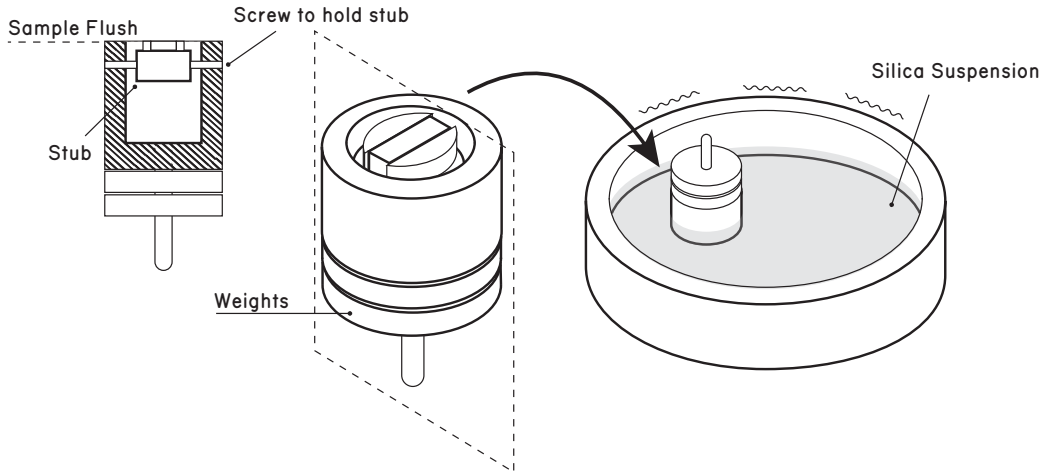


Figure 28: Showing a schematic of the sample holder and equipment setup for colloidal silica polishing.

ward may be collected by these detectors to provide an image with RBG contrast defined by the EBSP. This imaging mode is highly sensitive to Z number, surface topography and crystal orientation. This imaging mode is commonly utilised to scan an area prior to EBSD analysis in order to locate sites of crystallographic interest.

Sample preparation: EBSD is a technique that is highly sensitive to surface roughness and surface quality. As such, an additional polishing step using a colloidal silica suspension was required after the standard protocol defined in Section 3.2.3.Before removing samples from the brass stub, the stub was inserted into a holder ensuring that the surface of the samples was flush with the holder. A solution of 30% water and 70% colloidal silica was placed into a Buehler 'Vibromet 2' vibratory polisher with a cloth pad at the base of the solution. Approximately 200g of weight was added to the holder before it was submerged into the colloidal silica and the vibromat turned on. A schematic of the experimental setup is shown in Figure 28. To achieve a sufficiently smooth surface finish LSCF samples were polished for at least 24 hours. After polishing, silica residue and hydrocarbons on the surface were removed by cleaning samples subsequently in acetone, isopropanol and distilled water using an ultrasonicator.

Experimental regime: EBSD analysis was carried out on two sets of samples: samples to be analysed in the HT-ESEM and samples to characterise the twin struc-

Table 2: EBSD analysis settings used for both the HT-ESEM and twin analysis.

Setting	**HT-ESEM**	**Twin Analysis**
Working Distance (mm)	19.4	16.1
Beam Energy (keV)	20	20
Exposure Time (ms)	33	90
EBSD map area (μm^2)	60.4×45.3	13.4×10
Step Size (nm)	100	100
EBSP Resolution (px^2)	400×300	400×300

ture seen in LSCF. Both sets of samples were freshly sintered and polished with no prior heat treatment.

HT-ESEM samples were marked using a diamond tipped scribe. Using the FSE imaging mode, a region of interest (suitably far away from the scratch) was found on each sample. Then, using SE imaging mode sequential images of decreasing magnification were taken in order to locate the same area when using HT-ESEM. After enough images were collected, the original area was re-focussed and EBSD analysis was run using the settings detailed in Table 2. These are not the optimal EBSD settings, however, it allows high lateral resolution map capture in a reasonable acquisition time. The goal was to measure a significant number of grains to provide representative texture of the material.

Samples analysed for Chapter 7 did not require a mark to be made on the surface. A region of interest was found using FSE imaging and EBSD analysis was run using the settings detailed in Table 2. The chosen analysis area and step size was smaller for this analysis as it was necessary to resolved finer features of the microstructure.

4.1.3 *Auger Electron Spectroscopy*

As can be seen in Figure 25 auger electron emission occurs very close to the surface (approximately 2 - 10 atomic layers) [1] . Incident electrons hitting the sample have a probability to displace core electrons from an atom creating a hole. Electrons from outer shells may then relax into the hole. During the relaxation process an X-ray may be emitted, but there is also a chance another outer shell electron is emitted from the atom (leaving it doubly ionised). Electrons that are emitted are

referred to as 'Auger Electrons'. The mean free path of inelastic scattering processes ensures that only electrons very close to the surface of the sample escape, thus ensuring surface sensitivity of the technique. The energy of Auger electrons is characteristic of the orbital transition energy, therefore, electrons emitted in this process provide chemical information of the surface. In this work Auger electron maps were collected by Dr. Nikolai Tsvetkov at the Massachusetts Institute of Technology (MIT). AES provided elemental mapping of nano-scale features observed on samples annealed in the HT-ESEM.

4.2 DIFFUSION MEASUREMENTS

In order to compare the rate of oxygen exchange to the morphological and chemical changes observed using electron microscopy, Isotopic Exchange (IE) experiments were performed. One of the primary features of the experiment is that it eliminates chemical diffusion effects by using dry, high purity oxygen gases. However, it is common for an SOFC to utilise ambient air as a cathode gas stream due to cost considerations. Ambient air contains a number of active, oxygen containing, species that will have an effect on the surface exchange of a material. With this in mind the 'Back Exchange' technique was developed to measure the overall effect these impurity gases may have on the surface exchange of the material. This work was done in collaboration with Dr Samuel Cooper. This work focusses upon the development of the experimental procedure and implications of the material's response, whilst how to analyse the data is discussed in detail in Dr Cooper's thesis [18]. Samples for both techniques were analysed using Secondary Ion Mass Spectrometry (SIMS) which is discussed in Section 4.3.

4.2.1 *Isotopic Exchange*

Isotopic Exchange (IE), as developed by Kilner et al. [19], utilises isotopic oxygen as a tracer in order to measure both oxygen self-diffusivity and surface exchange rate of oxide materials. As shown in Table 3 the natural abundance of the ^{17}O and ^{18}O isotopes is significantly lower than ^{16}O, therefore, changes in the isotopic ratio will be apparent even if they are small. The isotopic exchange technique utilises thermal anneals in oxygen atmospheres enriched with ^{17}O or ^{18}O in order to

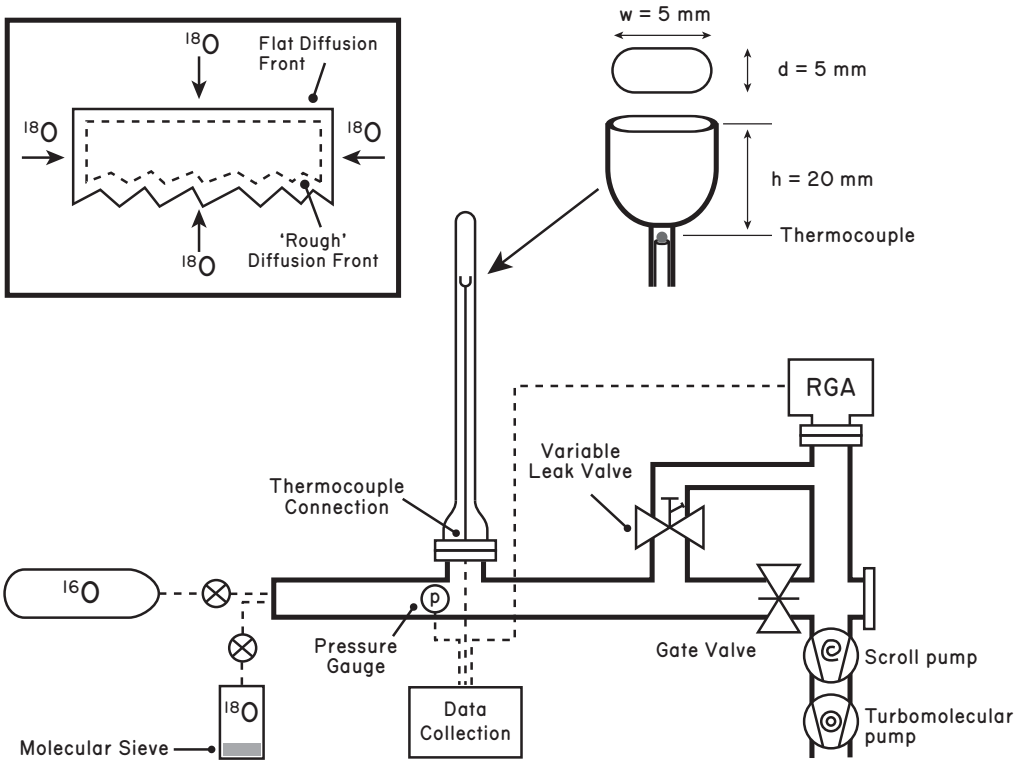


Figure 29: Showing a schematic of the isotopic exchange equipment. Inset: how the surface roughness of a sample affects the shape of the diffusion front.

introduce tracer diffusion profiles that may be measured using a form of mass spectrometry (SIMS in this case). It is more common for ^{18}O to be used as a tracer as ^{17}O has a very similar mass[4] to the hydroxyl species $^{16}O^{1}H$. This species may exist within the residual vacuum of the SIMS equipment, therefore, it is possible it may cause interference when measuring the 17 amu signal. A mass resolution of greater than 6000 is required to differentiate the two peaks. Although possible with the equipment utilised in this work, ^{18}O was used as the tracer isotope for simplicity.

The Isotopic exchange technique relies upon the assumption that the isotopic tracer acts identically to the naturally abundant isotope. Although different by 2 amu, the difference in behaviour between ^{18}O and ^{16}O is considered negligible. The technique also relies upon the introduction of diffusion profiles where the diffusion front is constant, as shown in Figure 29 (inset). To achieve this the technique requires high quality samples and rigorous experimental protocols. The primary factors that may alter the diffusion front are sample density and surface

4 Actual mass differs by 0.01 amu [20]

Table 3: Atomic mass and natural abundance for the three stable oxygen isotopes [22].

Isotope	Atomic Mass (amu)	Natural Abundance (%)
^{16}O	15.995	99.762
^{17}O	16.999	0.038
^{18}O	17.999	0.200

roughness. If a sample is insufficiently dense it will contain open porosity and allow gas phase transport within material. This process is significantly faster than solid state diffusion and as such will increase the apparent diffusion surrounding the pore. Roughness effects are closely associated with variations in surface exchange coefficient [21]. An increase in roughness corresponds to an equivalent increase in surface area and, consequently, surface exchange coefficient. This is due to a larger number of sites available for oxygen exchange. Roughness also has an influence upon SIMS analysis, however, this is discussed in Section 4.3 and Chapter 9.

As detailed in Figure 30 the experimental protocol for isotopic exchange involves two thermal anneals. The first 'Pre-anneal' is performed using research grade ^{16}O (99.999%) at the desired temperature, T, and partial pressure of oxygen, $p(O_2)$. This step is carried out in order to equilibrate the number of oxygen vacancies (and therefore the self-diffusivity of the material), but also alleviate mechanical damage induced by the polishing process. The pre-anneal step is generally carried out for 3-10 times longer than the exchange time in order to ensure the stoichiometric region is significantly longer than the desired exchange profile. The second 'Exchange anneal' involves replacing the ^{16}O environment with isotopically enriched ^{18}O then annealing at the same temperature and partial pressure of oxygen. During this step the tracer diffusion profile is introduced.

In order to prevent chemical effects during both anneals, considerable effort is put into ensuring impurities in the gas stream are low. As mentioned previously, research grade ^{16}O directly from the gas cylinder is used for the pre-anneal step. For the exchange step, 99.9% pure[5] isotopically enriched oxygen is used. This gas is stored in a reservoir containing a molecular sieve (type 5A[6]). This system has two main functions: firstly, due to the high cost of isotopically enriched oxygen

5 This value should not be confused with the '^{18}O gas concentration', or, isotopic fraction in the gas phase

6 https://en.wikipedia.org/wiki/Molecular_sieve

using a molecular sieve makes it possible to recover the gas after an experiment[7]. Secondly, the zeolite material that comprises the sieve has a high affinity for water, keeping the gas dry over multiple recoveries. Before any atmosphere is introduced into the system, turbo-molecular pumps are necessary to evacuate the sample chamber to a high vacuum ($<10^{-7}$ mbar). This further helps prevent impurities from entering the anneal atmosphere.

As will be discussed in Chapter 9 the most significant experimental errors associated with the IE technique occur during SIMS analysis, however, the primary causes of uncertainty during the IE technique are involved with calculation of anneal time and accurate temperature measurement. As can be seen in Figure 29 the thermocouple sits below the sample holder by approximately 5 mm. With the sample sitting in the holder vertically the discrepancy between the top of the sample and the thermocouple will be in the range of 10-20 mm depending upon the precise geometry of the sample. Inside a typical furnace there is a region of uniform temperature known as a 'hotzone'. If the sample is outside of the hotzone the will be a temperature gradient across the sample. In this work the hotzone of the furnace was found to be 25 mm with a temperature variation of ± 1 °C, therefore, samples were heated uniformly. If a sample is sufficiently resistant to thermal shock, application and removal of the furnace from samples may be done quickly in order to minimise heating and cooling times. Due to the thermally activated nature of the processes involved the rate of diffusion and oxygen exchange will differ during heating and cooling. A commonly accepted method for correcting for heating and cooling is described by Killoran [23] if the activation energy for diffusion is known. One method of reducing this error is to have an isothermal anneal region significantly longer than the heating and cooling steps, reducing their effect upon the corrected anneal time. It is generally accepted that the minimum time (regardless of diffusion length) an anneal may take is approximately 15 minutes [24]. For this work LSCF is sufficiently resistant to thermal shock that quenching the sample after an anneal was possible. The temperature profiles were corrected for using the Killoran method with an activation energy of 1.861 eV (taken from [25])

Prior to annealing the exchange time must be calculated. This is determined by the capabilities of the SIMS equipment and the diffusivity of the material.

7 Cooling the reservoir with liquid nitrogen will reduce the chamber pressure and allow flow of gas back into the reservoir

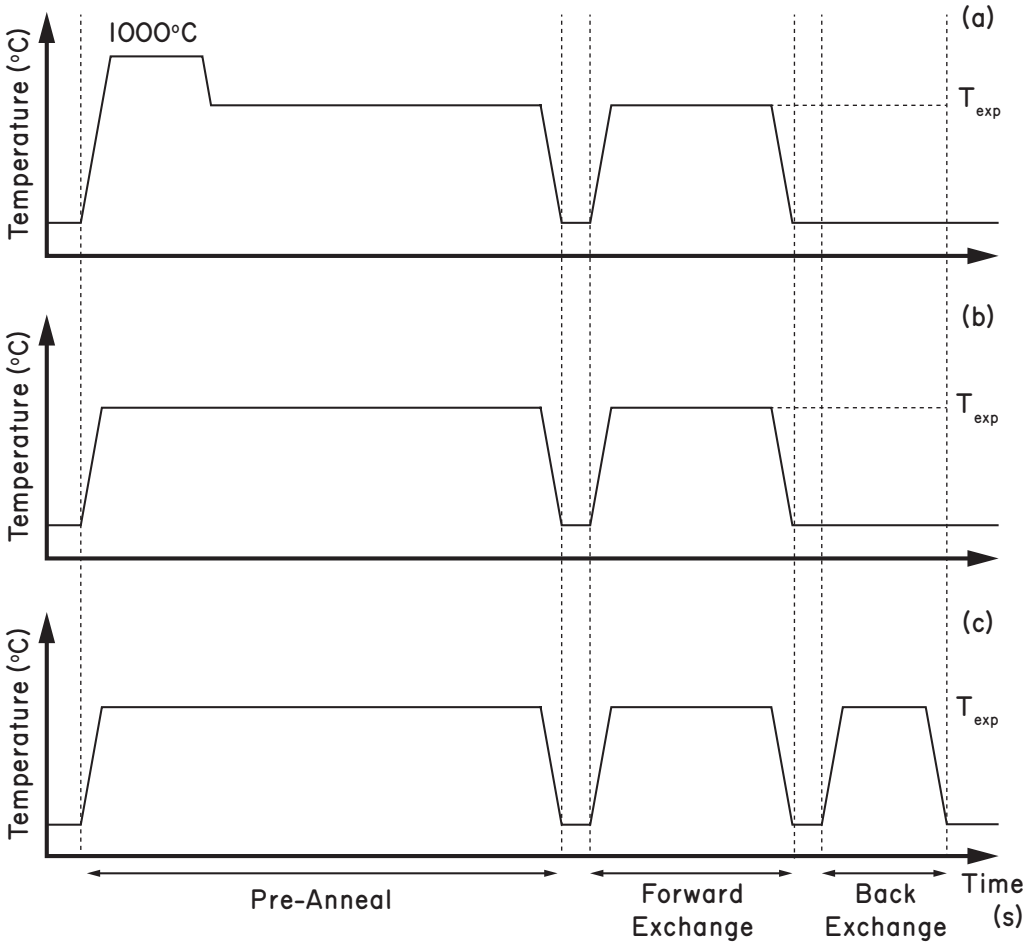


Figure 30: Typical temperature/time profiles for a forward exchange using a 1000°C pre-anneal step, (b) a standard forward exchange and (c) back exchange experiment.

Diffusion length, L_D, is a measure of how far the tracer has diffused into the material. Diffusion length is related to the diffusivity of a material using Equation 4.1:

$$L_D = n\sqrt{D_{T,P}t_e} \tag{4.1}$$

Where $D_{(T,P)}$ is diffusivity at a given temperature and $p(O_2)$, n is an integer (commonly n = 2) and t_e is total anneal time. Although analysis of any diffusion length is theoretically possible, there are practical considerations that must be made related to what SIMS analysis modes are available to the researcher. These will be discussed in more detail in Section 4.3.2, however, generally speaking there are two regimes available: 'depth profiling' and 'line scanning'. Both modes of analysis have practical upper and lower measurable diffusion lengths. The ex-

Table 4: Summary of practical diffusion length limts for depth profile and linescan analysis modes (using a single region).

	Depth Profile (μm)	**Linescan (μm)**
Minimum diffusion length	0.1	10
Maximum diffusion length	5	300

perimental diffusion length must be within one of these two length ranges. For depth profiles the minimum measurable diffusion length is approximately 0.1 μm, and the maximum is determined by the point at which the sputter-induced roughness at base of the crater reduces depth resolution (typically around 5 μm) [26]. The minimum diffusion length for line scanning is determined by the lateral resolution of the SIMS instrument, however, a practical minimum is 10 μm [24]. The maximum value depends on the capabilities of the SIMS instrument. Some modern SIMS instruments have the ability to 'stitch' together multiple analysis regions, making the maximum measurable diffusion length theoretically any length. However, for the equipment used in this work to measure line scans, maximum area for a single analysis was 500 μm. Therefore, as analyses must reach the background level, a practical definition for the maximum diffusion length using a single analysis region may be taken as 300 μm. A summary is presented in Table 4.

To analysis isotopic exchange data (discussed in Section 4.3.2), the isotopic ratio of the enriched gas must be known. Due to the recovery process of the enriched gas, the ratio of gas will steadily decrease over time as gas impurities are introduced and gases leak from the system. Attached to the main chamber is a leak valve in parallel to a Residual Gas Analyser (RGA). The RGA enables quick analysis of the concentration of the gas species, however, a more accurate method is to oxidise a piece of silicon. The oxide layer formed on the silicon may be analysed using SIMS to calculate the precise isotopic ratio of the enriched gas.

Sample Preparation: In order to minimise experimental errors that may arise from porosity and roughness effects, dense polished samples were fabricated as described in section 3.2. Samples were sectioned to 3.5 x 3.5 x 8 mm in order to fit into the sample holder (see Figure 29b). No further processing was required prior to performing the experiment. Depending upon the experimental regime

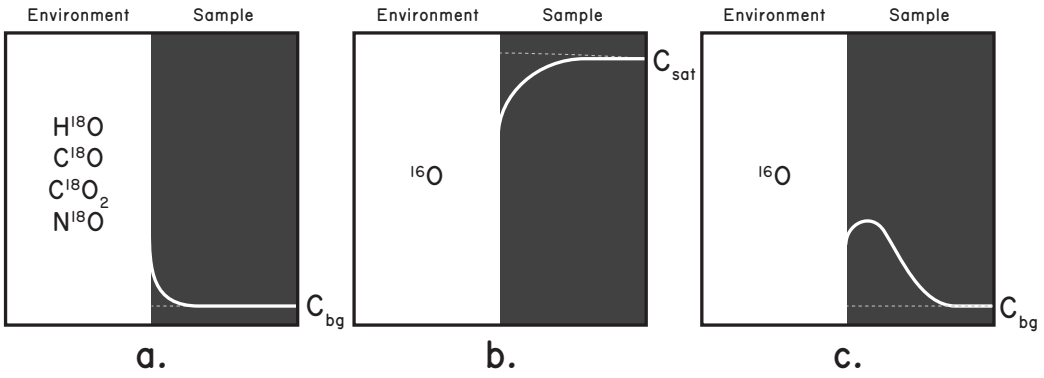


Figure 31: Schematic diagrams showing the tracer isotope profiles using (a) labelled impurity species, (b) the saturated exchange technique and (c) a typical 'Back Exchange' experiment.

samples may require additional preparation before SIMS analysis. The details of this are discussed in Section 4.3 and Chapter 9.

Experimental Regime: Numerous experiments with different anneal temperatures and times were performed during this work. The process for using the equipment may be found at Appendix A.1, however, all experiments in this work samples were exposed to a $p(O_2)$ of 200 mbar to simulate the partial pressure of oxygen in ambient air.

4.2.2 *Back Exchange*

The isotopic exchange technique deliberately utilises pure gases to eliminate chemical effects caused by other oxygen containing gas species. As discussed in Chapter 2, however, it is clear that these gases have a profound effect upon the surface chemistry and therefore the exchange properties of the material. In collaboration with Dr Sam Cooper the 'Back Exchange' technique was developed as a cost effective extension to the IE technique that enabled the use of any gas environment.

As shown in Figure 31 there are a number of methods that could be employed to study the effect oxygen containing impurities such as NO, CO and CO_2. Firstly, using 'labelled' versions of these species (i.e. $C^{18}O$ or $C^{18}O_2$) could be used to identify the exchange contribution from the impurity. However, high purity labelled gases have a high cost attached to them and consequently would also require additional recovery equipment in order to use them efficiently. Secondly,

it is also possible to 'saturate' a sample with a tracer such that the effective background level of the tracer becomes elevated. Therefore annealing in an environment with a low concentration of the tracer (such as ambient air or research grade ^{16}O) will introduce an inverse diffusion profile which can be analysed using the same method as the standard IE technique. The main issue with this approach is that the time required to fully saturate[8] a sample will be very high (on the order of days to weeks). From a practical viewpoint this is undesirable, however, as has been discussed throughout Chapter 2, many candidate cathode materials are meta-stable and will degrade significantly during such a long anneal time. This is perhaps a suitable approach for long term degradation studies, but it is less useful for fundamental studies of material properties. Finally, there is the 'Back Exchange' technique. This utilises an additional anneal step *after* a standard diffusion profile has already been introduced (referred to as the 'Forward exchange' from this point). This second anneal will change the shape of the measured profile and, given knowledge of the original diffusion profile, the extent to which the profile changes will be characterised by a diffusion and surface exchange coefficient. This may be carried out in any environment, provided this atmosphere contains the same partial pressure of oxygen and is annealed at the same temperature as the forward exchange.

The experimental framework discussed in Chapter 8 was first developed in this work. Concurrently, the mathematics of the back-exchange solution and profile fitting method was completed by Dr Cooper [18]. The primary goal of this work was to develop the technique and fully understand systematic errors.

Sample Preparation: No additional processing between the forward and back-exchange was required. However, back-exchange anneals were carried out as soon as possible after the forward exchange to minimise systematic errors.

Experimental Regime: The back-exchange anneal is simply an additional exchange step, see Figure 30. Theoretically this step may be carried out in any furnace that can control the atmosphere, however, for consistency, the isotopic exchange equipment was used. When using ^{16}O for the back-exchange environment, the rig was setup as in Section 4.2.1. For ambient air anneals the same procedure was followed, but no pump down step was necessary prior to the anneal. In

8 Such that the background level is linear and equal to the isotopic ratio in the gas

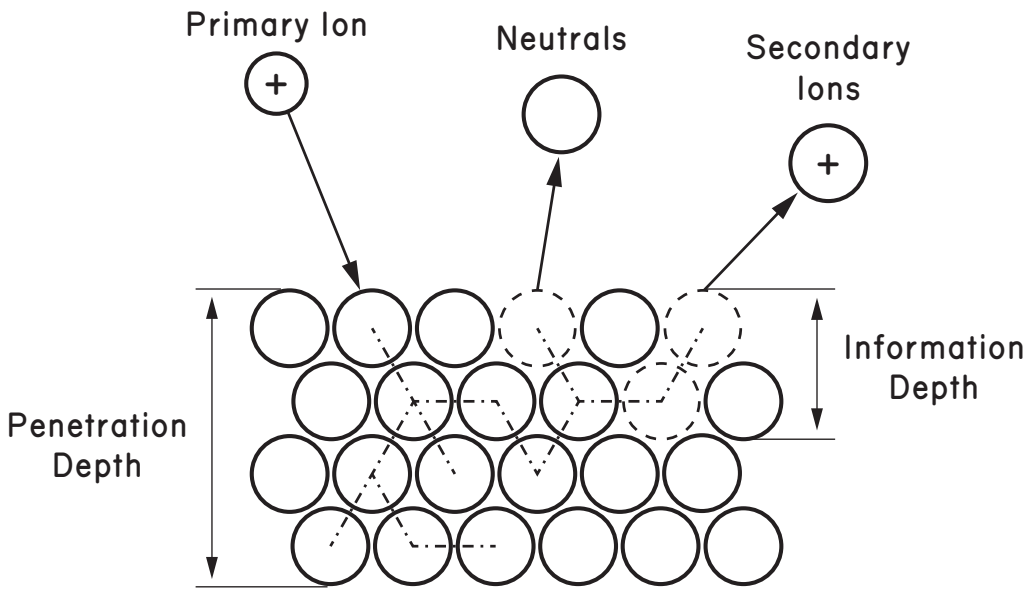


Figure 32: Schematic of ion impact on a material showing collision paths and secondary particle emission.

this work only pure ^{16}O and ambient air back-exchanges were performed. The back-exchange anneal time was chosen to be half that of the forward exchange to exaggerate the influence of the back-exchange step [18].

4.3 ION BEAM ANALYSIS

The analysis techniques described previously utilised electrons as their primary illumination source. The unique property of electron microscopy is its very high lateral resolution, however, this often comes at a cost of lower chemical sensitivity, depth resolution and the inability to distinguish isotopes. Ion beam analysis techniques commonly exhibit high chemical sensitivity (<1 ppm) and depth resolution (1-10 nm), making them very suitable for chemical analysis of the surface. There are numerous techniques available [1], however, this work predominantly employed Secondary Ion Mass Spectrometry (SIMS) and Low Energy Ion Scattering (LEIS). These techniques were used to characterise the chemical nature of the surface and detect the isotopic changes to study the exchange properties of LSCF.

4.3.1 *Secondary Ion Mass Spectrometry (SIMS)*

SIMS involves the bombardment of the sample with high energy primary ions (0.5-40 keV). The energy of the impact is transferred into the material which causes a series of 'billiard-ball-like' collisions to occur beneath the surface of the material. Some collisions will dissipate their energy by entering deeper into the material and causing ion beam induced mixing, however, some are likely to return to the surface and result in the expulsion of electrons, atoms or clusters of atoms. The point of emission is generally within 10 nm of the original impact and particles have significantly lower energy than the primary ion (~20 eV); as a result, the majority of emission originates from the top two atomic layers of the material. Some of these species may be ionised during this process. Secondary ions emitted in this manner may be collected by a simple detector for imaging, or separated in accordance to their mass to charge ratio using a mass spectrometer. The destructive process of secondary ion formation is commonly referred to as 'sputtering' and is shown schematically in Figure 32.

The extent to which the surface is altered is used to define two distinct modes of SIMS operation: *static* and *dynamic* SIMS. In dynamic SIMS, material is sputtered by the primary ion beam and secondary ions are measured concurrently as a function depth. In static SIMS, significantly lower ion beam doses are used, such that statistically each ion impact impinges a region that has received no previous ion beam damage. The 'Static Limit' defines this dose and it is widely accepted that (for inorganic materials) this value is 10^{13} particles/cm^2 [1]. SIMS is considered surface sensitive in the *static* regime.

Secondary ion yield is defined by the following equation:

$$I_s^m = I_p y_m \alpha^{\pm} \theta_m \eta \tag{4.2}$$

Where I_s^m is the secondary ion current (yield) of species m, I_p is the primary ion flux, y_m is the sputter yield, $\alpha^{\pm}$ is the ionisation probability of the charged particle (positive or negative), θ_m is the fractional concentration of species m in the surface layer and η is the transmission factor describing the ion extraction efficiency of the analysis system. However, absolute quantification of secondary ion signal is not simple. Ionisation probability (α) is dependent upon the electronic characteristics of the sample. Therefore, there will be contributions not only from

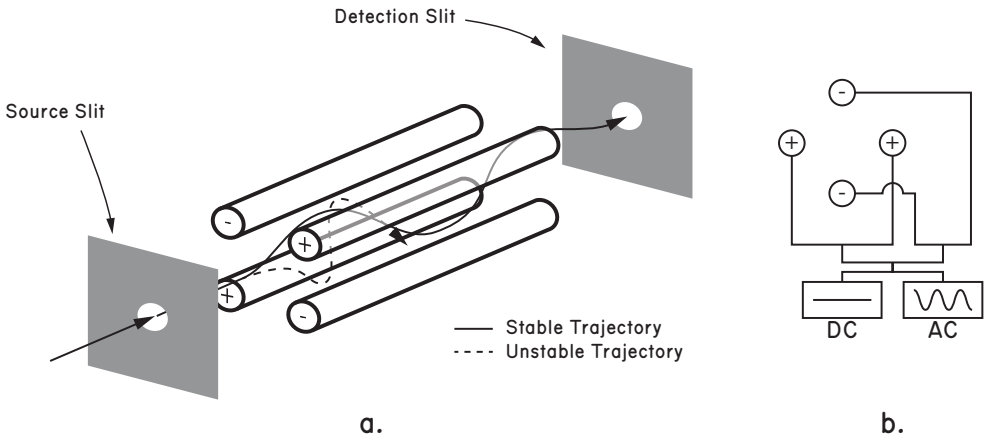


Figure 33: Schematic of a quadrupole mass analyser showing (a) the stable and unstable ion trajectories and (b) a cross section of the rods with applied voltages.

the measured species but also the surrounding matrix of atoms (referred to as 'matrix effects'). Using standard materials enables the quantification of the data, however, producing these is a complex and time consuming process. For the purpose of this work, relative quantification of the oxygen isotopic fraction was used to measure tracer diffusion profiles. Oxygen isotopes are chemically identical, therefore both species' will have the same α term. Secondary ion yield is therefore proportional for each isotope and isotopic ratio ($^{16}O/^{18}O$) may be extracted directly from the SIMS data. As can be seen from Equation 4.2 the sputter rate will be proportional to primary ion current. As such the depth resolution of the SIMS analysis will be dependent upon this value.

Two SIMS instruments were used in this work. The primary differences between the two instruments are their operational mode (static or dynamic) and detection mechanism. Both systems offered unique advantages and are discussed in the following sections.

4.3.1.1 *Quadrupole SIMS*

One system was equipped with a 'Hiden EQS' quadrupole mass analyser and run under dynamic conditions. A quadrupole mass analyser utilises a combination of DC and oscillating radio frequency bias applied to four parallel rods as shown in Figure 33. The DC and AC bias applied to the rods is equal and opposite. This rapid, periodic switching of the field causes the trajectory of ions entering the analyser to oscillate. Most ions are sent into unstable oscillations and will eventually hit the rods. Ions with a certain mass to charge ratio (m/z) will follow

a stable trajectory and be detected. By varying the DC and AC bias different mass to charge ratios may be selected. The relationship between mass resolution and ion transmission is discussed in more detail here: [27, 1]. Quadrupole detector systems may only detect one mass to charge ratio at any instance. As such, the total mass range of an experiment may be reduced to increase detection rates of specific species.

This system utilised a Gallium (Ga^+) Focussed Ion Beam (FIB) source. This primary ion beam, operated at 30 keV, enabled analysis with a very high lateral resolution (<5 nm). The primary ion current was able to be varied between 0.001-20 nA. The equipment also contained a secondary electron detector and as such SIMS images and SE images were able to be correlated very quickly. Due to the high current density available the 'FIB-SIMS' technique was primarily used to perform depth profiles.

4.3.1.2 *Time-of-Flight SIMS (ToF-SIMS)*

Another system employed a 'Time of Flight' (ToF) mass analyser. The principle of detection differs from quadrupole mass analysers. Extracted secondary ions are decelerated and reflected by an *electrostatic mirror*. They are then accelerated with a defined electric field. This gives each ion approximately the same kinetic energy. After acceleration they are then allowed to drift in a field free space towards the detector over a known distance. According to the equation for kinetic energy, heavier masses will take longer to reach the detector. Thus, the mass to charge ratio may be calculated from the 'time of flight' of the ion. This process is shown schematically in Figure 34a. The primary advantage of this detection mechanism is that it allows simultaneous measurement of all mass to charge ratios.

Due to the nature of ToF detection, very short controlled pulses of primary ions are used for two reasons: to prevent detector saturation and increase mass resolution [28]. Ions reflected by the electrostatic mirror will contain a Gaussian distribution of kinetic energies. Therefore, using short primary ion pulses reduces the absolute number of secondary ions and will increase peak definition in the resulting spectra (therefore mass resolution). The intensity and pulse length may be altered in order to select the desired secondary ion yield to mass resolution ratio. Equipment used in this study, TOF-SIMS^5 (ION-TOF GmbH, Münster, Germany), contains two methods of generating pulses. The first sends an ~20 ns pulse of ions through a condenser in order to 'bunch' the ions together such that

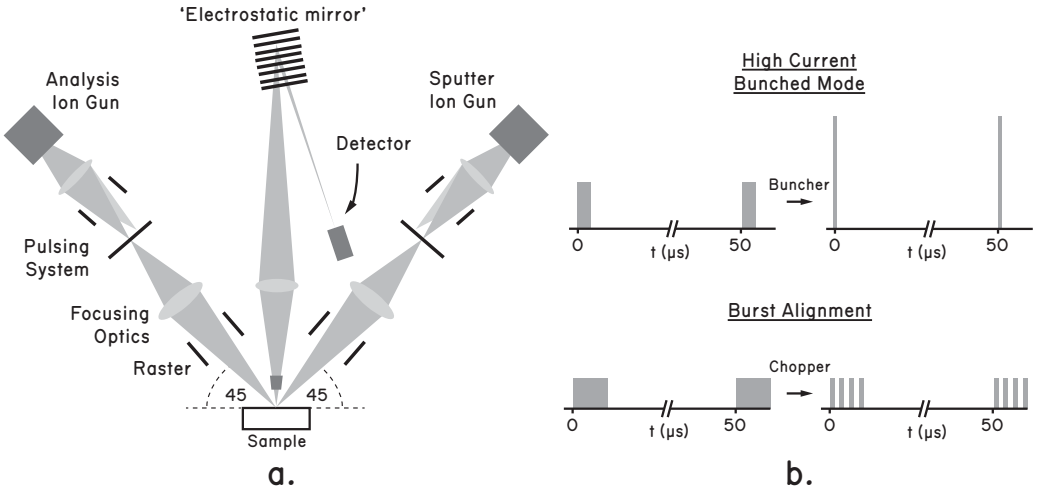


Figure 34: (a) A schematic of the TOF-SIMS[5] equipment including both ion guns and 'electrostatic mirror' and (b) a schematic diagram illustrating the main beam modes.

the overall ion pulse duration is shorter (~0.6 ns) and the ion current is increased. This mode provides the greatest mass resolution and secondary ion count, but offers reduced lateral resolution. The second is to modulate a long pulse (~100 ns) to 'chop' multiple short pulses (~1 ns each) out of a larger ion packet [29]. This mode exhibits a reduced secondary ion yield (per pulse) and lower mass resolution (due to the generation of multiple peaks), however, is vital when studying species with very high ionisation rates. These two modes are schematically shown in Figure 34b and are referred to as 'High Current Bunched Mode' (HCBM) and 'Burst Alignment' (BA) respectively according to the ION-TOF nomenclature. It should also be noted that due to the high numbers of counts associated with the ToF-SIMS technique, Poisson statistics are employed to correct for detector dead time effects [29]. The effect this has on the analysis is discussed fully in Chapter 9.

ToF-SIMS is fundamentally a static SIMS instrument, utilising a dual beam setup to create a distinct analysis and sputter step. Interlacing the beams makes it possible to operate this technique in a *pseudo-dynamic* analysis regime (the result of which is discussed in more detail in Chapter 9). The analysis beam is a Bi^+ Liquid Metal Ion Gun (LMIG) operated at a very low current (0.3 pA) to ensure ion dose is kept below the static limit. The sputter beam was able to be selected depending upon the application. Used in this work was a caesium (Cs^+) thermal

ionisation source (~150 nA primary ion current) and an argon (Ar^+) gas cluster source (~600 nA primary ion current).

ToF-SIMS measurements were primarily performed to analyse 'line-scan' samples using burst alignment mode and a caesium sputter beam. Caesium has been widely shown to enhance the emission of negative species during sputtering. This beam source acts to sputter the material as well as enhance the oxygen signal [30, 31]. Due to this, when studying LSCF burst alignment mode is necessary to minimise counting errors and preventing detector saturation from occurring.

Analysis areas of 300x300 - 500x500 μm^2 were used depending on the diffusion length of the sample. To avoid analysing the edge of the crater formed during the sputter step, the diameter of the sputter beam should aim to be approximately 400-500 μm larger than the analysis beam (see Figure 36). In-depth discussion of the systematic errors of this type of analysis are discussed over Chapter 8 and 9.

4.3.2 *Analysis of Diffusion Data*

As mentioned in Section 4.2.1 the desired diffusion length will determine the sample preparation and subsequent SIMS analysis route. Both forward and back-exchanges from the same sample set will have approximately the same diffusion length, therefore may be analysed using the same method. However, data treatment differs due to the differences in profile shape. In "The Mathematics of Diffusion" [32], Crank solves Fick's second law of diffusion for a series of boundary conditions. Forward exchanges may be fit to the analytical solution of 'diffusion in a semi-infinite medium' [19] as shown in Equation 4.3:

$$\begin{aligned} C'(x,t) &= \frac{C(x,t) - C_{bg}}{C_g - C_{bg}} \\ &= \operatorname{erfc}\left(\frac{x}{2\sqrt{D^* t}}\right) - \left[\exp\left(\frac{k^* x}{D^*} + \frac{k^{*2} t}{D^*}\right) \times \operatorname{erfc}\left(\frac{x}{\sqrt{D^* t}} + k^* \sqrt{\frac{t}{D^*}}\right)\right] \end{aligned} \tag{4.3}$$

Where $C'(x,t)$ is the isotopic fraction at a given position, x, and time, t, normalised to the isotopic fraction in the annealing gas (C_g) and background isotopic fraction (C_{bg}), D^* is the tracer self-diffusivity and k^* is the tracer surface exchange coefficient. It is assumed the tracer self-diffusivity and surface exchange coefficient is approximately the same as ^{16}O.

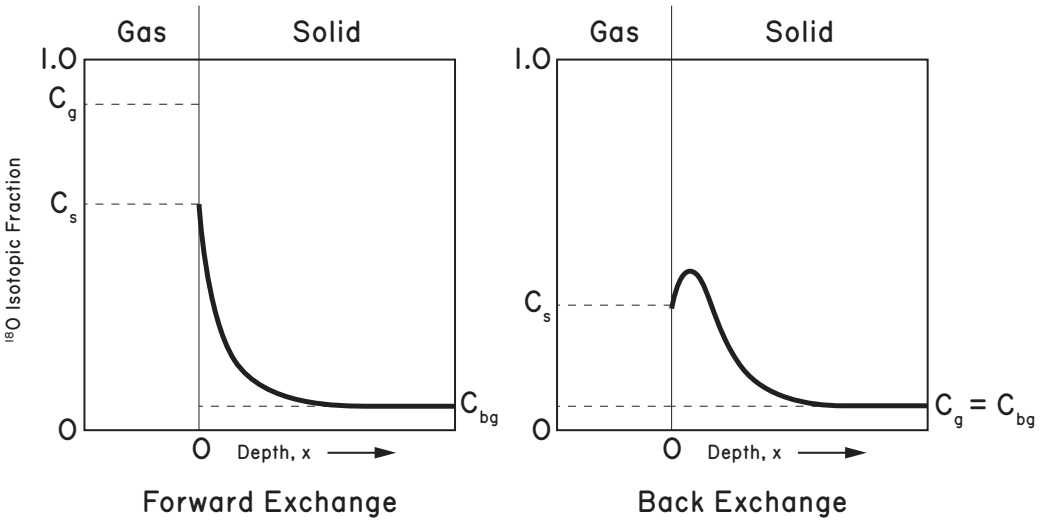


Figure 35: Illustrative examples of a forward exchange profile and a back-exchange profile showing the 'effective' inverted diffusion profile during the back-exchange.

Back exchanges are more complicated to analyse as they are defined by 4 parameters: D_1, k_1, D_2 and k_2 representing the forward and back-exchange respectively. For the special case where the diffusion and surface exchange coefficients are constant in the two exchange steps (D_1=D_2, k_1=k_2), the profile can be shown to be the difference between two single step profiles (see Figure 35), however, in all other cases a finite-difference scheme was used to model this two step diffusion process. The full analytical solution and numerical method may be found in S. J. Cooper's thesis [18]. Forward and back diffusion profiles were constructed from depth profile or line-scan SIMS analysis using the methodology described in the following Sections.

4.3.2.1 *Depth Profiles*

If the diffusion length is below a few micrometres, a SIMS depth profile is the most suitable analysis method as it provides the depth resolution required to resolve the diffusion profile. After each sputter step the isotopic fraction (averaged across the whole analysis area) is measured. This provides a plot of isotopic fraction against sputter time that may then be plotted to produce the diffusion profile. Measurement of the sputter crater depth (detailed in Section 4.4.1) must then be performed to provide a plot of isotopic fraction against depth. This profile may then be fit to Equation 4.3 to extract values of D^* and k^*.

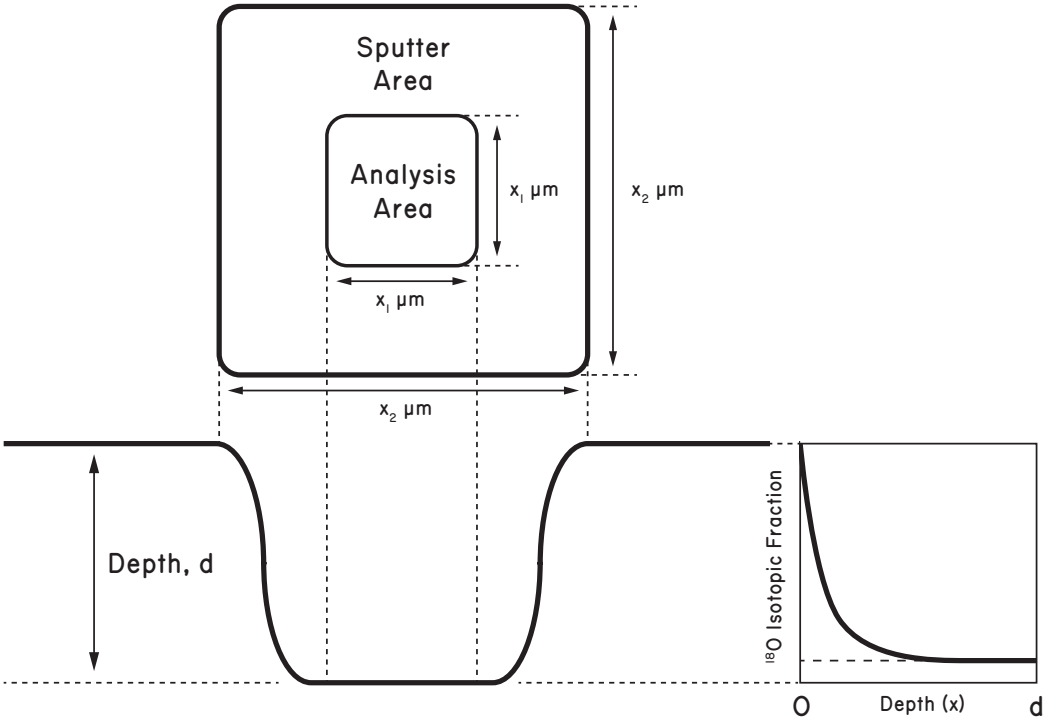


Figure 36: Schematic of a standard sputter crater and its relation to the diffusion profile showing analysis and sputter areas when depth profiling with ToF-SIMS.

SIMS analysis relies upon achieving a constant sputter rate, therefore, considerations must be made when choosing the dimensions of a depth profile analysis. The aspect ratio between sputter depth and crater width should not exceed approximately 10 to ensure constant secondary ion yield. If the crater becomes very deep, secondary ions may not escape from the crater and as such the ion count will drop. Another consideration during a depth profile is the roughness that may be induced at the base of the sputter crater. Sputter rate is related to the incident angle [33] (in a similar manner to electrons - see Figure 25), thus as the crater is sputtered, high angle topographical features will steadily be enhanced. At a certain point the roughness will cause noticeable uncertainty as what the actual analysis depth is at any point. Therefore, to reduce systematic errors, the crater aspect ratio and sputter time should be calibrated to the sample and equipment available.

Sample Preparation: As SIMS is a destructive technique, any relevant analysed used to study the effect of the thermal anneal were performed before depth profile. For SIMS depth profiles it is advisable to clean samples using the standard three step cleaning protocol immediately before placing samples into the SIMS. Doing so

aims to remove as many contaminants from the surface in order to obtain accurate isotopic fractions from the first few data points of the depth profile. Sputter cleaning using the SIMS sputter beam is also an option, however, is very likely to remove a small region of the diffusion profile at the surface.

Experimental Regime: In this work depth profiles were primarily collected using the FIB-SIMS due to the technique's high current density (and hence sputter rate). Analysis areas used was 10x10 μm^2. The ToF-SIMS is deliberately designed to provide high depth resolution and in general is impractical when trying to analyse diffusion profiles longer than 1 μm. Using the Argon cluster sputter beam it is possible to depth profile 10s of microns. However, as will be discussed in Chapter 9, accurate results are only really attainable if the ToF system is equipped with Extended Dynamic Range (EDR) equipment to allow Selective Attenuation of Secondary Ions (SASI) [34]. Forward and back-exchange samples with a diffusion length of approximately 3 μm were prepared at Imperial, then analysed by Dr. Helena Tellez and Dr. John Druce at the International Institute for Carbon-Neutral Energy Research (I^2CNER), Kyushu University. The same TOF-SIMS^5 equipment was used, however, their equipment is equipped with the EDR system.

4.3.2.2 *Line Scans*

As mentioned previously the lower limit of an anneal in the IE technique is approximately 15 minutes. This limit exists to reduce systematic errors in temperature measurement. For materials with sufficiently high self-diffusivity at a given temperature, the lower time limit may still introduce a diffusion profile with a diffusion length well above the depth profile range. It is therefore more practical to increase the anneal time and introduce a diffusion profile with diffusion length suitable for line-scan analysis (see Table 4).

As shown in Figure 37 a line scan profile must be collected from a face *perpendicular* to the original exchange surface. A SIMS 'image' is collected by raster scanning at regular and known intervals across the analysis area. Each interval, or pixel, builds up the SIMS image. The pixels perpendicular to the original surface represent the diffusion profile. Thus, applying a 'line scan' to these pixels a diffusion profile may be constructed. To reduce experimental noise an average is taken from every line scan across the analysis area.

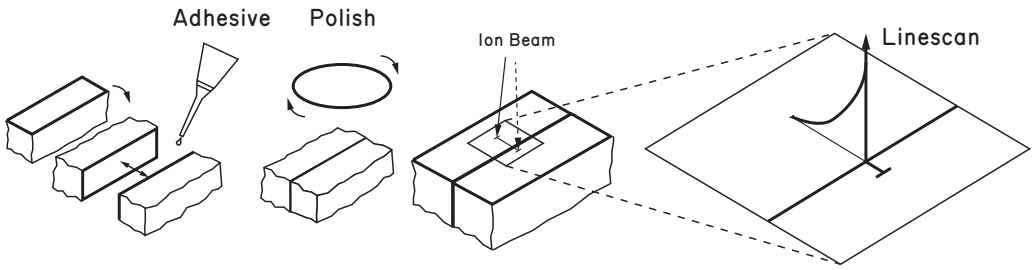


Figure 37: A schematic diagram showing sample preparation for linescan samples showing the resulting diffusion profile from a line-scan.

The technique avoids some of the problems associated with depth profiling. At each depth, every pixel of the image should be identical (ignoring defects that may exist in the sample), therefore depth uncertainty cause by sputter crater roughness may be disregarded. Sputter cleaning of the sample is also made possible due to this reason. However, there are significant experimental errors associated with the first few data points of the diffusion profile. This is discussed in depth in Chapter 9.

Sample Preparation: Prior to line-scan analysis it is vital to perform any relevant analyses used to study the effect of the thermal anneal as the original exchange surface is heavily modified during line-scan sample preparation. Once ready, samples must be polished on a face perpendicular to the original exchange surface . As will be discussed fully in Chapter 9, prior to polishing it is necessary to adhere the original exchange surface to another sample. This is usually another sample to be analysed in the SIMS, however, as long as it is the same material, approximately the same geometry and has the same surface finish, any sample may be used. Once adhered, a side perpendicular to the original exchange surface must be polished using the standard polishing regime. In this stage it is vital to remove enough material such that the diffusion front from this face is completely removed. The amount of material required to be removed should be calculated from the diffusion length of the forward exchange.

Upon removal of the stub there is often resin residue. This must be cleaned using the appropriate solvents. Care was taken to ensure minimal modifications were made to prevent removal of the adhesive between the two samples.

Experimental Regime: In this work diffusion lengths ranging from 100-250 μm were introduced during isotopic exchanges. Line scans were performed on these sam-

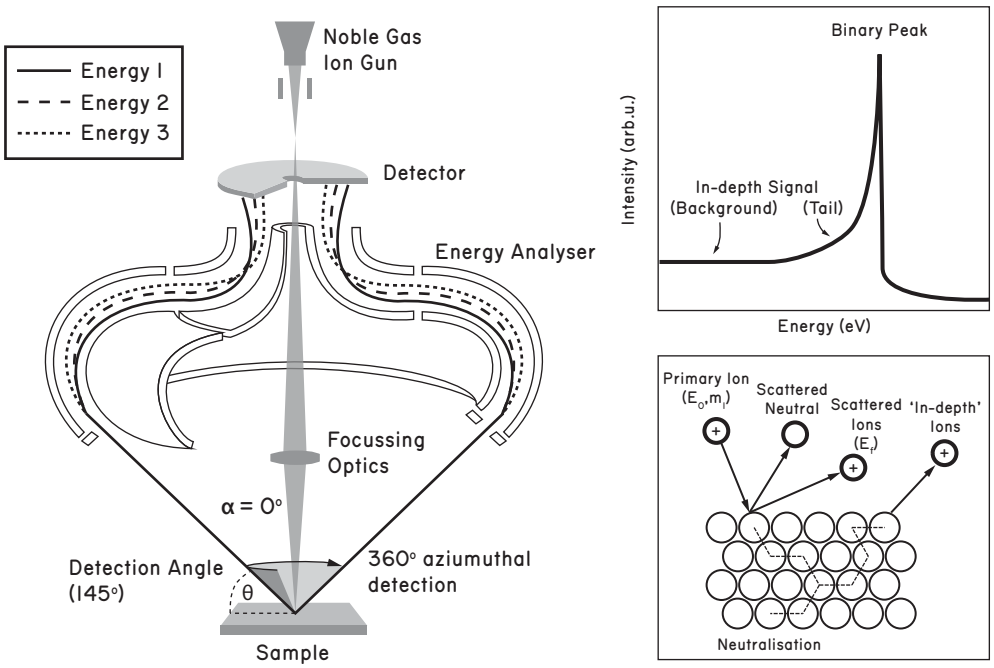


Figure 38: Schematic of the 'tulip' detector employed in the qtac[100] showing beam incident angle and ion detection. The inset shows a schematic of the scattering process and a typical peak shape.

ples using ToF-SIMS with a Bi^+ analysis beam in burst alignment mode and Cs^+ sputter beam. Depending upon the diffusion length of the sample, analysis areas of 300x300 μm or 500x500 μm were used. Appropriate sputter areas were choses based upon the analysis area. The analysis and sputter beam were interlaced during analysis.

4.3.3 *Low Energy Ion Scatting (LEIS)*

LEIS is an analytical tool that enables compositional analysis of the outermost atomic layer. A sample is bombarded with low energy (0.5-10 keV) noble gas ions (He^+, Ne^+ or Ar^+) at an incident angle α. As shown in the inset of Figure 38, binary collisions between the incident ion (m_1,E_0) and the sample cause some ions to be backscattered with an angle θ. The relatioship between the initial en-

ergy and detected energy (E_f) enables calculation of the target atom's mass from energy and momentum conservation if the detection angle (θ_d) is known:

$$E_f = \left(\frac{\cos\theta_d \pm \sqrt{\left(\frac{m_2}{m_1}\right)^2 - \sin^2\theta_d}}{1 + \frac{m_2}{m_1}} \right)^2 .E_0 \tag{4.4}$$

The technique is highly surface sensitive due to the use of noble gas primary ions. As described in Section 4.1 and 4.3 incident species will have an associated interaction volume. Noble gas ions are very readily neutralised, thus, each subsequent collision within the sample will have a high probability that an incident ion is neutralised (and therefore undetected). For this reason, binary peaks in a LEIS spectra are considered to represent the top atomic layer of the material and are thus unaffected by matrix effects. There is a chance, however, that incident ions do re-emerge after penetrating further into the material after lose some energy due to inelastic interactions. These ions appear as 'background' and 'tail' components on binary peaks. Therefore, LEIS is considered to be 'generally free' from matrix effects [35]. In order for spectra to be defined as 'surface spectra', the ion dose must be below the static limit. Due to the low probability of backscattered particles, surface sensitivity often must be balanced with the signal to noise ratio. For further reading on the fundamentals of the LEIS technique, please refer to: [36].

The integral of the spectra can be used to quantify the elements detected during an analysis. Absolute quantification requires well defined standard scattering intensities, however, fabrication and analysis of said standards was beyond the scope of this work. From a single spectra the surface composition was able to be calculated from the fraction of each element. This was achieved through peak fitting of the spectra. As mentioned, binary peaks also contain background components due to sub-surface interactions. In a pure material each interaction will lose the same amount of energy, thus the background is linear and dependent only on the number of collisions. For materials with multiple elements the energy lost during these interactions will have a distribution depending upon the structure of the material. For simplicity it is assumed background components are also linear in multi-component materials.

Due to the sensitivity of the technique there are numerous issues regarding the analysis of polycrystalline bulk materials, including surface roughness and surface contamination. Significant roughness (whether this be from surface finish or secondary phase formation) causes 'shadowing' of scattered ions [37, 38]. These effects result in signal reduction and as such induce errors associated with compositional analysis. Small quantities of surface contamination are capable of 'blocking' the analysis beam from probing the sample, resulting in significant or total signal loss. It is therefore vital to clean the surface of the sample thoroughly prior to analysis.

The equipment used in this work was an ION-TOF qtac^{100}. This equipment provides 3000 times greater sensitivity than conventional ion scattering spectrometers [39] by collecting ions at all azimuthal angles (shown in Figure 38). Therefore, high signal to noise ratio surface spectra could be collected using this lab equipment. Similar to the TOF-SIMS^5, the qtac^{100} is also equipped with a dual analysis/sputter beam setup; enabling LEIS depth profiling. In this regime surface sensitivity is lost due to sputtering of the material and beam mixing effects, however, LEIS depth profiles offer two main advantages over SIMS analysis. Firstly, binary scattering is unaffected by matrix effects, therefore, atomic composition (of cations in particular) as a function of depth is more easily determined. Secondly, as the analysis step does not rely on sputtering, it is not necessary to wait for a steady state sputter regime [40].

In this work samples were analysed using both He^+ (3 keV) and Ne^+ (5 keV) primary ion beams. Helium 'survey' spectra were collected to qualitatively define the 'cleanliness' of the surface by detecting common contaminates such as sodium, chlorine, potassium and magnesium. Cobalt and iron binary peaks cannot be resolved using He^+ and as such are not suitable to quantify cation composition. To do so, Ne^+ spectra are necessary.

Sample Preparation: In this work LEIS analysis was carried out on exchanged samples. Modification/cleaning of the surface was generally undesirable as to probe the true nature of the surface. As such samples were transferred from the IE equipment to the LEIS as quickly as possible to prevent the use of a standard clean using solvents. Care was taken to not touch the analysis surface. Due to the fact samples were transferred through ambient conditions small quantities of common contaminants were inevitable. The qtac^{100} used in this work was setup

with an 'oxygen plasma cleaning equipment'[9] to remove many of these contaminants from the surface. Once sparked, the oxygen plasma is directed towards the sample. By the time it reaches the sample surface, all of the ionic species will have recombined to form atomic oxygen. This gas phase will react with many of the hydrocarbon contaminants on the surface to form gaseous species. These are then removed by the vacuum. Approximately 30 minutes of 'oxygen cleaning' was required per sample.

Experimental Regime: Each sample was analysed using the same method. After cleaning, 3 keV He^+ survey spectra were collected. The beam raster area was large (1x1 mm) to improve signal to noise ratio and remain within the static limit. On a fresh area of the sample 5 keV Ne^+ surface spectra were collected. After collection, using another fresh sample area, LEIS depth profiles were performed. The sputter beam used was a 1 keV Ar^+ gas cluster source with a raster area of 1.5x1.5 mm. Depth profiles were run until the composition reached stoichiometry. Beam currents and sputter times are quoted next to the relevant data.

4.4 TOPOGRAPHY MEASURMENTS

For both electron and ion beam techniques, edge effects tend to introduce systematic errors. Therefore, defining surface roughness and topography is an equally important part of surface analysis. In this work, two methods of topography measurement were employed. For macro-scale features White Light Interferometry (WLI) provided sufficient lateral and depth resolution, however, to resolve micro and nano scale features Atomic Force Microscopy (AFM) was required.

4.4.1 *White Light Interferometry*

White Light Interferometry is a non-contact optical method of generating a 3D representation of surface topography. The equipment used in this work was a Zygo New View 200 and is schematically show in Figure 39. White light is passed through a Mirau objective lens[10]. This lens splits the light such that one portion of the light is directed towards the sample and the other towards a reference

9 Hydrogen plasma was also available
10 https://en.wikipedia.org/wiki/Mirau_interferometer

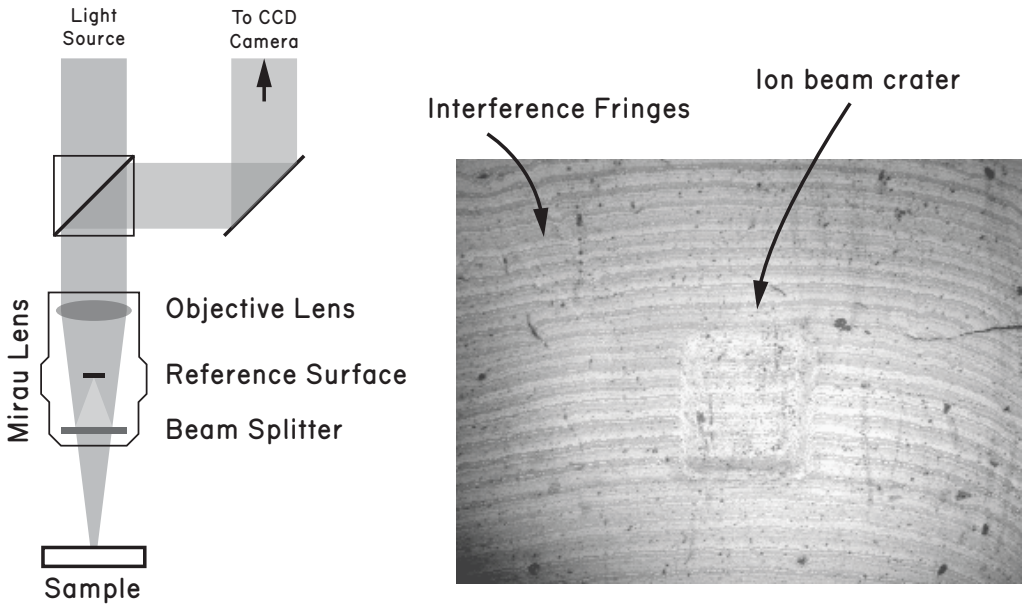


Figure 39: Schematic diagram of the optics of a white light interferometer and an example interference pattern.

material. After reflection from an in-focus sample, light from both the sample and reference path are recombined and directed towards a CCD camera. Changes in sample path length cause reflected light to be 'out of phase' with the light from the reference path. Constructive and destructive interference between the two wave fronts results in an image with light and dark regions defined by the sample path length. The reference sample is adjusted using an internal motor to 'scan' over a height range to change the focal plane. This is then analysed by the accompanying software, MetroPro[11], and is able to construct a 3D data set with a maximum depth resolution of 1-2 nm (depending upon the objective lens and analysis method). Defining the objective lens also allows calculation of the analysis area.

The technique relies upon the reflectivity of a sample being above 5% [41] to reduce signal noise and increase repeatability. Reflectivity in this case refers to specular reflection from a flat surface. The optical limit of reflected angles that will be accepted is defined by the numerical aperture of the objective lens. As analysis is associated with flat samples, changes in reflected angle are often associated with sample defects or edges. Here these will be referred to as 'sample tilt'. Table 5 shows the numerical aperture for the objective lenses used in this work and their associated maximum sample tilt. Above the maximum tilt angle light

11 It should be noted the algorithms to do are not detailed by the manufacturer

Table 5: Associated properties of the 10x and 50x object lenses used in this work - data from the Zygo documentation [43].

Objective Lens	**x10**	**x50**
Working Distance	7.4 mm	3.4 mm
Numerical Aperature	0.3	0.55
Maximum Sample Tilt	7.5°	33.4°
Depth Resolution	5 nm	3 nm

cannot be collected and consequently cause erroneous values in these regions [42].

Sample Preparation: Many MIEC electrode materials have a relatively low electronic conductivity at room temperature. Although the precise reflectivity of LSCF is not known, polished samples exhibit a 'mirror finish', clearly indicating they are above the lower reflectivity limit. Therefore, no further processing was required.

Experimental Regime: In this work WLI was used to measure the crater depth of SIMS depth profiles and characterise systematic errors associated with line-scan analyses. Generally, the features of interest were small enough to fit into the field of vision of the 50x objective lens. However, in order to locate the desired feature and ensure the sample was flat the 10x object lens was used first. Once located and set-up, the lens could be switched with the 50x object lens to perform the analysis.

For some features, the aspect ratio was high and as such the equipment could not measure the middle of the feature due to a lack of light escaping from it. The MetroPro software has a 'stich' mode that allows two concurrent analyses to be stitched together to solve this. One analysis is run as normal, but the second intensifies the illumination source to increase the probability of light escaping from the feature. Pixels that saturate the detector in the second scan are discarded and the two analyses are combined to form a single data-set.

4.4.2 *Atomic Force Microscopy*

In order to study nano scale topographical features, Atomic force microscopy was used. The technique uses a sharp probe on a cantilever that is raster scanned parallel to the surface. When the tip gets close to the surface of the sample small contact forces[12] are observed. These cause deflection of the cantilever that may be measured to provide topographical information. The probe may be operated in constant force or tapping mode. In constant force (or constant height) mode the probe cantilever height is adjusted to ensure a constant force at the probe-sample interface. This mode has the highest accuracy when measuring surface topography, however, can cause mechanical damage to the sample surface and is prone to probe damage if the sample contains large defects (such as pores). To reduce the rate of energy dissipation by the probe 'tapping' mode oscillates the cantilever at high frequency such that it makes intermittent contact with the surface. As the surface is not constantly measured, the lateral resolution of this mode is lower, however, aids in preventing sample and probe damage. Additionally, as the probe is oscillating, phase images may be collected. The response to the probe is mechanical in nature, therefore, the elastic modulus of the sample will define the energy dissipated upon contact with the sample. If the surface of the sample contains heterogeneity, the cantilever will fall slightly out of phase when travelling between the different regions. Thus, contrast in a phase map allows characterisation of surface chemistry.

Sample Preparation: AFM was also performed primarily on exchange samples. The technique is highly sensitive to topographical changes. Significant roughness may cause damage to the probe. For this work no additional sample preparation was required for polished and exchanged samples.

Experimental Regime: In this work a Bruker Innova AFM was used to perform experiments. Samples polished and exchanged (or simply annealed) were analysed in tapping mode. The lateral resolution of the technique is dependent upon the total analysis area and pixel count. In this work pixel count was kept at 512x512 px whilst analysis area was varied between 1 - 10 μm^2. The analysis area is quoted with the relevant data.

12 Including van der Waals forces, capillary forces and electrostatic forces

BIBLIOGRAPHY

[1] J C Vickerman and Ian S Gilmore. *Surface Analysis – The Principal Techniques 2nd Edition*. 2009. ISBN 9780470017630.

[2] Joseph I. Goldstein, Dale E. Newbury, Patrick Echlin, David C. Joy, Charles E. Lyman, Eric Lifshin, Linda Sawyer, and Joseph R. Michael. *Scanning Electron Microscopy and X-ray Microanalysis*. Springer US, Boston, MA, 3 edition, 2003. ISBN 978-1-4613-4969-3. doi: 10.1007/978-1-4615-0215-9. URL http://link.springer.com/10.1007/978-1-4615-0215-9.

[3] Rayleigh. XXXI. Investigations in optics, with special reference to the spectroscope. *Philosophical Magazine Series 5*, 8(49):261–274, 1879. ISSN 1941-5982. doi: 10.1080/14786447908639684. URL http://www.tandfonline.com/doi/abs/10.1080/14786447908639684.

[4] Bob Hafner and Bob Hafner. Scanning Electron Microscopy Primer. *Cities*, pages 1–29, 2007.

[5] G D Danilatos and V N E Robinson. Principles of scanning electron microscopy at high specimen chamber pressures. *Scanning*, 2(39):72–82, 1979. ISSN 0161-0457. doi: 10.1002/sca.4950020202.

[6] S Jennings. The Mean Free Path in Air. *Journal of Aerosol Science*, 19(2):159–166, 1988. ISSN 00036951. doi: 10.1063/1.3027060. URL http://linkinghub.elsevier.com/retrieve/pii/0021850288902194.

[7] Robert Johnson. Environmental Scanning Microscopy: An introduction to ESEM. pages 1–56, 1996.

[8] Martin Munz, Mark T. Langridge, Kishore K. Devarepally, David C. Cox, Pravin Patel, Nicholas A. Martin, Gergely Vargha, Vlad Stolojan, Sam White, and Richard J. Curry. Facile synthesis of titania nanowires via a hot filament method and conductometric measurement of their response to hydrogen sulfide gas. *ACS Applied Materials and Interfaces*, 5(4):1197–1205, 2013. ISSN 19448244. doi: 10.1021/am302655j.

[9] S K Verma, G M Raynaud, and R A Rapp. Hot-stage scanning electron microscope for high-temperaturein-situ oxidation studies. *Oxidation of Metals*, 15(5):471–483, 1981.

[10] Judith M. Cohen, Kenneth J. Hartley, and Malcolm B. Waldron. A simply constructed heating stage for the scanning electron microscope. *Journal of Microscopy*, 118(4):463–470, apr 1980. ISSN 00222720. doi: 10.1111/j.1365-2818.1980.tb00296.x. URL http://doi.wiley.com/10.1111/j.1365-2818.1980.tb00296.x.

[11] Renaud Podor, Damien Pailhon, Johann Ravaux, and Henri-Pierre Brau. Development of an Integrated Thermocouple for the Accurate Sample Temperature Measurement During High Temperature Environmental Scanning

Electron Microscopy (HT-ESEM) Experiments. *Microscopy and microanalysis*, 21(2):307–312, 2015. ISSN 1435-8115. doi: 10.1017/S1431927615000252. URL http://www.ncbi.nlm.nih.gov/pubmed/25898837.

[12] L. Joly-Pottuz, A. Bogner, A. Lasalle, A. Malchere, G. Thollet, and S. Deville. Improvements for imaging ceramics sintering in situ in ESEM. *Journal of Microscopy*, 244(1):93–100, 2011. ISSN 00222720. doi: 10.1111/j.1365-2818.2011.03512.x.

[13] Srinivas Subramaniam. *In Situ High Temperature Environmental Scanning Electron Microscopic Investigations of Sintering Behavior in Barium Titanate*. PhD thesis, 2006.

[14] A.M Brown and P.L Surman. Oxidation of iron within the scanning electron microscope: Oxide crystallite growth kinetics during the oxidation of iron in CO2. *Surface Science*, 52(1):85–102, sep 1975. ISSN 00396028. doi: 10.1016/0039-6028(75)90010-2. URL http://linkinghub.elsevier.com/retrieve/pii/0039602875900102.

[15] ICSM. Institut de chimie séparative de marcoule. URL http://www.icsm.fr/.

[16] S Kikuchi. Diffraction of cathode rays by calcite. *Nature*, 122(3080):726, 1928. ISSN 0028-0836. doi: 10.1038/1211019a0.

[17] Bruker. EBSD Argus Imaging. URL https://www.bruker.com/products/x-ray-diffraction-and-elemental-analysis/eds-wds-ebsd-sem-micro-xrf-and-sem-micro-ct/quantax-ebsd/hardware/argus-fsebse-imaging-system.html?key=1-2.

[18] S J Cooper. *Quantifying the Transport Properties of Solid Oxide Fuel Cell Electrodes*. PhD thesis, Imperial College London, 2015.

[19] JA Kilner, BCH Steele, and L Ilkov. Oxygen self-diffusion studies using negative-ion secondary ion mass spectrometry (SIMS). *Solid State Ionics*, 12 (1984):89–97, 1984. URL http://www.sciencedirect.com/science/article/pii/0167273884901346.

[20] A. Benninghoven, F. G. Rudenauer, and H. W. Werner. *Secondary Ion Mass Spectrometry: Basic Concepts, Instrumental Aspects, Applications and Trends*. 1987. ISBN 0471010561. URL https://books.google.com/books?id=zVKkMQEACAAJ{&}pgis=1.

[21] M. J. Pietrowski, R. a. De Souza, M. Fartmann, R. ter Veen, and M. Martin. Oxygen Isotope Transport Properties of Yttria-Stabilized Zirconia (YSZ) in O 2 - and H 2 O-Containing Atmospheres. *Fuel Cells*, (0):n/a–n/a, jul 2013. ISSN 16156846. doi: 10.1002/fuce.201300087. URL http://doi.wiley.com/10.1002/fuce.201300087.

[22] Juris Meija, Tyler B. Coplen, Michael Berglund, Willi A. Brand, Paul De Bièvre, Manfred Gröning, Norman E. Holden, Johanna Irrgeher, Robert D. Loss, Thomas Walczyk, and Thomas Prohaska. Atomic weights of the elements 2013 (IUPAC Technical Report). *Pure and*

Applied Chemistry, 88(3):265–291, 2016. ISSN 1365-3075. doi: 10.1515/pac-2015-0305. URL http://www.degruyter.com/view/j/pac.2016.88.issue-3/pac-2015-0305/pac-2015-0305.xml.

[23] D. Killoran. The Effective Duration of a Linear Slow-Cool. *Journal of The Electrochemical Society*, pages 7–8, 1962. doi: 10.1149/1.2425354.

[24] R.J. Chater, S. Carter, J.A. Kilner, and B.C.H. Steele. Development of a novel SIMS technique for oxygen self-diffusion and surface exchange coefficient measurements in oxides of high diffusivity. *Solid State Ionics*, 53-56:859–867, jul 1992. ISSN 01672738. doi: 10.1016/0167-2738(92)90266-R. URL http://linkinghub.elsevier.com/retrieve/pii/016727389290266R.

[25] Sarah Benson. *Oxygen Transport and Degradation Processes In Mixed Conducting Perovskites*. PhD thesis, Imperial College London, 1998.

[26] R. a. De Souza. *Ionic transport in acceptor-doped perovskites*. PhD thesis, 1996.

[27] K. Wittmaack. Successful operation of a scanning ion microscope with quadrupole mass filter. *Review of Scientific Instruments*, 47(1):157, 1976. ISSN 00346748. doi: 10.1063/1.1134472. URL http://scitation.aip.org/content/aip/journal/rsi/47/1/10.1063/1.1134472.

[28] G Van Tendeloo. Handbook of Microscopy. *New York*, II(5):321–321, 1997. ISSN 0027769X. doi: 10.1002/9783527620647. URL http://doi.wiley.com/10.1002/food.19970410534.

[29] R De Souza, J Zehnpfenning, M Martin, and J Maier. Determining oxygen isotope profiles in oxides with Time-of-Flight SIMS. *Solid State Ionics*, 176(15-16):1465–1471, may 2005. ISSN 01672738. doi: 10.1016/j.ssi.2005.03.012. URL http://linkinghub.elsevier.com/retrieve/pii/S0167273805001001.

[30] Victor E. Krohn. Emission of negative ions from metal surfaces bombarded by positive cesium ions. *Journal of Applied Physics*, 33(12):3523–3525, 1962. ISSN 00218979. doi: 10.1063/1.1702439.

[31] G Doucas. Energy distribution of negative ions sputtered from caesiated surfaces. *International Journal of Mass Spectrometry and Ion Physics*, 25(1):71–87, 1977. ISSN 0020-7381. doi: http://dx.doi.org/10.1016/0020-7381(77)80106-X. URL http://www.sciencedirect.com/science/article/pii/002073817780106X.

[32] J Crank. *The mathematics of diffusion*. Clarendon Press, Oxford, 1975. URL http://catalog.enu.kz:55555/guid/9f5ec001-d0f7-4633-abd6-182b02c75429.pdf.

[33] N Warmoltz, H W Werner, and A E Morgan. The dependence on the angle of incidence of the steady state sputter yield of silicon bombarded by oxygen ions. *Surface and Interface Analysis*, 2(2):46–52, 1980. ISSN 1096-9918. doi: 10.1002/sia.740020203. URL http://dx.doi.org/10.1002/sia.740020203.

[34] Helena Tellez, John Druce, Jong Eun Hong, Tatsumi Ishihara, and John A. Kilner. Accurate and precise measurement of oxygen isotopic fractions and

diffusion profiles by selective attenuation of secondary ions (SASI). *Analytical Chemistry*, 87(5):2907–2915, 2015. ISSN 15206882. doi: 10.1021/ac504409x.

[35] John Druce, Neil Simrick, Tatsumi Ishihara, and John Kilner. "Imaging" LEIS of micro-patterned solid oxide fuel cell electrodes. *Nuclear Instruments and Methods in Physics Research Section B: Beam Interactions with Materials and Atoms*, 332:261–265, aug 2014. ISSN 0168583X. doi: 10.1016/j.nimb.2014.02.074. URL http://linkinghub.elsevier.com/retrieve/pii/S0168583X14003310.

[36] H Brongersma, M Draxler, M Deridder, and P Bauer. Surface composition analysis by low-energy ion scattering. *Surface Science Reports*, 62(3):63–109, mar 2007. ISSN 01675729. doi: 10.1016/j.surfrep.2006.12.002. URL http://linkinghub.elsevier.com/retrieve/pii/S0167572906001221.

[37] G. C. Nelson. Influence of surface roughness on the intensity of elastically scattered low energy noble gas ions. *Journal of Applied Physics*, 47(4):1253–1255, 1976. ISSN 00218979. doi: 10.1063/1.322847.

[38] W. P. a. Jansen, A. Knoester, a. J. H. Maas, P. Schmit, A. Kytokivi, a. W. Denier v.d. Gon, and H. H. Brongersma. Influence of compaction and surface roughness on low energy ion scattering signals. *Surface and Interface Analysis*, 36(11):1469–1478, nov 2004. ISSN 0142-2421. doi: 10.1002/sia.1921. URL http://doi.wiley.com/10.1002/sia.1921.

[39] IoN-ToF. Quantitative elemental characterisation of the. URL https://www.iontof.com/download/IONTOF{_}Qtac{_}Brochure.pdf.

[40] Richard J. Chater, Alan J. Smith, and Graham Cooke. Simultaneous detection of positive and negative secondary ions. *Journal of Vacuum Science & Technology B, Nanotechnology and Microelectronics: Materials, Processing, Measurement, and Phenomena*, 34(3):03H122, 2016. ISSN 2166-2746. doi: 10.1116/1.4943531. URL http://scitation.aip.org/content/avs/journal/jvstb/34/3/10.1116/1.4943531.

[41] Richard Leach, Xiangqian Jiang Leigh Brown, Roy Blunt, and Darian Mauger Mike Conroy. Guide for the Measurement of Smooth Surface Topography using Coherence Scanning Interferometry. *Manual*, (108):56, 2008. ISSN 1368-6550.

[42] F. Gao and RK Leach. Surface measurement errors using commercial scanning white light interferometers. *Measurement Science . . .*, 19(1):015303, 2008. ISSN 0957-0233. doi: 10.1088/0957-0233/19/1/015303. URL http://iopscience.iop.org/0957-0233/19/1/015303{%}5Cnhttp://iopscience.iop.org/0957-0233/19/1/015303/pdf/0957-0233{_}19{_}1{_}015303.pdf.

[43] Zygo. New View 200. URL http://www.zygo.com.

Part III

RESULTS AND DISCUSSION

The data presented throughout the following chapters builds a story of the LSCF surface and ideally should be read in the order presented. Initial data from characterisation experiments were used to setup the framework for the subsequent experiments. It was observed that the LSCF surface reacted differently when heat treated in dry and ambient environments. Systematic experimentation *in-situ* provided fundamental understanding of the LSCF surface reaction after exposure to these different environments. This data enabled comparison between the evolution of the LSCF surface and *ex-situ* kinetic data.

5

POWDER AND SAMPLE CHARACTERISATION

In this chapter, results of the techniques used to characterise as-received LSCF powder are presented. Phase purity of the power was verified using X-ray diffraction and chemical stoichiometry was determined using ICP. Of particular interest to this work was surface modification due to high temperature thermal anneals in ambient air atmospheres. Prior to the experiments discussed throughout Chapters 6 - 9, high-temperature x-ray diffraction was performed to determine if the powder underwent a phase change when heated from room temperature to 1000°C. Additionally, initial *ex-situ* observations of surface modification over this temperature range were studied using SEM. The data presented from this initial data will provide the relevant context for the experiments discussed in the proceeding chapters.

5.1 POWDER CHARACTERISATION

5.1.1 *X-Ray Diffraction*

Although sold by a reputable supplier, it was necessary to ascertain the true nature of the as-received powder. XRD was performed in order to ensure the powder did in-fact represent single phase $La_{0.6}Sr_{0.4}Co_{0.2}Fe_{0.8}O_{3-\delta}$. The experimentally observed diffraction pattern collected from the as-received powder is shown in Figure 40. The characteristic peak positions of $La_{0.6}Sr_{0.4}Co_{0.2}Fe_{0.8}O_{3-\delta}$ as calculated by Itoh and Nakayama [1] are shown as ticks below the pattern. It can be seen that there is good agreement between observed peak positions and the expected reflections of LSCF. This suggests that the as-received powder is single phase $La_{0.6}Sr_{0.4}Co_{0.2}Fe_{0.8}O_{3-\delta}$. Overlaying the data is a solid line representing the Le Bail refinement. Starting parameters for the fit were also taken from Itoh and

Table 6: Crystallographic data presented by Itoh and Nakayama [1] and experimentally calculated from the Le Bail refinement.

Parameter	**Itoh and Nakayama**	**This work**
Space Group	$R\bar{3}c$	$R\bar{3}c$
a = b (Å)	5.529	5.484
c (Å)	3.5248	3.4869
$\alpha = \beta$	90°	90°
γ	120°	120°
Unit Cell Volume ($Å^3$)	358.1	351.3
Theoretical Density (g/cm^3)	6.20	6.32

Nakayama and are shown in Table 6. As can be seen by a residual plot below the spectra there is good agreement between the fit and experimental data, therefore the calculated lattice parameters for the as-received powder, shown in Table 6, are reliable. The powder used in this work compares closely to the literature data.

Over the course of this work the LSCF powder was stored in a sealed container at room temperature in an ambient air environment. After two years the powder was re-analysed to ensure the material had not changed. A comparison of the powder diffraction patterns between the as-received and two year old powder is shown in Figure 41. The patterns display the same primary reflection peaks, suggesting that the powder did not undergo any alterations during storage. Differences in background and peak intensity may be attributed to the use of different equipment for each scan.

5.1.1.1 *High Temperature X-ray Diffraction*

In order to understand experimental results taken at high temperature it was necessary to understand if the material underwent crystallographic transformations. Tai et al. [2] showed that $La_{0.6}Sr_{0.4}Co_{0.2}Fe_{0.8}O_{3-\delta}$ displays a rhombohedral structure from room temperature to 600 °C, however, there is a lack of data above this temperature in the literature. Figure 42 shows the diffraction patterns collected at room temperature (before and after heating), 600 and 1000 °C. The patterns have been offset to allow comparison. As the samples were heated the patterns begin to shift to the left. This decrease in the Bragg diffraction angle is due to thermal expansion of the lattice spacing (d), however, as can be seen from the spectra as a

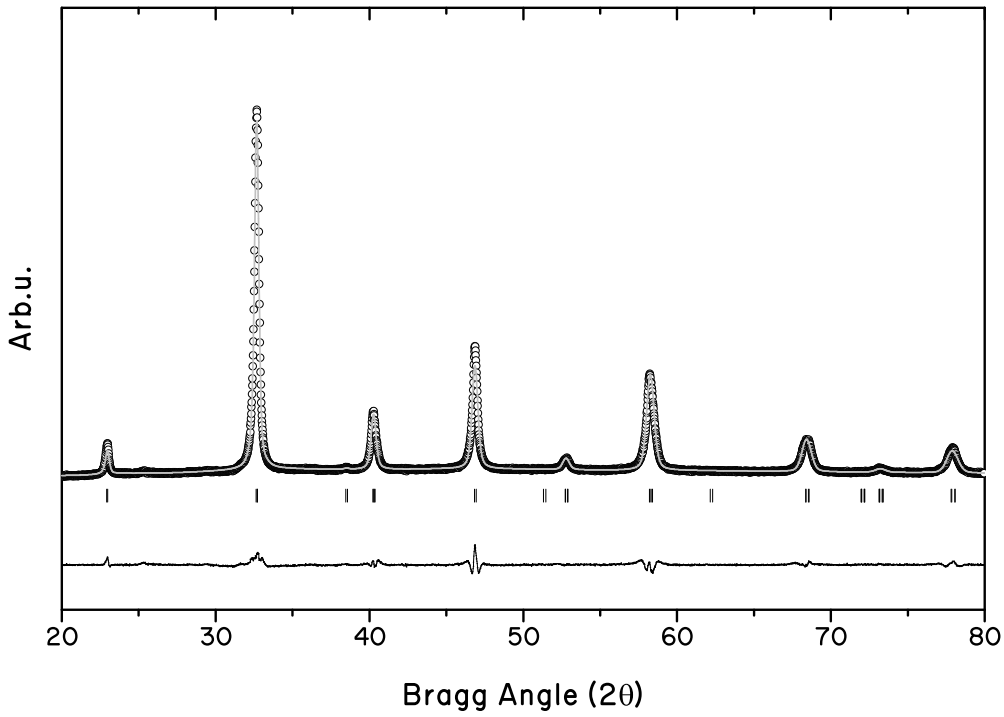


Figure 40: Showing the observed powder x-ray diffraction pattern for the as-received LSCF, the associated Le Bail fit and residual showing the difference between the two data sets.

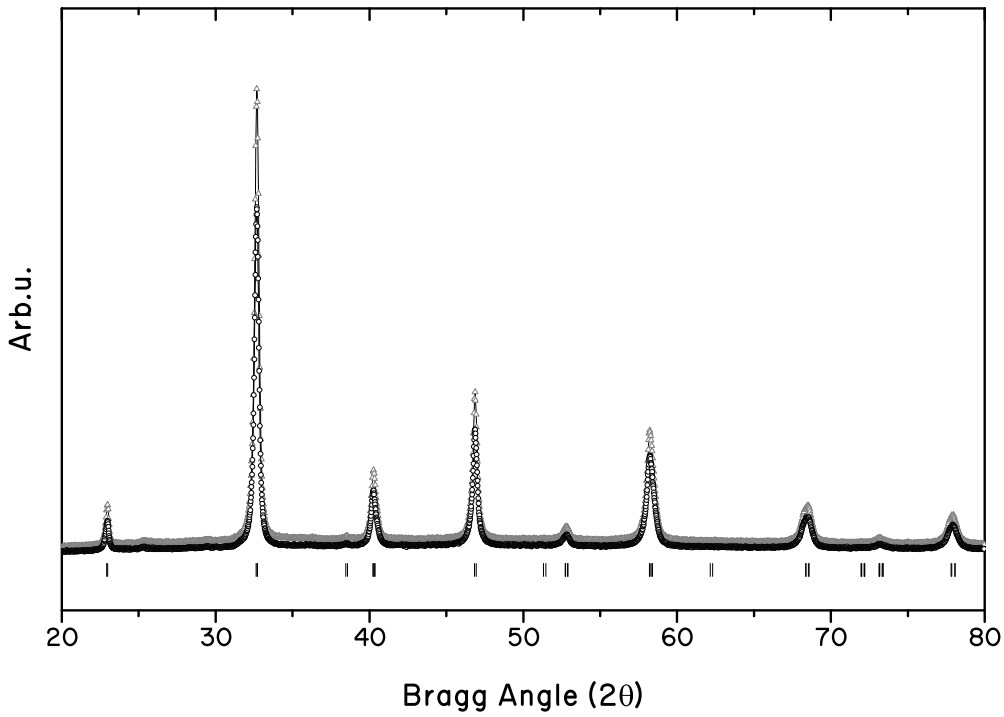


Figure 41: Comparison of diffraction patterns for the as-received powder and after two years of storage.

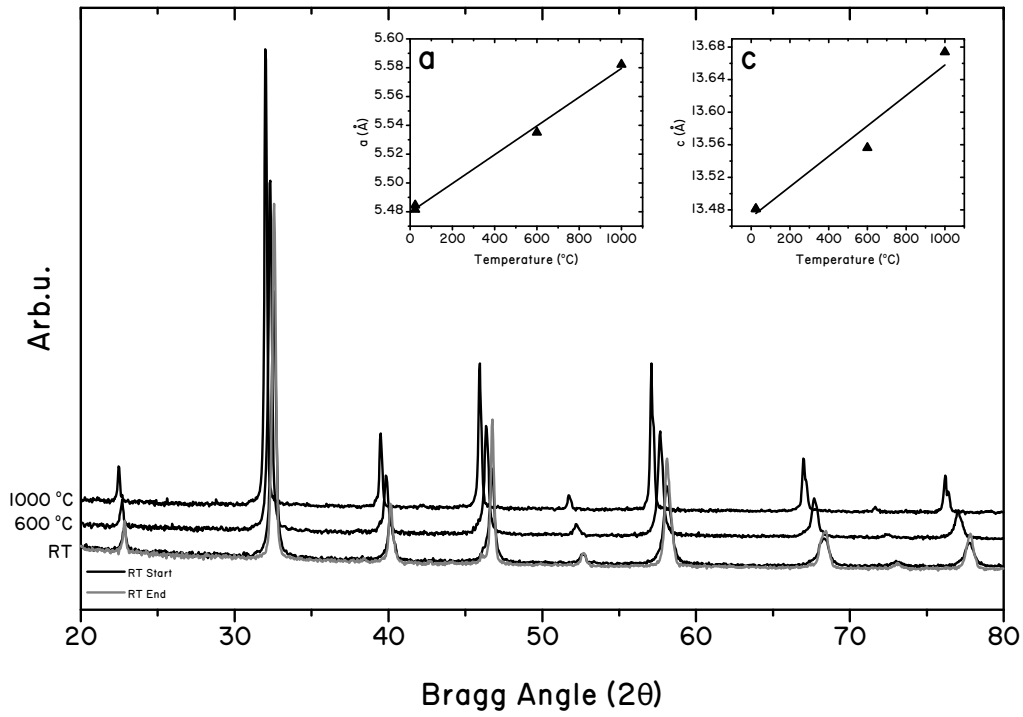


Figure 42: Showing the diffraction pattern taken at room temperature before heat treatment, at 600°C, 1000°C and after cooling back to room temperature. The inset shows the lattice parameter change during heating.

whole the primary reflections have not changed. Each pattern was also fit using a Le Bail refinement to calculate the magnitude of the observed lattice expansion. The inset of Figure 42 shows that the lattice parameters increased linearly with respect to temperature, but also relaxed back to the same value upon cooling. The total expansion was seen to be approximately 2% in both the *a/b* and *c* directions.

It is therefore clear that $La_{0.6}Sr_{0.4}Co_{0.2}Fe_{0.8}O_{3-\delta}$ does not undergo a bulk phase transformation when heated to 1000°C. However, if a comparison is made between the spectra taken before and after heating, small differences in peak width and intensity may be observed. Peak narrowing is generally indicative of an increase in crystallite size or material strain [3] and greater peak intensity is indicative of increased crystallinity. It is therefore probable that the powder underwent a small degree of sintering during the analysis. As discussed in Chapter 2 the surface of LSCF is not stable, therefore, observed changes in spectra may also be influenced by these transient effects. However, the penetration depth of x-rays in a standard XRD experiment is on the order of tens of microns [4], well above the reported surface feature size [5]. Grazing-Angle XRD may be used to increase

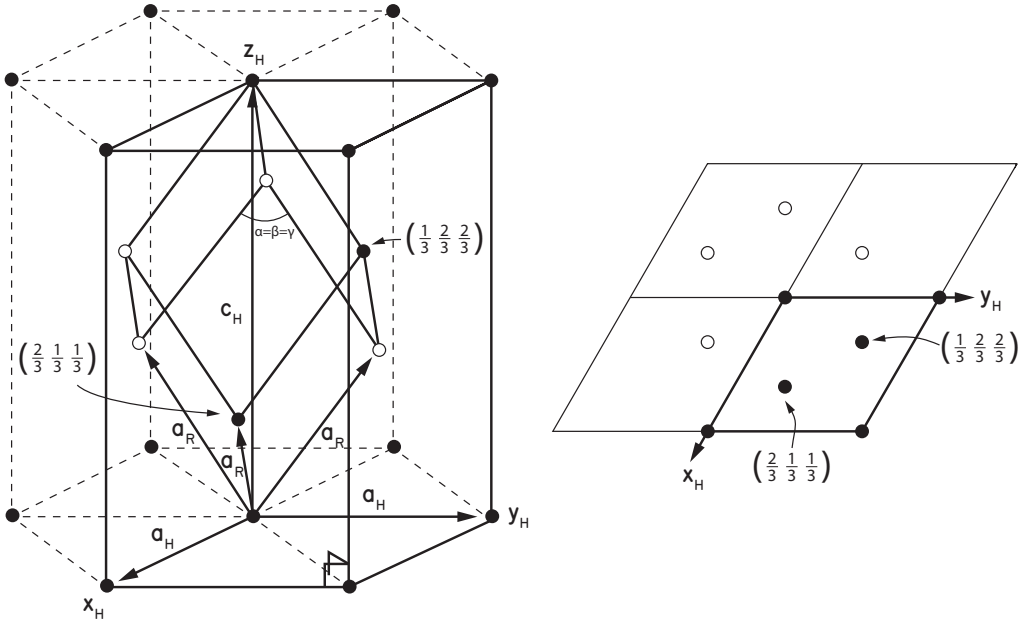


Figure 43: Representation of a Trigonal, or rhombohedrally-centred hexagonal, unit cell.

the depth resolution of the technique to the nanometer scale [6], however, in this work alternative techniques with greater lateral resolution were utilised.

5.1.1.2 *Theoretical Density*

In order to calculate the density of sintered samples the theoretical density of the material must be known. $La_{0.6}Sr_{0.4}Co_{0.2}Fe_{0.8}O_{3-\delta}$ has a rhombohedral primitive unit cell, however, it is common to represent the Bravais lattice as a Trigonal, or rhombohedrally-centred hexagonal cell, due to the symmetry of the system [7]. This is shown schematically in Figure 43. In a rhombohedral unit cell the lattice parameters are related as follows: $a = b = c$ and $\alpha = \beta = \gamma$, however, as a hexagonal system the unit cell is now defined by $a = b$, c and $\alpha = \beta = 90°$, $\gamma = 120°$. It also follows that the cell volume and number of atoms will be greater than that of the primitive unit cell. For a detailed description of the rhombohedral to hexagonal conversion please refer to: [8]. For the case of $La_{0.6}Sr_{0.4}Co_{0.2}Fe_{0.8}O_{3-\delta}$ there are 6 repetitions of the primitive rhombohedral cell contained within hexagonal unit cell [1]. Table 6 details the lattice parameters calculated from the Le Bail refinement and therefore, using Equation 3.3, the theoretical density of the as-received LSCF powder was calculated to be 6.32 g/cm^3. This shows strong agreement with the literature value.

Samples sintered throughout this work were measured using the Archimedes principle. The principle measures the weight of a sample in air and water. The buoyancy force that water exerts upon the sample accounts for difference in measured weight. The technique assumes that samples are fully dense and that the surface is fully wetted by the water. However, LSCF pellets are likely to contain a degree of closed porosity and/or small pores at the surface that may prevent wetting due to surface tension effects. The air trapped within these pores will not be replaced by the water and will artificially increase the buoyancy force, consequently reducing the measured weight of the sample. To aid in wetting the surface samples were placed in boiling water to increase the flow rate of the water, however, closed porosity could not be corrected for.

To ensure closed porosity was not causing significant errors, density measurements using the Archimedes principle were compared to simple geometric density measurements[1]. The discrepancy between the two density measurements was on average 1 - 2%, thus it is believed that effect of closed porosity was negligible. Samples fabricated using the regime described in Section 3.2 consistently exhibited a relative density between 95 - 97%. For the remainder of this work it may be assumed that sintered samples were sufficiently dense.

5.2 INDUCTIVELY COUPLED PLASMA ATOMIC EMISSION SPECTROSCOPY

The results from XRD have showed that the sample is single phase $La_{0.6}Sr_{0.4}$-$Co_{0.2}Fe_{0.8}O_{3-\delta}$, however, they do not indicate the stoichiometry of the material. In order to determine the stoichiometry ICP-AES was used. The ICP-AES technique requires experimental comparison to accurate standards in order to quantify the elemental composition. The linear relationship between photon emission and concentration for each element is shown in Figure 44. In this work experimental standards for lanthanum, cobalt and iron were produced using Sigma-Aldrich ICP single element standard solutions [9]. These elements were diluted in nitric acid to 1, 5, 10 and 20 ppm using weight measurements. A strontium ICP standard solutions was not available and as such was produced manually by diluting solid $SrCO_3$ in nitric acid. Weight measurements were again used to produce dilute the solutions, however, the quantity of $SrCO_3$ required was close to the mass

1 The sample dimensions were measured using a Vernier calliper to measure the volume. Density could then be measured from the measured mass. This technique is not preferred as it assumes a perfect sample geometry, ignoring surface roughness.

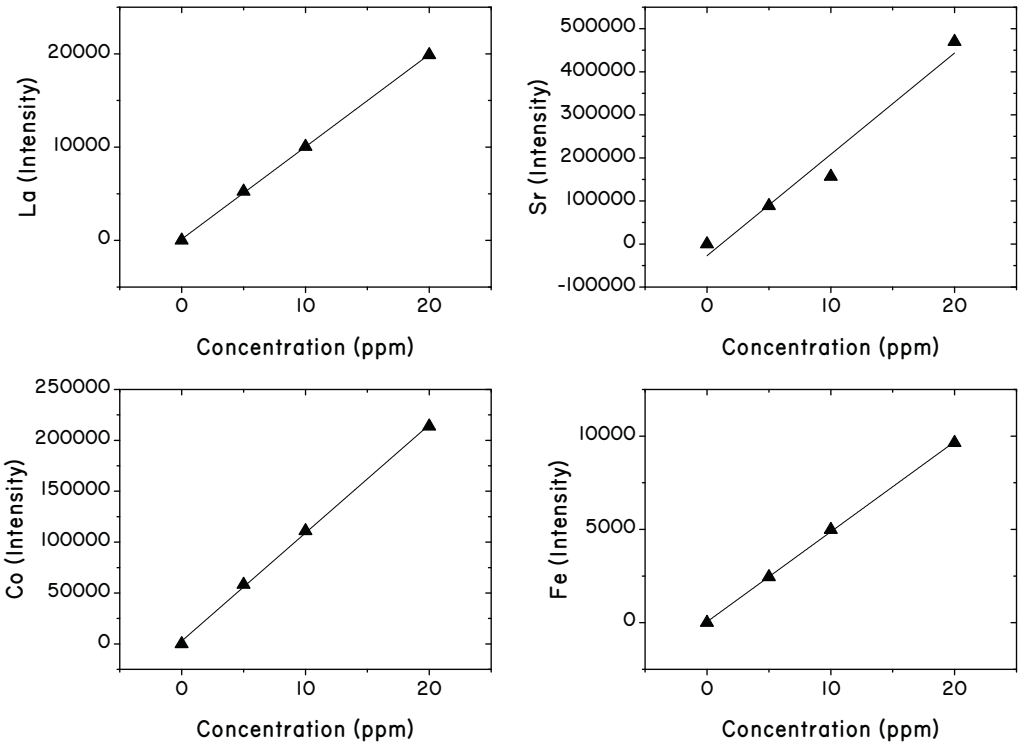


Figure 44: ICP experimental standard results showing the linear relationship of photon intensity against concentration.

Table 7: A comparison between the theoretical and experimentally calculated cation stoichiometry.

Method	**La**	**Sr**	**Co**	**Fe**
Theoretical	60	40	20	80
ICP-AES	57.4	42.6	15.9	84.1

resolution limit of the balance. As can be seen in Figure 44 the Sr standard contains a small degree of error due to the difficulty of weight measurement. Despite this, the calculated stoichiometry shows good agreement to the theoretical values as shown in Table 7.

5.3 INITIAL SURFACE CHARACTERISATION

As described in Section 4.2.1 the IEDP technique enables measurement of the surface exchange coefficient and self-diffusivity of an oxide material. Prior to recent work on the surface evolution of perovskite materials, much of the diffusion data

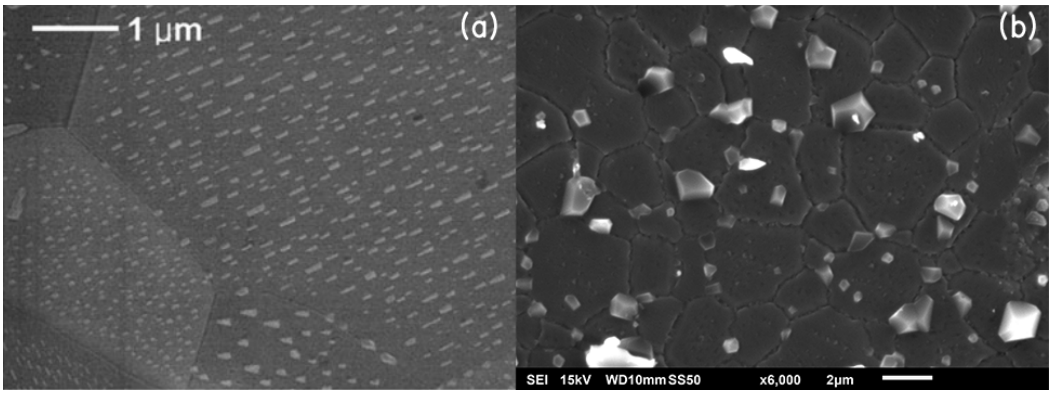


Figure 45: Secondary electron SEM image of (a) polished LSCF surface annealed in 'stagnant air' at 900°C for 50 hours [5] and (b) the LSCF surface after an initial exchange experiment showing secondary phase particle growth and thermal etching of the surface.

measured using IEDP contained an additional high temperature anneal before the standard exchange procedure described in Section 4.2.1. It was shown that mechanical damage induced by polishing enhanced self-diffusivity and surface exchange properties in single crystal Al_2O_3 [10], so it was assumed this was also true for perovskite MEICs. Therefore, a 1000°C thermal anneal was commonly performed in order to remove sub-surface mechanical strain (refer back to Figure 30). It was assumed that the anneal renewed the surface and sub-surface to a low energy 'standard' state. Initial exchanges performed in this work employed the use of this 'damage reducing' 1000°C anneal as the effect upon the LSCF surface was not yet well documented at the beginning of this work. As discussed in Chapter 2 more recent research has been performed on perovskite material surface properties and it is been widely reported that A site dopant segregation occurs in many potential MEIC materials. Therefore, after the initial experiments detailed in this section, the high temperature anneal was no longer performed.

In late 2012[2] Oh et al. [5] first reported that $La_{0.6}Sr_{0.4}Co_{0.2}Fe_{0.8}O_{3-\delta}$ forms submicron secondary phase particles during high temperature thermal anneals in oxygen containing environments. Figure 45(a) shows a representative SEM micrograph of what they observed from a sample annealed at 900°C for 50 hours. Small crystallographic Sr containing secondary phase particles may be seen to be periodically coating the surface. These particles appear to form in the centre of the grain, with minor growth on the grain boundaries (or other long order defects at the surface). Figure 45(b) shows secondary electron SEM images of the LSCF

2 Coinciding with the beginning of this work

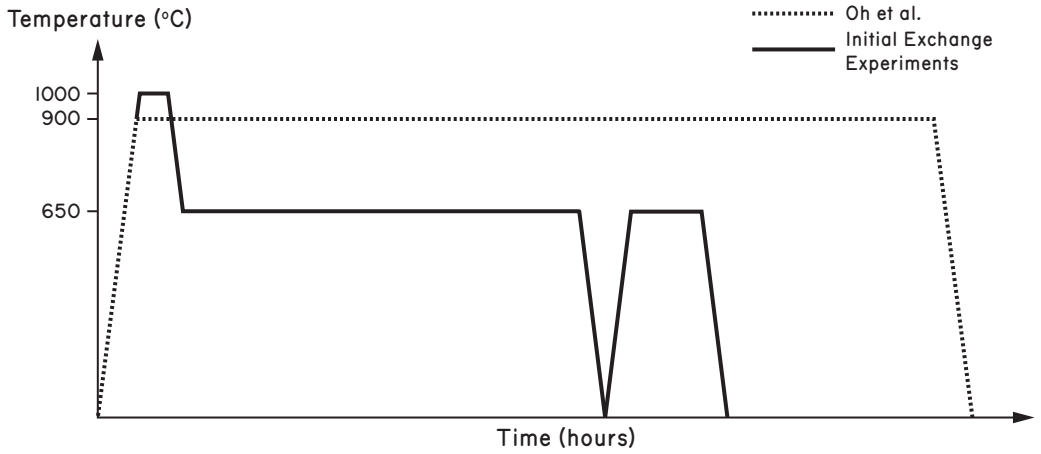


Figure 46: Schematic temperature-time profiles representing Oh et al. [5] and initial exchange experiments carried out in this work.

surface after initial isotopic exchange experiments that included the 'damage reducing' anneal step. Large, crystallographic secondary phase formation is very apparent, rather than small particles periodically coating the surface. A high proportion of the particles appear to have grown on the grain boundaries, however, some appear to remain in the centre of the grain.

The primary differences between each experiment were the anneal temperature, total anneal time and anneal atmosphere. Schematic representations of temperature-time profiles are shown in Figure 46. Oh et al. annealed polished and freshly sintered samples isothermally at 900°C for 50-100 hours using 'stagnant air', N_2 and N_2/0.1% O_2. Whereas, in this work, initial exchange experiments performed were annealed using research grade 99.999% pure oxygen. Polished samples were first annealed at 1000 °C for 1 hour prior to performing the standard exchange regime. The total anneal time was dependent upon the exchange temperature but was in the range of 24-36 hours. Comparison of this data suggests that all three parameters (temperature, time and atmosphere) influence the nature of secondary phase growth, however, cannot be decoupled from this alone.

The effect of the particles on the exchange properties of the material were tested using FIB-SIMS. Due to the long pre-anneal step particles are likely to exist prior to the exchange in ^{18}O, therefore, it was possible to assess the exchange properties of the particles using the high spatial resolution of the FIB-SIMS. Figure 47 shows FIB-SIMS elemental maps collected on a sample exposed to a standard IEDP experiment. Figure 47(a) shows an elemental map of ^{16}O and Figure 47(b) shows

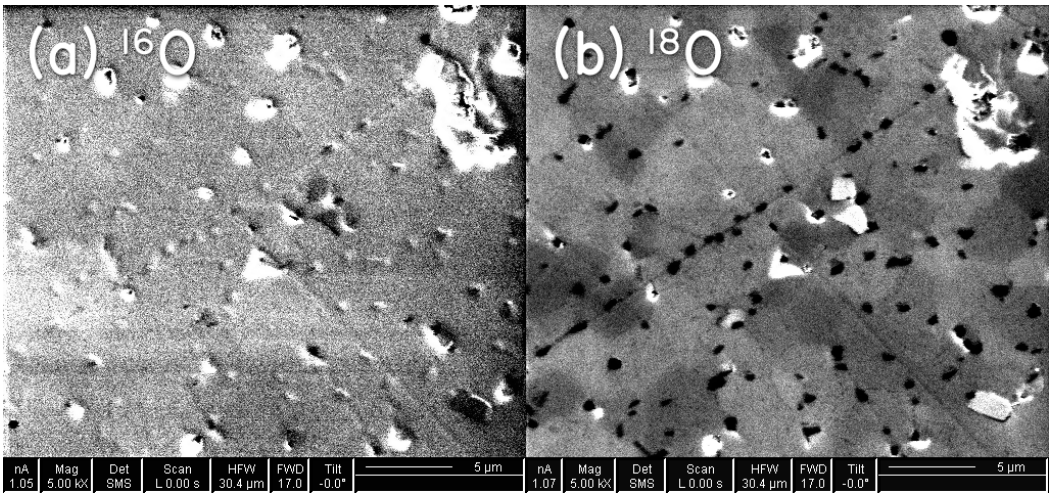


Figure 47: FIB-SIMS elemental maps for (a) ^{16}O and (b) ^{18}O showing that strontium-based particles prevent the oxygen exchange reaction from occurring directly underneath them. It should be noted that the ^{16}O map was collected *after* the ^{18}O map. As this is a quadrupole system, the particles were likely removed during collection of the ^{18}O map and thus do not appear strongly on the ^{16}O image.

an elemental map of ^{18}O. As can be seen, an assortment of black 'dots' may be seen in the ^{18}O image indicating a deficiency of this isotope. The dots appear to pattern grain boundaries and scratches induced by polishing, therefore, it is sensible to assume that they are strontium-based particles grown during ^{16}O pre-anneal step[3]. This result clearly shows that the particles completely block the oxygen reduction reaction and surface exchange process.

In addition to initial IEDP experiments, polished samples were annealed in ambient air at 900°C for 50 hours in a box furnace, as shown in Figure 48. Sub-micron particles that may be seen on the micrograph appear to be distributed randomly across the surface and do not display consistent crystallographic features. Therefore, these particles are not secondary phase growth but are contaminants from the environment. It can also be seen that there is a roughening effect upon the surface, the degree of which differs from grain to grain, suggesting a crystallographic orientation effect upon the surface evolution of LSCF.

The results of this experiment appear to differ from Oh et al. due to the use of 'stagnant' and 'ambient' air. Stagnant air suggests a static environment using compressed synthetic air, whereas, ambient air implies a flowing gas environ-

3 The FIB-SIMS is equipment with a quadrupole detector. Due to the size of the particles, after one round of collection, the particles had been sputtered away. It was not possible to analysed the same area, however, an additional analysis in positive mode confirmed the surface was covered in strontium-based particles.

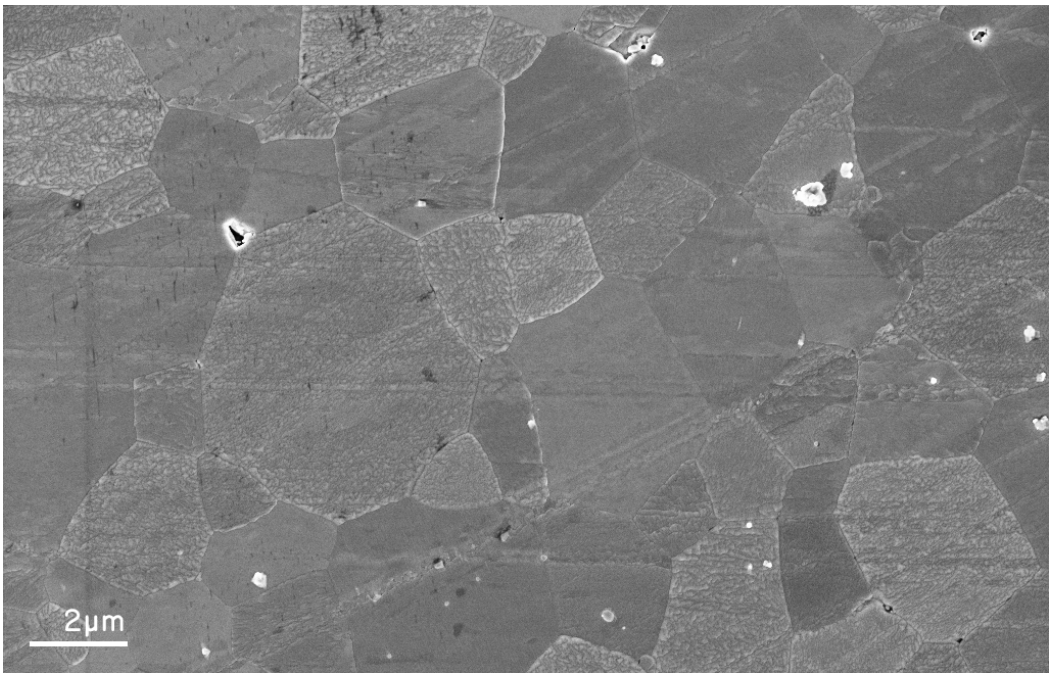


Figure 48: Showing an SEM micrograph of the LSCF after a 50 hour anneal in ambient air.

ment using air from the atmosphere. Synthetic air is commonly dried to prevent the condensation of water within the gas cylinder, therefore the relative humidity of synthetic air is typically much lower than ambient air. As discussed in Chapter 2 water has a notable effect upon the exchange properties of LSCF, thus it follows that the surface will react with the H_2O molecule differently than pure oxygen.

5.4 CONCLUSION

Powder characterisation experiments have proven that the LSCF powder used throughout this work is single phase $La_{0.6}Sr_{0.4}Co_{0.2}Fe_{0.8}O_{3-\delta}$. Additionally HT-XRD confirmed that LSCF remains as a rhombohedral structure up to 1000°C. Experiments performed at the beginning of this work have shown that LSCF surfaces react very different under the influence of anneal temperature, anneal time and anneal atmosphere. The initial experiments detailed here were not systematic studies and as such the effect of each parameter was not able to be decoupled. However, these initial observations provided the hypothesis to plan the experiments presented in Chapters 6-9.

BIBLIOGRAPHY

[1] Takanori Itoh and Masanobu Nakayama. Using in situ X-ray absorption spectroscopy to study the local structure and oxygen ion conduction mechanism in (La0.6Sr0.4)(Co0.2Fe0.8)O3-d. *Journal of Solid State Chemistry*, 192: 38–46, 2012. ISSN 00224596. doi: 10.1016/j.jssc.2012.03.021. URL http://dx.doi.org/10.1016/j.jssc.2012.03.021.

[2] L.-W. Tai, M M Nasrallah, H U Anderson, D M Sparlin, and S R Sehlin. Structure and electrical properties of La1-xSrxCo1-yFeyO3. Part 2. The system La1-xSrxCo0.2Fe0.8O3. *Solid State Ionics*, 76(3–4):273–283, mar 1995. ISSN 0167-2738. doi: http://dx.doi.org/10.1016/0167-2738(94)00245-N. URL http://www.sciencedirect.com/science/article/pii/016727389400245N.

[3] Yoshio Waseda, Eiichiro Matsubara, and Kozo Shinoda. *X-Ray Diffraction Crystallography*. Springer Berlin Heidelberg, Berlin, Heidelberg, 2011. ISBN 978-3-642-16634-1. doi: 10.1007/978-3-642-16635-8. URL http://link.springer.com/10.1007/978-3-642-16635-8.

[4] H. Stanjek and W. Häusler. Basics of X-ray diffraction. *Hyperfine Interactions*, 154(1-4):107–119, 2004. ISSN 03043843. doi: 10.1023/B:HYPE.0000032028.60546.38. URL http://dx.doi.org/10.1023/B:HYPE.0000032028.60546.38.

[5] Dongjo Oh, Danijel Gostovic, and Eric D. Wachsman. Mechanism of La0.6Sr0.4Co0.2Fe0.8O3 cathode degradation. *Journal of Materials Research*, 27(15):1992–1999, jul 2012. ISSN 0884-2914. doi: 10.1557/jmr.2012.222. URL http://www.journals.cambridge.org/abstract{_}S0884291412002221.

[6] B.A. van Brussel and J.Th.M. De Hosson. Glancing angle x-ray diffraction: A different approach. *Applied Physics Letters*, 64(12):1585–1587, 1994. ISSN 00036951. doi: 10.1063/1.111847.

[7] Neil Ashcroft and David Mermin. *Solid State physics*. Elsevier, 1st edition, 1976. ISBN ISBN 0-03-083993-9.

[8] MIchael O'Keeffe and Bruce Hyde. *Crystal Structures: Patterns and Symmetry*. 1996. ISBN 0-939950-40-5.

[9] SigmaAldrich. Sigma-Aldrich ICP Standards, 2016. URL http://www.sigmaaldrich.com/analytical-chromatography/analytical-products.html?TablePage=18823644.

[10] DAVID J. Reed and B. J. Wuensch. Ion-Probe Measurement of Oxygen Self-Diffusion in Single-Crystal Al2O3. *Journal of the American Ceramic Society*, 63 (1-2):88–92, jan 1980. ISSN 0002-7820. doi: 10.1111/j.1151-2916.1980.tb10655.x. URL http://doi.wiley.com/10.1111/j.1151-2916.1980.tb10655.x.

6

SURFACE EVOLUTION AND DEGRADATION IN HUMID ATMOSPHERES

In this chapter the investigation into the influence of high temperature thermal anneals in ambient air is presented. *In-situ* HT-ESEM experiments were performed in atmospheres of pure O_2, pure H_2O ambient air and a high vacuum. Secondary electron images at high magnification were collected during the heating phase (and isotherm) to directly observe microstructural modifications induced by the anneal regime. Backscattered images were collected post-anneal and correlated with AES elemental maps to characterise the chemical nature of any observed degradation features. LEIS surface spectra were collected to quantify cation ratios of the outermost atomic layer and LEIS depth profiles were performed to study changes occurring at the sub surface.

6.1 HIGH-TEMPERATURE ENVIRONMENTAL SEM

As has been discussed and demonstrated in the previous chapter, $La_{0.6}Sr_{0.4}Co_{0.2}Fe_{0.8}O_{3-\delta}$ surfaces are influenced by different species within the atmosphere, however, the growth of secondary phases on the surface had not yet been observed *in-situ*. Prior to this work HT-ESEM had never been used to observe SOFC cathode materials, therefore initial experiments were performed to test the suitability of the technique. Initial experiments directly observed the growth of secondary phases particles in response to a pure oxygen environment. After successful initial results, further experiments were performed to study the response of the LSCF surface in different gas environments. Full details of the technique may be referred to in Section 4.1.1, however, for convenience, a reminder of the experimental regime will be given: samples were annealed from room temperature (RT) to 1000°C at a heating rate 300°C/hr under 3 mbar of pure O_2, pure H_2O, ambient

Table 8: Temperature conversion table for HT-ESEM videos. Values in brackets represent the set temperature (seen on the HT-ESEM micrographs) when the actual temperature was 1000 °C.

Set Temperature (°C)	Actual Temperature (°C)			
	O_2	H_2O	Ambient Air	Vacuum
100	70	143	-	-
200	260	310	320	327
300	440	422	447	416
400	599	537	573	511
500	744	647	684	626
600	890	754	793	774
700	(679) 1000	860	900	877
800	-	962	1000	960
900	-	(828) 1000	-	(877) 1000

air and a 10^{-6} mbar vacuum. It should be noted that videos associated with the data sets presented in this thesis are provided as supplementary material. They will be referred to as 'Video X' in the text and correspond to a video file with the same file name[1]. As discussed previously, the thermocouple used to measure the stage temperature was independent of the HT-ESEM software, thus Table 8 must be used to correlate the set temperature (that seen on the HT-ESEM micrographs) to the actual temperature of the stage. Image analysis was performed using 'ImageJ' [1] and details of the functions are discussed in Section 6.1.5.

6.1.1 *Pure O_2*

Initial 'proof of concept' experiments were performed in pure oxygen to ensure the HT-ESEM technique could provide the desired data. Direct observation of SrO-based secondary phase formation was observed. EDX analysis confirmed that these particles contained strontium, however, the chemical sensitivity of technique was insufficient to determine if the particles were the oxide, hydroxide or carbonate. Evidence in the literature suggests that in the presence of only pure oxygen the SrO phase will form. Therefore, this assumption was made. Video 6.1

1 Also included is the portable executable file 'VLCPortable.exe'. This may be found in 'SupplementaryMaterial/VLC/VLCportable.exe' and used to open the video files if the computer in question is incapable.

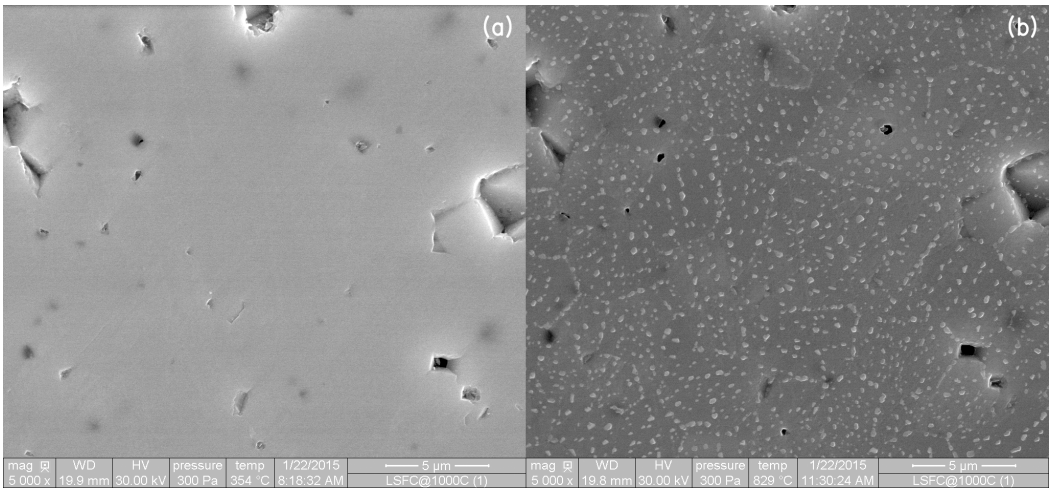


Figure 49: Showing (a) the surface prior to any noticeable surface modification and (b) the final image collected showing secondary phase precipitation after the anneal in pure oxygen.

represents an LSCF sample annealed under 3 mbar pure O_2 at 5000x magnification. Video 6.2 is the same experiment taken with a magnification of 10000x. For a quick reference, Figure 49 shows micrographs of the surface prior to any noticeable surface modification and at the end of the experiment. Figure 50 shows the particle growth and percent particle coverage with respect to time. Similar to Oh *et al.* [2] crystallographic particle growth occurs in the centre of the grains, however, in this work much of growth also appears on the grain boundaries.

From room temperature to approximately 550°C the surface appears to remain stable. Slightly above 550°C a small amount of particle growth can be seen on 'triple point' (between three grains) grain boundaries. These particles grow for approximately 15 minutes during heating from 550-650°C before appearing to dissolve or evaporate. It is assumed these particles are strontium based, however, experimentation was not stopped to confirm this. As shown in Figure 51 a 'ring' (characterised by a change in contrast) may be seen growing from the centre of the primary cluster of particles. It is difficult to establish the nature of this contrast change due to resolution limits of the HT-ESEM. Two possible explanations are: (i) particles smaller than the spot size of the beam are growing or (ii) sub-surface reconstruction is causing channelling of the electron beam. Previous work has suggested that the segregation of strontium in perovskite materials causes the sub-surface to reconstruct into the Ruddlesden-Popper phase [3]. This phase has an anisotropic crystal structure that could account for channelling contrast, however, as the sample is heated further it is observed that the 'ring' disappears

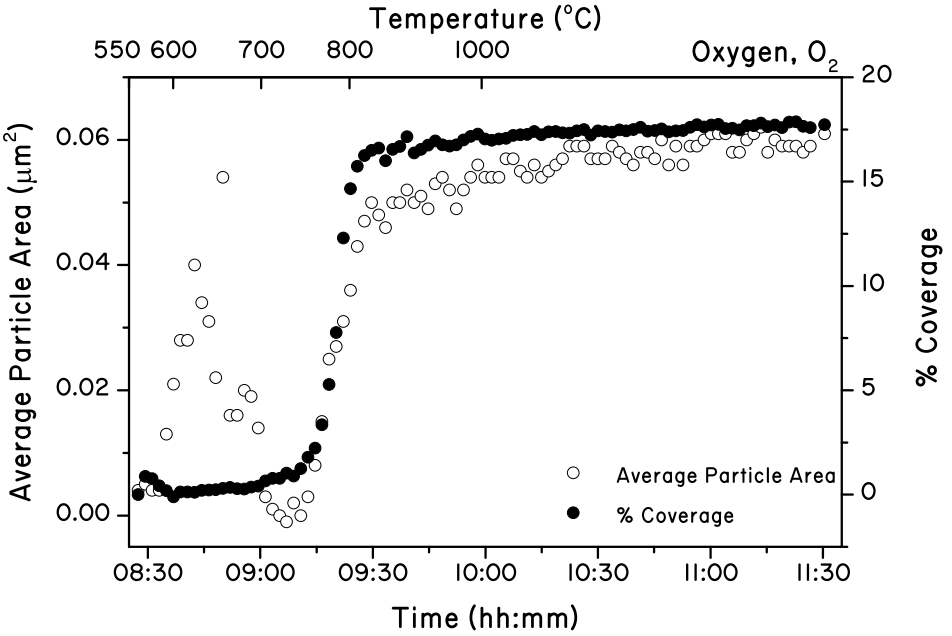


Figure 50: Showing average particle area and percent coverage with respect to time and temperature for an initial sample annealed in pure oxygen.

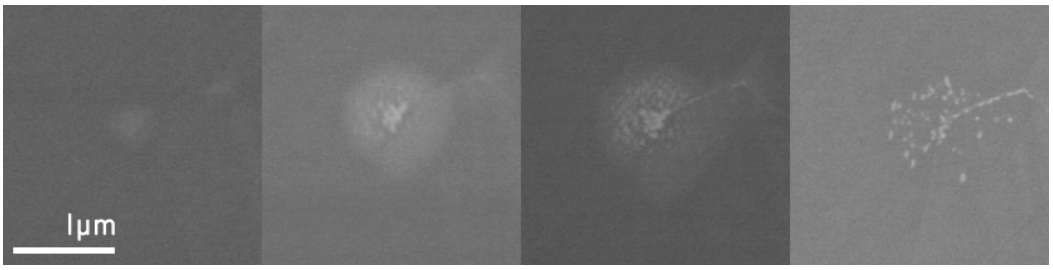


Figure 51: Showing the initial growth in pure oxygen between 550-650°C.

and the material surface appears homogenous once again. It is possible that continued strontium segregation at an elevated temperature may have enabled the sub-surface to revert back to a simple perovskite, however, without further analysis of the sub-surface using a technique sensitive to crystallography at the atomic scale (i.e. TEM) this cannot be confirmed. Small particles may be seen growing around the primary particle cluster at the triple point. They appear to decrease in size as a function of distance from the primary precipitate. The growth of the 'ring' could therefore be attributed to un-resolved (out of focus) particles smaller than the beam spot size. The subsequent reduction in 'ring' size would therefore most likely be explained by heterogeneous particle agglomeration (Ostwald ripening [4]) due to further increases in temperature. Unfortunately, the origin of this observation could not be established in this work.

Immediately after this initial behaviour, thermal etching of the grain boundaries may be observed, followed by the onset of wide spread particle growth at ~725°C. Growth is rapid for 30 minutes between 725-800°C before the particles appear to stabilise in size and quantity. Growth after 800°C is slow, but increasing at a constant rate. This is interesting as strontium segregation (or diffusion of strontium) is an activated process, thus occurs at a rate at higher temperatures. Therefore, you would not expect a reduction in growth rate. As particle size was measured by image analysis, values are only the 2D projection of a 3D particle[2]. It does not take into account particle growth out of the image plane and as such three-dimensional agglomeration may explain the change in growth rate. The result suggests that the surface transport of strontium is the dominant mechanism facilitating particle growth as, if either the gas phase or bulk diffusion was the main strontium source, then a constant growth rate should have been observed.

As strontium is leaving the surfce to form Sr-based particles it is likely that the near-surface is strontium (or more specficially, A-site) deficient. Due to a drop in measured ASR it has been suggested by Hansen *et al.* that heavily A-site deficienct LSCF ($(La_{0.6}Sr_{0.4})_{0.85}Co_{0.2}Fe_{0.8}O_{3-\delta}$) results in a reduction of strontium segregation [5]. To retain charge neutrality A-site deficiency will be compensated by the formation of oxygen vacancies (Equation 6.1) and, in the presence of an oxygen partial pressure, oxygen incorporation will also cause the disproportionation of the B atoms by generating holes (Equation 6.2). It has been shown [6, 7] that A-site deficiency alters the crystal structure, electronic and ionic conductivity, however, the thermodynamic stability of these phases have not been fully investigated. It may be speculated that, as a result of strontium segregation, the immediate and near surface is in a more stable A-site deficient state. Therefore, there would be a reduction in the formation of strontium-based particles and thus the observed reduction in particle growth rate.

$$\text{A-site Deficiency} : Sr'_{La} + O^{\times}_{O} \leftrightarrow V'''_{La} + V^{\bullet\bullet}_{O} + SrO \tag{6.1}$$

$$\text{Oxygen Incorporation} : \frac{1}{2}O_2 + V^{\bullet\bullet}_{O} \leftrightarrow O^{\times}_{O} + 2h^{\bullet} \tag{6.2}$$

$$\text{Overall Reaction} : \frac{1}{2}O_2 + Sr'_{La} \leftrightarrow V'''_{La} + 2h^{\bullet} + SrO \tag{6.3}$$

2 For this reason growth rates have not been quantified. The data does, however, provide excellent comparative data for secondary phase surface coverage.

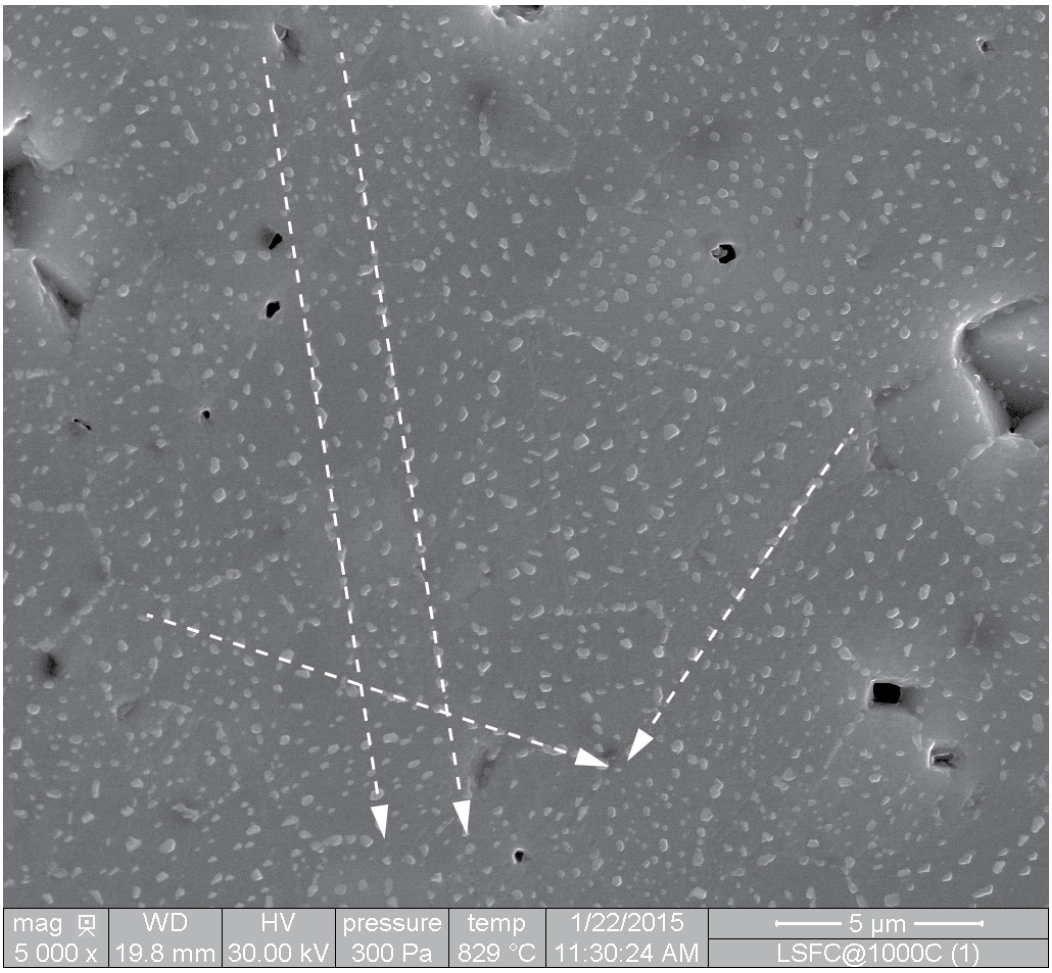


Figure 52: Showing directional trends of particle growth along polishing induced mechanical damage.

As shown in Figure 52 particles appear to grow along 'lines' that span across multiple grains. The lines are artefacts of the polishing process (hence their directionality), but may be more generally described as 'mechanical damage'. Below the surface it is probable that a dislocation network is produced, which may influence the localised segregation rate. There is still dispute over the effect of a strained lattice on the diffusivity of anions and cations [8], however, this result suggests that either there is enhanced segregation within the dislocation or that the damaged surface acts as a heterogeneous nucleation site for the particles. This will be discussed further throughout this chapter and the proceeding chapter.

6.1.2 *Pure H_2O*

Other than N_2 and O_2, water vapour is typically the most prevalent component of ambient air and as such was studied over other components such as CO_2 or impurities such as SO_2. Similar to observations in pure oxygen, secondary phase precipitation is seen, however, the rate and quantity of particle growth far exceeds that of pure oxygen. Video 6.3 represents an LSCF sample annealed under 3 mbar pure H_2O at 5000x magnification. Video 6.4 is the same experiment taken with a magnification of 10000x. For a quick reference, Figure 53 shows micrographs of the surface prior to any noticeable surface modification and at the end of the experiment. Figure 54 shows the particle growth and percent particle coverage with respect to time.

At approximately 850°C particles initially begin to form on the grain boundaries and soon after are seen to grow in the centre of the grains. Growth is rapid and over ten times the number of particles form as compared to the pure oxygen environment (see Figure 55). Above 950°C agglomeration of the particles may be clearly seen[3]. There appears to be no correlation between agglomeration and particle location (particles agglomerate in the centre of the grains and on the grain boundaries). During the 1000°C isotherm the particles continue to grow and there appears to be no halt to particle agglomeration. Although the experiment was stopped after the hour isotherm, it is reasonable to suggest that the surface coverage may reach 100% given enough time.

Figure 56 shows a micrograph at 950 °C where particle number is at a maximum (before agglomeration) where several grain patterning may be observed. Grain A shows homogenous particle distribution and growth across the grain surface, grains B and C show triangular shaped particles that appear to aligned along a particular direction, grain D shows rod shaped particles also aligned along a particular direction and grain E shows homogenous growth where the average particle size is larger than that of grain A. The shape of the particles observed in grains B - D suggests an epitaxial relationship with the underlying grain as SrO has a cubic structure. Rotated such that the (111) plane is parallel to the surface the particle would appear pyramidal (and thus triangluar to the HT-ESEM image). Figure 57 shows that the onset of particle growth rate in grains

3 A drop in % coverage is compensated for by an increase in particle size.

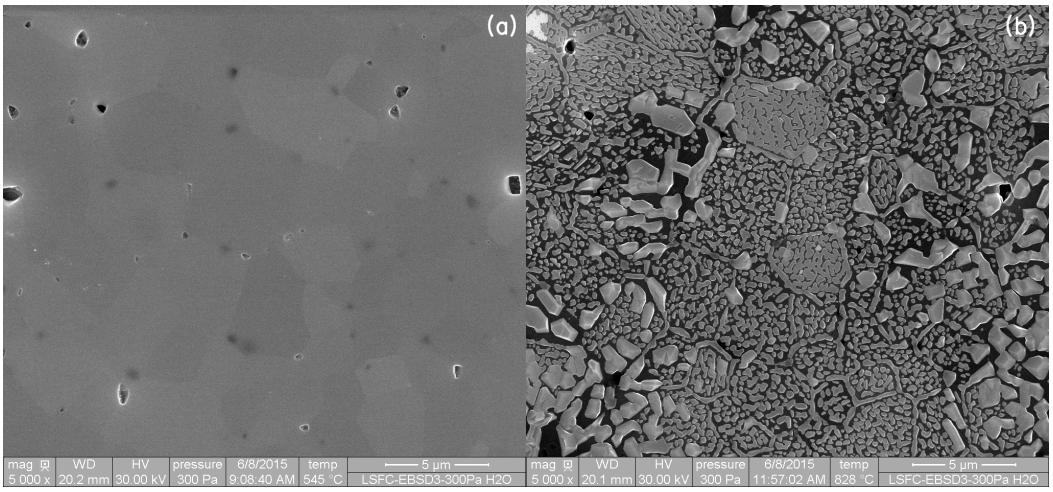


Figure 53: Showing (a) the surface prior to any noticeable surface modification and (b) the final image collected showing secondary phase precipitation after the anneal in pure water.

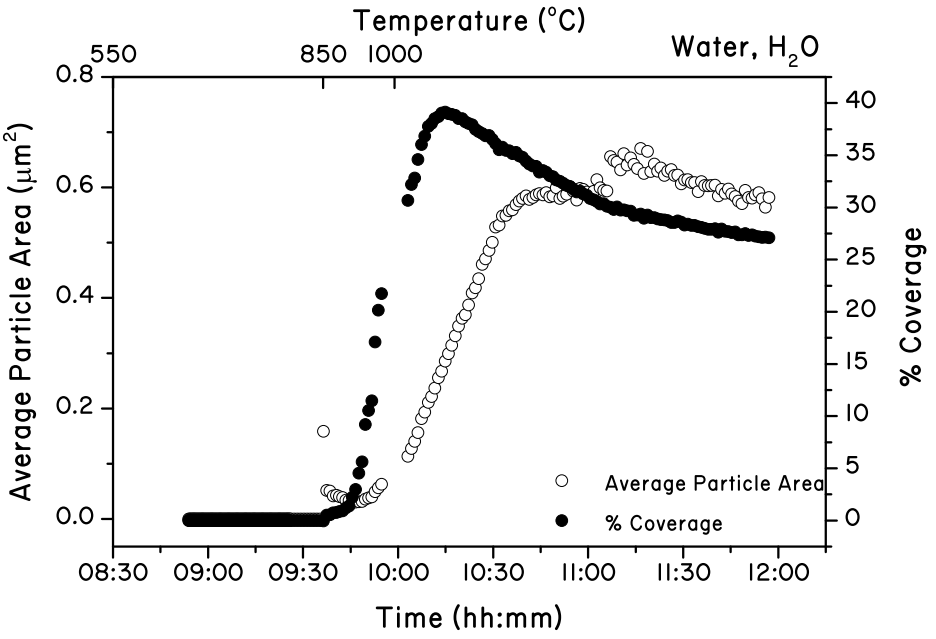


Figure 54: Showing average particle area and percent coverage with respect to time and temperature for a sample annealed in pure water.

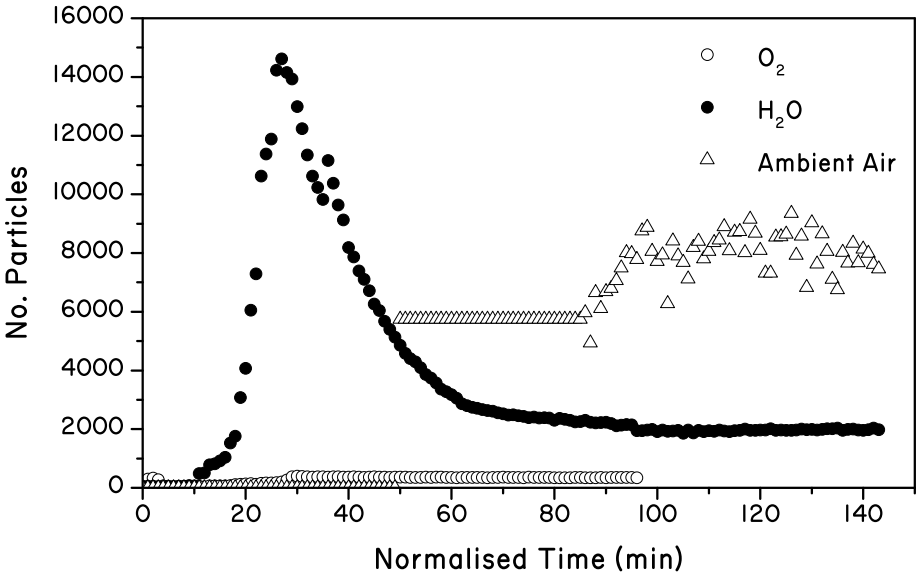


Figure 55: Comparing number of particles seen to grown in pure oxygen, pure water and ambient air as they were heated from RT-1000 °C.

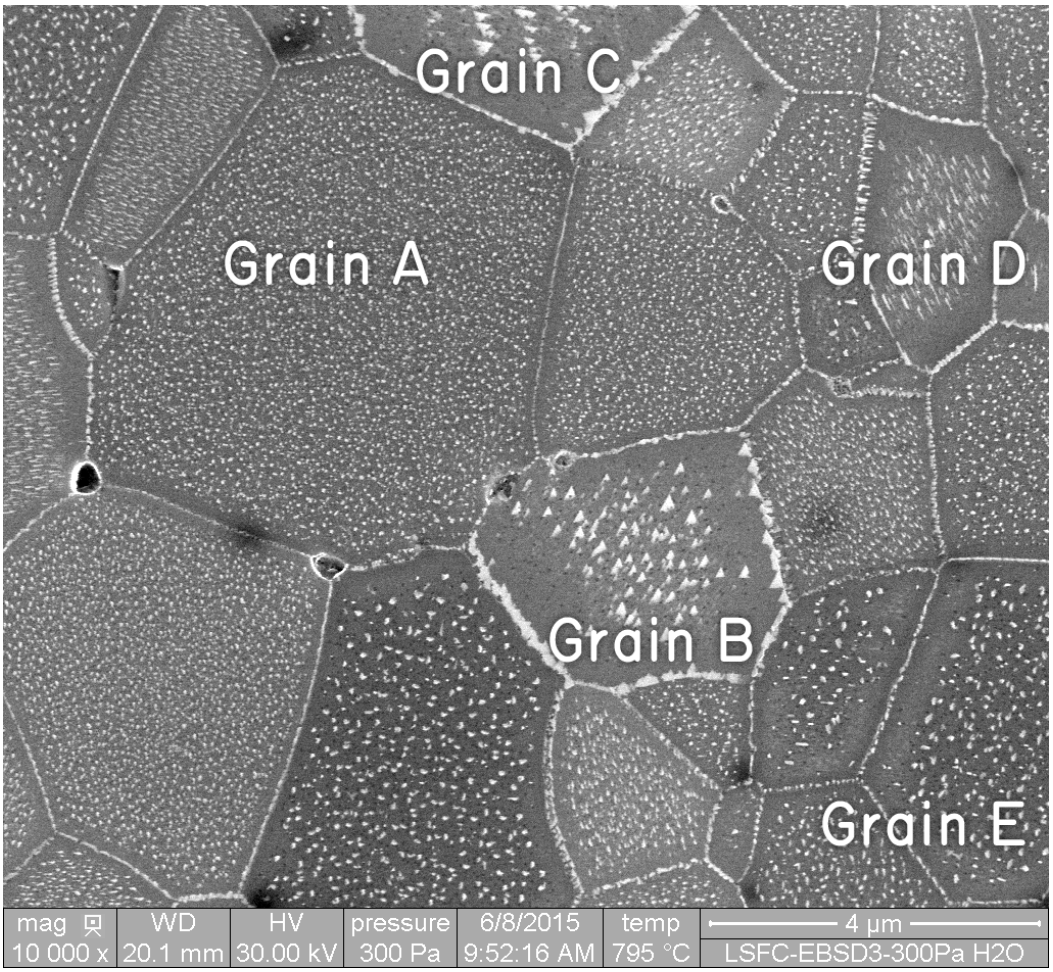


Figure 56: Showing a micrograph of LSCF heating in pure water where multiple grains show different particle growth patterns.

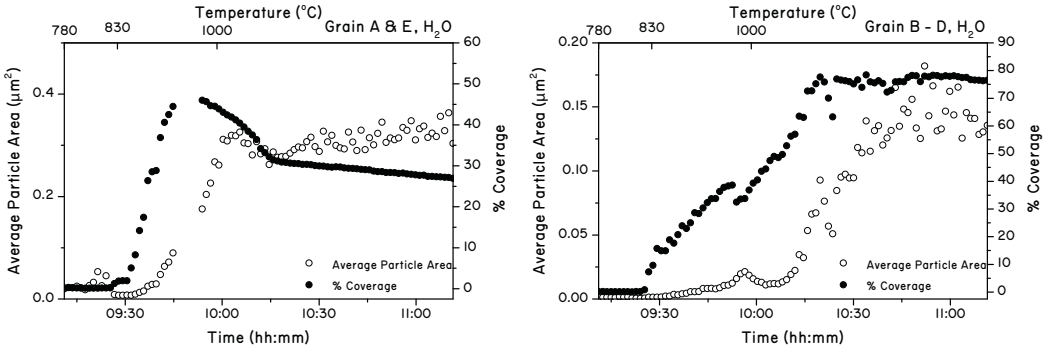


Figure 57: Growth rate of grains A & E and grain B - D respectively.

A and E[4] is observed at approximately 850°C. Growth is then rapid before agglomeration is seen at 950°C and during 1000°C isotherm. Grains B-D, however, exhibit reduced particle growth and agglomeration rate. From this data it was assumed that the microstructure of the underlying grain was the primary influence on the observed differences in particle growth, however, this topic is discussed further in Chapter 7.

Additionally, it may be seen that immediately surrounding the grain boundaries there is a region devoid of any particles. Oh *et al.* [2] observed a similar effect, however, did not comment upon it. For grains with a homogenous growth pattern (grains A and E) the 'denuded' region without particles may be seen to be 150 $\pm$25 nm in width. For grains exhibiting directional triangular/rod shaped growth (grain B-D) the region is 350 $\pm$ 250 nm in diameter. Again, there is a clear difference in growth behaviour between the two grain types. Particle size appears to increase with the denuded width, implying that Ostwald ripening is occurring, albeit at different rates between the grains.

Additional Observations 1: After the experiment was completed other areas of the sample were observed. Figure 58(a) shows a low magnification (250x) image of the surface immediately after the 1000°C isotherm (the temperature and atmosphere was retained). It is apparent that around the scratch used to locate areas there is a region depleted of particles. Figure 58(b) shows a magnified image of the highlighted region. As can be seen, particle growth and agglomeration has occurred within the depleted region, however, particle number and size is notably lower. Interestingly, the surface of the scratch is completely covered by Sr-based precipitation. Backscattered electron imaging (see figure inset) was used to con-

4 Particle growth rate of grain A approximately matched that of grain E

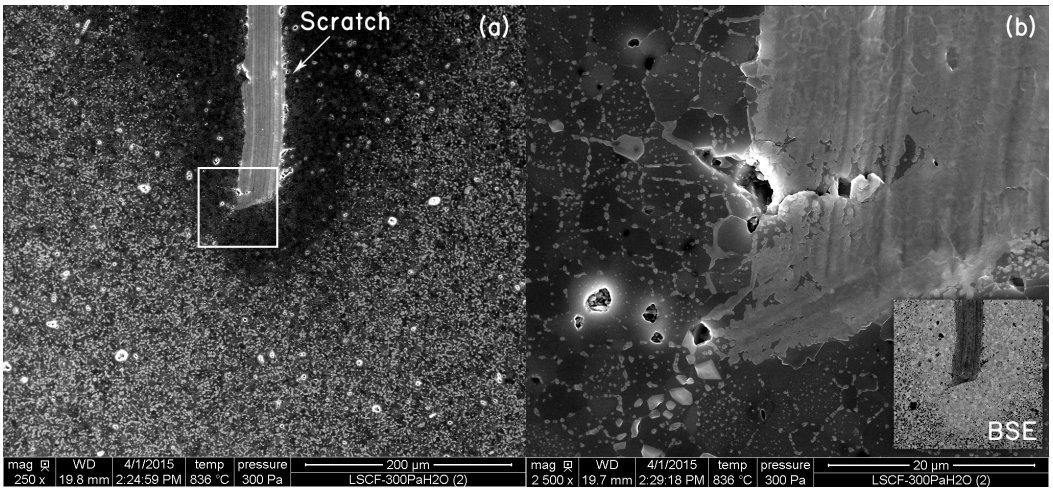


Figure 58: Showing the positioning scratch on the sample at (a) 250x magnification and (b) at 2500x magnification. The inset in (b) shows a backscattered electron image confirming that the phase covering the scratch differs to that of the bulk material.

firm the phase covering the scratch was different to the bulk and EDX was used to confirm this was a Sr-based phase.

Due to the brittle nature of the material, stresses induced by applying the scratch will have caused a degree of cracking. Figure 59 shows cracking at the surface post anneal. Along the cracks there is an increased number of particles similar to the observations of grain boundaries (the size is difficult to ascertain from top-down SEM images). Despite this, the quantity of cracks appears to be insufficient to explain the presence of a large depleted region[5]. Although not directly confirmed by this data, the large depleted region is most likely explained by sub-surface cracks increasing the free surface area for particle agglomeration.

The results presented in this section suggest that secondary phase growth is preferable on disordered regions on the surface. However, particles are still seen growing in (defect free) grain centres. Long range disorder (such as dislocations) is relatively uncommon in brittle materials such as LSCF, however, it is clear that the mechanical properties of the system will influence the degradation rate. Chapter 7 will discussed this relationship in more detail.

Additional Observations 2: Figure 60(a) shows a secondary electron image of the sample where two particles with differing contrast may be seen. Overlaid is a backscattered image of the same region also showing a change in contrast. The

5 Agglomeration of the particles hindered observation of cracks post anneal. However, such extreme behaviour was not expected and as such cracks were not searched for prior to the anneal.

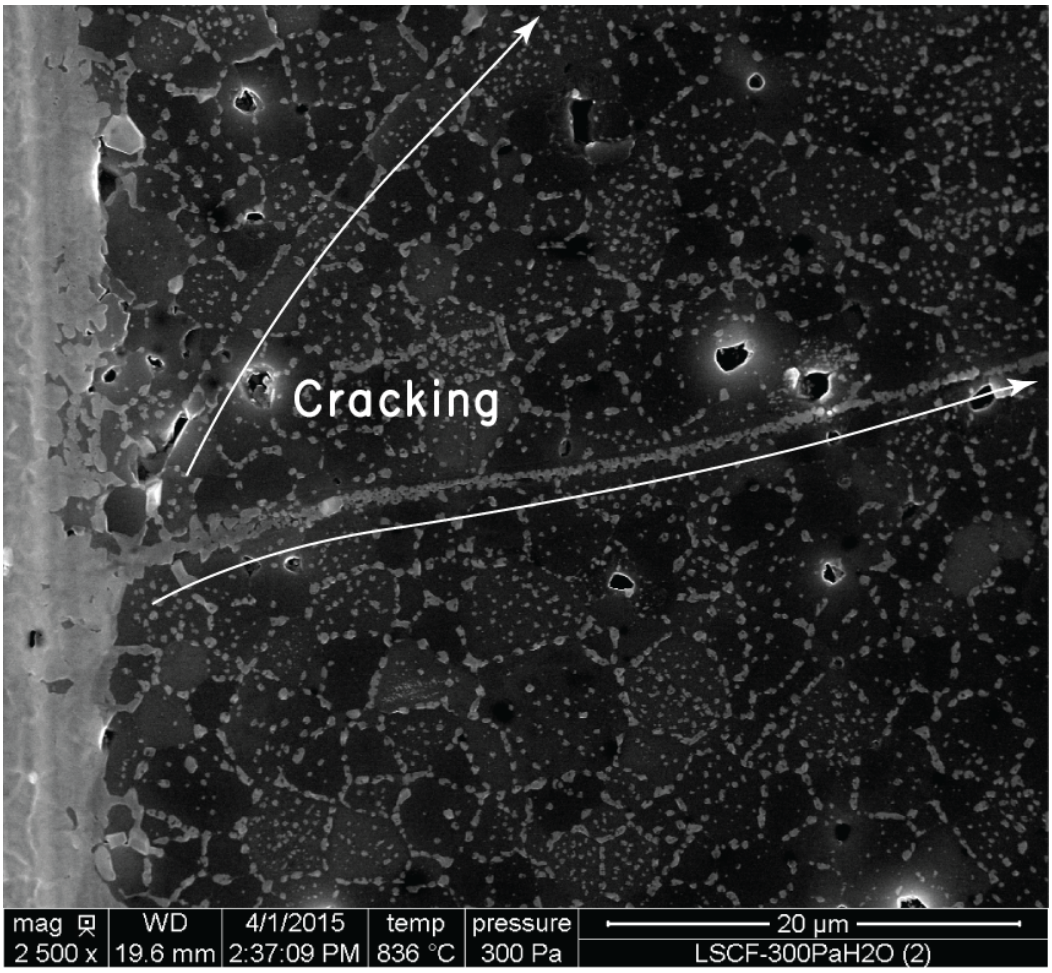


Figure 59: Showing cracking due to the scratch and preferential agglomeration across these features

contrast difference suggests that these particles are different phases, however, the precise nature could not easily be confirmed due to the fact that the particles are small (on the order of a few hundred nm) and predominantly covered by the larger particles. EDX confirmed that the larger white particle is Sr-based (Figure 60(b)), however, the lateral resolution of the equipment was insufficient to characterise the smaller (black) particle. AES was performed (see Section 6.2.1) and ascertained that every observable particles was strontium based. Therefore, this result suggests that both SrO and $Sr(OH)_2$ are formed in the presence of water vapour.

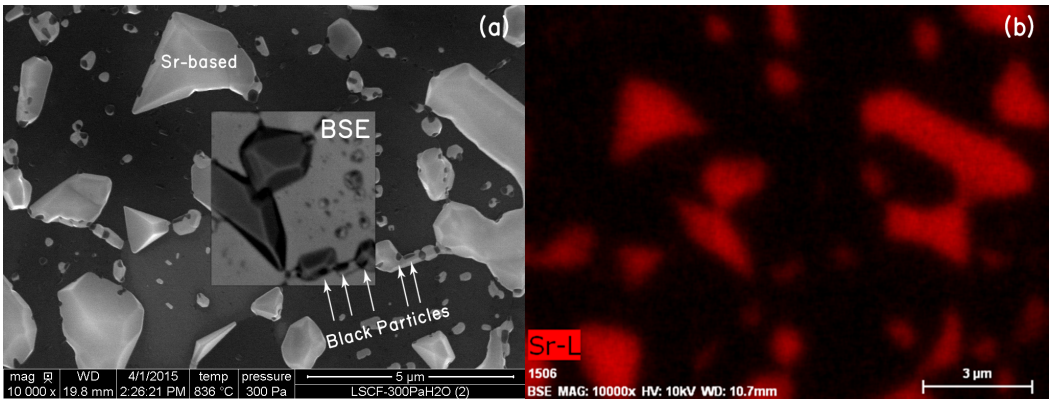


Figure 60: Showing (a) a micrograph of LSCF annealed in water where Sr-based particles are observed as well as an additional (black) phase in both SE and BSE (inset) mode, and (b) EDX image confirming the large white particles are strontium based.

6.1.3 *Ambient Air*

Both pure O_2 and H_2O are not representative of a typical SOFC cathode gas stream. Ambient air is the preferable cathodic gas stream despite the presence of many impurities (see Section 2.2.1). The behaviour of the LSCF surface is similar to the previous regimes in that secondary phase precipitation is seen, however, the rate and quantity of particle growth is more similar to the pure oxygen regime. Video 6.5 represents an LSCF sample annealed under 3 mbar ambient air at 5000x magnification. Video 6.6 is the same experiment taken with a magnification of 10000x. For a quick reference, Figure 61 shows micrographs of the surface prior to any noticeable surface modification and at the end of the experiment. Figure 62 shows the particle growth and percent particle coverage with respect to time.

The sample annealed in ambient air shows no growth until 950°C at which point a large number of particles form at approximately the same time. Figure 62 suggests instantaneous growth of a large number of particles, however, the time resolution of the image series was insufficient to ascertain initial particle growth patterns. After approximately 15 minutes, over the temperature range 950-1000°C, particle number and size increases as particles begin to agglomerate. The first thing to note about this data set is that the onset of secondary phase growth occurs at approximately 1000°C above the pure oxygen and water experiments. This would suggest the surface is more stable under ambient air, however, the effect of each gaseous species cannot be decoupled from this data.

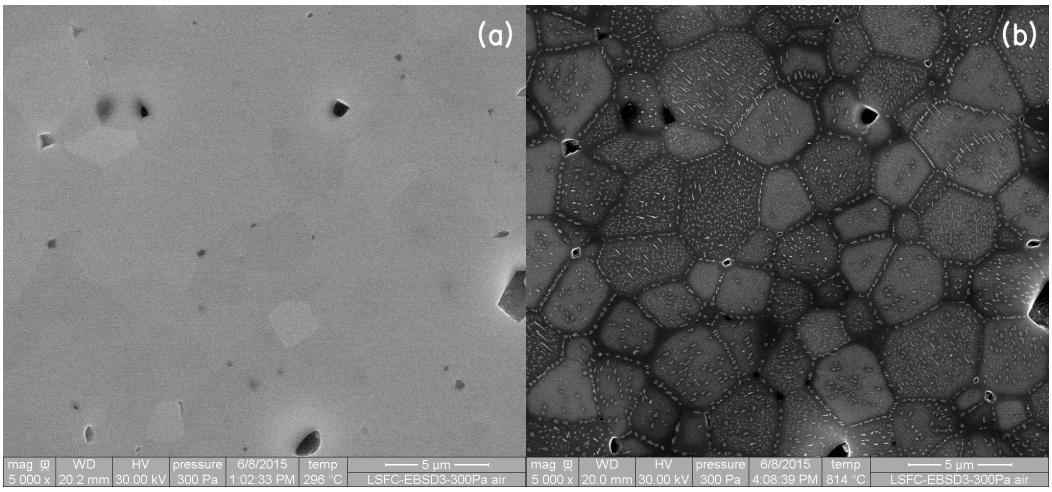


Figure 61: Showing (a) the surface prior to any noticeable surface modification and (b) the final image collected showing secondary phase precipitation after the anneal in ambient air.

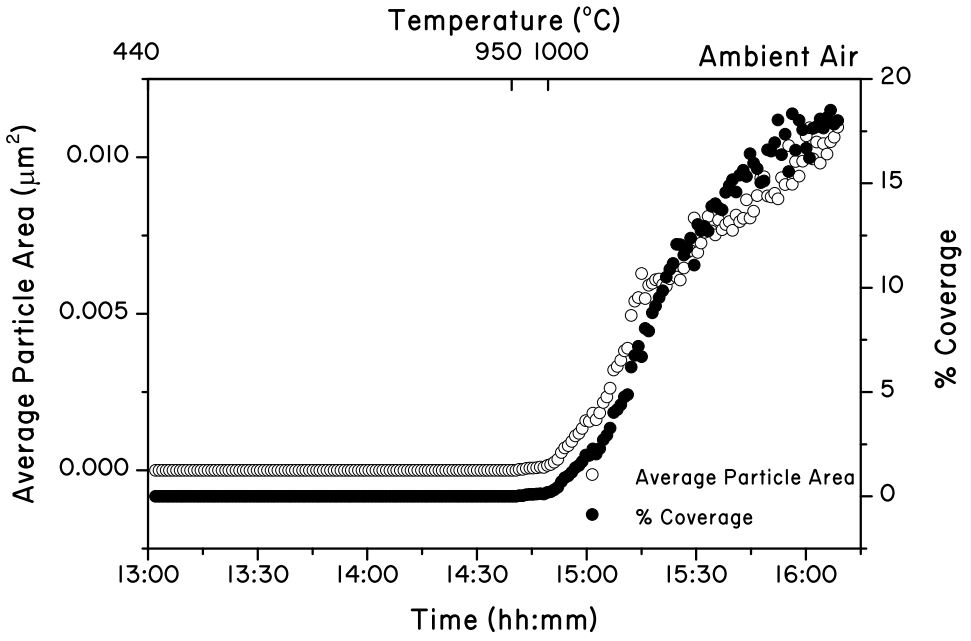


Figure 62: Showing average particle area and percent coverage with respect to time and temperature for a sample annealed in ambient air.

Gas analysis of the ambient air used in this experiment could not be performed during this experiment. As such, it has been assumed that typical ratios of gaseous species were present during the experiment (refer to Section 2.2.1.2). As discussed by Wachsman *et al.* [9] it has been shown that the surface of LSCF reacts with O_2, H_2O and CO_2 at different rates depending upon the temperature. Similar materials also show dependence upon these gases [10]. The partial pressure and the energy required to dissociate and adsorb these oxygen containing gas species has been used to explain the change to surface exchange rate, however, the role of each species in material degradation is currently unknown.

At temperatures below 500°C, $Sr(OH)_2$ will form preferentially in the presence of water. Above this temperature the strontium hydroxide begins to decompose into SrO and $SrCO_3$. In the presence of carbon containing gas species, surface carbonation (from gas phase decomposition) results in the reduction of SrO at the surface, ultimately promoting $SrCO_3$ formation. Between 500-800°C the percentage surface carbonation is dependent upon the temperature and partial pressure of gaseous carbon containing species. Above 800°C SrO is the stable phase [11]. Therefore, prior to particle growth, surface species should be primarily $Sr(OH)_2$ and $SrCO_3$. Only above 800°C will they begin to decompose into SrO. This may explain the delay in observable particle growth[6]. This also suggests that particle agglomeration is hindered by the presence of surface carbonation. Studies have shown that iron and cobalt containing materials react with strontium carbonate to form additional secondary phases [12, 13, 14], however, the presence of these phases could not be confirmed in this work.

6.1.4 *Vacuum*

Using typical fabrication and operational methods a SOCF cathode should not experience a high temperature anneal under a high vacuum. However, since the self-diffusivity of oxygen has a $p(O_2)$ dependence, the effect of a reducing environment was also of interest. Therefore, referring back to Figure 10, the sample will be in regime **V** where the material begins to release oxygen and become highly oxygen deficient. Video 6.7 represents an LSCF sample annealed 10^{-6} mbar high vacuum at 5000x magnification. Video 6.8 is the same experiment taken with

6 Of course, this experiment is limited by the electron imaging mode. Chemical changes could not be measured *in-situ*.

a magnification of 10000x. For a quick reference, Figure 63 shows micrographs of the surface prior to any noticeable surface modification and at the end of the experiment. Figure 64 shows the particle growth and percent particle coverage with respect to time.

It should first be noted that the HT-ESEM detector used in this experiment was optimised to perform in a gaseous environment. Replacing it with a detector optimised for a vacuum was not possible. As a result, to ability to focus the image was reduced due to low electron detection counts (a lack of an 'electron cascade' caused by the ionisation of gas particles - see Section 4.1.1). At low temperatures very few electrons were detected, however, as the temperature increased thermally generated electrons increased image quality. Observable contrast was still low even at 1000°C. Reducing the scan rate of the image increased imaged quality, however, was impractical to use when taking an image series as each image took a few minutes to collect. As such only the final image (after the isotherm) was taken at the reduced scan rate and is shown in Figure 63(b). Errors in Figure 64 are therefore significant, however, the general trend may still be observed.

Under a vacuum particle growth does not occur until approximately 1000°C. Particles were confirmed to be strontium based using EDX. Growth is seen to occur on both the grain boundaries and the centre of the grains. Similar to the observations seen in the pure water experiment, some grains exhibit a homogenous particle distribution, whereas others appear to show evidence of epitaxial growth. Agglomeration is more prevalent on particles at triple points grain boundaries, however, some particles within the grains may be seen to agglomerate. The chemical potential resulting from the reducing environment causes the material to lose of oxygen. Given that the concentration of adsorbed oxygen from the environment is very low it must be the case that oxygen released from the material reacts with segregated strontium to form particles.

An interesting observation may be seen in Video 7 and Figure 65. In this micrograph an instance of polishing damage running across multiple grains may be observed, however, in contrast to previous observations there does not appear to be preferential particle growth. This is unusual as the reduced surface free energy change associated with of disordered regions tends to promote heterogeneous nucleation. In an oxidising environment adsorbed, particle growth was observed to grow preferentially on these regions, however, in a reducing environment this is not observed. This implies that surface transport of ionic species is inhibited by

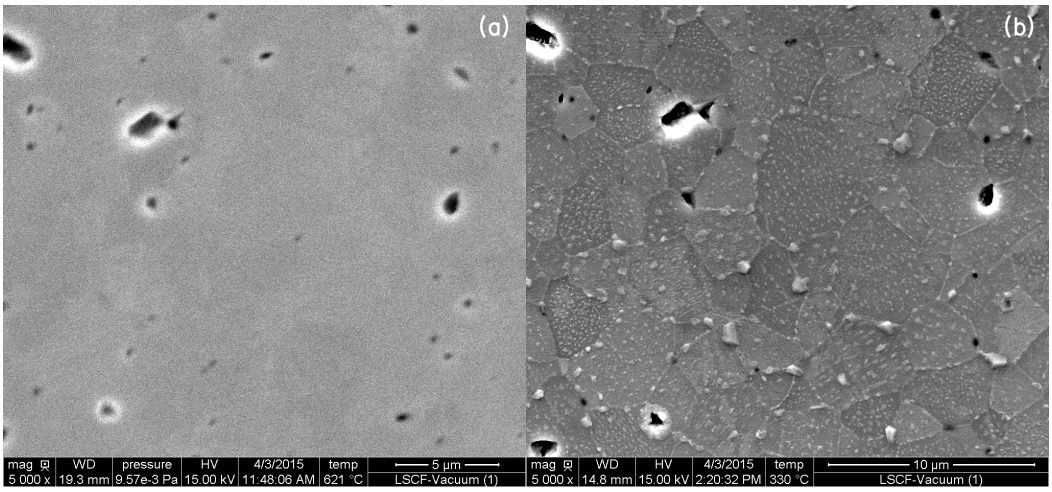


Figure 63: Showing (a) the surface prior to any noticeable surface modification and (b) the final image collected showing secondary phase precipitation after the anneal in a vacuum (10^{-6} mbar).

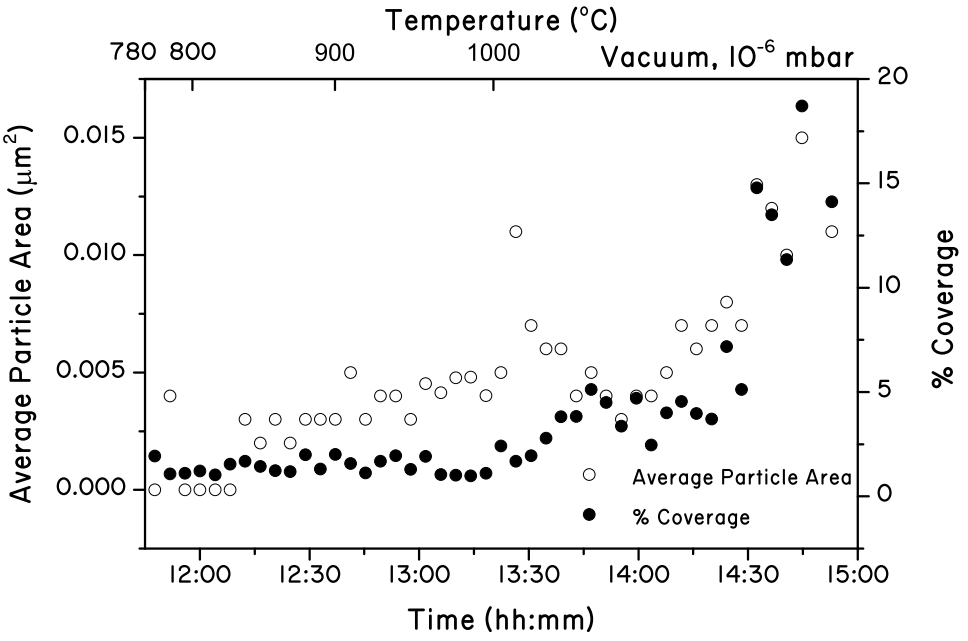


Figure 64: Showing average particle area and percent coverage with respect to time and temperature for a sample annealed in a vacuum (10^{-6} mbar).

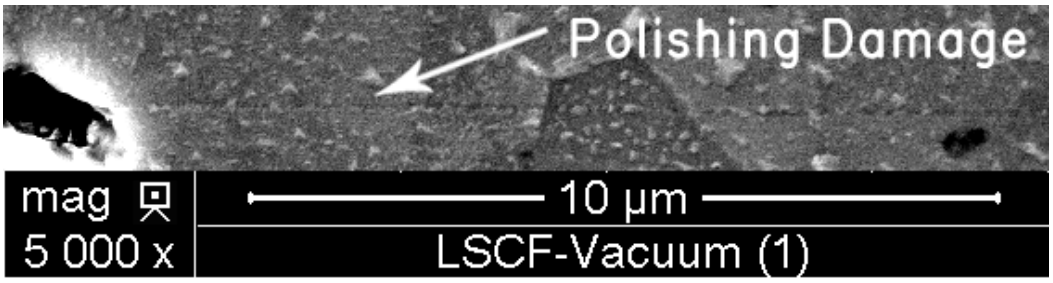


Figure 65: Showing polishing induced mechanical damage without preferential particle growth in a reducing environment.

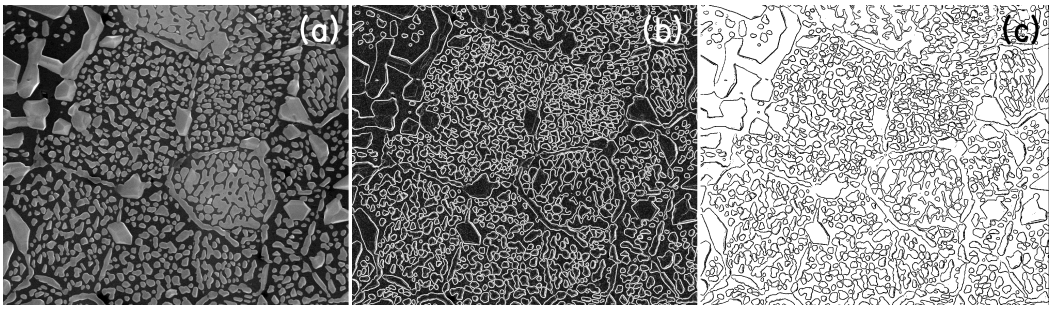


Figure 66: Showing (a) the original image, (b) the image after edge detection and (c) and conversion into a binary image.

the reducing environment and in a reducing environment the supply of ions is dependent upon where it reaches the surface of the material.

6.1.5 *Image Analysis Technique*

Particle growth was measured using the default edge detection methodology in ImageJ [1]. The software uses a Canny-Deriche [15, 16] algorithm to perform edge analysis. An edge may be defined as a region where there is a large change in contrast over a defined range of pixels[7]. The algorithm uses a multi-step approach to find strong edges:

1. Apply a Gaussian filter [18] to 'smooth' the image. This has the effect of reducing adjacent pixel contrast and thus reduces background noise (or remove weak edges). All edges are smoothed equally and as such some can be lost in this process, however, for the sake of particle analysis the benefit of noise reduction outweighs the loss of some edges.

2. Pixel contrast gradients are calculated for both the X and Y axes.

7 For example, the Sobel uses a 3x3 kernel[17]

3. A double threshold (high and low) is applied to bin weak edges that were not removed by the Gaussian filter and confirm possible edges.

4. Finalise edges by suppressing relatively weak edges not connected to a strong edge (isolated edges assumed to be noise).

After edge detection, remaining noise was removed by converting to a binary image (only black and white pixels). The threshold level was determined manually but generally fell within the range of 120-150 grayscale. Some edges are lost during this process, but may be re-added manually with relative ease. Once in binary form, particle analysis was performed using the default settings for particle analysis [1]. Figure 66 shows the progression of the image prior to particle analysis.

Errors estimation is difficult to define as error is a cumulative for each particle. This is strongly dependent upon the particle geometry and image quality of each frame and thus cannot be automated easily. The primary source of error is the uncertainty in edge position in relation to the pixel resolution of the image. The error will be greater using a lower magnification (using the same pixel resolution) and it may be seen that the lateral error of a pixel is ± 25 nm and ± 12.5 nm at 5000 and 10,000x magnification, respectively. For these reasons, data presented from image analysis in this work is primarily qualitative, however, trends may be observed and data may be correlated readily against the temperature and time profiles for each experiment.

6.2 THE SURFACE AND SUB-SURFACE

The previous section has shown the differences in particle growth with respect to pure oxygen, pure water, ambient air and a vacuum. The *in-situ* image series collected using the HT-ESEM clearly show growth patterns, however, the technique has limited chemical sensitivity, depth resolution and could not resolve three dimensional properties of the particles. A series of techniques were performed *ex-situ* to further characterise observed modifications of the surface. AES was performed by Dr. Nikolai Svetkov at the Massachusetts Institute of Technology (MIT) in order to characterise individual particles. Surface LEIS spectra were collected to analyse surface termination of the material post anneal. LEIS depth profiles were used to study the sub-surface and AFM was performed to provide

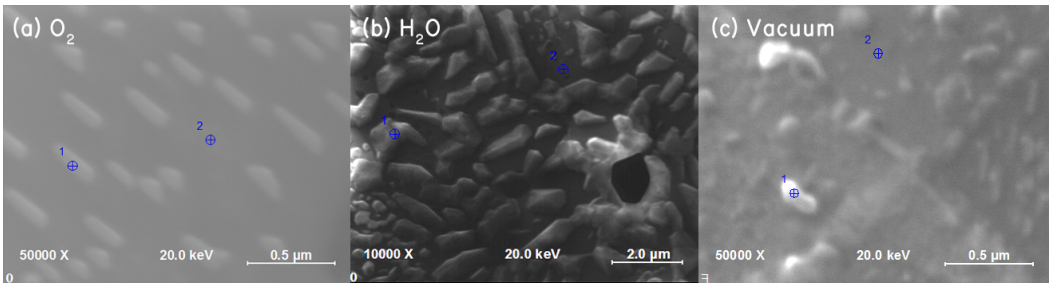


Figure 67: Showing AES spot analysis position at the (1) particle and (2) the grain surface for (a) pure oxygen, (b) pure water and (c) a vacuum.

topographical data of the particles and grain surface. The goal of this work was to study LSCF in 'realistic' conditions, therefore, samples annealed in ambient air were the focus of further analysis. However, as a large portion of the literature to date has used pure oxygen to anneal samples, comparisons were made between pure oxygen and ambient air where possible.

6.2.1 *Surface Chemistry*

6.2.1.1 *Auger Electron Spectroscopy*

Samples annealed in the HT-ESEM were analysed using AES. Figure 67 shows spot analysis positions for samples annealed in pure oxygen, pure water and a vacuum where spot (1) refers to a particle and spot (2) the grain surface. Table 9 shows the relative elemental composition for each point. As can be seen, the composition of the particles is predominantly strontium based, however, other elements are detected as the interaction volume of the electron beam extends into the bulk of the material. The composition of the particles is approximately equal for samples annealed in pure oxygen and a vacuum. This suggests that the particle size 'out of the image plane' is similar. Particles annealed in pure water display a greater strontium content, however, as the particle is larger there will be reduced electron beam interaction in the bulk. Interestingly, the composition of the grain surface for each sample is approximately equal.

Figure 68 shows spot analysis of the sample annealed in ambient air. AES analysis was performed on particles in the centre of the grain and on the grain boundaries. As can be seen from Table 10 this data confirms that these particles are strontium based and that the composition matches the values found for the other anneal environments. Once again, this suggests the particle size is compa-

Table 9: Table of values corresponding to the AES spot analysis seen in Figure 67.

Figure	Point	La (At. %)	Sr (At. %)	Co (At. %)	Fe (At. %)
Pure O_2	(1) Particle	8.0	89	1.0	2.0
	(2) Grain	17	75	2.0	6.0
Pure H_2O	(1) Particle	6.0	91	1.0	2.0
	(2) Grain	17	75	1.0	7.0
Vacuum	(1) Particle	10	85	2.0	3.0
	(2) Grain	17	78	2.0	3.0

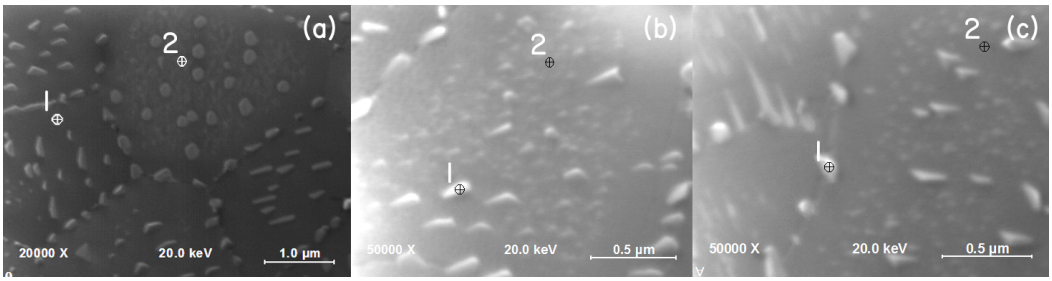


Figure 68: Showing (a) spot analysis position in an 'unsegregated' grain surface and 'segregated' grain surface, (b) a crystallographic particle in the centre of the grain and (c) a crystallographic particle on a grain boundary.

rable to the particles observed in pure oxygen and a vacuum. Figure 68(a) shows analysis of the grain surface for grains with different degrees of particle agglomeration. At point (1) the surface of the grain appears to be unmodified, whereas at point (2) there is a contrast difference that is typical of particle growth. Secondary electron contrast may also be due to surface roughness, however, the strontium content is greater in the segregated region implying that this contrast change is due to particle growth. This result is further evidence that the transport of strontium and oxygen species across the surface results in the agglomeration of the strontium-based particles.

6.2.1.2 *Low Energy Ion Scattering*

AES has a high depth resolution, however, as can be seen in Table 9 and 10 the electron beam is still interacting with the bulk material below the surface. Due to the use of noble gas primary ions, LEIS probes the *outermost* atomic layer (refer to Section 4.3.3). Figure 69 shows LSCF surface spectra taken using a 3 keV helium

Table 10: Table of values corresponding to the AES spot analysis seen in Figure 68.

Figure	Point	La (At. %)	Sr (At. %)	Co (At. %)	Fe (At. %)
(a)	(1) 'Unsegregated'	19	71	2.0	8.0
	(2) 'Segregated'	11	84	1.0	4.0
(b)	(1) Particle	10	85	1.0	4.0
	(2) Grain	22	70	2.0	6.0
(c)	(1) Particle	8.0	88	1.0	3.0
	(2) Grain	23	67	2.0	8.0

primary ion beam. The vertical dotted lines show the onset scattering energy of each surface atom. These are followed by primary scattering peaks for each element. Using helium as a primary ion it may be seen that peak separation is poor between lanthanum and strontium. Additionally, cobalt and iron have very similar masses and as such their scattering peaks overlap completely. This makes quantification of LSCF cation ratios difficult using a helium spectrum, however, the purpose of using helium was to 'survey' the surface and assess the cleanliness of the sample[8]. If the sample contains significant contamination the primary scattering peaks will be attenuated by an unknown factor, thus causing systematic errors. A large degree of contamination often results in a substantial loss of signal. Small peaks were detected for sodium, magnesium and potassium[9], however, the primary peaks are still well defined. Thus the samples were considered to be clean.

Even from the helium spectra it is clear that the sample annealed in ambient air shows significantly greater levels of strontium at the surface. In-fact, consistent with the observations of Druce *et al.* [19], there is almost complete depletion of lanthanum, cobalt and iron at the surface.

In order to quantify this effect 5 keV neon spectrum were required. Figure 70 shows LSCF surface spectra annealed in pure oxygen and ambient air. LEIS spectra are plots of scattering intensity against detected energy. Therefore, the area under the peak represents the number of ions scattered by an element. Scattering

8 If the incident ion is heavier than the target ion, no scattering will occur. Using the billiard ball analogy, if a heavier ball hits a small ball it will simply push the smaller ball and continue moving in the same direction. Helium is the lightest noble gas, thus can detect the largest number of target atoms.

9 Common contamination from handling the sample.

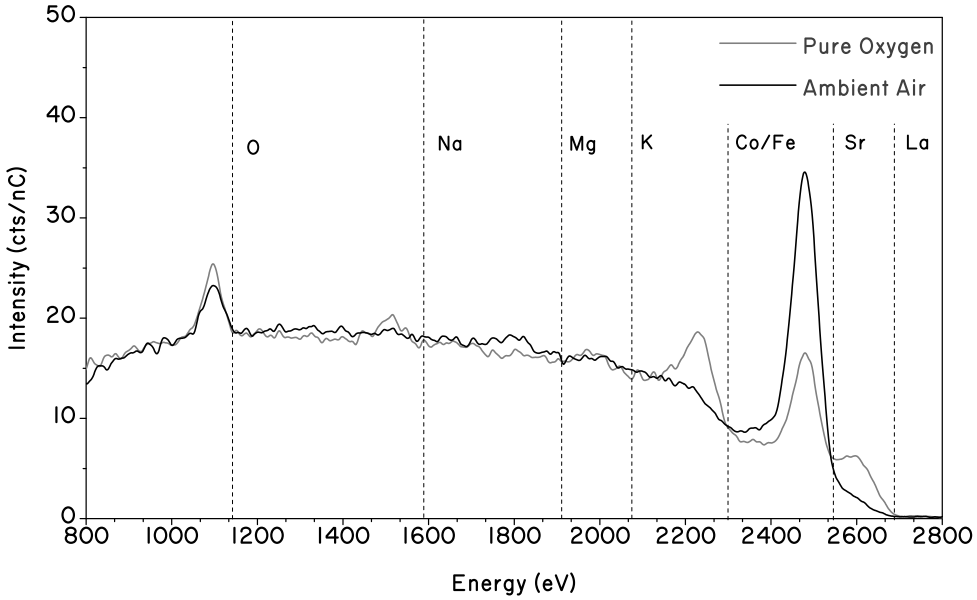


Figure 69: LEIS 3keV Helium survey spectra for a LSCF samples annealed in pure oxygen and ambient air.

peaks are the combination of a Gaussian primary peak from ions scattered at the surface, combined with an 'in-depth' background signal from inelastic collisions as primary ions penetrating the material. In a pure material the background 'in-depth' signal will be flat as each interaction below the surface results in identical energy loss, however, a polycrystalline material with numerous elements will produce complicated background signals. To simplify the fitting procedure in such a material each element is assigned as either a Gaussian peak (at the onset energy) or Gaussian peak with a flat background. This makes the assumption that the ion beam interacts with each element in isolation (as if it were a pure element). This is of course far from the truth, however, it is a non-trivial problem to model a multi-component polycrystalline system. Background signal at low energies is characteristic of sputtered material and may be modelled by an exponential decay function. Surface Lab 6 by ION-TOF was used to fit the data and Figure 71 shows the fit for a neon spectra collected in this work. Integrated intensity cation ratios were calculated from the fit of each element and are shown in Table 11.

LEIS data is strongly influenced by the presence of particles on the surface. The LEIS beam spot size is on the order of tens of microns, meaning that a LEIS spectrum represents the average composition across the surface (individual particles cannot be resolved). As mentioned previously, topographical effects will cause attenuation of the scattered signal, however, the presence of particles will

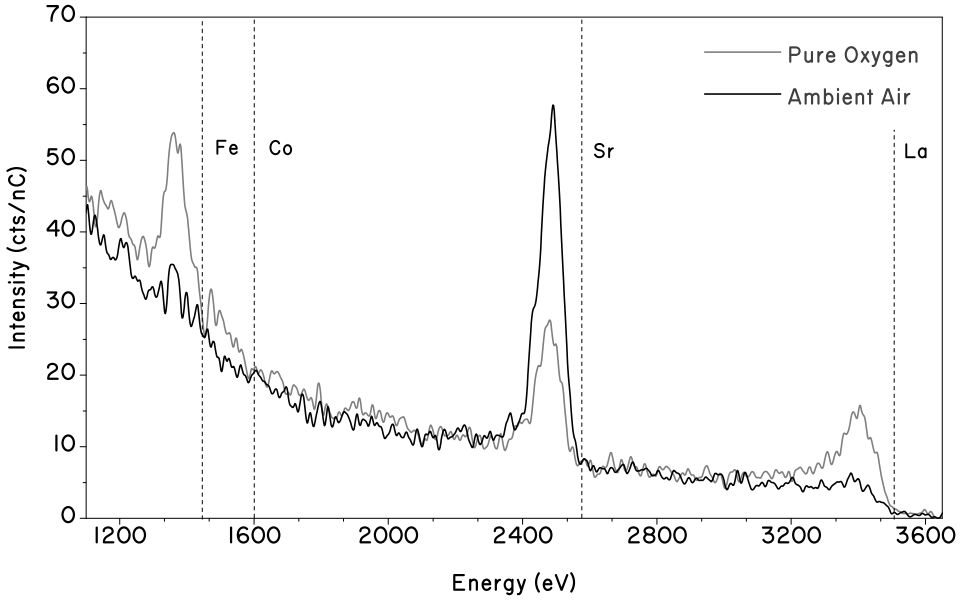


Figure 70: LEIS 5keV neon spectra for LSCF samples annealed at 650°C in 200 mbar pure oxygen and ambient air.

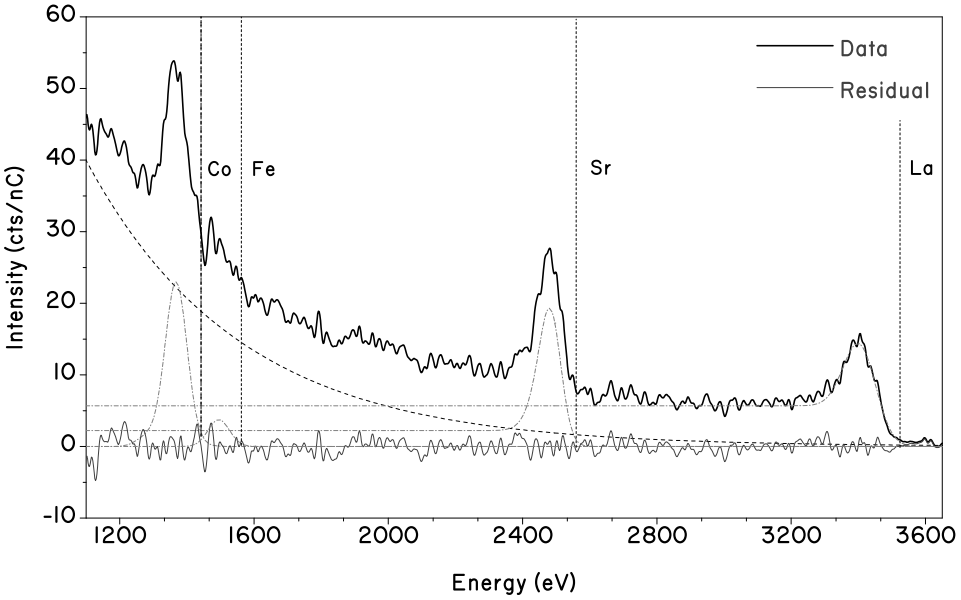


Figure 71: Showing an as polished LSCF surface spectra collected using a 5 keV neon primary ion beam with the peak fitting (dash-dot lines) superimposed onto the data.

Table 11: Cation ratio at the surface for LSCF samples annealed in pure oxygen and ambient air.

Environment	**La (At. %)**	**Sr (At. %)**	**Co (At. %)**	**Fe (At. %)**
Pure Oxygen	17.9 ±1	59.9 ±1	5.4 ±1	16.8 ±1
Ambient Air	1.9 ±1	90.5 ±1	1.5 ±1	6.1 ±1

prevent the 'material surface' from being probed. Therefore, any enhanced strontium signal must be the product of the strontium particles at the surface. The sample annealed in ambient air displays a significantly greater concentration of strontium and respective decrease in the other elements, however, the sample annealed in pure oxygen exhibits a lower strontium content at the surface. HT-ESEM data suggests that % of surface covered by particles is approximately equal (~17%) for pure oxygen and ambient air, thus the excess strontium must exist on the grain surface.

AES observed that the grain composition was constant between each environment. This may be true of a few nanometres into the material, however, the LEIS data suggests that the immediate surface contains a larger proportion of strontium when the samples were annealed in ambient air. In the presence of water vapour, adsorbed hydroxyl species tend to cover the surface. The formation of strontium hydroxide is more preferable in this case and it is clear from the HT-ESEM result (in pure water) that particle growth under that condition is facile. Therefore, it is suggested that strontium hydroxide molecules form at the grain surface in equilibrium with the concentration of adsorbed hydroxyl species and remain adsorbed species (rather than volatile) at high temperature.

LEIS Depth Profiles: It is known that adsorbed water (or OH^- molecules) enhances the oxygen exchange rate of perovskite material [20], however, it may only be speculated that bulk strontium segregation rates are also enhanced [21]. The AES data has suggested that there is no enhancement as the 'sub-surface' composition was constant across experimental conditions experiments. Figure 72(a) and 72(b) show LEIS depth profiles of the samples annealed in pure oxygen and ambient air, respectively. Samples were sputtered until cation counts became constant. It was assumed that at this point the 'bulk' stoichiometry had been reached and thus atomic ratios for each cation could be calculated relative to the 'bulk' value.

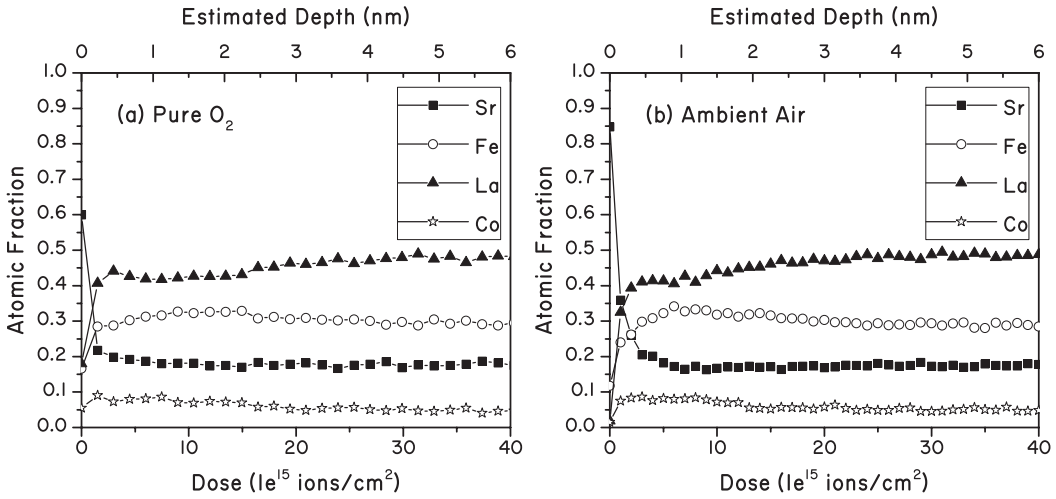


Figure 72: LEIS depth profiles of a sample (a) annealed in pure oxygen and (b) in ambient air.

Each sputter step was fit using the same protocol as described above and subsequently plotted as a function of ion dose. Due to very short sputter depths (a few nanometres) white light interferometry was unsuitable to measure the depth of the sputter crater, therefore, sputter depth has been estimated based upon the sputter rate of LSCF and the ion dose.

As can be seen from both profiles the sub surface is enhanced in strontium and deficient in lanthanum over approximately 4 nm of depth. It may be seen that the concentration of B site cations is enhanced slightly within this region. The cause for this is unknown, however, it very likely a response to the loss of strontium. Care should be taken, however, when interpretation this result. Each sputter step induces 'mixing' as a result of ballistic effects. The region affected by mixing is dependent upon the ion beam energy and incident angle. As such, during a depth profile, small changes seen in the integrated cation ratios may contain this error.

6.2.2 *Surface Topography*

6.2.2.1 *Atomic Force Microscopy*

Using HT-ESEM it was possible to analyse particle area. Atomic force microscopy was performed to characterise particle size and shape, but also the roughness of the grain surface. Surface roughness may be defined using multiple different metrics, however, in this work surface roughness was defined using the Root Mean

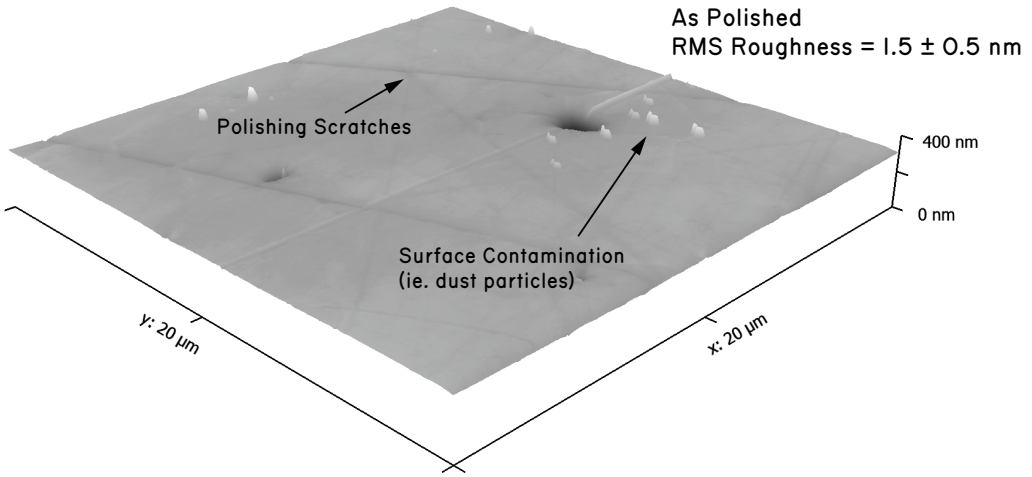


Figure 73: Showing an AFM topography map of an as polished LSCF sample taken with a 20x20 µm scan area using 512x512 px.

Square (RMS) in order to minimise errors induced by particles on the surface. RMS is the square root of the arithmetic mean of the squares of a set of numbers; as defined by Equation 6.4:

$$\mathrm{RMS} = \sqrt{\frac{1}{n}\sum_{i=1}^{n} x_i^2} \tag{6.4}$$

AFM data was analysed using the open source software Gwyddion [22]. Areas of interest could be defined to selectively analyse the RMS roughness value across the AFM image.

Figure 73 shows the surface of an as-polished sample. The RMS roughness was found to fall in the range of 1-2 nm showing that the polishing process produced very flat surfaces, however, shallow (15 nm) scratches were consistently observed across multiple samples. Small particles may be observed on the surface, however, these may be attributed to unavoidable atmospheric contamination such as dust particles.

Figure 75 shows the surface topography of a sample annealed in pure oxygen. As can be seen a large number of particles may be seen covering the surface in the centre of grain and on the scratches induced during polishing. The surface remains mostly flat and as such grain boundaries cannot be seen, except for the case where the grain has been 'pulled out' from the material during the thermal anneal. Average particle height was calculated to be 31.6±0.5 nm. It may

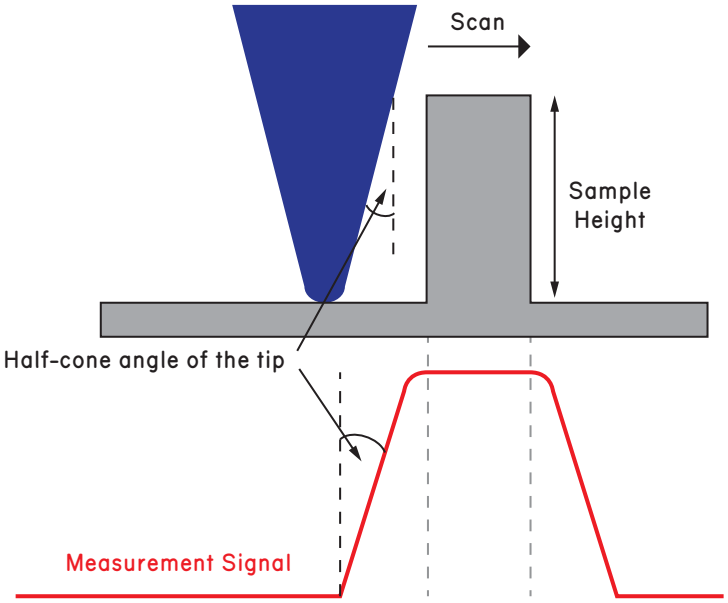


Figure 74: Showing edge 'smoothing' as a result of the AFM tip radius.

be seen that there are two grain roughness patterns (indicated by (1) and (2) in Figure 75). The RMS roughness of grain type 1 was seen to match that of the as-polished sample, however, grain type 2 displayed an increased RMS roughness where the maximum and minimum roughness were further apart. As observed in Section 6.1.2 grains exhibited differing particle growth patterns, therefore this result corroborates that grain orientation has an effect upon particle growth and surface modification.

Figure 76 shows a high resolution AFM topography map of the same sample (using 3x3 μm scan area). The higher lateral resolution shows differences in grain roughness more clearly, however, both grain roughness and particles appear smooth rather than crystallographic. This is due to the tip radius of the AFM and 'half-cone' angle as shown in Figure 74 and was unavoidable with the equipment available for this work. RMS roughness between grains 1 and 2 is seen to vary due to the faceting of the surface as a result of the thermal anneal.

Figure 77 and 78 shows a sample annealed in ambient air taken using a 10x10 μm and 5x5 μm scan area, respectively. Both display a different surface topography to the sample annealed in pure oxygen. The grain surface is exhibited a RMS roughness around 3 times greater than that of the rough grain 2 on sample annealed in pure oxygen. Average particle height was found to be 556±0.5 nm. Multiple grains should be visible in a 10x10 μm image, however, grain bound-

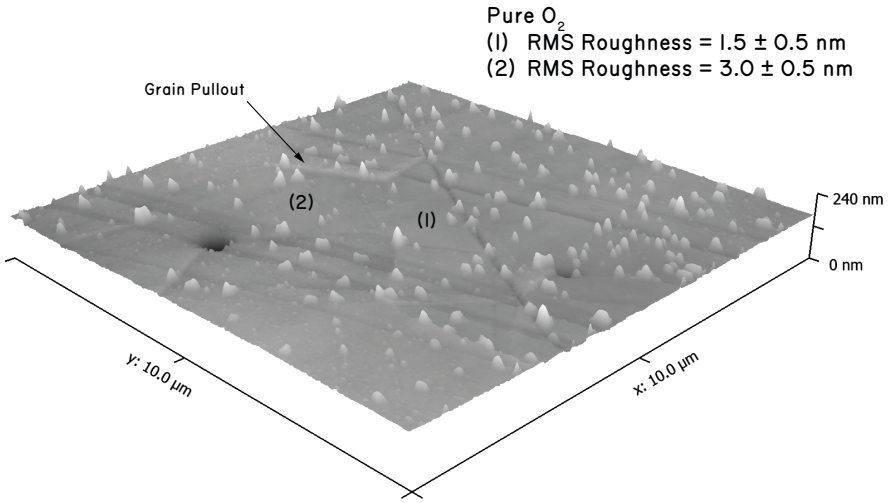


Figure 75: Showing an AFM topography map of a sample annealed in pure oxygen taken with a 10x10 µm scan area using 512x512 px with two grains exhibiting differing RMS roughness values.

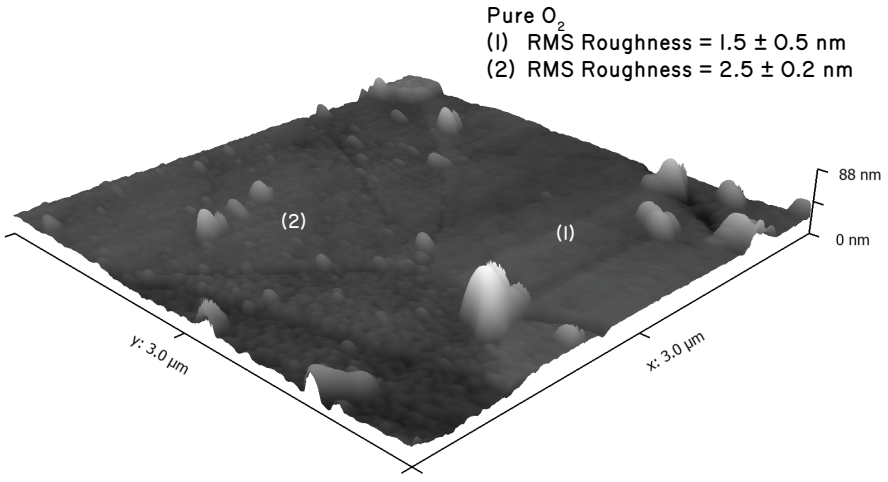


Figure 76: Showing an AFM topography map of a sample annealed in pure oxygen taken with a 3x3 µm scan area using 512x512 px with two grains exhibiting differing RMS roughness values.

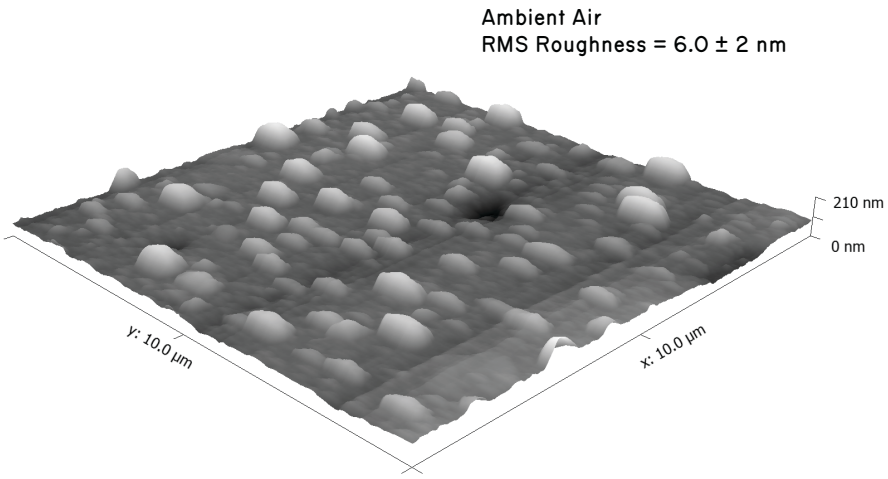


Figure 77: Showing an AFM topography map of a sample annealed in ambient air taken with a 10x10 µm scan area using 512x512 px.

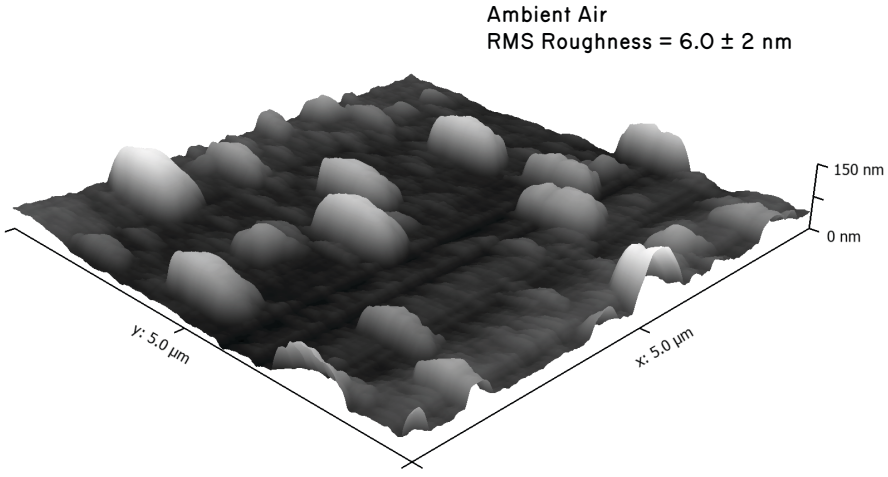


Figure 78: Showing an AFM topography map of a sample annealed in ambient air taken with a 5x5 µm scan area using 512x512 px.

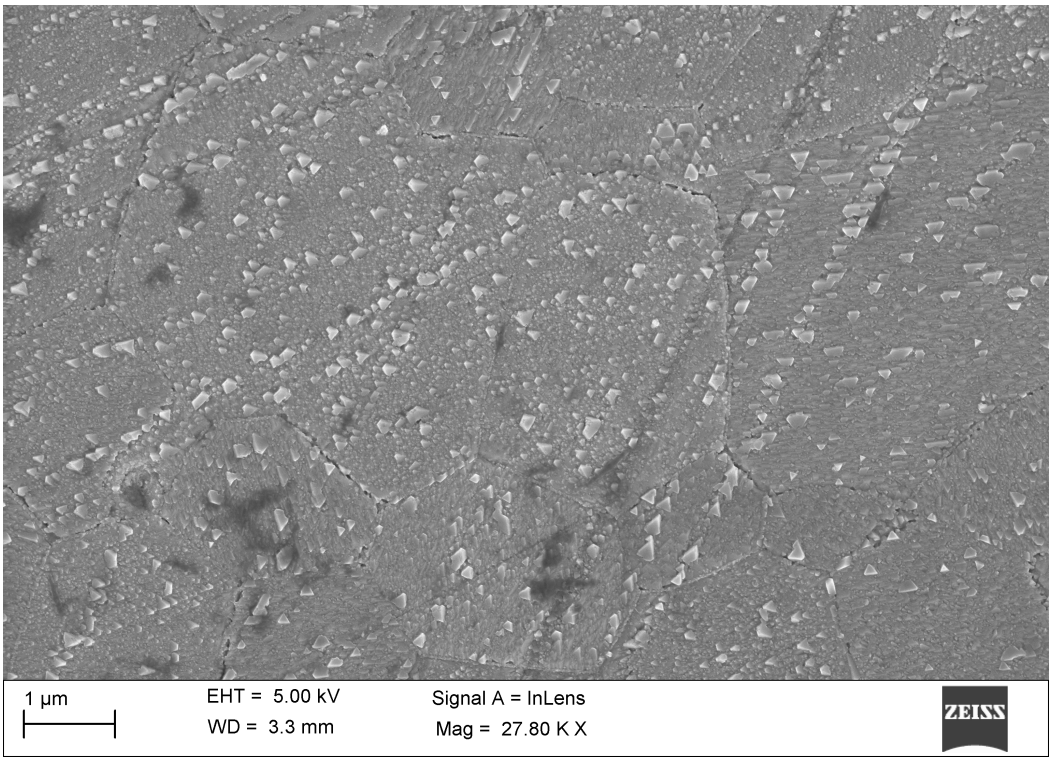


Figure 79: SEM micrograph of an LSCF sample annealed in ambient air at 800°C showing surface corrosion and particle growth.

aries cannot be discerned. Figure 79 shows an SEM image of a different sample annealed at 800°C in ambient air for a separate experiment. The micrograph correlates strongly to the AFM data despite not being from the same sample. As can be seen, particle growth appears pyramidal and tends to grow preferentially along polishing scratches. Corrosion of the LSCF surface has been observed in the presence of CO_2 [23]. Tan *et al.* observed similar surface roughening effects, however, also reported characteristic carbon phases (such as $La_2O_2CO_3$) which cannot be seen in Figure 79. Tan *et al.* used pure CO_2 or Helium/CO_2 gas mixtures, however, ambient air contains water vapour. The effect of a combined $O_2/CO_2/H_2O$ gas mixture has not been studied extensively and as such surface corrosion cannot be confirmed. An additional explanation might be crystallographic reconstruction into a new phase, however, further TEM work would be necessary to confirm this.

6.3 SUMMARY AND CONCLUSIONS

This chapter has detailed the chemical and physical surface modifications that occurred during thermal anneals in four different environments. HT-ESEM was used to analyse the particle growth rate and patterning in a pure oxygen, pure water, ambient air and vacuum environment. Strontium based particles were observed to grow in each environment, however, the growth onset temperature, agglomeration behaviour and surface coverage of the particles varied. In pure oxygen it was seen that particles grew from 750-800°C and reached a surface coverage of 17%. In pure water rapid particle growth occurred from 850-1000°C reaching a maximum surface coverage of 40%. During the 1000°C isotherm the particles were seen to agglomerate readily and form very large particles. Although the experiment was stopped after an approximately 1 hour isotherm the data suggests that agglomeration would continue until the whole surface was covered. The result for ambient air is similar to that of pure oxygen, however, the onset temperature of particle growth is 1000°C. It is suggested that the delayed growth is due to the decomposition of $Sr(OH)_2$ and $SrCO_3$ phases in SrO that have formed below 800°C. In a vacuum, strontium-based particles are also observed to grow, however, the low partial pressure of oxygen in the atmosphere appears to inhibit surface transport of oxygen and thus particle agglomeration is limited.

Surface chemical analysis was performed using AES and LEIS. Both technique confirmed that the particles observed were all strontium based particles. Samples annealed in environments that contained water vapour (such as ambient air) exhibited a greater surface concentration of strontium, suggesting that the strontium segregation rate is enhanced by the presence of water vapour. LEIS depth profiles showed that the sub-surface was strontium deficient as a result of segregation. A minor enhancement of B-site cations was also seen in the sub-surface, however, this is most likely due to relative increase in atomic fraction as the A-site strontium segregates.

AFM also showed that grain roughness is greater when the environment contains water vapour. Previous work [23] has shown that the surface of $La_{0.6}Sr_{0.4}$-$Co_{0.2}Fe_{0.8}O_{3-\delta}$ tends to corrode in the presence of CO_2 and form characteristic faceting of the grain surface. It would appear that this is also observed in this work.

The mechanical properties and crystallography was shown to influence particle growth. The results presented here suggest that long range defects such as damage induced during polishing and grain boundaries act as preferential heterogeneous nucleation sites. Long range defects may also influence the self-diffusivity of the material, however, there is no evidence to suggest this from the data presented. It is clear that the sub-surface influences the degradation of LSCF, however, this is discussed in more detail in Chapter 7.

BIBLIOGRAPHY

[1] Michael D. Abràmoff, Paulo J. Magalhães, and Sunanda J. Ram. Image processing with imageJ. *Biophotonics International*, 11(7):36–41, 2004. ISSN 10818693. doi: 10.1117/1.3589100.

[2] Dongjo Oh, Danijel Gostovic, and Eric D. Wachsman. Mechanism of La0.6Sr0.4Co0.2Fe0.8O3 cathode degradation. *Journal of Materials Research*, 27(15):1992–1999, jul 2012. ISSN 0884-2914. doi: 10.1557/jmr.2012.222. URL http://www.journals.cambridge.org/abstract{_}S0884291412002221.

[3] K Szot and W Speier. Surfaces of reduced and oxidized SrTiO3 from atomic force microscopy. *Physical Review B*, 60(8):5909, 1999. ISSN 0163-1829. doi: 10.1103/PhysRevB.60.5909.

[4] Wilhelm Ostwald. *Lehrbuch der allgemeinen Chemie*, volume 2. W. Engelmann, 1886.

[5] K. K. Hansen and K. Vels Hansen. A-site deficient (La0.6Sr0.4)1-sFe0.8Co0.2O3-δ perovskites as SOFC cathodes. *Solid State Ionics*, 178(23-24): 1379–1384, 2007. ISSN 01672738. doi: 10.1016/j.ssi.2007.07.012.

[6] G. Ch Kostogloudis and Ch Ftikos. Properties of A-site-deficient La0.6Sr0.4Co0.2Fe0.8O3-??-based perovskite oxides. *Solid State Ionics*, 126 (1):143–151, 1999. ISSN 01672738. doi: 10.1016/S0167-2738(99)00230-1.

[7] D. Waller, J.A. Lane, J.A. Kilner, and B.C.H. Steele. The structure of and reaction of A-site deficient La0.6Sr0.4-xCo0.2Fe0.8O3-δ perovskites. *Materials Letters*, 27(4-5):225–228, 1996. ISSN 0167577X. doi: 10.1016/0167-577X(95)00289-8. URL http://www.sciencedirect.com/science/article/pii/0167577X95002898.

[8] George F Harrington. *Oxygen Ion Transport and Dopant Segregation in Strained Oxide Thin Films*. PhD thesis, Imperial College London, 2015.

[9] Eric D Wachsman, Yi-lin Huang, Christopher Pellegrinelli, Joshua A Taillon, and Lourdes G Salamanca-Riba. Towards a Fundamental Understanding of the Cathode Degradation Mechanisms. *ECS Transactions*, 61(1):47–56, 2014. ISSN 19386737. doi: 10.1149/06101.0047ecst. URL http://ecst.ecsdl.org/content/61/1/47.abstract.

[10] Mirko Arnold, Haihui Wang, and Armin Feldhoff. Influence of CO2 on the oxygen permeation performance and the microstructure of perovskite-type (Ba0.5Sr0.5)(Co0.8Fe0.2)O3-?? membranes. *Journal of Membrane Science*, 293 (1-2):44–52, 2007. ISSN 03767388. doi: 10.1016/j.memsci.2007.01.032.

[11] D. R. Glasson. Reactivity of lime and related oxides. Production of Strontium oxide. *Journal of Applied Chemistry*, 8(12):793–797, 1958. ISSN 00218871. doi: 10.1002/jctb.5010081204. URL http://doi.wiley.com/10.1002/jctb.5010081204.

[12] S. J. Conway, J. A. Greig, and G. M. Thomas. Comparison of lanthanum oxide and strontium-modified lanthanum oxide catalysts for the oxidative coupling of methane. *Applied Catalysis A, General*, 86(2):199–212, 1992. ISSN 0926860X. doi: 10.1016/0926-860X(92)85148-5.

[13] K. Omata, N. Nukui, T. Hottai, Y. Showa, and M. Yamada. Strontium carbonate supported cobalt catalyst for dry reforming of methane under pressure. *Catalysis Communications*, 5(12):755–758, 2004. ISSN 15667367. doi: 10.1016/j.catcom.2004.09.012.

[14] T Brown and By J Beretka. Studies on the Reaction Between Stronticm Carbonate and Iron (Iii) Oxide. (Iii):237–242, 1971.

[15] J Canny. A computational approach to edge detection. *IEEE transactions on pattern analysis and machine intelligence*, 8(6):679–698, 1986. ISSN 0162-8828. doi: 10.1109/TPAMI.1986.4767851.

[16] Rachid Deriche. Using Canny's criteria to derive a recursively implemented optimal edge detector. *International Journal of Computer Vision*, 1(2):167–187, 1987. ISSN 09205691. doi: 10.1007/BF00123164.

[17] D Ziou and Salvatore Tabbone. Edge detection techniques - An overview. *International Journal of Pattern Recognition and Image Analysis*, 8(4):1–41, 1998. ISSN 10546618.

[18] Richard A. Haddad and Ali N. Akansu. A class of fast Gaussian binomial filters for speech and image processing. *IEEE Transactions on Signal Processing*, 39(3):723–727, 1991. ISSN 1053587X. doi: 10.1109/78.80892.

[19] John Druce, Tatsumi Ishihara, and John Kilner. Surface composition of perovskite type materials studied by Low Energy Ion Scattering (LEIS). *Solid State Ionics*, 262:893–896, 2014. ISSN 01672738. doi: 10.1016/j.ssi.2013.09.010. URL http://dx.doi.org/10.1016/j.ssi.2013.09.010.

[20] Natsuko Sakai, Katsuhiko Yamaji, Teruhisa Horita, Yue Ping Xiong, Haruo Kishimoto, and Harumi Yokokawa. Effect of Water on Oxygen Transport Properties on Electrolyte Surface in SOFCs. *Journal of The Electrochemical Society*, 150(6):A689, 2003. ISSN 00134651. doi: 10.1149/1.1568938.

[21] Per Hjalmarsson, Martin S??gaard, and Mogens Mogensen. Electrochemical performance and degradation of (La0.6Sr0.4)0.99CoO3 - ?? as porous SOFC-cathode. *Solid State Ionics*, 179(27-32):1422–1426, 2008. ISSN 01672738. doi: 10.1016/j.ssi.2007.11.010.

[22] David Nečas and Petr Klapetek. Gwyddion: an open-source software for SPM data analysis. *Open Physics*, 10(1), jan 2012. ISSN 2391-5471. doi: 10.2478/s11534-011-0096-2. URL http://www.degruyter.com/view/j/phys.2012.10.issue-1/s11534-011-0096-2/s11534-011-0096-2.xml.

[23] Xiaoyao Tan, Nan Liu, Bo Meng, Jaka Sunarso, Kun Zhang, and Shaomin Liu. Oxygen permeation behavior of La0.6Sr0.4Co0.8Fe0.2O3 hollow fibre membranes with highly concentrated CO2 exposure. *Journal of Membrane Science*, 389:216–222, 2012. ISSN 03767388. doi: 10.1016/j.memsci.2011.10.032. URL http://dx.doi.org/10.1016/j.memsci.2011.10.032.

7

CRYSTALLOGRAPHIC EFFECT UPON DEGRADATION

In the previous chapter, Sr-based particle growth was observed to vary from grain to grain where the shape of certain particles suggested that the growth was influenced by the underlying grain crystallography. Prior to annealing in the HT-ESEM, Electron Back-Scattered Diffraction (EBSD) was performed in order to characterise the crystal orientation for each grain. The same area could then be observed during an anneal in the HT-ESEM, allowing direct comparison between particle growth and crystal orientation. The size and quantity of particle growth observed during the pure water anneal enabled the greatest clarity for comparison between the two data sets.

In addition, twinning was observed in a large proportion of the material and believed to influence the particle growth of the material. Potential habit planes (plane shared by two domains) were able to be determined for the twin structure, however, a 'pseudo-symmetry' problem was observed due to the trigonal crystal structure of $La_{0.6}Sr_{0.4}Co_{0.2}Fe_{0.8}O_{3-\delta}$. This chapter also details the methodology used to deconvolute EBSD data.

7.1 PSEUDO-SYMMETRY OF LSCF

7.1.1 *Definition of Pseudo-Symmetry*

Analysing EBSD data is multi-step process, however, it may be performed relatively quickly using modern analysis hardware and software. In this work the Espirt 2.0 software by Bruker [1] was used. As detailed in Section 4.1.2 EBSD grain orientation maps were collected for the samples to be analysed in the HT-ESEM and for the twin habit plane analysis. To obtain information from the experimentally collected EBSPs, the software must locate the central trace of each Kikuchi

band using a 'Hough transform' [2]. If the EBSP pattern quality is high[1] it is then possible to index the system by comparing the experimental bands to 'simulated' Bragg-diffracting planes (reflector planes or 'reflectors') generated from a reference structure chosen by the user. If there is good correlation between the experimental Kikuchi bands and reference planes the crystallographic orientation may then be determined by calculating the planar angles between the detected bands and sample geometry.

In the case of $La_{0.6}Sr_{0.4}Co_{0.2}Fe_{0.8}O_{3-\delta}$, the Trigonal Bravais lattice (Figure 80(a)) is a complex crystal structure comprised of multiple rhombohedral unit cells and, as discussed in Section 2.1.6, a large percentage of the grains form twins. Translations of the crystal structure due to twinning generally correspond to very subtle shifts in EBSP features (such as minor changes in band contrast or position [3]). As a result, 'weak' reflections are commonly ignored or miss-matched by the automatic indexing process in the EBSD software, causing what is referred to as a 'Pesduo-symmetry' problem. Figure 80(b) shows an EBSD grain orientation map of an LSCF sample indexed using the trigonal phase. The Red, Green and Blue (RGB) colour space corresponds to the crystallographic direction normal to the viewing plane. The colour space is defined with respect to the inverse pole figure between common directions (see the legend in Figure 80(b)). As can be seen, in a pseudo-symmetry problem, every grain contains randomly distributed, abrupt, changes in crystal orientation which makes data difficult to interpret. A common method for solving this problem is to analyse the system using a simpler crystal structure and correlate common reflectors in order to construct a reference data set for the complex crystal structure.

7.1.2 *Pseudo-Symmetry Correction in LSCF*

In order to analyse the EBSD data for LSCF it was first necessary to index the system using a simplified crystal structure. This may be performed as many of the symmetry elements in the more symmetric (ie. BCC) phase are also found in the less symmetric (ie. LSCF) phase. Figure 81 shows a experimentally collected EBSP for LSCF using a ferritic Body Centred Cubic (BCC) cell crystal structure to index the EBSPs. The green lines represent the 'simulated' bands when using a BCC structure to index the system. As can be seen, multiple reflectors are shared

1 Where the band contrast is high.

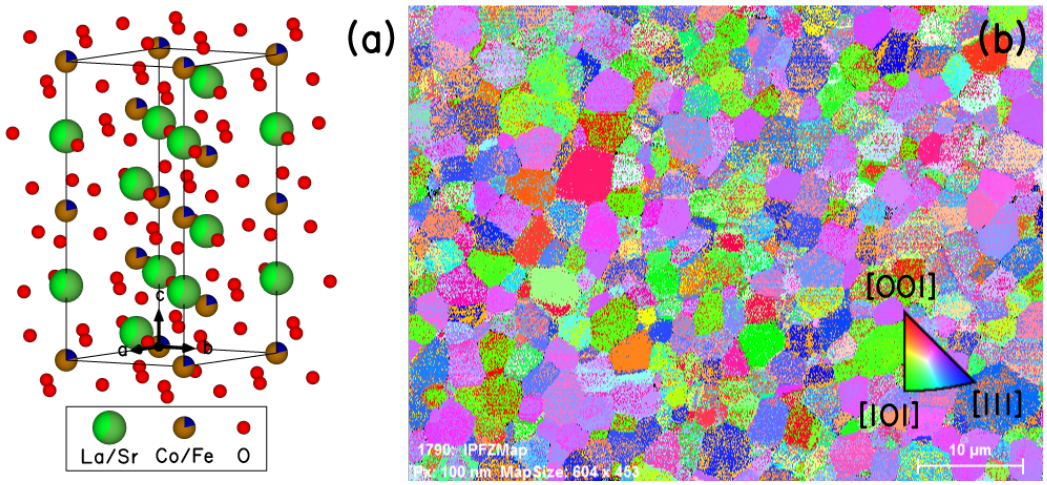


Figure 80: Showing (a) the trigonal crystal structure of $La_{0.6}Sr_{0.4}Co_{0.2}Fe_{0.8}O_{3-\delta}$ (where $a = b, c, \alpha = \beta = 90°$ and $\gamma = 120°$) and (b) the corresponding EBSD grain orientation map (where z-axis is out of plane) of $La_{0.6}Sr_{0.4}Co_{0.2}Fe_{0.8}O_{3-\delta}$ with a pseudo-symmetry problem.

between the BCC and trigonal phase, however, some higher order reflectors are absent from the indexing processes (indicated by the white arrows). This may arise because they are simply absent from the BCC index lookup table[2], however, it is more likely that the reduced symmetry of the LSCF structure results in a higher number of reflectors. Figure 82 shows a comparison between (a) the experimental EBSP, (b) the simulated BCC diffraction pattern and (c) the simulated diffraction pattern for the trigonal LSCF phase. Again, differences may be observed in reflector width and intensity, however, many similar reflectors may be observed in both diffraction patterns.

Figure 83 shows the effect of re-indexing using the BCC phase. The simpler structure enables a clearer representation of each grain's crystal orientation, however, the trigonal system contains multiple rhombohedral unit cells. Thus, multiple equivalent orientations of the measured diffraction pattern will necessarily exist. Therefore, BCC indexing cannot be used to confirm crystallographic orientation as the different variants cannot be distinguished. As mentioned, however, this ultimately may be negated by re-analysing the sample using the trigonal phase with the BCC indexing as a reference.

2 Typically, not every reflector is indexed in order to speed up the computational analysis.

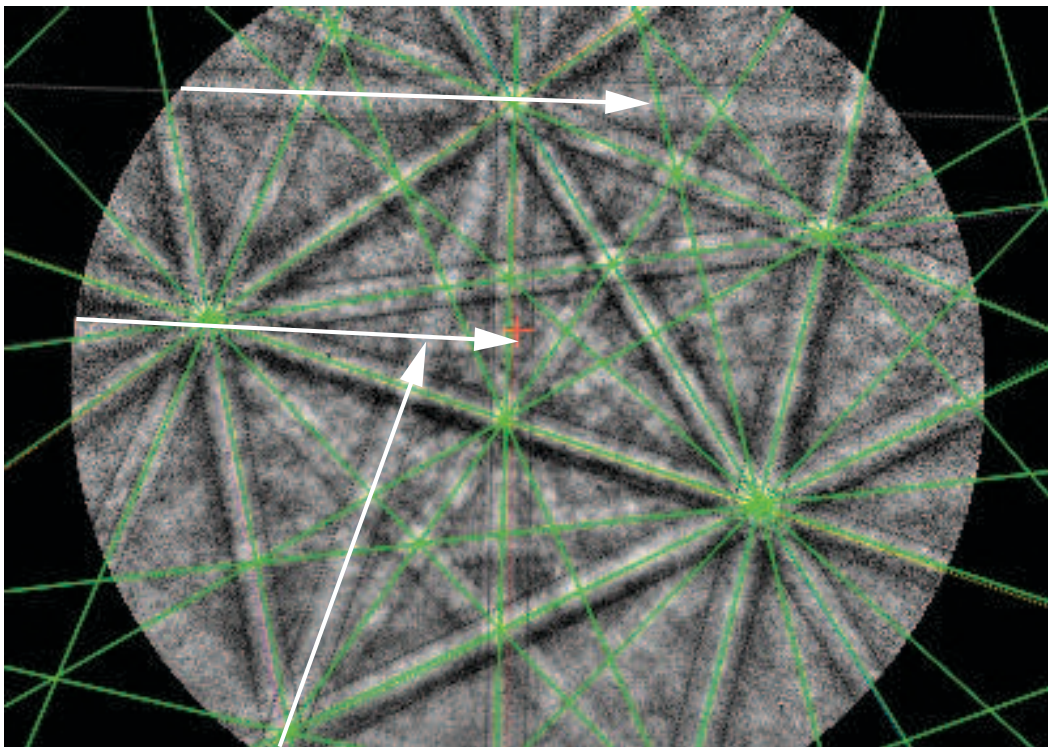


Figure 81: Showing experimentally collected EBSP of LSCF (trigonal phase). The green lines represent the expected position of the Kikuchi bands based on a BCC crystal structure and the white lines show missing high-order reflectors absent from the indexing.

7.2 TWINNING IN LSCF

Vullem *et al.* [4] observed that the percentage of grains containing a 'twin-like' domain structure in $La_{0.5}Sr_{0.5}Co_{0.5}Fe_{0.5}O_{3-\delta}$ was close to 100%. They suggested that 'traditional' twinning did not exist (in that a shared habit plane was not observed), however, very small (5-20 nm) periodic monoclinic domains sat side by side with a 'stress-free planar domain wall'. Figure 84 confirms that a domain structure also exists in $La_{0.6}Sr_{0.4}Co_{0.2}Fe_{0.8}O_{3-\delta}$. In agreement with the observations of Vullem *et al.*, a large proportion of the grains show evidence of a 'twin-like' structure, however, contrary to their findings $La_{0.6}Sr_{0.4}Co_{0.2}Fe_{0.8}O_{3-\delta}$ appears to exhibit more traditional twinning. Large domains approximately 1-3 μm in width were observed across multiple grains. In both images some grains exhibit high contrast between domains, however, it is difficult to distinguish the domains in other grains. In order to increase the clarity of the domains Figure 85 was generated from the EBSPs after conversion to Rodrigues-Frank space [5, 6]. The 'Rodrigues rotation formula' is an efficient algorithm for rotating a vector with respect to a given axis and an-

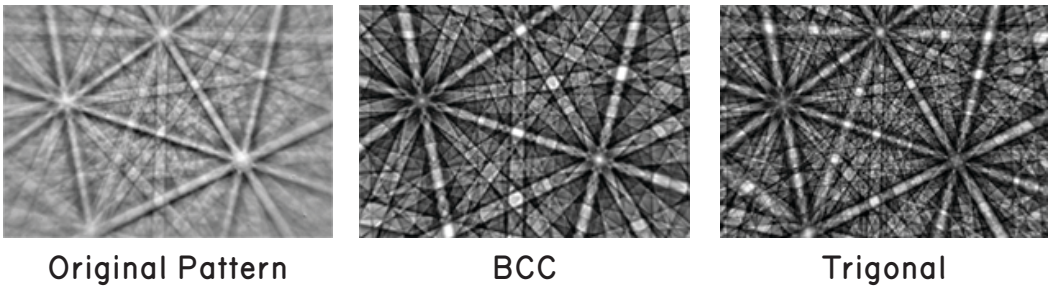


Figure 82: Showing the similarities between the experimentally measured electron diffraction pattern, simulated diffraction pattern for a simple ferrite BCC crystal and LSCF trigonal crystal at the same crystal orientation.

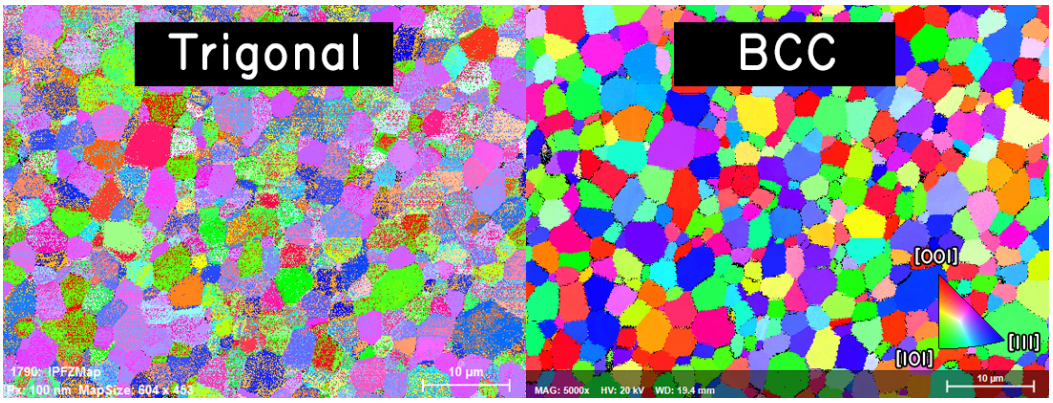


Figure 83: Showing the effect of simplifying the indexing process from a trigonal phase to a BCC phase.

gle of rotation. In this work the rotation of the crystal from a reference vector (the plane normal of a grain) could be calculated and assigned a corresponding RGB change where the angle rotation from the x,y and z axis corresponded to change in R,G and B, respectively[3]. Each grain is treated separately (as most are likely to exhibit a different plane normal) therefore the contrast is non-comparable across the image, however, the twinning is significantly clearer across all of the grains.

Notably, some grains appear to contain two twin orientations. This is clearly observed in the top left grain of Figure 85. Huang *et al.* [7] observed a microstructure similar to that presented here and noted that the domains reacted to external stresses by switching orientation. Therefore, it is possible that strain effects induced during sintering or polishing may have begun to rotate the domains. However, this result might also suggest that multiple twin habit planes might exist within the system. It is clear from the previous chapter that the growth nature of Sr-based particles is affected by the underlying crystallography, however,

3 This work was completed in collaboration with by Dr Aimo Winkelmann (Bruker Nano GmbH).

it is unknown whether the mechanical properties of the system influence the segregation rate of the material or offer alternate nucleation sites on the material surface.

7.2.1 *Twinning Habit Plane*

In order to correlate the HT-ESEM data with the crystal orientation the habit plane must be found. To confirm that a domain structure and therefore twinning was actually being observed, two EBSPs were collected from adjacent domains. Figure 86 shows the microstructure and the domains from which the EBSPs were taken. The greyscale intensity of both EBSPs was normalised to allow the image of domain 1 to be subtracted from domain 2. As can be seen from the difference map the primary reflectors are very similar, however, they have been slightly shifted and expanded due to the superstructure of the LSCF phase. The distortion is characteristic of a switch along a particular crystallographic axis and thus confirms that twinned domains are present.

The EBSD grain orientation maps presented so far have shown the orientation of the z-axis direction with respect to the viewing plane. For simplicity, the viewing plane was chosen to be the (100) plane and thus the crystallographic orientation from each EBSP may be plotted on a standard stereographic projection[4]. The distribution of directions on a stereogram is referred to as the 'texture' of the material and may be used to provide an overview of the distribution of crystallographic orientations within a system. It is often necessary to correlate texture with respect to multiple planes in order to define the crystallographic relationships within a system. A 'pole figure' is the general name given to a stereographic projection where viewing plane may be chosen.

In order to calculate the twin habit plane a simple stereographic analysis may be performed comparing the habit plane direction and texture observed on specific pole figures[5]. In Figure 84 and 85 the viewing plane is defined by a crystallographic plane. If it is assumed that the viewing plane is the (100) plane, a 'standard' stereographic projection may be used. Under this regime a 'trace' made along a twin plane (see Figure 87(a)) may be directly correlated to a rotation in the x-y plane. The trace direction then defines a direction parallel to

4 Of course the grain orientation map with respect to x and y may be used if an appropriate rotation of the stereogram is made.

5 Only the knowledge of how stereographic plots are constructed is necessary here.

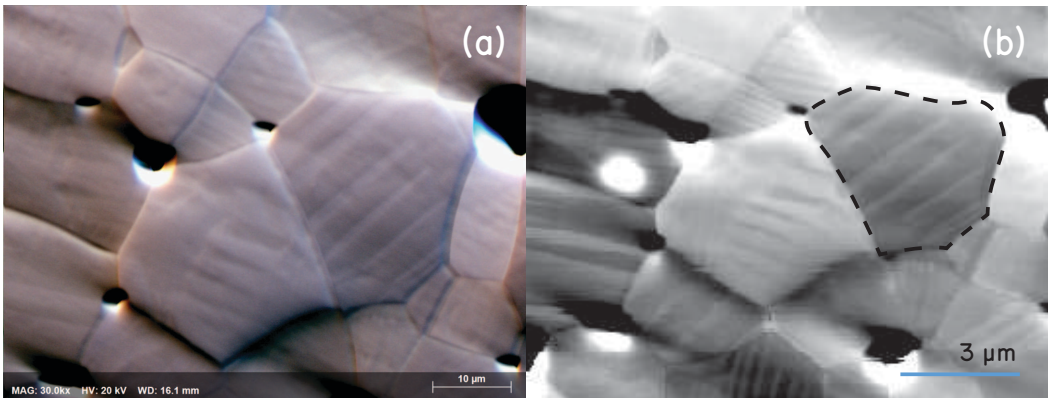


Figure 84: Showing (a) a forescattered electron image of $La_{0.6}Sr_{0.4}Co_{0.2}Fe_{0.8}O_{3-\delta}$ and (b) an image constructure from the EBSPs. The contrast in both images is representative of orientational differences and thus isoloated regions confirms domains and twinning.

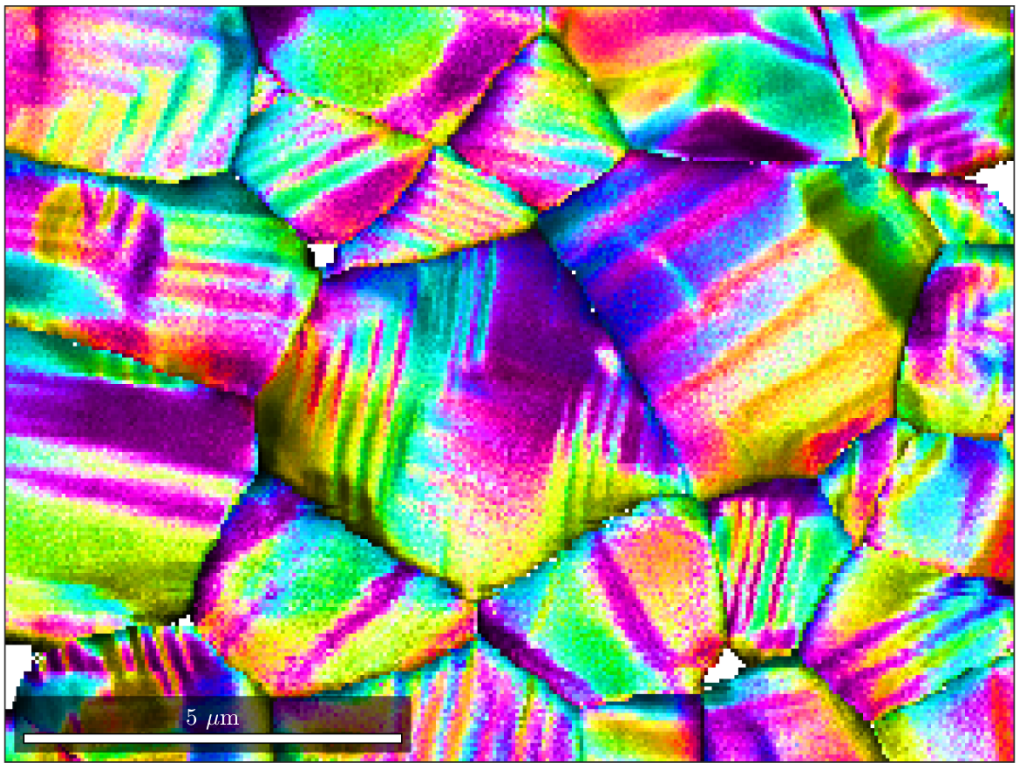


Figure 85: Image generated from the EBSPs after conversion to Rodrigues-Frank space where the shift in RGB from white represents a rotation of the crystal. Each grain is treated separately, therefore the colour contrast is non-comparable across the image.

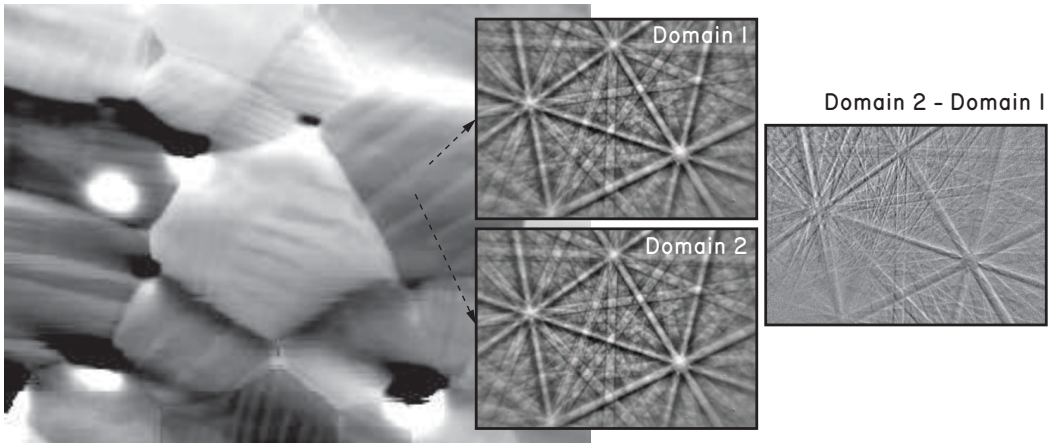


Figure 86: Showing the experimental EBSPs from two different domains within the same grain. The greyscale intensity was normalised then the pattern of domain 1 was subtracted from domain 2 to produce a difference image.

the habit plane. As shown in Figure 87(b), by extending this trace to the great circle through the centre of the stereogram a plane perpendicular and aligned to the trace direction is defined. The only degree of freedom for this plane is a rotation *around* the trace direction. The construction plane (blue) may therefore be used to define any perpendicular plane (yellow) as the intersection with the stereogram must be contained along the bi-sector of the original trace. In the case where the construction plane is orthogonal to the viewing plane (Figure 87(c)) the perpendicular plane is therefore represented by two points at great circle along the bi-sector. However, if the construction plane contains a degree of rotation, the intersection with the stereogram will be shifted along the bi-sector accordingly (Figure 87(d)). The relationship continues to hold when the viewing plane is changed as shown in Figure 87(e) (although the trace direction and thus the intersection positions on the stereogram may change). Therefore, it is possible to use this analysis method to define planes that are parallel to the trace direction and, by inference, potentially the habit plane of the twinned domains.

Ideally an image reconstructed using the EBSPs should be used to measure the trace direction. However, it should be noted that the electron beam may shift during the analysis, causing distortions in the reconstructed image that may result in trace misorientation. Use of a forescattered or SE image alleviates image distortion, however, orientation information contained within the image must be considered and aligned appropriately[6].

6 Matching the shape of the grains is usually enough to align two images sufficiently.

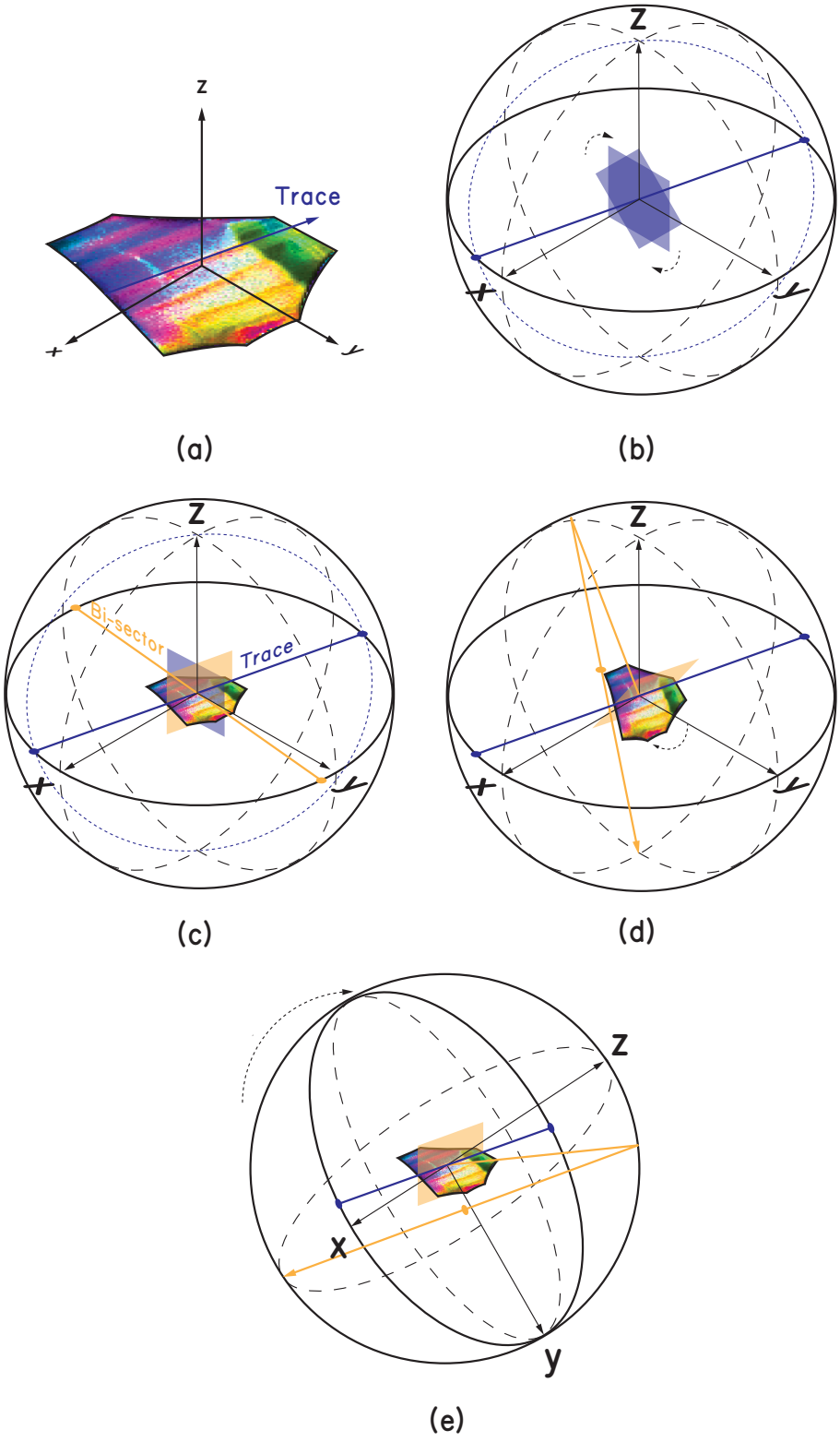


Figure 87: Schematic of (a) an isometric view of a grain containing twinning (from Figure 85) where the viewing plane is perpendicular to the surface of the material, (b) the rotational degree of freedom of the plane constructed by the trace, (c) the same plot with the perpendicular plane (yellow) defined by the trace, (d) the grain rotated around the trace direction and the corresponding plane orientation and equatorial interaction (note that this is perpendicular to the trace direction) and (e) the plane in its original orientation but with the viewing plane rotated.

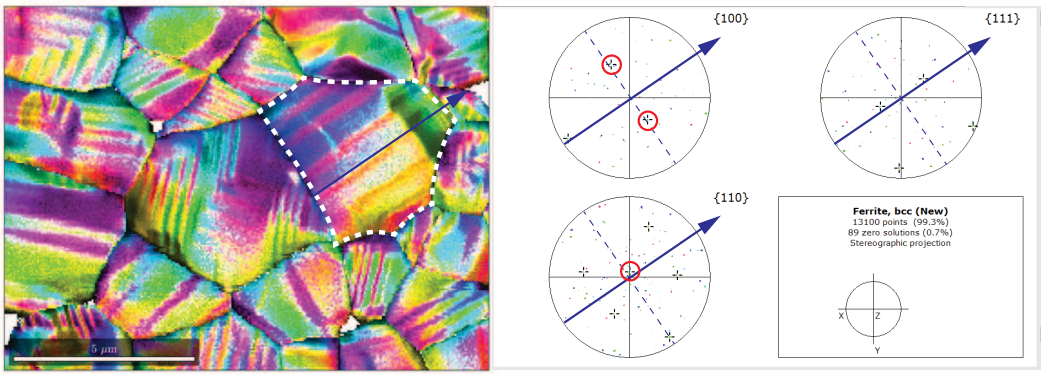


Figure 88: Showing the twin structure and associated texture on pole figures of the {100}, {110} and {111} family of planes. The trace of the twin plane and bi-sector (dotted line) has been overlaid across the pole figures. The crosses on the pole figures represent the crystal orientation of a pixel within the selected grain.

In order to narrow the search for potential planes, the BCC indexed EBSD map was used initially. Figure 88 shows the texture for the grain highlighted where the black crosses on the pole figures represent the stereographic intersections (and thus the grain orientation). Along each stereogram the trace (solid arrow) and bi-sector (dotted line) have been overlaid on the {100}, {110} and {111} pole figures. As can be seen the {100} and {110} contain a plane that is perpendicular to the trace. This observation agrees with Vullem *et al.* [4] when considering a pseudo-cubic structure, however, further analysis is required when considering the trigonal system.

As can be seen from Figure 89 the $\{100\}_{BCC}$ family is equivalent to the (010) and $(\bar{1}20)$ (or $(1\bar{2}0)$ plane) in the trigonal system. Due to the different space group, the (110) plane cannot be directly translated, however, the intersection between the (110) and $(\bar{1}20)$ plane has threefold rotational symmetry around the z-axis [8]. As a result, these planes appear equivalent at specific orientations such that this analysis method cannot distinguish which plane is dominant. Figure 90 shows the same analysis as in Figure 88, however, the EBSD map has been indexed using the trigonal LSCF phase. In this particular grain only the {110} and $\{\bar{1}20\}$ family of planes are contained along the bisector. In the grain to the left (Figure 91) the reverse is true where only the {001} is contained along the bi-sector.

This result suggests that two habit planes co-exist, corroborating the speculation made earlier in this chapter. Once again observing the top left grain in Figure 85 it can be seen that the twin domains are orientated in two directions,

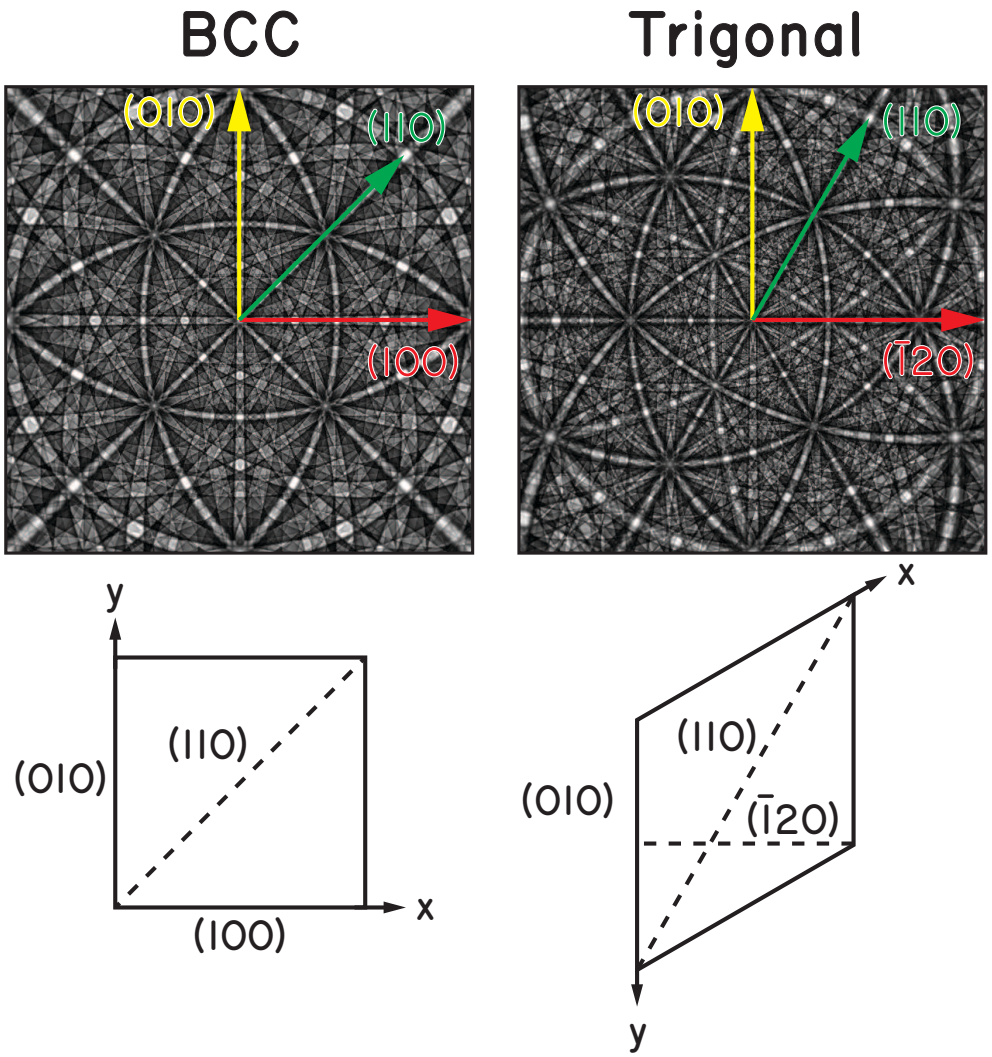


Figure 89: Showing a sterographic projection of the EBSP and unit cell along the z-axis for both the BCC and trigonal crystal structure. Equivalent planes between the two structures gave been indicated.

approximately orthogonal to one another[7]. Bi-sector analysis confirms that both potential twin habit planes are contained within this grain, however, it is unclear from this analysis the precise nature of the twin plane at each orientation. From Figure 85 it can be seen that the interface between the two domain orientations is not fully coherent. There appears to be a disordered region at interface due to the presence of a change in orientation (colour change on the image), suggesting that this interface is not a shared habit plane. Therefore, it would appear that the observed twinning is a result of two distinct twin orientations within the same grain. As can be seen in Figure 89, the {001} and {$\bar{1}$20} planes are orthogonal

7 Beam drift and surface roughness effects the image will distorted the image slightly. As a result, measuring the image for the angular difference will contain some error.

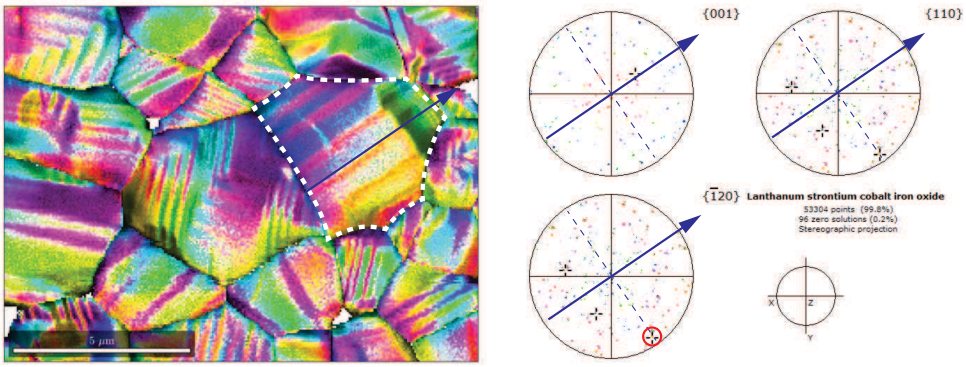


Figure 90: Showing the twin structure and associated texture on pole figures of the {001}, {110} and {1̄20} family of planes for the grain outlined. The trace of the twin plane and bi-sector (dotted line) has been overlaid across the pole figures. The crosses on the pole figures represent the crystal orientation of a pixel within the selected grain.

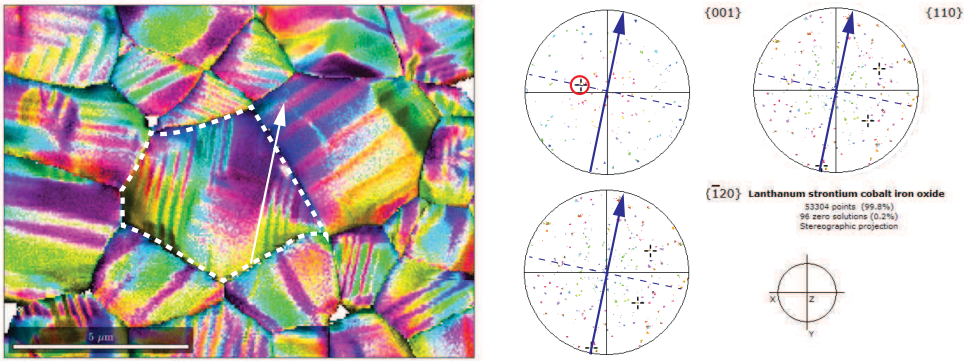


Figure 91: Showing the twin structure and associated texture on pole figures of the {001}, {110} and {1̄20} family of planes for the grain outlined. The trace of the twin plane and bi-sector (dotted line) has been overlaid across the pole figures. The crosses on the pole figures represent the crystal orientation of a pixel within the selected grain.

to one another, therefore, this results suggests that these are the dominant twin habit planes (rather than the {110}).

7.3 EFFECT OF DOMAINS ON PARTICLE GROWTH

As mentioned, the sample analysed using the HT-ESEM was analysed by EBSD prior to annealing. Figure 92 shows the forescattered electron image and grain orientation map indexed using the BCC cell. The area analysed using the HT-ESEM has been outlined. Figure 93 shows an HT-ESEM taken during the analysis at the point where particles have grown but have not begun to agglomerate. The EBSD

map has been overlaid on the HT-ESEM image as accurately as possible[8] in order to compare grain orientation to the observed particle growth. The different growth behaviour is seen to be different from grain to grain, however, consistent between the same grain orientations (represented by the same colours). Grains labelled 1 and 2 (dark blue) display the characteristic pyramidal growth along a specific direction within the grain. Grain 3 and 4 (light blue) also display directional growth, however, the particles appear smaller, 'rod like' and greater in quantity. Grain 5 (purple) shows a homogenous distribution of rounded particles. Grain 6 (red) similarly shows a homogenous distribution of the rounded particles, however, they appear larger and reduced in quantity. The RGB colour space is representative of the grain orientation. Therefore, it is clear that grains 1 & 2 and 3 & 4 share similar orientations, whereas, grain 5 and 6 are orientated at a notably different angle.

As shown previously, twinning may be observed in the forescattered electron image. However, due to the large analysis area a compromise in lateral resolution was required in order to reduce the analysis time. As a result, the low resolution of the forescattered image makes it difficult to resolve the domain structure in some grains. A direct comparison of the BCC EBSD map, trigonal EBSD map and forescattered electron image for grains 1-6 is shown in Figure 94. It is clear that in grain 1 the twin orientation aligns with the observed particle growth, however, the afore mentioned low resolution prevents direct correlation for grains 2-4. Instead the particle growth direction was used. Interestingly, grain 5 shows distinct signs of twinning in the forescattered image, however, growth on the surface appears homogenous and unaffected by the underlying crystallography.

As shown previously, twinning may be observed in the forescattered electron image. However, due to the large analysis area a compromise in lateral resolution was required in order to reduce the analysis time. As a result of the low image resolution twinning in some grains cannot be resolved. A direct comparison of the BCC EBSD map, trigonal EBSD map and forescattered electron image for grains 1-6 is shown in Figure 94. It is clear that in grain 1 the twin orientation aligns with the observed particle growth, however, the afore mentioned low resolution prevents correlation for grains 2-4. Interestingly, grain 5 shows distinct signs of twinning in the forescattered image, however, growth on the surface appears ho-

8 Again, beam drift during analysis will account for the apparent distortion in grain size and position.

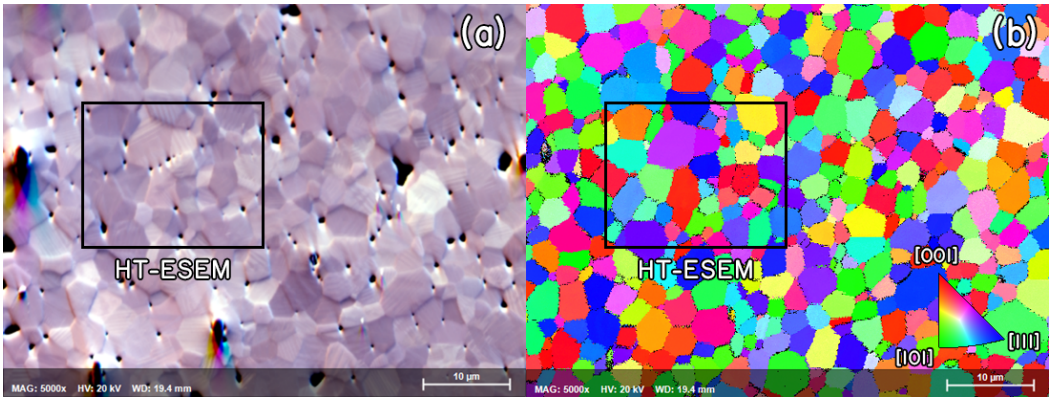


Figure 92: Showing (a) a forscattered electron image of a polished sample prior to the thermal anneal in the HT-ESEM and (b) the EBSD orientation map indexed using a simple BCC unit cell. Both images show the area analysed during the pure water HT-ESEM analysis.

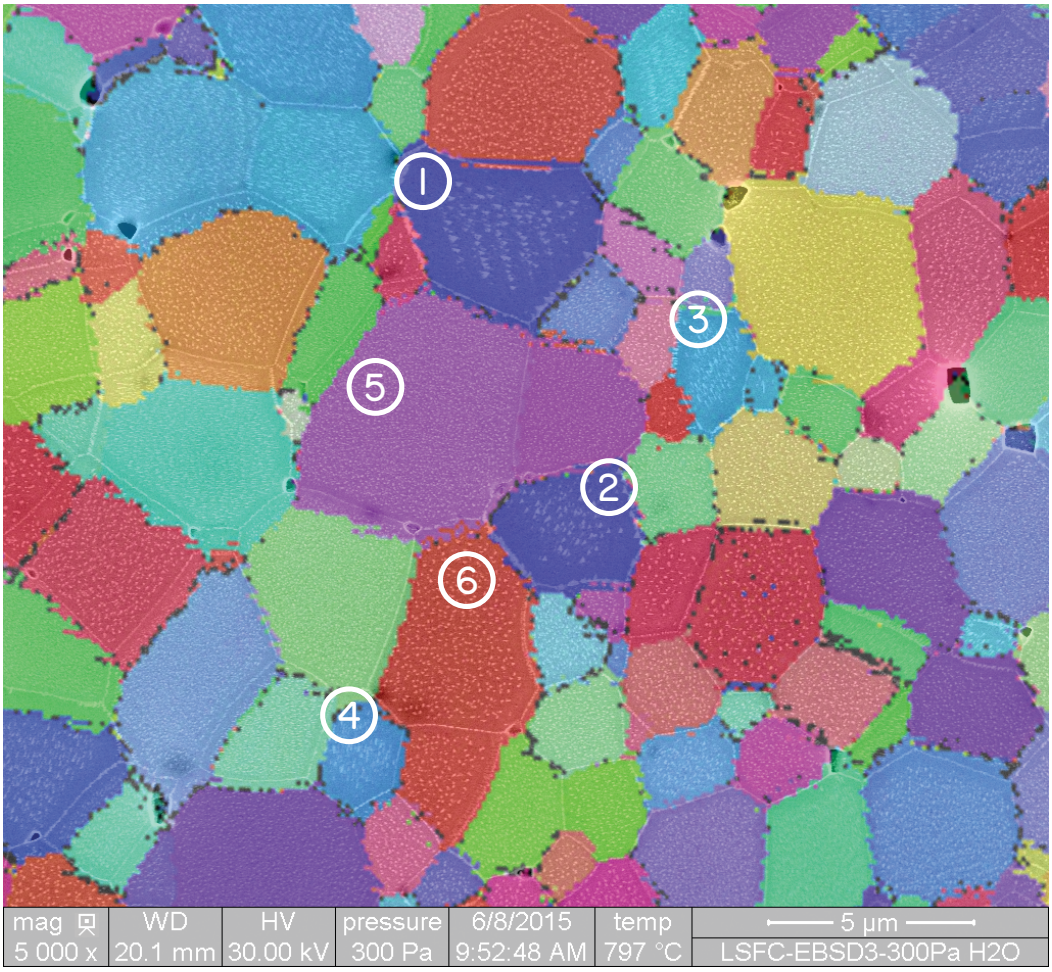


Figure 93: Showing a frame of the sample annealed in pure water (Video 3) prior to the particle agglomeration. The EBSD map shown in Figure 92(b) has been overlaid on top of the SE image. Discrepancies between the two images are to the low resolution of the EBSD orientation map in comparison to the SE image.

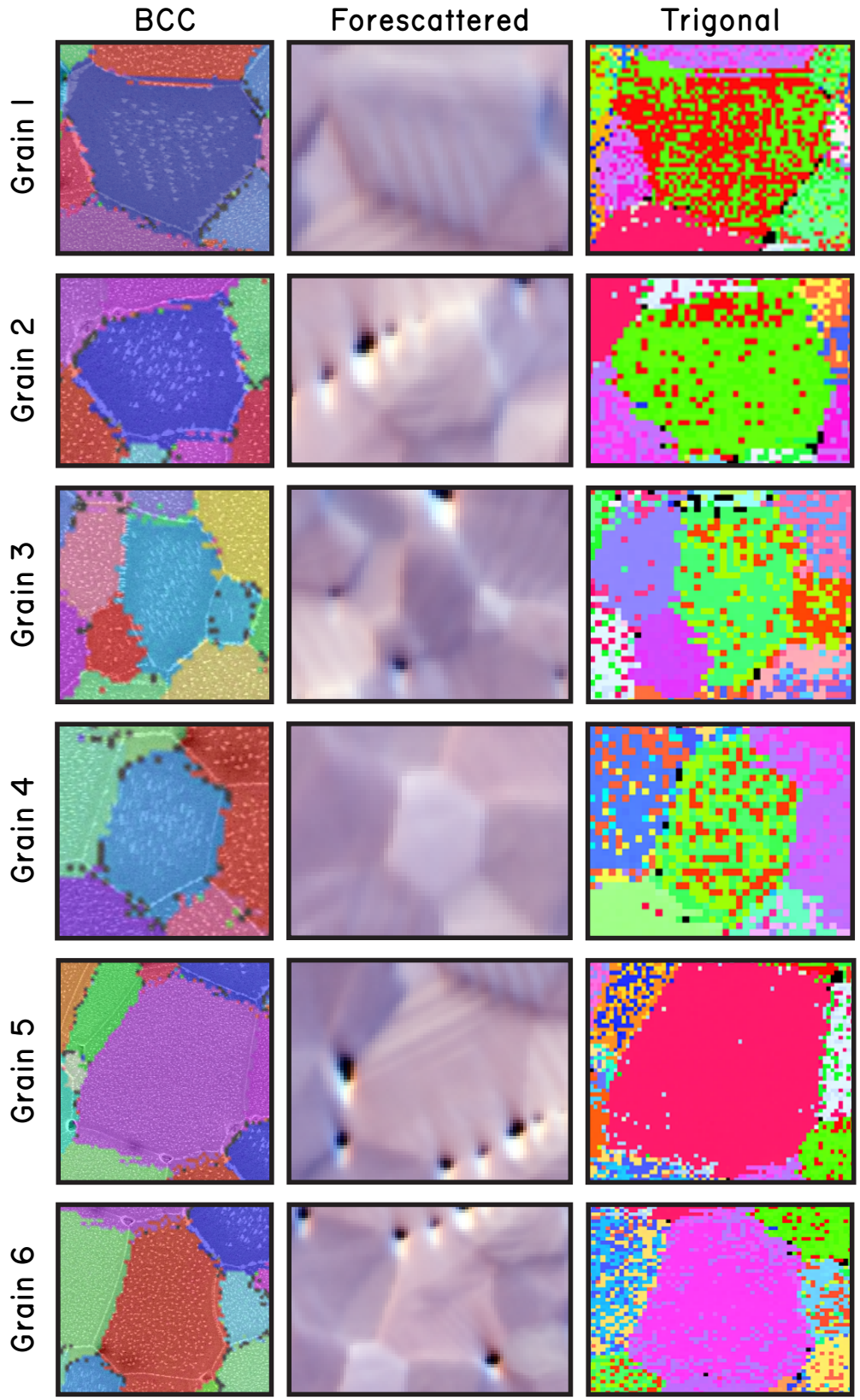


Figure 94: Showing the HT-ESEM/BCC EBSD map, forescattered electron image and trigonal EBSD map. The low resolution of the forescattered image prevents observation of twin orientations within some grains.

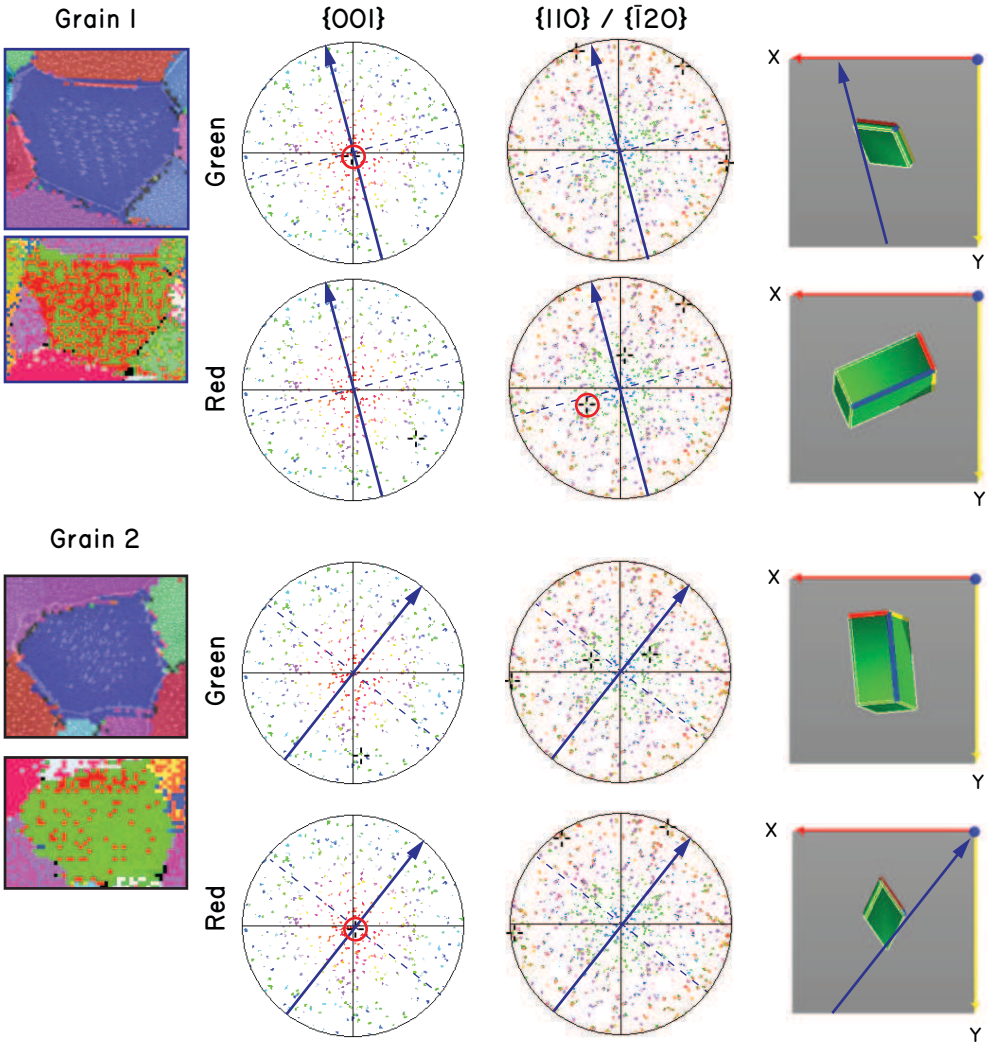


Figure 95: Showing the bi-sector analysis and trigonal crystal orientation for the different pixel colours found within grains 1 and 2.

mogenous and unaffected by the underlying crystallography.

Grains 1 and 2: After indexing using the trigonal phase, similarities between grains 1 & 2 and grains 3 & 4 were also observed. As can be seen in Figure 94 each grain contains a randomly distributed set of crystallographic orientations due to the pseudo-symmetry problem. As such it is difficult to establish precisely which orientation is truly representative of the grain. It can be seen that the domains in the forescattered image are approximately aligned with the particle growth in the HT-ESEM image (see Figure 94), therefore it was assumed that the particles were aligned to the twin habit plane. Due to the low resolution of the forescattered

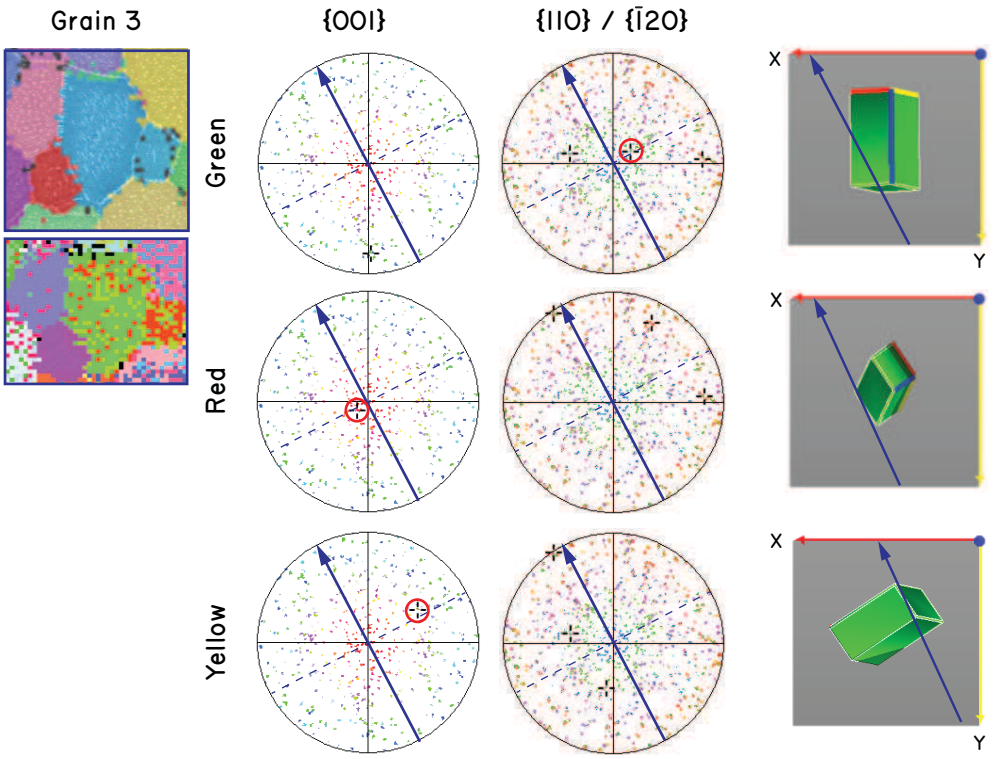


Figure 96: Showing the bi-sector analysis and trigonal crystal orientation for the different pixel colours found within grains 3. As seen in the analysis of grains 1 & 2, grains 3 & 4 are equivalent but orientated slightly differently.

image the HT-ESEM image was ultimately used to determine the trace direction. Using an image from a separate system is likely to cause some misorientation error, however, alignment of the grain shape was carried out to minimise this effect.

Specific pixels may be observed on the EBSD grain orientation map where the orientation of the pixel is represented by black crosses (or 'texture marks') on the pole figures. Multiple texture marks represent symmetric equivalencies within the system. Figure 95 shows the bi-sector analysis and crystallographic orientation for the green and red pixels found in grain 1. The green pixel has a crystallographic orientation where the [001] direction is pointing almost directly out of the page. In this situation it may be determined that the habit plane is parallel to the trace, however, a second pole figure must be used in order to calculate the correct orientation of the x-y plane. The software used in this work was able to run this process automatically and produce a three-dimensional reconstruction of the crystallographic orientation (shown to the right of the pole figures). In the green pixel the {001} lies directly along a bi-sector, however, in the red pixel

the {110} and {$\bar{1}$20} bi-sector lies approximately 10° away from the texture mark. Therefore, the results show that this grain contains {001} type twinning. This observation is corroborated by the observation that [100] direction and (001) plane matches the trace direction (see the crystallographic reconstruction for the green pixel in Figure 95).

The results for Grain 2 are reversed in terms of pixel colour, however, present the same result. It would appear that {001} twin habit plane (when the the z-axis is orientated along the [001] direction) has a direct effect upon the particle growth. The alignment of the particles shows preferential sites for growth or nucleation and the pyramidal shape of the particles suggests they have grown epitaxially. It is also possible that disorder contained within domain walls could causes an increase in strontium diffusion rate, however, it is not possible to make this distinction from these analyses.

Grains 3 and 4: The 'colour scheme' (and thus crystal orientation) of grains 3 & 4 is very similar to that of grains 1 & 2. As can be seen from Figure 96 the green and red pixel share the same characteristics to that observed in grain 2. Both the {110} and {$\bar{1}$20} planes lie approximately along the bi-sector, however, in both cases the texture mark is misorientated by approximately 2°. As the misorientation is low, it may be assumed that there was a discrepancy between the HT-ESEM image and EBSD data. In the red pixel, the trace direction can be seen to match the {001} plane and as such may be assumed to behave in a similar manner to grain 1 & 2. The primary difference is that the [001] is tilted slightly off centre. This change in orientation will alter the termination of the twin plane at the surface of the material and change the effective width of the twin at the surface. Figure 97 shows schematically how the domain width of the twinned region may be reduced as the angle between the habit plane and surface plane changes. As can be seen in Figure 94 the particles on the surface of grains 3 & 4 appear to have formed in a directional manner, however, the particles appear smaller and closer together than in grains 1 & 2. This observation would suggest that the reduction in effective domain width also affects the particle distribution at the surface.

It should be noted that a third pixel colour (yellow) is observed in grains 3 & 4. Neither habit plane is contained along the bi-sector, however, the trace along the crystal reconstruction agrees with the [100] in agreement with the previous analysis. It is unclear what the significance of this crystal orientation is in comparison

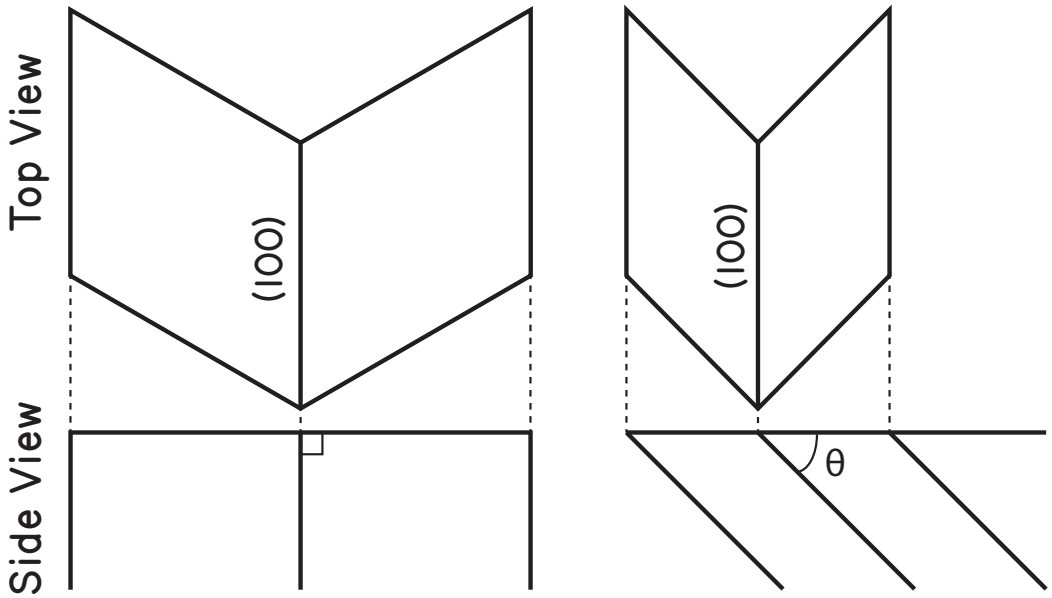


Figure 97: Showing a schematic of {001} type twinning where the twin habit plane is orthogonal to the surface or orientated at an angle θ. If the twin habit plane not orthogonal the effective 'width' of the twinning is reduced at the surface.

to the red or green pixels.

Grains 5 and 6: Observing the forescattered image of grain 5 in Figure 94 it is clear that twinning exists within the grain, however, the homogenous growth pattern of the particles suggests that, at this orientation, the twinning plane does not influence particle growth. The trigonal EBSD map shows that a single crystal orientation (red pixel) is dominant within the grain, however, bi-sector analysis (using the forescattered image to produce the trace) shows that neither the {001} or {$\bar{1}$20} habit planes were possible within this grain. Without the presence of {001} twinning it can be seen that the particles do not exhibit directional growth across the grain surface, however, the discrepancy between bi-sector analysis and the forescattered image makes it difficult to provide an explanation for this type of growth. As such, further investigation is required. Figure 98 shows the grain orientation within the dominant pixel for both grain 5 (red) and 6 (purple). As can be seen, this orientation is similar to that of grains 1-4. As mentioned previously, the particles in grain 6 appear greater in size and more spread out compared to grain 5. As can be seen in Figure 98, the orientation around the x-y plane is approximately equal, however, grain 6 has a greater rotation around the x-z plane. Given that a rotation around the x-z was seen to modify the particle

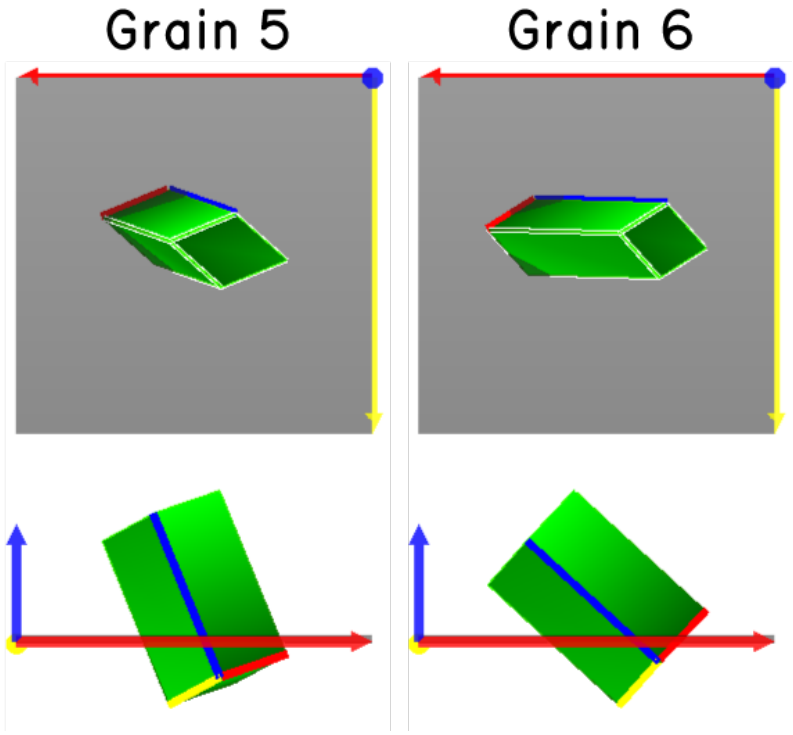


Figure 98: Showing the crystallographic orientation of the trigonal unit cell for the dominant pixel colour found in grains 5 and 6.

growth pattern between grains 1 & 2 and 3 & 4 it is possible that a similar effect is being observed in grains 5 & 6.

7.4 SUMMARY AND CONCLUSIONS

This chapter has investigated effect of crystallographic orientation had on the growth of Sr-based particles using direct comparison of EBSD and HT-ESEM data. In agreement with the literature, a large percentage of the material was observed to contain twinning and initial comparison between the data suggested that particle growth was consistent with observable domain walls. In order to determine the twin plane, bi-sector analysis was carried out, however, due to the complicated nature of the trigonal system a pseudo-symmetry problem was observed whilst trying to index the LSCF system. By simplifying the indexing process using a ferritic BCC structure, a reference analysis was able to be produced to guide analysis when using trigonal indexing. {001} and {110} twinning was confirmed as potential habit planes in the BCC structure and therefore relevant planes to analyse using trigonal indexing. It was shown that {001} and {110}

were also potential twin planes in the trigonal system, however, the symmetry of the trigonal structure meant that the {110} was equivalent to the $\{\bar{1}20\}$ and $\{1\bar{2}0\}$ planes. Bi-sector analysis simply infers which planes may be habit planes and as such could not be used to distinguish between the planes. However, it was observed that, within a single grain, two orthogonal twin planes exist. This suggests that the primary twin planes are the {001} and $\{\bar{1}20\}/\{1\bar{2}0\}$. The existence of two twin planes and their interaction requires further investigation.

Direct comparison between the EBSD and HT-ESEM data showed that {001} type twinning influences particle growth when the trigonal z-axis was aligned to the [100] direction. If the unit cell is rotated around the x-z plane the effective width of the twin domains will be reduced. Smaller, tightly packed particles were observed to form on these grains, therefore, it would appear there is a direct correlation between the termination of domain walls at the surface and particle formation.

Particles exhibiting homogenous particle growth appeared to be influenced by the underlying crystallography as an increase in particle size (and corresponding reduction in quantity) was correlated to a rotation around the x-z plane. Bi-sector analysis showed that neither of the potential habit planes were present in those particular grains, however, twinning was observed in the forescattered image. This dichotomy made it difficult to determine the cause of homogenous particle growth.

It is still unknown what mechanisms are occurring at the surface, however, it is clear that twinned material and the crystallographic orientation of the grains will affect surface properties. The results presented in this chapter suggest that twinning either: (a) enhances diffusion rates within the domain structure or (b) that the termination of the domain walls act as heterogeneous nucleation sites. Given the high activation energy of cation diffusion, the latter is more probable, however, at this point this is up for debate.

BIBLIOGRAPHY

[1] Bruker. Esprit 2.0 Software for Micro- and Nano-Analysis, 2016. URL https://www.bruker.com/products/x-ray-diffraction-and-elemental-analysis/eds-wds-ebsd-sem-micro-xrf-and-sem-micro-ct/esprit-2.html.

[2] R O Duda, D G Stork, and P E Hart. *Pattern Classification*. 2001.

[3] G. Nolze, C. Grosse, and A. Winkelmann. Kikuchi pattern analysis of noncentrosymmetric crystals. *Journal of Applied Crystallography*, 48:1405–1419, 2015. ISSN 16005767. doi: 10.1107/S1600576715014016.

[4] P E Vullum, H L Lein, M A Einarsrud, T Grande, and R Holmestad. TEM observations of rhombohedral and monoclinic domains in LaCoO3-based ceramics. *Philosophical Magazine*, 88(8):1187–1208, 2008. ISSN 1478-6435. doi: 10.1080/14786430802082016.

[5] R. Becker and S. Panchanadeeswaran. Crystal Rotations Represented as Rodrigues Vectors. *Textures and Microstructures*, 10(C):167–194, 1989. ISSN 0730-3300. doi: 10.1155/TSM.10.167.

[6] Youliang He, Stéphane Godet, and John J. Jonas. Representation of misorientations in Rodrigues-Frank space: Application to the Bain, Kurdjumov-Sachs, Nishiyama-Wassermann and Pitsch orientation relationships in the Gibeon meteorite. *Acta Materialia*, 53(4):1179–1190, 2005. ISSN 13596454. doi: 10.1016/j.actamat.2004.11.021.

[7] B X Huang, R W Steinbrech, and J Malzbender. Direct observation of ferroelastic domain effects in LSCF perovskites. *Solid State Ionics*, 228:32–36, 2012. ISSN 0167-2738. doi: 10.1016/j.ssi.2012.08.025. URL http://dx.doi.org/10.1016/j.ssi.2012.08.025.

[8] Jeremy Cockroft. R-3c Space Group (Trigonal), 1997. URL http://img.chem.ucl.ac.uk/sgp/large/161bz1.htm.

8

BACK EXCHANGE TECHNIQUE DEVELOPMENT

In this chapter, the experimental development process of the novel 'Back-Exchange' technique is detailed. An extension to the well-established IEDP technique, back-exchange adds an additional anneal step in order to measure the self-diffusivity and surface exchange coefficient of a material in any gas environment (containing the same $p(O_2)$ as the initial exchange). Although capable of measuring both parameters, the primary focus of the technique was to measure changes in surface exchange coefficient. This work was completed in conjunction with Dr Sam Cooper who developed the analytical and numerical modelling methods for analysing back-exchange data. A short summary will be presented here, however, for the full details behind the analytical and numerical method please refer to [1].

8.1 BACK-EXCHANGE THEORY

Crank's semi-infinite solution to the diffusion equation has been used for many years to analyse experimental diffusion data. The additional anneal step complicates the solution as there is a change to the surface boundary condition in between anneals. Cooper has proven that an analytical solution exists for the case where $D_1 = D_2$ and $k_1 = k_2$. This solution was used to validate the finite-difference numerical model used to fit experimental data.

Using the validated numerical method, a wide range of idealised back-exchange curves could be generated in order to predict optimal experimental conditions. A back-exchange consists of 6 parameters: D_1,k_1, t_1 of the forward exchange and D_2,k_2, t_2 of the back-exchange. For the sake of clarity, tracer diffusion and surface coefficients will be referred to without the * sign in this chapter. Figure 99 shows a plot of all possible back-exchange curves by varying the key metrics: k_2/k_1

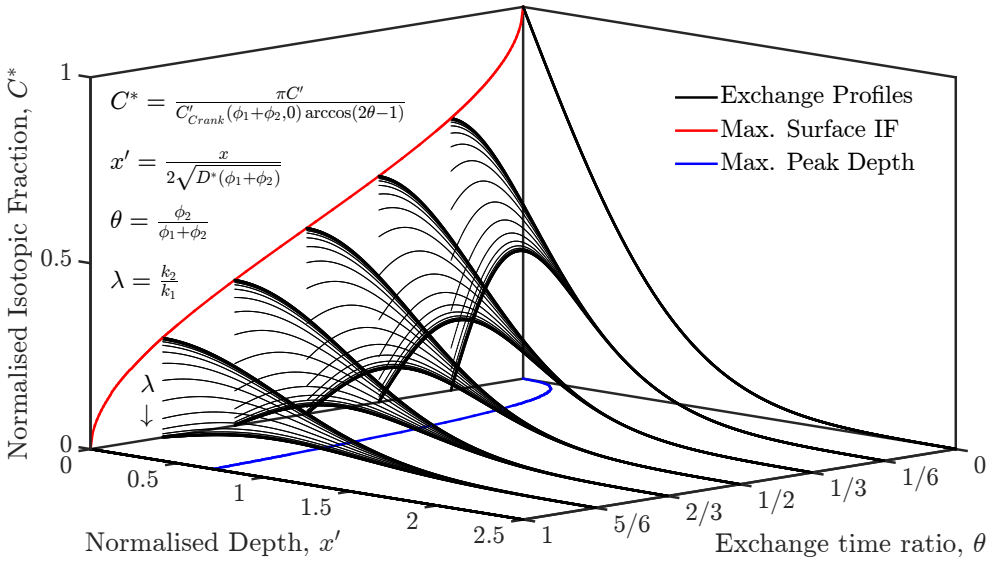


Figure 99: Plot containing normalised back-exchange profiles across the full range of possible exchange time ratios, where D is constant for both exchanges. A family of curves is shown at 7 values of the time ratio, θ. Each family is generated by varying the ratio of effective surface exchange coefficients, k_2/k_1. The maximum depth of the turning point is shown for each family, as well as the maximum surface concentration. To account for variation in k_1, all profiles have been normalised with respect to the surface concentration found in the $\theta = 0$ case. Recreated with permission from [1].

ratio (λ) and exchange time ratio ($t_2/(t_1 + t_2)$)[1]. To minimise fit uncertainty, an ideal back-exchange curve should exhibit a large surface isotopic fraction range and a well-defined peak[2]. As can be seen, an exchange time ratio of between 0.33 ($t_1/2 = t_2$) and 0.5 ($t_1 = t_2$) offers the ideal experimentation range.

It is important to note that there is an upper limit for the measurement of k values due to the asymptotic behaviour of the diffusion equation. The metric 'h' is often used to define the relationship between surface exchange and self-diffusivity is:

$$h = k/D \tag{8.1}$$

1 Assuming a constant $D_1 = D_2$ as the material bulk should remain unchanged during both anneal steps.

2 Well defined in this case is related to the peak position into the material. If the peak is close to the surface the definition of the initial 'downturn' of the curve will be poor and thus increase uncertainty of k_2.

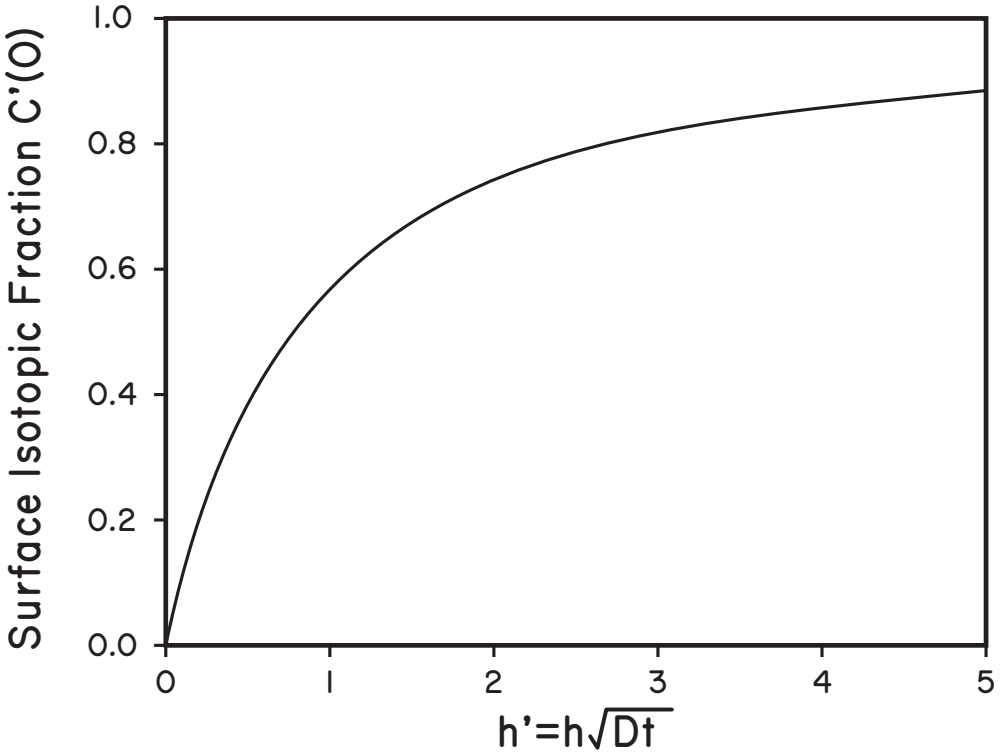


Figure 100: Surface isotopic fraction against $h\sqrt{Dt}$ for a single value of D.

The 'surface' may be defined where $x = 0$, therefore, Equation 4.3 may be simplified to:

$$C'(0) = \frac{C(0) - C_{bg}}{C_g - C_{bg}} = 1 - exp\left(h^2 Dt\right) erfc\left[h\sqrt{Dt}\right] \tag{8.2}$$

Figure 100 shows a plot of surface concentration against $h\sqrt{Dt}$ for standard exchanges with a constant D value. As h increases (therefore k) it can be seen that surface concentration increases, but, tends towards an asymptote. When k is high it can be seen that the equivalent surface concentration will lie along the horizontal asymptote. Interpretation of data then becomes difficult as small differences in surface concentration could represent significant changes in k. As will be discussed in Chapter 9 it is often the case that the first few points of a line-scan measurement often contain the highest uncertainty, further reducing the accuracy of k measurement. Most materials tend not to have very high h values, however, in the presence of water vapour surface exchange may be enhanced causing an effective increase in h. For the back-exchange step the same limitation

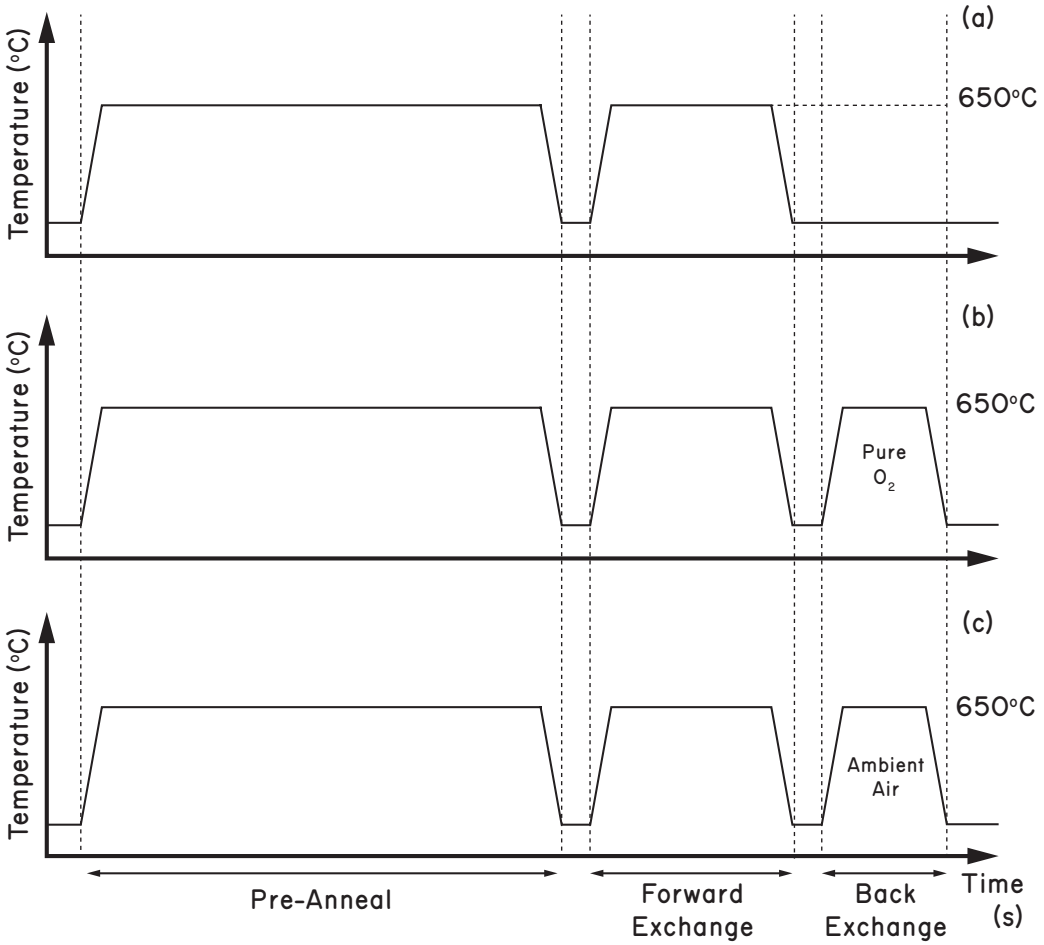


Figure 101: Showing schematic temperature-time profiles for the validation experiment where (a) is a standard forward exchange, (b) is the back-exchange using pure oxygen and (c) is the back-exchange using ambient air.

exists, and as such Cooper has suggested that a maximum measurable change between k_1 and k_2 is approximately 100 times [1].

8.2 EXPERIMENTAL DEVELOPMENT

8.2.1 *Experimental Validation*

To validate the technique experimentally, a pair of experiments were necessary. Multiple samples were exchanged at the same time using the standard IEDP technique. One sample was left 'as-exchanged' and the second was treated to a back-exchange using pure oxygen. If each of the D and k values across both experiments were equal it would show that the technique and analysis methodology

could be used to observe changes in k_2. A third sample (exchange at the same time as the first two) was back-exchanged in ambient air to demonstrate that technique can provide data in alternate environments. The k_2 value in the third experiment was compared to the that of the pure, dry, oxygen back-exchange. Figure 101 shows idealised temperature-time profiles of these experiments.

Samples were exchanged at 650°C as this is representative of an IT-SOFC operating temperature. The chosen exchange time for both forward and back-exchange was 1.5 hours ($\theta = 0.5$) in order to provide a convenient diffusion length for line-scan analysis (~100 μm). A 1.5 hour timer was started as the furnace was placed over the sample. When the timer finished the furnace was removed. The activation energy for diffusion in $La_{0.6}Sr_{0.4}Co_{0.2}Fe_{0.8}O_{3-\delta}$ at 650°C was taken to be 1.9 eV from [2] which resulted in a 'corrected' anneal time of 1.38 hours. The gas concentration was calculated to be 85% from both an oxidised piece of silicon and RGA analysis. The back exchange in ambient air was performed in an air-conditioned laboratory room (with no windows) where room temperature was 26°C and relative humidity at 30% (~10 mbar $p(H_2O)$). A relatively long pre-anneal was applied to the samples. The reasons for this will be discussed in Section 8.2.2. Samples were analysed using a ToF-SIMS 5 instrument in burst-alignment mode with a 300x300 px analysis area.

Figure 102, 103 and 104 show the measured diffusion profiles for the forward exchange, back-exchange in pure O_2 and back-exchange in ambient air respectively. Each Figure shows the D and k fit parameters for the experiment and are summarised in Table 12. Each fit exhibits very high 'goodness of fit', however, it is clear that there is a degree of noise in each diffusion profile. Next to each diffusion profile is an uncertainty contour map representing a range of potential fitting parameter values. For the forward exchange D and k are the only variables, however, for the back-exchanges k_1 and k_2 are compared for a single D value (where $D_1 = D_2$ is assumed). As can be seen from each contour map an 'area' within the D-k and k_1-k_2 plane offers identical goodness of fit for each diffusion profile. A range of fit parameters therefore satisfy the data, and as a result diffusion profiles are more accurately represented by a 'band' rather than a single line of best fit. Figure 105 shows a schematic representation of diffusion profile 'bands'. Methodology for generating 'band' plots has been shown by Cooper [1], however, the contour plots already enable error quantification and as such were not necessary here.

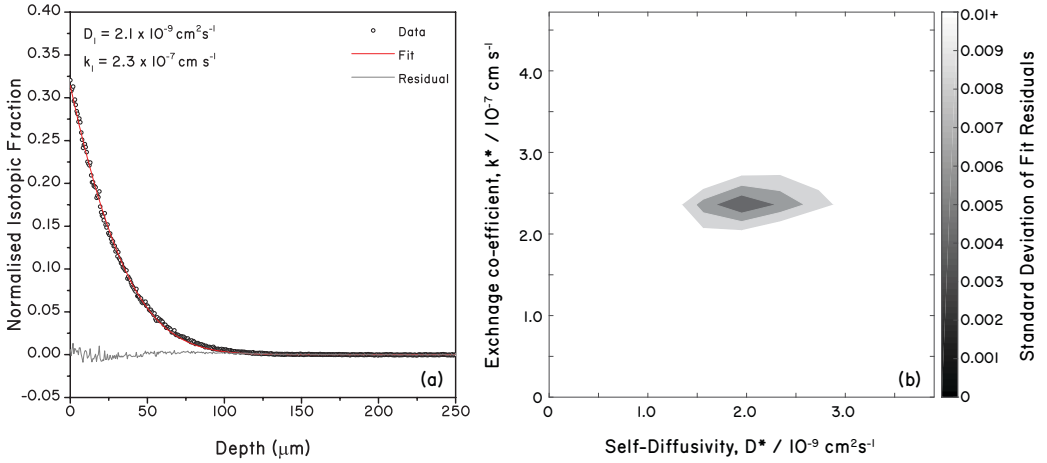


Figure 102: Showing (a) the forward exchange diffusion profile for the validation and (b) uncertainty contour map in D and k as a result of data noise.

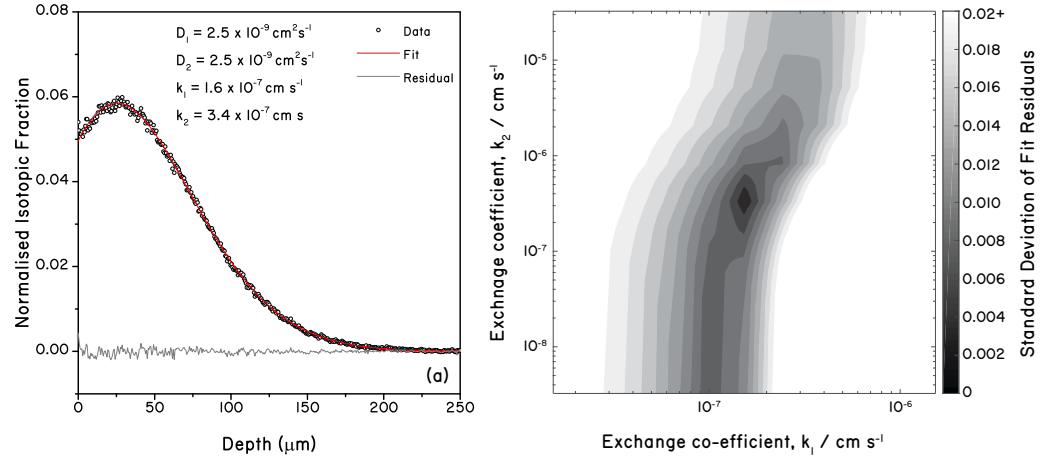


Figure 103: Showing (a) the back-exchange diffusion profile for the validation and (b) uncertainty contour map in k_1 and k_2 as a result of data noise.

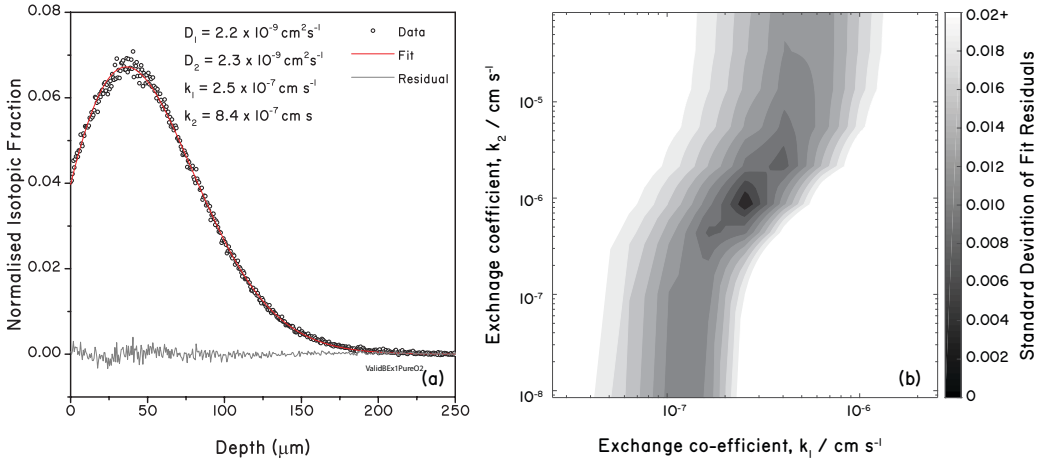


Figure 104: Showing (a) the back-exchange diffusion profile for the validation and (b) uncertainty contour map in k_1 and k_2 as a result of data noise.

Table 12: Cation ratio at the surface for LSCF samples annealed in pure oxygen and ambient air.

Experiment	**D_1 ($10^{-9}cm^2s^{-1}$)**	**k_1 ($10^{-7}cm\ s^{-1}$)**	**D_2 ($10^{-9}cm^2s^{-1}$)**	**k_2 ($10^{-7}cm\ s^{-1}$)**	**R^2**
Forward Exchange	2.1 ±0.2	2.3 ±0.2	—	—	0.998
Back Exchange (Pure O_2)	2.5	1.6 ±0.1	2.5	3.4 ±0.3	0.999
Back Exchange (Ambient)	2.	2.5 ±0.2	2.3	8.4±0.2	0.999

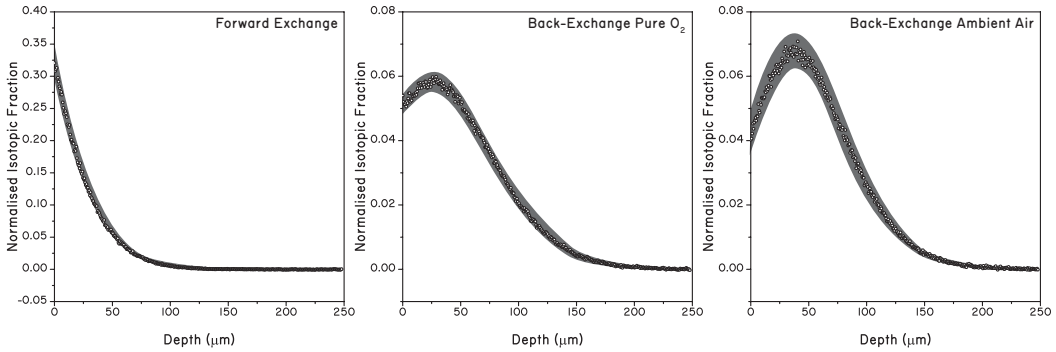


Figure 105: Schematic of uncertainty 'bands' when fitting both forward and back-exchange diffusion profiles.

Self-diffusivity values show good correlation across the samples, however, k_1 values (and k_2 for the pure oxygen back exchange) disagree by a factor of 2 in some cases. Uncertainty in k measurement is in the region of 0.2-0.3 cms^{-1}, therefore such differences cannot be explained by data treatment. For the back-exchange in ambient air k_2 was found to be 3-4 times larger than the dry oxygen cases, displaying the capability of the technique. However, further investigation was required in order to address the discrepancy of k_1 values.

8.2.2 *State of the Surface*

Until this point it has been assumed that the surface state between forward and back exchange is identical. However, as has been shown (in the literature and the previous chapters) the surface of many common perovskite materials is readily

modified at temperatures as low as 400°C [3]. Degradation processes are kinetically limited, as such the state of the surface is highly dependent upon anneal time. Therefore, the surface will not be identical at the beginning of the forward and back-exchange. Two solutions were proposed to normalise the surface state:

1. Remove the 'pre-anneal' and apply a short polishing step after the forward exchange in order to return the surface to an 'as-polished' state. Both exchanges would therefore be performed on an 'as-polished' surface.

2. Increase the pre-anneal time in an attempt to 'stabilise' the surface such that the forward exchange has a relatively insignificant effect upon the state of the surface.

8.2.2.1 *Removing the Pre-Anneal step*

The pre-anneal step is used as part of the IEDP technique to equilibrate the oxygen vacancy concentration in the sample for a desired temperature and $p(O_2)$. The sintering protocol in this work involved an 8 hour 1250°C anneal. At this temperature $La_{0.6}Sr_{0.4}Co_{0.2}Fe_{0.8}O_{3-\delta}$ is highly oxygen deficient, however, as the sample is cooled it will begin to recover oxygen. At 800°C the oxygen content nears stoichiometry [4]. Between 800°C and 1250°C the self-diffusivity is high, thus, given enough time, much of the bulk should have an oxygen content close to stoichiometry. Samples in this work were cooled at 300°C/hour, therefore it may be assumed that a large percentage of the bulk is near stoichiometry.

As diffusion slows at around 600°C a concentration gradient of oxygen vacancies will form over approximately the first few hundred micrometres of material.

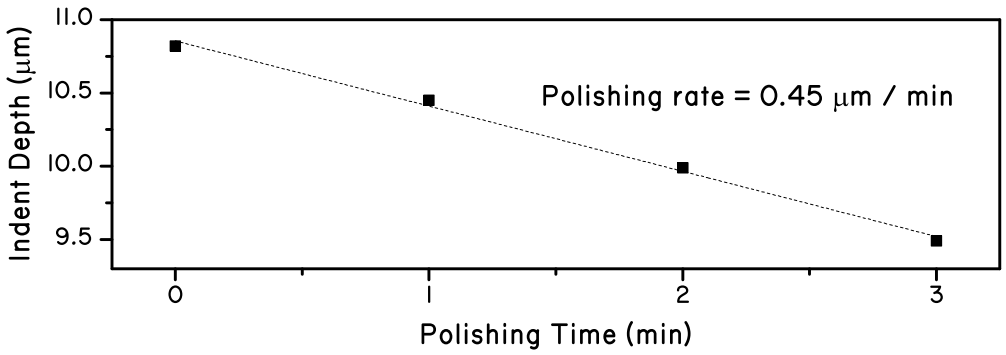


Figure 106: Showing the indent depth with respect to polishing time. The polishing rate was found to be 0.45 $\mu m\, min^{-1}$.

Typically, over 1 mm of material is removed during the polishing process so it is safe to assume that the surface of an 'as-polished' sample is representative of the *near-stoichiometric* bulk.

As the surface does not roughen significantly at temperatures below 800°C it was assumed that a short polish after the forward exchange step could be performed to return the surface to an 'as-polished' state. To characterise this, two polished samples were exchanged at the same time at 650°C for 1.38 hours (corrected anneal time) without a pre-anneal step. After exchange, an indent was impressed into the surface of one sample using Vickers hardness testing equipment. The depth of the indent was measured using WLI and the surface roughness measured by AFM. The sample with the indent was then subjected to a 1 minute polish using 1/4 micron diamond suspension, holding the sample to the polishing plate by hand. Once complete, the sample was re-analysed using WLI and AFM to assess the change in surface roughness and measure the polishing rate. This process was repeated two more times (the same indent was measured each time). The depth of the indent before and after each polishing step may be seen in Figure 106. The polishing rate was found to be 0.45 $\mu m\ min^{-1}$.

Figure 107-110 show AFM topography maps for the sample prior to polishing and after 1, 2 and 3 minutes polishing, respectively. The polishing process can be seen to increase surface roughness by approximately 3.6 times and appears to deposit large amount of material on the surface (and in porosity). It cannot be confirmed if this is polishing residue or damage caused to the sample surface.

After topographical analysis was complete, the sample with the indent was back-exchanged in a pure oxygen environment for 0.85 hours (corrected anneal time). Both samples were then analysed using the line-scan method. Figure 111 and 112 show the diffusion profiles and uncertainty contour maps for the forward exchange and back-exchange, respectively. Again, D shows good correlation between experiments, however, k values are not as expected. The polishing step removes material; therefore, the original diffusion profile was shifted by approximately 2 μm at the beginning of the back-exchange. The effective surface concentration for this step was thus lower. A drop in effective k_1 was expected, however, a larger k_1 value is observed. The k_2 value is also larger and different to k_1. D, k_1 and k_2 are all coupled parameters, therefore the removal of material results in an effective *decrease* in D as the profile is shifted towards the surface. The fitting algorithm cannot account for this and thus compensates by increasing sur-

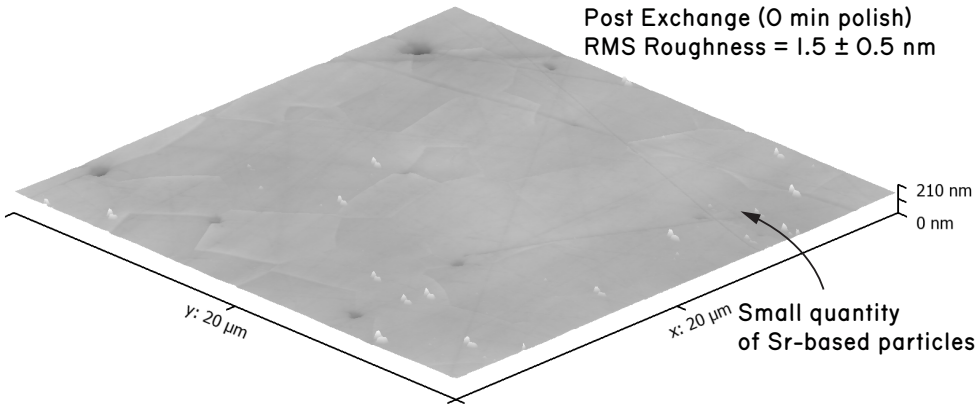


Figure 107: Showing an AFM topographic map of the sample surface immediately after a standard exchange at 650°C.

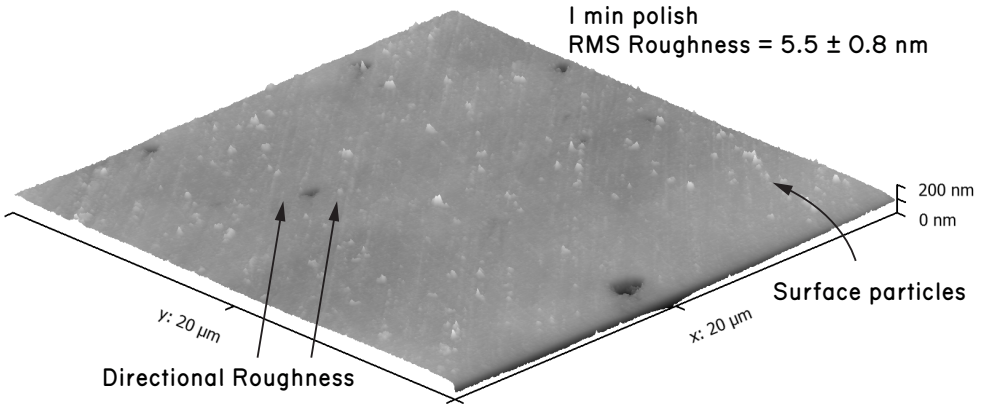


Figure 108: Showing an AFM topographic map of the sample surface after 1 minute of hand polishing using 1/4 micron diamond suspension.

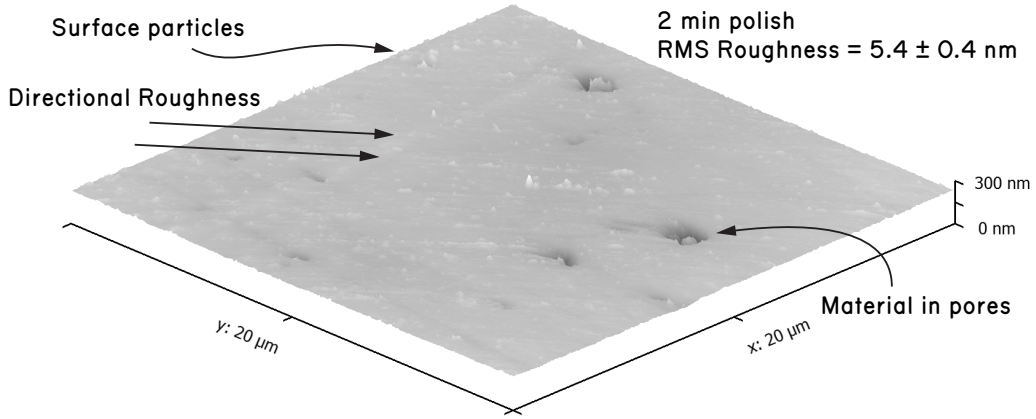


Figure 109: Showing an AFM topographic map of the sample surface after 2 minutes of hand polishing using 1/4 micron diamond suspension.

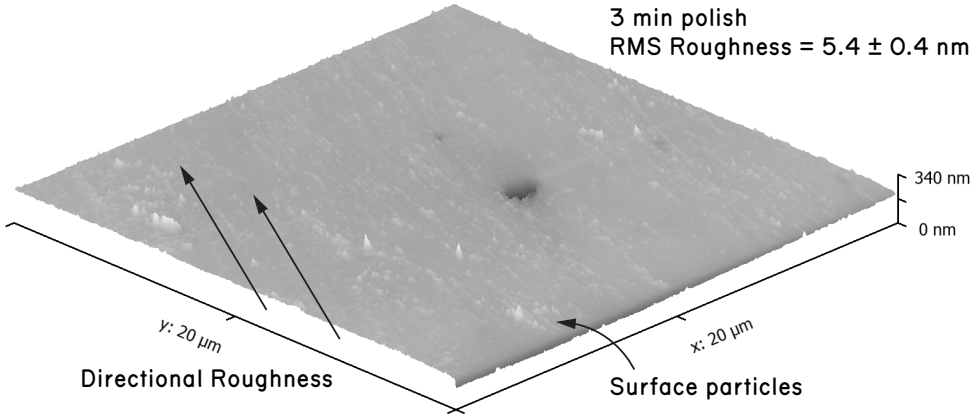


Figure 110: Showing an AFM topographic map of the sample surface after 3 minutes of hand polishing using 1/4 micron diamond suspension.

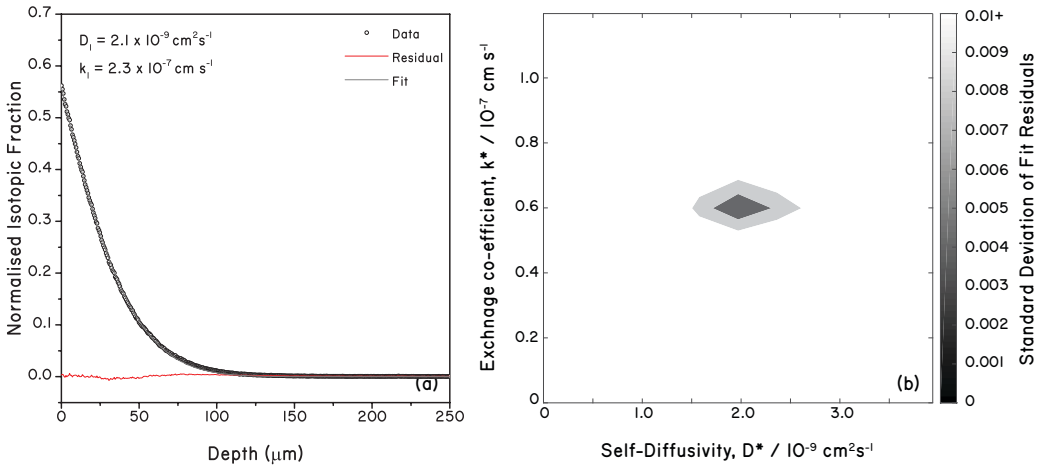


Figure 111: Showing (a) the forward exchange diffusion profile for a sample that has not been exposed to a 'pre-anneal' step, and (b) uncertainty contour map in D and k as a result of data noise.

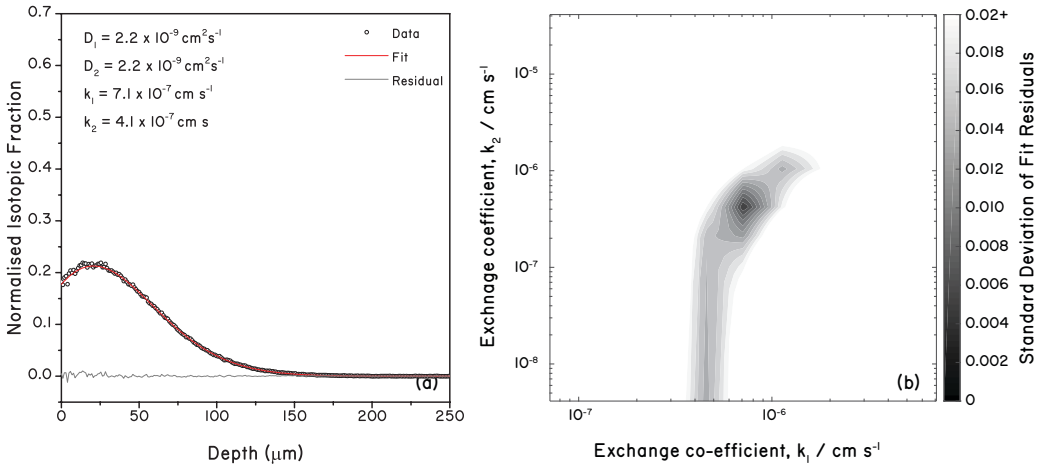


Figure 112: Showing (a) the back exchange diffusion profile after 3 minutes of polishing and (b) uncertainty contour map in k_1 and k_2 as a result of data noise.

face exchange values. It is clear that significant systematic errors were introduced by an intermediary polishing step and, as such, the practice was discontinued.

8.2.2.2 *Increasing Pre-Anneal time*

By now it should be strongly evident that the surface of $La_{0.6}Sr_{0.4}Co_{0.2}Fe_{0.8}O_{3-\delta}$ is not stable. Strontium segregation is unavoidable, however, the rate of growth is connected to the anneal temperature, anneal time and the state of the surface. As shown in Chapter 6, the presence of pure oxygen causes the formation and agglomeration of Sr-based (SrO) particles. Once particles are formed, heterogeneous agglomeration appears to be the preferential behaviour of surface stron-

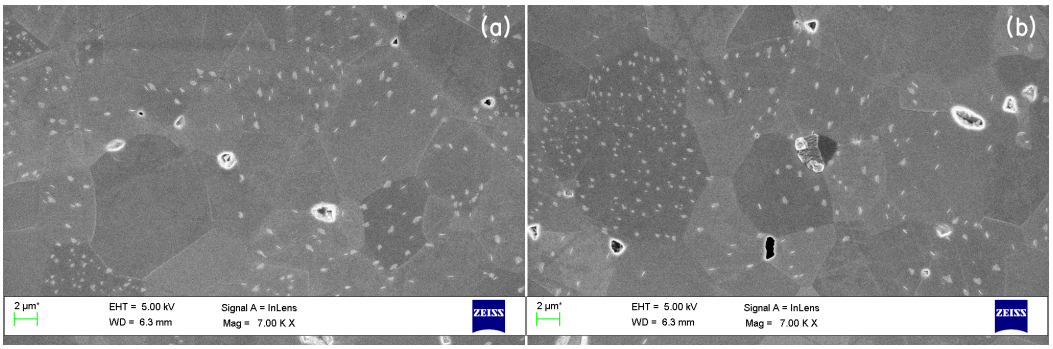


Figure 113: Showing the surface of a polished LSCF sample annealed at 650°C for (a) 20 hours and (b) 40 hours.

tium. Therefore, the rate of surface coverage due to particles slows dramatically as they agglomerate in three dimensions. Sub-surface depletion of strontium (and thus strontium concentration at the grain surface) varies depending upon the segregation rate, however, this has been shown to only affect the first few nanometres of the material; well below the desired diffusion length. The following assumptions could therefore be made:

1. In a pure oxygen atmosphere, once particles are formed, the percentage of coverage remains approximately constant for a long period of time.

2. During this time the effect strontium segregation (both through particle formation and reduction of transition metal B atoms at the surface) has on the oxygen exchange rate is homogenous.

3. The strontium content of the immediate grain surface only affects the first few nanometres of diffusion.

Video 8.9 (see Supplementary Material) shows a polished sample annealed in the HT-ESEM under a 600°C isotherm for 24 hours. Interestingly, no particle growth occurs during this time. Figure 113(a) shows a sample that has undergone a 20 hour anneal at 650°C. As can be seen particle growth has occurred in a similar manner as in Chapter 6, thus the thermally activated strontium diffusion is increased significantly somewhere between these temperatures. Figure 113(b) shows the same sample annealed for an additional 20 hours. The percent coverage of particles is almost identical, proving that the surface state may be normalised somewhat using a long pre-anneal step. Of course, at temperatures greater than 650°C the rate of strontium segregation will be greater and as a result increase

the rate of surface modification. Further investigation is required at temperatures above 650°C.

8.3 SUMMARY AND CONCLUSIONS

This section has shown that back-exchanges may be performed to measure the oxygen exchange rate in any gas environment containing 200 mbar of oxygen. However, it is clear that definition and normalisation of the surface state is of great importance. For a material where the surface is not stable this is a non-trivial problem. Figure 114 shows multiple sets of back-exchange experiments performed at 650°C. Each set contained a forward exchange, back-exchange in pure oxygen and back-exchange in ambient air[3]. Corresponding D, k_1 and k_2 values may be seen in Table 13. D was assumed to be constant between forward and back-exchanges.

Figure 114 shows that variation in D values is small, therefore bulk diffusivity is largely unaffected by the presence of gas phase impurities. Within each set k_2 values from the back-exchange in ambient air were larger than k_1 and k_2 in pure oxygen, further showing that the technique is capable of measuring exchange rate enhancement. However, values of k_1 both between *and* within data sets show large variation. The technique should show identical values of k_1 (and k_2 in pure oxygen), however, some are observed to increase and others decrease. There appears to be no specific trend, therefore individual differences between each sample are the most probably cause of the observed variation.

As has been discussed, the surface state prior to the back exchange will strongly affect the consistency of the data *within* a set. However, it is not enough to explain variance *between* sets. No sample is identical, and even sections from the same sintered sample may have significant microstructural differences depending on the quality of sample processing. For example, changes in the average grain size due to poorly pressed green pellets will affect the volume of grain boundaries and consequently the rate of strontium segregation. It is clear that ensuring experimental consistency is essential to the back-exchange technique and will require further thought in order to be applied to any material. Please see Chapter 10 for discussion of this.

3 Back-exchanges performed in ambient air were performed in the same air conditioned room at room temperature and approximately 30-40% relative humidity

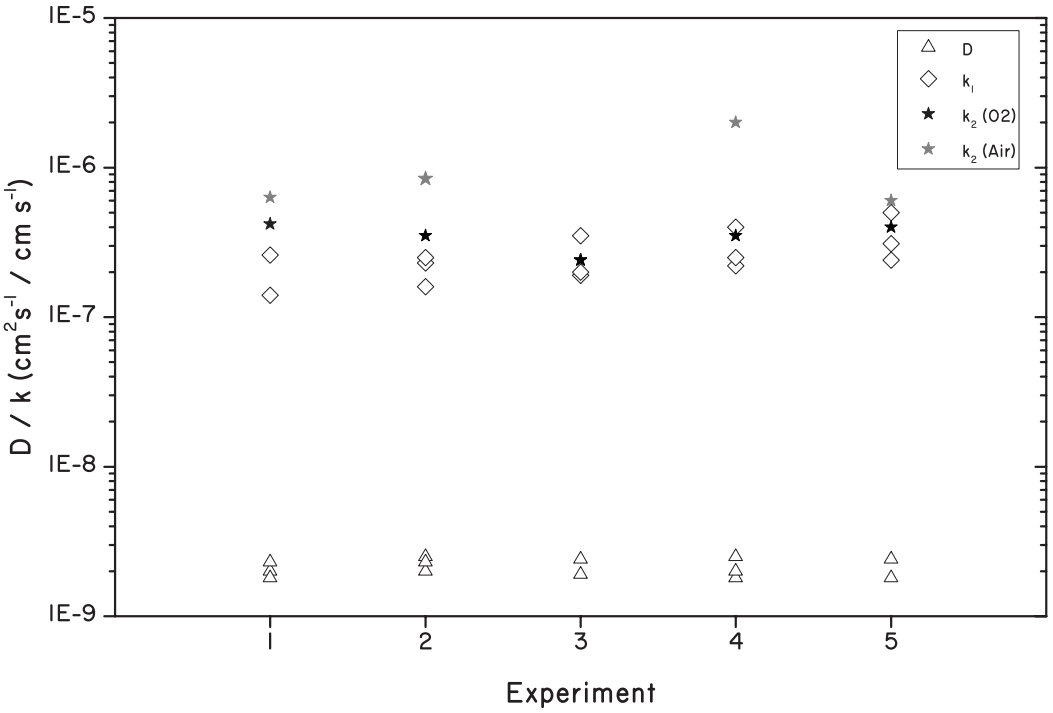


Figure 114: Showing D, k_1 and k_2 values for back-exchange sample sets.

Table 13: D, k_1 and k_2 values for back-exchange sample sets.

Experiment	D (10^{-9}cm^{2}s^{-1})	k_1 (10^{-7}cm s^{-1})	k_2 (10^{-7}cm s^{-1})	θ	Gas
1	2	2.6 ±0.1	N/A	0.5	O2
	2.3	1.4 ±0.2	4.2 ±0.2	0.5	O2
	1.8	1.4 ±0.1	6.3 ±0.1	0.5	Air
2	2	2.3 ±0.1	N/A	0.5	O2
	2.5	1.6 ±0.1	3.5 ±0.1	0.5	O2
	2.3	2.5 ±0.2	8.4 ±0.2	0.5	Air
3	1.9	3.5 ±0.2	N/A	0.38	O2
	2.4	1.9 ±0.2	2.4 ±0.2	0.38	O2
	2.4	2 ±0.1	2.4 ±0.1	0.38	Air
4	1.8	2.2 ±0.1	N/A	0.38	O2
	2	4 ±0.2	3.5 ±0.1	0.38	O2
	2.5	2.5 ±0.2	20 ±0.2	0.38	Air
5	2.4	3.1 ±0.1	N/A	0.38	O2
	2.4	2.4 ±0.2	4 ±0.1	0.38	O2
	1.8	5 ±0.1	6 ±0.2	0.38	Air

BIBLIOGRAPHY

[1] S J Cooper. *Quantifying the Transport Properties of Solid Oxide Fuel Cell Electrodes*. PhD thesis, Imperial College London, 2015.

[2] Sarah Benson. *Oxygen Transport and Degradation Processes In Mixed Conducting Perovskites*. PhD thesis, Imperial College London, 1998.

[3] John Druce, Tatsumi Ishihara, and John Kilner. Surface composition of perovskite type materials studied by Low Energy Ion Scattering (LEIS). *Solid State Ionics*, 262:893–896, 2014. ISSN 01672738. doi: 10.1016/j.ssi.2013.09.010. URL http://dx.doi.org/10.1016/j.ssi.2013.09.010.

[4] L.-W. Tai, M M Nasrallah, H U Anderson, D M Sparlin, and S R Sehlin. Structure and electrical properties of La1-xSrxCo1-yFeyO3. Part 2. The system La1-xSrxCo0.2Fe0.8O3. *Solid State Ionics*, 76(3–4):273–283, mar 1995. ISSN 0167-2738. doi: http://dx.doi.org/10.1016/0167-2738(94)00245-N. URL http://www.sciencedirect.com/science/article/pii/016727389400245N.

9

TOF-SIMS ERROR ANALYSIS

The previous chapter outlined the methodology behind 'back-exchange' and potential sources of systematic error explicitly for experimentation on $La_{0.6}Sr_{0.4}Co_{0.2}Fe_{0.8}O_{3-\delta}$. However, errors associated with ToF-SIMS data collection and analysis are applicable to any sample. Due to the demand of 'fast diffuser' materials, the line-scan technique will continue to remain relevant and thus understanding how errors can affect the measured materials properties is essential. Non-linearity at the sample edge is the cause of numerous systematic errors and can significantly alter isotopic ratio measurements if not carefully considered. Despite this, surface error has largely been ignored by the literature. This chapter attempts to quantify errors associated with line-scan analysis using ToF-SIMS and propose methodology to minimise them.

9.1 LINE-SCAN SURFACE ERROR

9.1.1 *The Poisson Problem*

Most ToF-SIMS equipment employ single count ion detectors. This means that upon detection of an ion the detector cannot respond for a period of time as the electronic properties of the detector recover. The time it takes for the detector to recover is referred to as detector 'dead time'. The dead time of a detector varies per-instrument and also changes over time as the detector degrades through use. According to the SIMS equation (Equation 4.2), secondary ion yield is proportional to the primary ion flux. However, above a certain secondary ion yield, multiple secondary ions will impinge the detector within the dead time. This results in a percentage of the secondary ion pulse being 'missed' and result in a drop

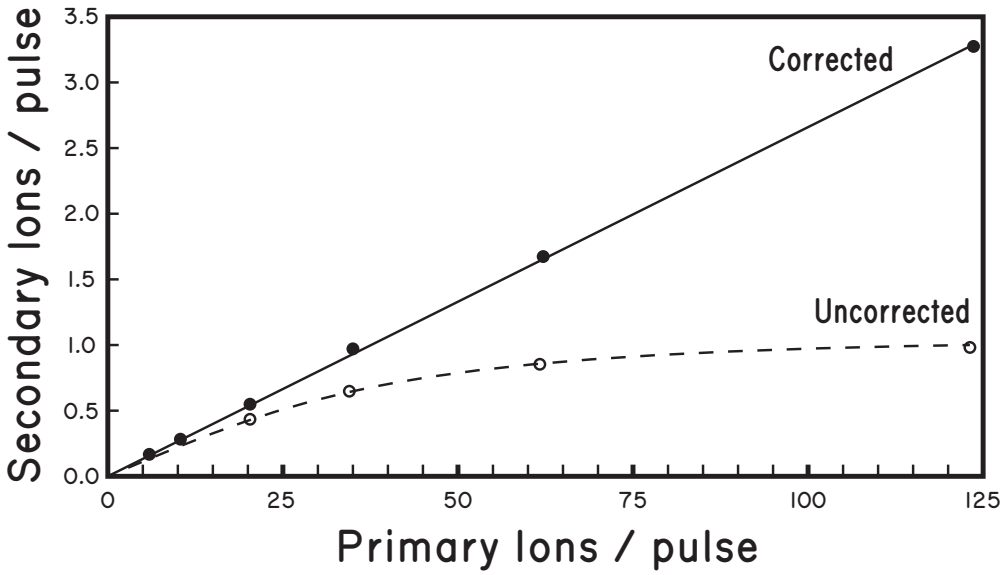


Figure 115: A plot of measured and corrected secondary ion yield per pulse against primary ion per pulse. Recreated from [1].

of secondary ion counts. Figure 115 shows how dead time causes a reduction in secondary ion signal as primary ion flux increases if left uncorrected.

A characteristic, and generally very useful, feature of ToF detection is the simultaneous detection of all mass to charge ratios as it guarantees each ion species was collected from the same mixing region. Consequently, it is very common for secondary ion yield to be close to or well above the threshold where dead time effects are present[1], therefore a form of correction is necessary. Stephan *et al.* [1] have discussed that the most practical approach to correcting secondary ion yield is to apply Poisson statistics[2]. Equation 9.1 shows the suggested correction for a single count detector. Figure 115 also shows how the correction may be used to ensure a linear relationship between secondary ion yield and primary ions per pulse.

$$I_{corr} = -N \ln\left(1 - \frac{I_{ex}}{N}\right) \tag{9.1}$$

Where I_{corr} is the corrected counts, I_{ex} is the experimental data in counts and N is the number of shots (primary ion pulses) per pixel.

1 This is particularly true when measuring oxygen as it is very readily ionised.
2 This correction method is employed by the ION-TOF SurfaceLab 6 software used in this work.

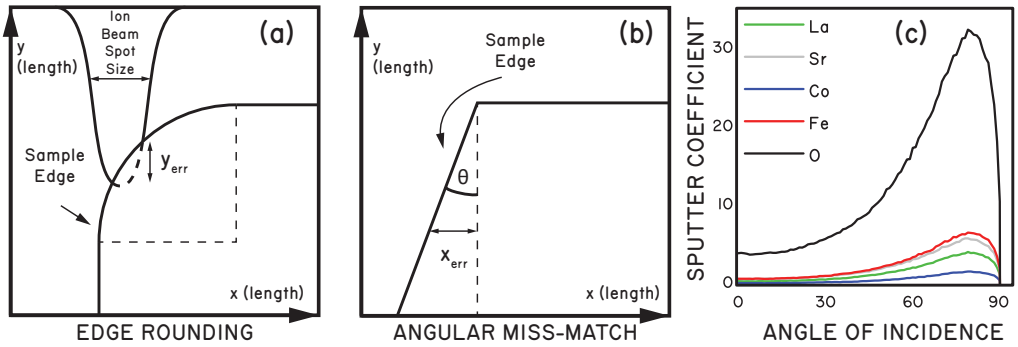


Figure 116: Showing a schematic of (a) the effect edge rounding has on the ion beam and (b) the effect of non-orthogonal surfaces and (c) the sputter rate of each component of $La_{0.6}Sr_{0.4}Co_{0.2}Fe_{0.8}O_{3-\delta}$ with respect to incidence angle.

As can be seen from Equation 9.1 the correction simply modifies the measured ion yield by a factor rather than applying a correction associated with the exact detector dead time. The correction factor is an exponential term which will modify the experimentally detected ion count. Therefore, larger ion counts will be increased by a factor greater than smaller ion counts. This implies that at the *total* secondary ion yield remains constant such that every ion species is corrected proportionally. This has a large implication for isotopic measurements as only where the concentration of each isotopic species is equal will they be corrected uniformly. For $^{18}O/^{16}O$ isotopic measurements Langer-Hansel *et al.* [2] found that the 'Poisson correction factor' (the difference between an uncorrected signal and corrected signal count) should not exceed 3.5 and that and that this is optimised by approximately 1 ion pulse (shot) per pixel.

9.1.2 *Geometric Effects*

For a flat sample, a depth profile is generally unaffected by geometric effects until the roughness of the sputter crater increases. However, the line-scan technique requires analysis at the edge of a sample. In an ideal world the two polishing steps used in the line-scan method (Section 4.3.2, [3]) would produce perfectly flat, orthogonal surfaces; however, in reality there will always be a degree of edge rounding and angular mismatch (Figure 116(a) and (b), respectively). The curvature of the rounded edge results in an uncertainty of analysis height (y_{err} shown in Figure 116) related to the radius of curvature and spot size of the ion beam. Angular miss-match will cause an effective extension of the surface (x_{err}

shown in Figure 116). As the diffusion profile is orthogonal to the original exchange surface, the line-scan technique suffers less from uncertainty with regard to the instaneous sputter depth. Each pixel comprising the ion image theoretically contains the same isotopic fraction regardless of its depth into the material. Multiple sputter steps are therefore *necessary* in order to improve the statistics of the diffusion profile. However, uncertainty when defining the surface position within the ion image may have significant effects on the diffusion profile due to the exponential nature of the diffusion profile. The first few points are asymptotic and thus tend to have the large concentration gradient. Accurate analysis of these points is therefore essential when measuring the surface exchange coefficient.

An additional consequence of surface unevenness is that sputter yield is influenced by the angle of incidence. Figure 116(c) shows secondary ion yield of $La_{0.6}Sr_{0.4}Co_{0.2}Fe_{0.8}O_{3-\delta}$ with respect to incident angle as a result of a 20 keV Bi^+ primary ion beam (calculated using the Stopping Range In Matter, SRIM, software [4]). As is shown, sputter rate increases with incident angle reaching a maximum at 80°; after which there is a decrease in sputter yield as incident ions begin to arrive at a glancing angle. It is clear that direct modification to the secondary ion yield will occur over a rounded edge of a sample.

Interaction of the primary ion beam and geometric unevenness will directly affect the rate of secondary ion *generation*, however, it may also affect ion extraction. In this work a TOF-SIMS^5 (ION-TOF GmbH, Münster, Germany) instrument was used to the collect SIMS ion images. The extractor lens (set at a constant height of 1 mm) applies an electric field with a constant potential towards the sample surface to collect sputtered ions. Edge geometry changes the angle subtended between the electric field direction and sample surface, consequently varying the rate of ion extraction.

Measuring the contribution each geometric effect has on the detected quantity of secondary ions is a non-trivial problem, however, total ion count may be assumed to represent the net modification of secondary ion yield.

9.1.3 *Analysis Orientation*

The incident angle of the analysis and sputter beam are set at 45° in the ToF-SIMS^5 equipment. As a result, edges appear differently to the ion beam depending upon if the incident beam direction is parallel or perpendicular. Figure 117(a) shows

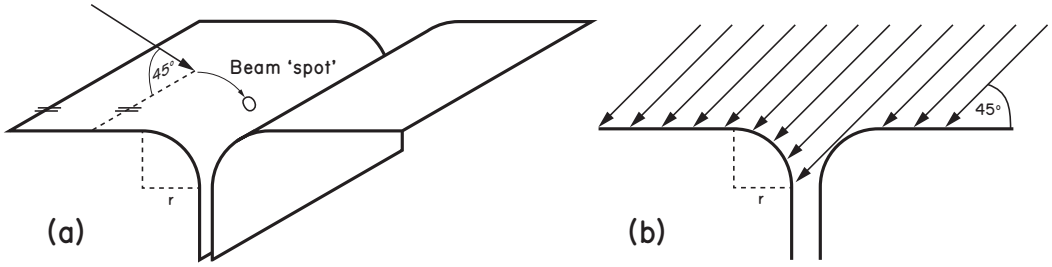


Figure 117: Showing (a) a schematic of an ion beam at an incident angle of 45° parallel to the sample edge and (b) a schematic of the ion beam at an incident angle of 45° perpendicular to the sample edge.

the beam interaction with the sample edge when the beam direction is parallel to the edge. As can be seen secondary ion yield will be a function of the beam spot size, radius of curvature of the edge and position along the edge. Modelling this system is non-trivial and beyond the scope of this work, however, it is clear to see that minimisation of the edge will reduce systematic errors.

Curvature will affect the beam in a similar manner when the sample edge is perpendicular to the incident beam, however, depending upon the radius of curvature, the beam will 'miss' a portion of the surface of one sample; beginning to probe the other sample below the analysis plane. Sputter yield will be altered over the curvature as the incident angle changes, however, of particular concern is that the ion image will be shifted in the direction of the 'missed' sample. Therefore, an increase in lateral uncertainty is also present in this analysis regime.

Figure 118 shows a comparison of samples prepared using method (3) (detailed in Section 9.2) where the incident analysis beam was parallel and perpendicular to the sample edges (achieved by simply rotating the analysis stage). The region of non-linear ion count is seen to increase by approximately 2-3 μm, however, the location of the sample edges cannot be confirmed from the ion images due to the uncertainty of the edge positions.

9.1.4 *Effect on Isotope Ratio*

Theoretically, whatever causes a change in sputter yield, the sputter rate of isotopes (such as ^{16}O and ^{18}O) will increase or decrease proportionally as they are chemically identical[3]. However, it is the *absolute* number of the secondary ion

3 The influence of the mass difference between isotopic species is generally considered to be negligible.

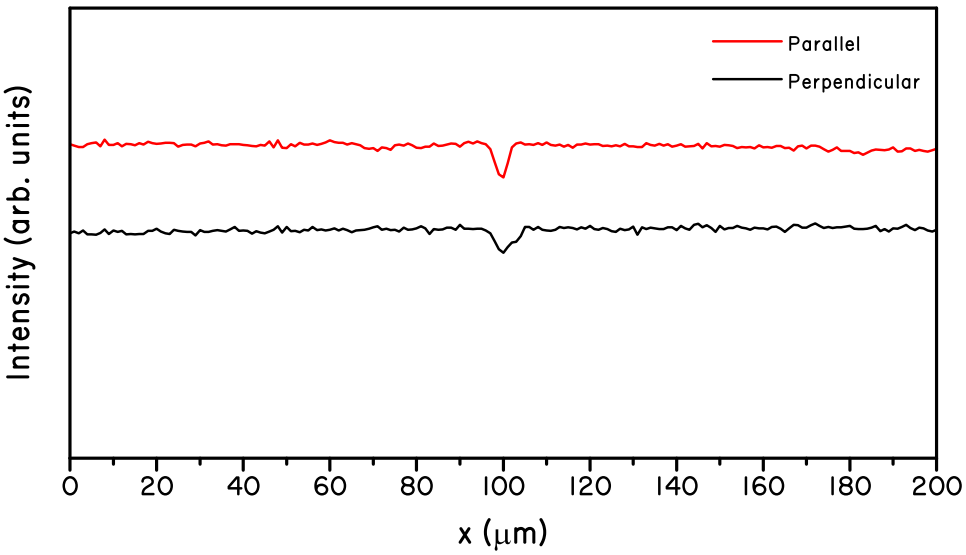


Figure 118: A comparison of the total ion line-scan profiles for the sample prepared using method (3) (detailed in Section 9.2). The profiles have been normalised and offset for comparison. A false change in non-linear ion count may be seen in the sample aligned perpendicular to the incident ion beam.

count that will be corrected by Equation 9.1. Therefore, unless the isotopic fraction was equal before correction, the isotopic ratio will be altered by applying a Poisson correction. Figure 119 shows a back-exchange diffusion profile of a sample analysed with significant variation in total ion counts near the surface. As can be seen the isotopic ratio (and definition of the diffusion profile) is heavily altered by the correction. Understanding and minimising this error is vital for both standard and back-exchange line-scan analyses.

9.2 SURFACE ERROR QUANTIFICATION

It is clear that unevenness of the sample edge must be minimised in order to define the 'surface uncertainty' of a diffusion profile. The ideal edge is no edge at all (for this reason standard depth profiles avoid these geometric errors), however, an edge at the sample surface is unavoidable using the line-scan technique.

A relatively simple approach was taken in order to minimise, and ideally remove, the effect of edges during the SIMS analysis. As shown in Figure 120, two samples were joined using a liquid-based adhesive where the gap between the samples was completely filled. The pair of samples were then polished to remove

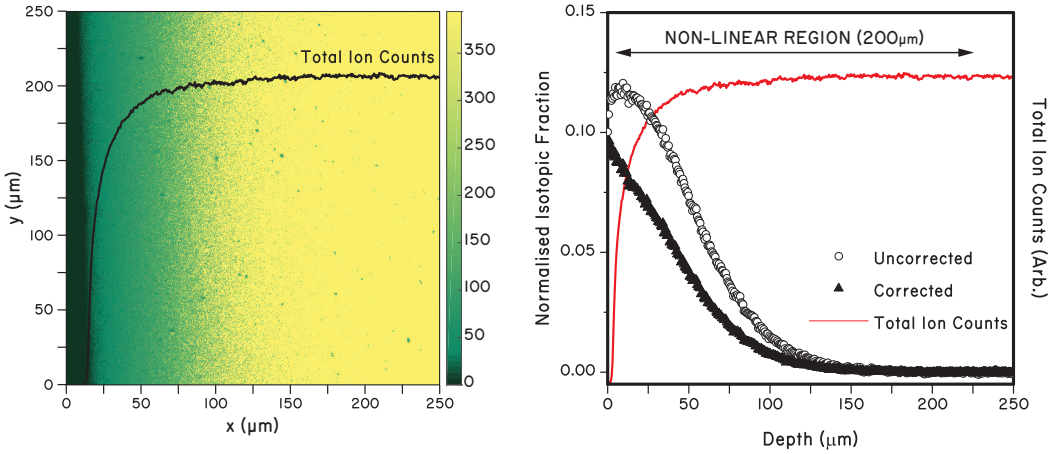


Figure 119: Showing (a) a false colour image of the ^{18}O signal and (b) the back-exchange curves for both the corrected and un-corrected data. Total ion counts (arbitrary units) are overlaid over both figures.

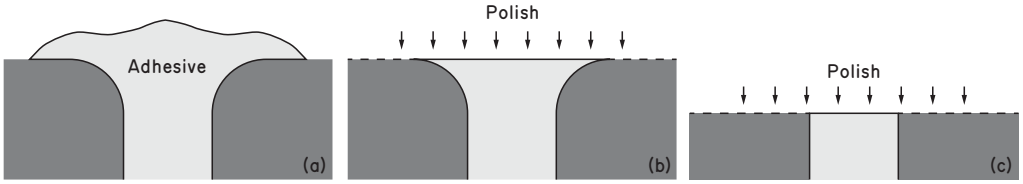


Figure 120: Showing (a) two samples adhered together using a liquid-based adhesive, (b) the sample after polishing away the excess adhesive from the surface and (c) further polishing to remove the edges of the sample.

any excess adhesive and the remaining curvature of the surface. In theory this process would leave a planar analysis surface and a sharp sample edge.

To show the significance of correct sample preparation and SIMS analysis, three experiments were performed. Five polished LSCF samples were subsequently prepared using the following methodology:

1. A face orthogonal to the original polished surface of one sample was ground and polished using the standard polishing regime. This sample was mounted alone in the SIMS holder such that there was no material beyond the sample edge.

2. Two samples were ground and polished using the same method above as in (1). The recently polished surfaces were then attached together using a liquid-based adhesive. Pressure was applied to ensure the gap was completely filled and the surfaces were aligned as accurately as possible. Excess adhesive on the surface was cleaned using appropriate solvents. The attached samples were mounted in the SIMS holder together.

Table 14: Analysis and sputter beam settings used to analyse the samples prepared using methods (1)-(3).

Setting	**Bi^+**	**Cs^+**
Energy (keV)	20	2
Current (nA)	0.0003	100
Beam Mode	Burst Alignment (7 pulses)	—
Raster Area	500x500	750x750
Pixels	512x512	—
Interlacing	Non-interlaced	—

3. Two polished samples were exchanged for 1.5 hours at 650 °C. One sample was then back exchanged in a O_2/H_2O environment for 0.75 hours. The original polished surface of two samples were attached together using a liquid-based adhesive *prior* to the second polishing step. The samples were polished together at the same time. After polishing, no further cleaning of the surface was required. Samples were also mounted together in the SIMS holder.

The first experiment was set-up to demonstrate the significance of performing a ToF-SIMS analysis on a sample with a free edge. Ideally, the adhesive join would create a planar surface between samples in method (2) and (3); however, the solvent used to clean the surface in method (2) could not be prevented from etching away the adhesive in the gap and the polymeric adhesive exhibits a different polishing rate to the LSCF. As such, non-planar surfaces were expected. Samples were then analysed in the ToF-SIMS using the settings presented in Table 14.

Figure 121(a)-(c) shows false colour images of the samples prepared and analysed using methodology (1)-(3), respectively. Overlain are line-scan profiles of the total ion counts (averaged parallel to sample surface(s)) to show the size of the non-linear total ion count region for each sample preparation method. As can be seen the sample with a free edge has a very large non-linear ion count region of approximately 200 μm. The samples adhered after the second polishing step displayed a non-linear ion count region of approximately 50-75 μm per sample. A peak may be seen on the left-hand sample due to adhesive residue unable to be removed by the solvent cleaning step. Figure 121(c) shows that the

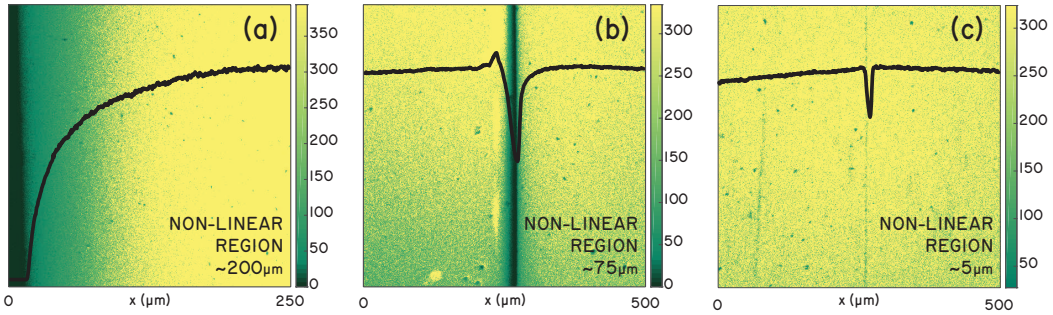


Figure 121: Showing false colour images of $La_{0.6}Sr_{0.4}Co_{0.2}Fe_{0.8}O_{3-\delta}$ total ion images (ion counts per pixel). The samples were mounted with (a) no sample at the edge, (b) samples adhered together after the second polish step and (c) samples glued together before the second polishing step. A total ion 'line-scan' is overlaid across the image. Ion counts (arbitrary units) have been normalised to the final data point of (a) to compare the relative 'depth' of the gap between samples. Ion images were rotated by 90° to aid in comparison with the total ion count.

samples adhered prior to the polishing step display a non-linear ion count region significantly smaller than the previous methods.

Isolating the total effect of each geometric effect is difficult due to the complicated interaction between a Gaussian shaped ion beam and the curved surface edge. Figure 122 and 123 show the surface topography of the samples adhered using method (2) and (3). The primary difference between the two methods is the z-axis miss-match between the analysis plane. As can be seen, the analysis plane of the samples prepared using method (2) are offset by approximately 18 μm, whereas, the samples prepared using method (3) appear to have a maximum offset of approximately 200 nm. The quality of the join could not be assessed for method (2) as, in addition to a planar offset, one sample extends over the lower sample by approximately 8 μm. Even after tilting the stage to compensate for the angular miss-match, the height difference was too great to resolve features close to the edge of the both samples (the de-focussed region due to the height difference obscured sample edges).

As can be seen from Figure 123 the gap between the samples prepared using method (3) varies. At some points the two surfaces are in direct contact and the gap size varies from approximately 1-5 μm in width. Figure 124 shows a direct comparison between a line-scan of the total ion count and the average topographic profile across the gap[4]. The large aspect ratio at the base of the gap

4 This was produced in the same way as an ion image line-scan. Pixels, perpendicular to the sample edge, were averaged to produce a single profile.

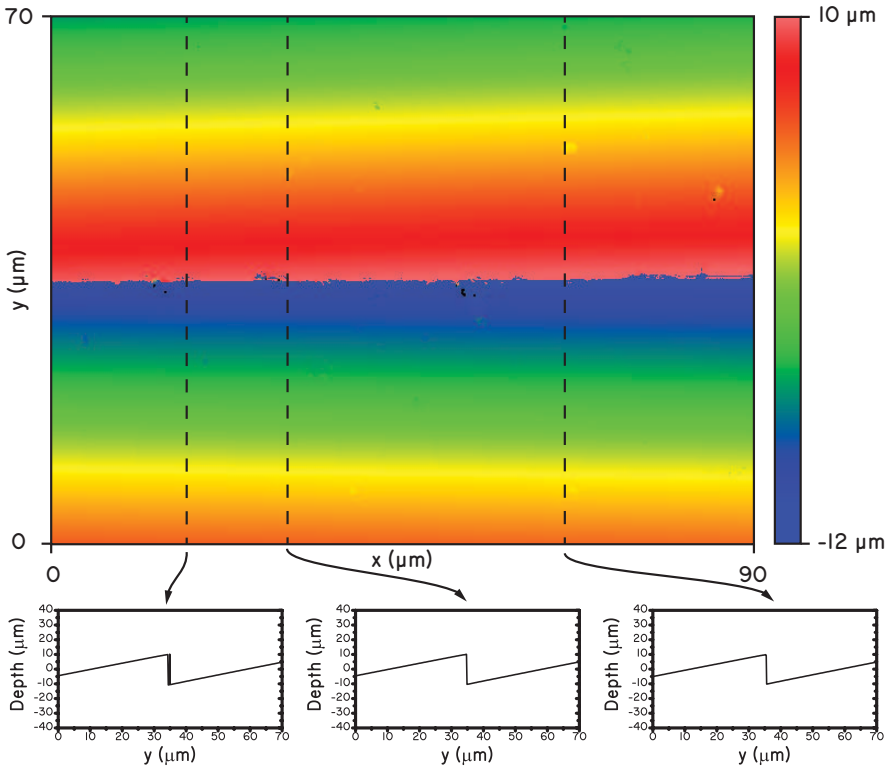


Figure 122: Showing a false colour WLI image of the gap between samples prepared using method (2). The 'overhang' between samples may be seen from the linescan profiles (below).

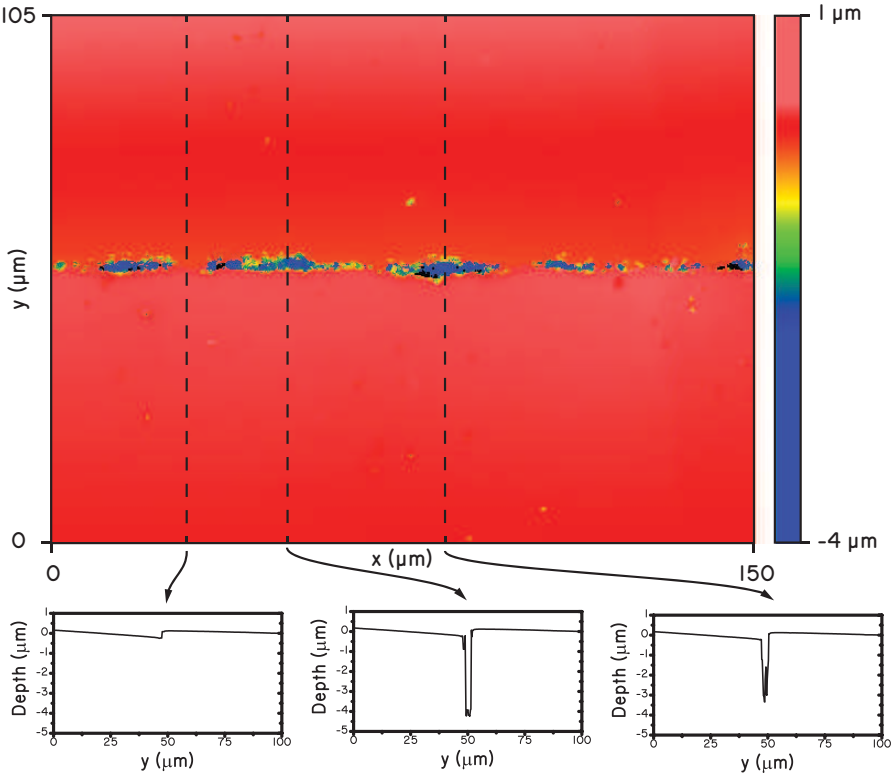


Figure 123: Showing a false colour WLI image of the gap between samples prepared using method (3). As can be seen the gap is non-uniform and in some places the samples are directly in contact. Representative profiles have been taken from a region where the samples are touching, a large gap and a small gap.

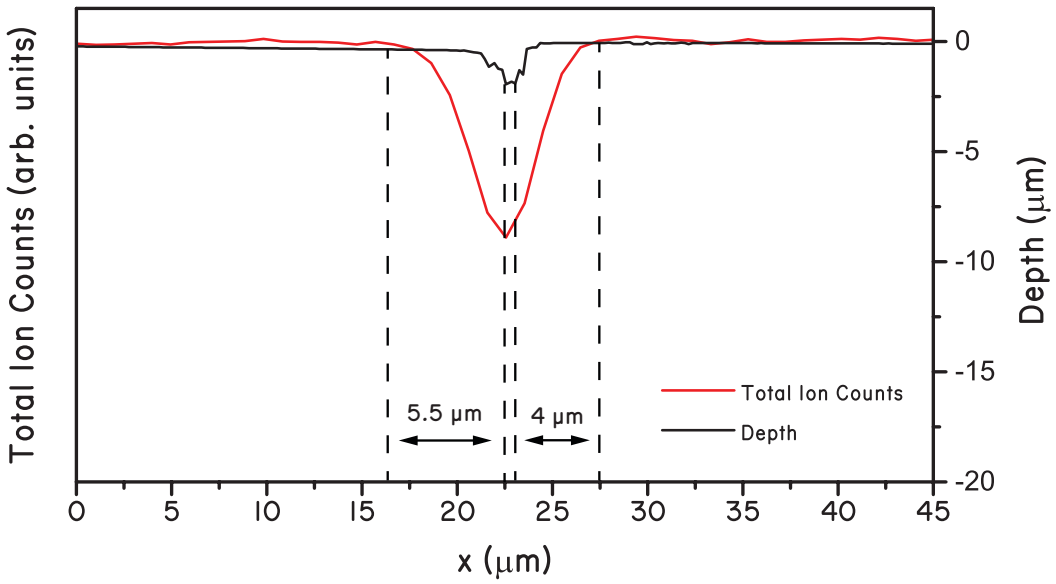


Figure 124: A direct comparison between the total ion and topographic line-scan profiles showing the non-linear ion count region to be between approximately 4-5.5 μm. The profiles have been normalised to the final data point and aligned to the minima of each profile.

will prevent secondary ions from escaping, therefore it has been assumed that the minimum secondary ion count is (on average) at the centre, and therefore bottom, of the recess. Consequently, the profiles have been aligned to the minima of each profile. The profiles were then normalised to the final data point as the linear region of the ion image and topography are effectively equivalent. The non-linear ion count region of each sample could then be estimated to be between 4 and 5.5 μm per sample.

With a reasonable value for the non-linear ion count region it is then possible to assess potential error in measured self-diffusivity and surface exchange values. Using the measured non-linear ion count region and alignment of the total ion image the data point corresponding to the true edge of the sample could be located. With this, the completed diffusion profile could then be constructed with the erroneous data points included. To date, line-scan profiles throughout literature neglect to define how they have calculated the 'surface point' within presumably present non-linear ion count regions of a line-scan profile. As a result the D and k values presented may have a large degree of error depending upon how the data was treated. If only a line-scan profile was collected, it may be assumed that the data within the non-linear ion count region was either excluded and extrapolated for.

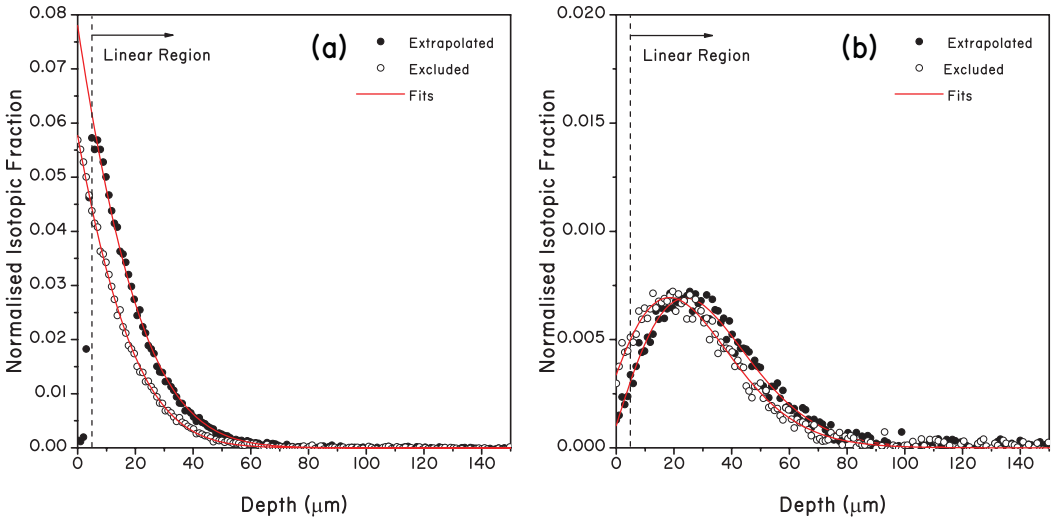


Figure 125: Showing the effect of extrapolating or ignoring the non-linear ion count region of the diffusion profile for (a) a forward exchange and (b) a back-exchange. The linear region indicated on the graphs only applies to the extrapolated curve.

To investigate the effect exclusion and extrapolation has on the self-diffusivity and exchange coefficient, a forward and back-exchange diffusion profile was analysed by excluding or extrapolating for the non-linear ion count region. Figure 125 shows a comparison of the measured diffusion profiles for the sample prepared using method (3) (D was held constant for the back-exchange). Table 15 shows the comparative self-diffusivity and surface exchange coefficients with the percentage difference between the excluded and extrapolated values indicated in brackets. Simply observing shift in the profiles it is clear to see that by excluding the non-linear ion count regions, values of D and k will be reduced. The self-diffusivity for both exchanges is relatively unaffected by the shift, however, the shift in surface concentration has a strong effect on k values. The forward exchange saw k_1 increase by 54% between the two methods of data treatment.

Between the surface and the peak of a back-exchange curve, k_1 and k_2 strongly influence the surface concentration and peak position. By excluding the non-linear ion count data, the peak position is shifted by a relatively large amount and a correspondingly large change in k_2 of 315% may observed in this particular data set. Excluding the data is unsuitable and as such must be considered when analysing both forward and back-diffusion profiles. Extrapolation is possible, however, assumes that the surface and sub-surface of the material behaves identically to the bulk. Depending on the sample in question, this may be an unsuitable method of analysis.

Table 15: Cation ratio at the surface for LSCF samples annealed in pure oxygen and ambient air. Where Exc. = excluded data and Extp. = extrapolated data.

Sample	**D (Exc.) (10^{-10} cm^2s^{-1})**	**D (Extp.) (10^{-10} cm^2s^{-1})**	**k_1 (Exc.) (10^{-8} cm s^{-1})**	**k_1 (Extp.) (10^{-8} cm s^{-1})**	**k_2 (Exc.) (10^{-8} cm s^{-1})**	**k_2 (Extp.) (10^{-8} cm s^{-1})**
FEx	5.4	6.8 (25%)	1.7	2.6 (54%)	—	—
BEx	7.7	8.3 (8%)	0.9	1.1 (22%)	84	349 (315%)

Chater [5] suggested that in addition to a line-scan the first 'few micrometres' of the diffusion profile must be measured by depth profiling the original exchange surface prior to the line-scan. The two data sets may then be combined in order to provide 'complete' diffusion profile with a high degree of certainty over the first few data points. However, the non-linear ion count region must be well defined in order to locate the true surface position of the line-scan profile; thus enabling the two profiles to be combined accurately[5].

9.3 SUMMARY AND CONCLUSIONS

High oxygen self-diffusivity is a desirable materials property for the next generation of MIEC materials, thus, the line-scan technique will continue to be remain a relevant technique. Additionally, the prevalence of using ToF-SIMS to measure isotopic ratio is on the rise. To date, errors due to both sample preparation and data treatment has been largely ignored by the literature, however, this chapter has shown that it is essential to understand and define the non-linear ion count region of the sample to provide an accurate diffusion profile. Sample preparation is key in achieving a small non-linear ion count region. The methodology of adhering two samples together prior to the second polishing step has been shown to reduce the non-linear ion count region to approximately 5 μm or less, however, this length scale is still sufficient to alter surface exchange coefficient values for forward and back-exchanges. As suggested by Chater [5] a depth profile of the

5 The depth profile cannot be performed after adhering the samples, thus the non-linear count region of the samples must be estimated. Multiple samples were fabricated throughout this work and the non-linear ion count region ranged from approximately 4-7 μm. It is therefore sensible to depth profile within this depth range.

original exchange surface should be performed prior to line-scan analysis in order to obtain accurate data from the first few points of the diffusion profile within a line-scan. The depth required for this step must extend beyond the non-linear ion count region, however, this must be estimated as the samples cannot be depth profiled once adhered together.

BIBLIOGRAPHY

[1] T Stephan, J Zehnpfenning, and A Benninghoven. Correction of dead time effects in time-of-flight mass spectrometry. *Journal of Vacuum Science & Technology A*, 12(2), 1994.

[2] K. Langer-Hansel, A. Schintlmeister, J. Fleig, and H. Hutter. Oxygen transport in electroceramics investigated by electrochemical 18O/16O isotope exchange and ToF-SIMS. *Surface and Interface Analysis*, 45(1):486–489, 2013. ISSN 01422421. doi: 10.1002/sia.5134.

[3] R.J. Chater, S. Carter, J.A. Kilner, and B.C.H. Steele. Development of a novel SIMS technique for oxygen self-diffusion and surface exchange coefficient measurements in oxides of high diffusivity. *Solid State Ionics*, 53-56:859–867, jul 1992. ISSN 01672738. doi: 10.1016/0167-2738(92)90266-R. URL http://linkinghub.elsevier.com/retrieve/pii/016727389290266R.

[4] James F. Ziegler, M.D. Ziegler, and J.P. Biersack. SRIM – The stopping and range of ions in matter (2010). *Nuclear Instruments and Methods in Physics Research Section B: Beam Interactions with Materials and Atoms*, 268(11-12):1818–1823, jun 2010. ISSN 0168583X. doi: 10.1016/j.nimb.2010.02.091. URL http://linkinghub.elsevier.com/retrieve/pii/S0168583X10001862.

[5] Richard John Chater. *Oxygen self-diffusion and surface exchange measurements of the polycrystalline oxide (Lao.8Sro.2)(Cro.2Feo.8)O3-d using Secondary Ion Mass Spectrometry*. PhD thesis, 2014.

10

CONCLUSIONS AND FUTURE WORK

This thesis has presented work analysing surface exchange and surface microstructural properties of the $La_{0.6}Sr_{0.4}Co_{0.2}Fe_{0.8}O_{3-\delta}$ material system after exposure to ambient air atmospheres. Microstructural changes were observed *in-situ* using High-Temperature Environmental Scanning Electron Microscopy (HT-ESEM) and correlated directly to the domain structure observed using Electron Backscattered Diffraction (EBSD). Exchange properties in ambient air were assessed using the novel 'Back-Exchange' technique and it was shown that the presence of common oxygen containing contaminant species such as CO, CO_2, H_2O, SO_2 and NO_x affect the oxygen exchange rate.

10.1 CONCLUSIONS

Microstructural Observations: Microstructural changes were observed under four different atmospheres: pure oxygen, pure water, ambient air and a vacuum (reducing environment). In all atmospheres particles were observed to grow on the surface of the sample. The onset temperature and rate of growth varied between atmospheres, however, a number of common observations were made: (a) only strontium-based particles were observed, (b) particles were seen to grow both on the grain boundaries and the centre of the grain, (c) defects such as scratches induced during polishing were preferable nucleation sites and (d) particles would agglomerate above a particular temperature in each atmosphere.

In the pure oxygen regime particle growth occurred from 750-800°C with a surface coverage of approximately 17%. Under pure water particle growth is rapid from 850-1000°C reaching a maximum surface coverage of approximately 40%. Agglomeration occurs above 1000°C and very large particles were formed. Although the experiment was stopped after only a couple of hours, it would appear

that the surface would eventually be covered completely by the agglomeration of the strontium-based particles. Under ambient air the onset of particle growth did not occur until 1000°C and was seen to cover approximately 17% of the surface. The delayed growth was attributed to the gradual decomposition of $Sr(OH)_2$ and $SrCO_3$ formed due to presence of CO_2 and H_2O. Under a vacuum particle growth was observed, however, oxygen lost as a result of the chemical potential generated by the reducing environment was the source of oxygen for particle formation (rather than the atmosphere). Interestingly, particle growth behaviour was similar to that seen in ambient air. It was also observed that a defect induced by polishing did not contain any particles, thus, it would appear that without the presence of an oxygen containing atmosphere the surface transport of strontium is inhibited due to the low concentration of oxygen ions adhered to the surface. Mechanical damage often forms dislocations within the bulk of the material and it is often the case that dislocation networks exhibit enhanced transport properties due to the presence of additional point defects. It has been shown that diffusion of strontium is enhanced within grain boundaries of perovskite materials [1], therefore, it may be speculated that mechanical damage may also exhibit a similar enhancement. However, this cannot be determined from the data in this work.

$La_{0.6}Sr_{0.4}Co_{0.2}Fe_{0.8}O_{3-\delta}$ readily forms twin domains. Direct comparison between the HT-ESEM and EBSD data showed that the twin structure affects particle growth as particles were seen to grow along twin habit planes. It was observed that two twin habit planes co-exist within $La_{0.6}Sr_{0.4}Co_{0.2}Fe_{0.8}O_{3-\delta}$: the (001) and $(\bar{1}20)$ plane in the trigonal phase. Bi-sector analysis showed that the (001) habit plane influences the location of particle growth and agglomeration on the surface of each grain. It was unclear whether the $(\bar{1}20)$ had any effect upon particle growth. At one particular grain orientation neither habit plane appeared to affect particle growth as a homogenous distribution of particles on the grain surface was observed. Due to the pseudo-symmetry problem it was not possible to accurately define each grain's orientation, therefore, comparison between the HT-ESEM and EBSD data required fitting the most appropriate result. As discussed below, further work is required to confirm these results.

Exchange Rate Analysis: To date, much of the experimentation regarding oxygen surface exchange properties has been performed in pure oxygen atmospheres in order to isolate the effect of oxygen, however, real SOFC systems aim to use

ambient air as a cathode gas stream in order to reduce costs. As such, the back-exchange technique was developed in order to quantify surface exchange rates in any gas environment. This thesis presented the initial experimental work performed using the technique in conjunction with the numerical methods in Dr. S. Cooper's thesis. The validity of the technique was demonstrated by a series of three experiments: (a) a standard forward exchange, (b) back-exchange in pure oxygen and (c) back-exchange in ambient air. The exchange rate was observed to be approximately equal 'in' and 'out' during the pure oxygen back-exchange and an enhancement of the oxygen exchange rate was observed during the ambient air back-exchange. This result shows that the technique may be used to distinguish changes in exchange rate. However, discrepancies between k_1 values were observed over multiple samples, suggests that accurate sample preparation and analysis is required to discern small changes in k values.

Materials with relatively high self-diffusivity values are often required to be analysed using the 'line-scan' methodology. This work discussed the errors associated with this technique with respect to analysis using ToF-SIMS and Poisson correction. It was shown that with good sample preparation the errors associated with the surface could be limited to approximately 5μm or below, however, it is of the opinion of the author that it is still necessary to perform a depth profile for the first few microns in order to produce an 'accurate' or 'complete' diffusion profile.

10.2 MECHANISTIC CONCLUSIONS

In this thesis: (1) HT-ESEM has shown that strontium-based particle growth in $La_{0.6}Sr_{0.4}Co_{0.2}Fe_{0.8}O_{3-\delta}$ occurs in many environments, (2) HT-ESEM in combination with EBSD has shown that particle growth and agglomeration is influenced by the underlying microstructure and (3) SIMS based experiments have shown that particles 'block' the catalytically active surface of the material and themselves do not facilitate the reduction of oxygen.

It is known that particle formation is limited kinetically rather than thermodynamically [2], however, the mechanisms for particle growth have yet to be fully defined in the literature. The data presented in this work cannot be used to explicitly explain the mechanisms that are occurring at the surface of LSCF, however,

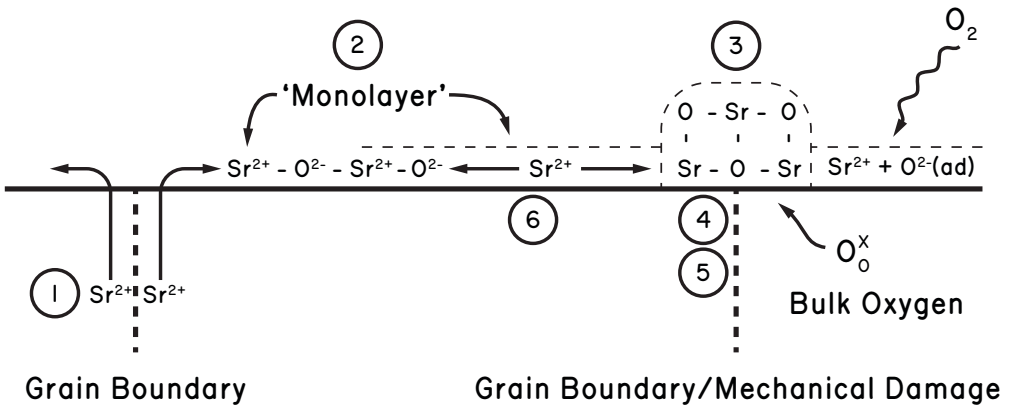


Figure 126: Schematic of the proposed particle formation process. The numbers in the figure may be related to the corresponding process described in the text.

as shown in Figure 126, the following process for particle formation may be suggested:

1. Strontium segregates to the surface.
2. Once at the surface the strontium forms a monolayer as shown by LEIS data in this work and by Druce *et al.* [2].
3. Over time, sufficient strontium reaches the surface to form strontium-based particles as shown by Oh *et al.* [3] and the HT-ESEM data in this work.
4. Nucleation occurs preferentially at grain boundaries as shown in the HT-ESEM data due to the increased strontium segregation rate (greater Sr^{2+} diffusivity).
5. Mechanically induced defects may also act as a heterogeneous nucleation sites if surface transport of Sr^{2+} and O^{2-} species is facile.
6. Agglomeration occurs due to surface transport of the strontium[1].

This generalised process describes what was observed, however, specific mechanisms may be speculated from the data in this work and the literature. Strontium ions segregate as a reaction to a charge difference between the surface and the bulk [4] and tend to form charge neutral Sr-O layers at the surface. Due to the presence of a strontium concentration gradient and other elements it is not strictly a 'monolayer' that forms, however, it may be considered analogous. As the concentration of Sr^{2+} species increase it is believed that the monolayer begins to 'saturate' and forms SrO particles in order to compensate.

1 It should be noted that the HT-ESEM data shows agglomeration occurs more rapidly in the presences of oxygen-containing gaseous species, thus it may be speculated that the monolayer facilitates surface transport of strontium.

In pure oxygen the particle formation process should not deviate from the generalised process and it may be assumed that SrO or SrO_2 [5] particles form directly. However, in the presence of water vapour and/or CO_2 the particle formation process is more complicated. In previous work, it has been shown that the dissociation of H_2O and CO_2 occurs at a different rate to O_2. In this work, it was seen that particle growth rate varied depending upon the atmosphere and it is believed to be associated with the formation of additional phases on the surface of the material prior to particle formation.

LEIS surface spectra has shown that as anneal time and temperature increase the only cation remaining at the surface is strontium, therefore, it may be assumed that a monolayer of a strontium-based phase is formed at the surface. In the presence of water, it has been proposed that chemisorbed hydroxyl groups sit on the surface of the material [6], therefore, segregating strontium will react to form $Sr(OH)_2$. In pure oxygen particle growth was observed at approximately 700°C, however, in pure water particle growth was not observed until approximately 850°C. $Sr(OH)_2$ is stable below 800°C, therefore, it may be speculated that particle growth only occurs after the decomposition of $Sr(OH)_2$ into SrO:

$$Sr(OH)_2 \rightleftharpoons SrO + H_2O(g) \tag{10.1}$$

The mechanisms by which the SrO decomposition product grows into a particle cannot be determined from this work, however, it can be speculated that particles will only grow as SrO (or SrO_2) and not as $Sr(OH)_2$. An 'outer layer' at particle-environment interface may form $Sr(OH)_2$ in equilibrium with the gas phase, however, at high temperature it is likely to decompose readily and continue SrO particle growth.

In an ambient air environment a similar observation was made, however it is suggested that the surface monolayer would be comprised of both $Sr(OH)_2$ and $SrCO_3$[2]. In the presence of H_2O and CO_2 the $Sr(OH)_2$ phase is thermodynamically stable below 400°C. From 400-800°C the $Sr(CO)_3$ phase is the stable and above 800° the SrO phase is stable. Therefore, above 800°C, a similar behaviour is observed where the phases comprising the monolayer decompose and form strontium based-particles. In ambient air the onset of particle growth was delayed to

2 It is possible that a hydroxyl-carbonate phase exists, however, there is currently no evidence to suggest this.

950°C, suggesting that the energy cost of $Sr(CO)_3$ decomposition is greater than that of $Sr(OH)_2$.

From the experiments performed here it is unclear if pure $Sr(OH)_2$ and $SrCO_3$ particles would form if annealed at lower temperature in pure H_2O or CO_2 environments. As these processes are kinetically limited it is suggested that SrO particles will still form as described above, however, at a lower rate.

In a vacuum (reducing environment) the process is similar, however, the low supply of oxygen appears to prevent surface transport of strontium due to low agglomeration rates of the particles. This would suggest that the formation of the monolayer influences the surface transport rate of strontium. The high agglomeration rate seen in pure water corroborates this hypothesis, however, further investigation is required to confirm this.

10.3 FUTURE WORK

The work performed in this thesis is the first instance of using both HT-ESEM and back-exchange for the analysis of a SOFC cathode material. Careful consideration has been carried out to ensure the data collected from each technique was accurate, however, this limited the time available to explore additional experiments.

Firstly, the back-exchange technique requires refinement in order to validate small changes in k values. The observed variation in k_1 is believed to be attributed to minor microstructural differences between samples. Therefore, the validation experiment must be repeated, taking extra care to characterise each step during sample preparation to ensure that the surface of each sample is effectively identical. It would also be preferable to introduce diffusion profiles short enough to be analysed with a depth profiles in order to eliminate errors due to the line-scan technique.

The overarching aim of this thesis was to expand current experimentation techniques by using experimental conditions more representative of a real SOFC. Therefore, it would be interesting to repeat the same studies whilst applying an electrical bias across the sample as it is currently unknown what effect an electrical bias has on the microstructural degradation of these materials.

Finally, to confirm which twin planes are present within each grain, Transmission Electron Microscopy (TEM) should be performed. The resolution capable by

this technique allows the observation of individual atoms and thus the stacking of a system. A FIB-section taken across twin domains from multiple grains may be used to quantify the precise habit plane in each grain. Given the small amount of material removed it would then be possible to re-analyse the same sample in the HT-ESEM to confirm or rebut the results discussed with the EBSD data.

BIBLIOGRAPHY

[1] Markus Kubicek, Ghislain M Rupp, Stefanie Huber, Alexander Penn, Alexander K Opitz, Johannes Bernardi, Michael Stöger-Pollach, Herbert Hutter, and Jürgen Fleig. Cation diffusion in La(0.6)Sr(0.4)CoO(3-δ) below 800 °C and its relevance for Sr segregation. *Physical chemistry chemical physics : PCCP*, 16(6):2715–26, feb 2014. ISSN 1463-9084. doi: 10.1039/c3cp51906f. URL http://www.ncbi.nlm.nih.gov/pubmed/24390268.

[2] John Druce, Tatsumi Ishihara, and John Kilner. Surface composition of perovskite type materials studied by Low Energy Ion Scattering (LEIS). *Solid State Ionics*, 262:893–896, 2014. ISSN 01672738. doi: 10.1016/j.ssi.2013.09.010. URL http://dx.doi.org/10.1016/j.ssi.2013.09.010.

[3] Dongjo Oh, Danijel Gostovic, and Eric D. Wachsman. Mechanism of La0.6Sr0.4Co0.2Fe0.8O3 cathode degradation. *Journal of Materials Research*, 27 (15):1992–1999, jul 2012. ISSN 0884-2914. doi: 10.1557/jmr.2012.222. URL http://www.journals.cambridge.org/abstract{_}S0884291412002221.

[4] Walter a. Harrison. Origin of Sr segregation at La_{1-x}Sr_{x}MnO_{3} surfaces. *Physical Review B*, 83(15):155437, apr 2011. ISSN 1098-0121. doi: 10.1103/PhysRevB.83.155437. URL http://link.aps.org/doi/10.1103/PhysRevB.83.155437.

[5] Yan Chen, Helena Téllez, Monica Burriel, Fan Yang, Nikolai Tsvetkov, Zhuhua Cai, David W. McComb, John A. Kilner, and Bilge Yildiz. Segregated chemistry and structure on (001) and (100) surfaces of (La1-xSrx)2CoO4 override the crystal anisotropy in oxygen exchange kinetics. *Chemistry of Materials*, (001):150630082136008, 2015. ISSN 0897-4756. doi: 10.1021/acs.chemmater.5b02292. URL http://dx.doi.org/10.1021/acs.chemmater.5b02292.

[6] Per Hjalmarsson, Martin S??gaard, and Mogens Mogensen. Electrochemical performance and degradation of (La0.6Sr0.4)0.99CoO3 - ?? as porous SOFC-cathode. *Solid State Ionics*, 179(27-32):1422–1426, 2008. ISSN 01672738. doi: 10.1016/j.ssi.2007.11.010.

Part IV

APPENDIX

A

APPENDIX

A.1 ISOTOPIC EXCHANGE METHODOLOGY

1. It is good practice to leave the equipment under vacuum in between experiments/users. Therefore, the first step is to introduce a gas (^{16}O or Nitrogen depending on the setup) to raise the experimental chamber to ambient pressure.
2. The quartz tube is then removed and samples placed into the sample holder.
3. Using a fresh copper seal, the quartz tube is then re-attached to the flange and tightened to create an air tight seal.
4. The low pressure gauge must be turned off to prevent damage under exposure to pressures above its operating limit.
5. At this point the attached nitrogen cylinder should be opened to fill the gas line, then closed once the pressure is stable.
6. The pumping system must now be turned off and sufficient time should be left such that the turbomolecular pump rotation is below 10 Hz.
7. The gate valve of a system may now be opened.
8. The pumping system may now be turned on again.
9. When the rotation of the turbomolecular pump reaches 450 Hz the low pressure gauge may be turned on again[1].
10. It is necessary to wait until the pressure of the system is below 2 x 10^{-7} mbar.
11. When the pressure has dropped sufficiently the gate valve may be closed.
12. The relevant gas now may be introduced. For the pre-anneal step this will be ^{16}O.
13. The data collection must be set up and set to record. In this work the software collected the chamber pressure and thermocouple temperature every 2 seconds.

1 To ensure the high vacuum will spark

14. The furnace may now be lowered over quartz tube such that the sample is in the hotzone. This was considered t = 0 for the experimental anneal time.
15. Once the desired anneal time has finished the furnace is lifted off the quartz tube and the sample is allowed to cool to room temperature.
16. Data collection may now be stopped.
17. Steps 4 - 11 must now be repeated in order to pump the system.
18. Steps 12 - 15 may now be repeated, however, the enriched gas must be introduced to the sample chamber.
19. Upon completion the leak valve is opened and the RGA is turned on. Masses 16, 18, 32, 34 and 36 are measured until there is linear measurement is achieved.
20. Once the RGA data has been collected the leak vale may be closed and the RGA turned off.
21. To recover the enriched gas, the reservoir must be enveloped in liquid nitrogen.
22. When the pressure of the reservoir is below 1 mbar the reservoir valve may be opened to recover the gas.
23. Step may is repeated to increase the chamber pressure once again.
24. The quartz tube is then removed and samples may be removed.
25. If another sample is to be exchanged the process is started again.
26. If not, steps 4 - 11 are repeated to pump the system.